



Le rôle des états interactifs des régulateurs des points de contrôle immunitaires dans le cancer : déterminé par l'imagerie quantitative avancée.

James Miles

► To cite this version:

James Miles. Le rôle des états interactifs des régulateurs des points de contrôle immunitaires dans le cancer : déterminé par l'imagerie quantitative avancée.. Human health and pathology. Université de Bordeaux; Universidad del País Vasco, 2022. English. NNT : 2022BORD0051 . tel-03881715

HAL Id: tel-03881715

<https://theses.hal.science/tel-03881715>

Submitted on 2 Dec 2022

HAL is a multi-disciplinary open access archive for the deposit and dissemination of scientific research documents, whether they are published or not. The documents may come from teaching and research institutions in France or abroad, or from public or private research centers.

L'archive ouverte pluridisciplinaire **HAL**, est destinée au dépôt et à la diffusion de documents scientifiques de niveau recherche, publiés ou non, émanant des établissements d'enseignement et de recherche français ou étrangers, des laboratoires publics ou privés.

THE ROLE OF INTERACTIVE STATES OF IMMUNE CHECKPOINT REGULATORS IN CANCER: DETERMINED BY QUANTITATIVE IMAGING

James Miles

Supervisors:

Prof Banafshé Larijani

Prof Antoine Italiano

Thesis submitted for the award of Doctor of
Philosophy (2022)

THÈSE EN COTUTELLE PRÉSENTÉE
POUR OBTENIR LE GRADE DE
DOCTEUR DE
L'UNIVERSITÉ DE BORDEAUX
ET DE L'UNIVERSITÉ DE PAYS BASQUE

ÉCOLE DOCTORALE UBX : Science de la vie et de la santé

ÉCOLE DOCTORALE DU PARTENAIRE : Biologie moléculaire et biomédecine

SPÉCIALITÉ : Bioimagerie

Par James MILES

**Le Rôle des États Interactifs des Régulateurs des Points de
Contrôle Immunitaires dans le Cancer: Déterminé par L'imagerie
Quantitative Avancée.**

Sous la direction de Prof Banafshe Larijani
et de Prof Antoine Italiano

Soutenue le
25/02/2022

Membres du jury :

	Professeur Emerite	Président
M. Goñ, Felix	Professeur	Rapporteur
M. Vaux, David	Professeur	Rapporteur
M. Bankaitis, Vytas M.	Professeur Assistant	Examineur
McIntyre, Alan Mme	Docteure	Examineur
M. Soubeiran, Pierre	Professeur	Examineur
M. Vivanco, Maria	Professeur	Examineur
M. Vaux, David		

Titre : Le Rôle des États Interactifs des Régulateurs des Points de Contrôle Immunitaires dans le Cancer: Déterminé par L'imagerie Quantitative Avancée.

Résumé : [4000 caractères maximum, espaces compris]

Les points de contrôle immunitaires, tels que PD-1/PD-L1 et CTLA-4/CD80, sont des mécanismes de régulation du système immunitaire conçus pour favoriser l'autotolérance et éviter les maladies auto-immunes. Une variété de cancers modulent ces points de contrôle immunitaires, en augmentant l'expression de leurs ligands apparentes, afin d'éviter la détection et la destruction immunitaires. Les thérapies de blocage des points de contrôle immunitaires ont amélioré le traitement du cancer dans les cancers du poumon et du rein ainsi que dans le mélanome. Cependant, seul un petit sous-groupe de patients obtient des effets durables et la plupart acquièrent une résistance primaire ou secondaire. La plupart des patients sont stratifiés pour les traitements anti-PD-1 ou anti-CTLA-4 en fonction de l'expression de leur ligand PD-L1. L'expression du ligand est actuellement évaluée par des approches traditionnelles d'immunohistochimie (IHC), qui sont subjectives, manquent de quantification et n'ont pas de gamme dynamique. Les progrès de l'IHC quantitative ont permis de résoudre spatialement l'expression des ligands des points de contrôle immunitaires, mais cela ne correspond pas à l'engagement du récepteur-ligand. Nous avons développé une nouvelle plateforme d'imagerie quantitative, étayée par le transfert d'énergie de résonance de Förster (FRET) résolu dans le temps et déterminé par la microscopie d'imagerie de durée de vie de fluorescence (FLIM) à domaine de fréquence, afin de quantifier spatialement ces interactions de points de contrôle immunitaires à une résolution nanoscopique (<10nm). Ce test est appelé immune-FRET (iFRET). Nous avons validé la capacité de l'iFRET à mesurer les engagements de PD-1/PD-L1 et CTLA-4/CD80 dans un essai de co-culture cellulaire, puis nous avons appliqué l'iFRET pour déterminer les interactions PD-1/PD-L1 dans une étude rétrospective sur le mélanome malin et le cancer du poumon « non à petites cellules » (CPNPC) malin. Dans les mélanomes et les CPNPC, il a été observé que l'augmentation de l'état d'interaction PD-1/PD-L1, déterminée par l'iFRET, était corrélée à une détérioration de la survie globale. L'expression de PD-L1, le critère de stratification actuel de l'immunothérapie, n'a pas permis d'établir une corrélation avec le résultat des patients. Nous avons appliqué l'iFRET à PD-1/PD-L1 et CTLA-4/CD80 dans une étude prospective. Un sous-groupe de patients atteints de cancer colorectal avec des métastases pulmonaires qui ne répondent pas aux traitements classiques voient leurs métastases traitées par ablation par radiofréquence (ARF). Entre les traitements par ARF, il a été documenté qu'un effet abscopal peut se produire entre le traitement des poumons un et deux. Nous avons donc appliqué l'iFRET pour évaluer ces interactions de points de contrôle dans les métastases pulmonaires traitées avant et après l'ARF. Bien que nous n'ayons pas pu rendre compte directement

des mécanismes d'un effet abscopal, nous avons détecté des modèles d'interaction PD-1/PD-L1 et CTLA-4/CD80 différentiels chez les patients, qui peuvent être utilisés pour prédire à quelles thérapies un patient répondra. Nous avons également détecté une corrélation négative entre l'interaction PD-1/PD-L1 et la densité CD3⁺ intratumorale. De manière critique, aucun des deux points de contrôle n'était corrélé à l'expression du ligand. Cela pourrait changer le paradigme de l'immuno-oncologie actuelle et le raisonnement derrière la sélection des traitements des patients. Enfin, nous avons cherché à appliquer l'iFRET et CRISPR/Cas12 pour sonder les mécanismes intracellulaires par lesquels le ITSM de PD-1 exerce ses effets négatifs. Nous avons généré des mutations Y248A et Y248E dans l'ITSM de PD-1 et prévoyons de vérifier si la SHP-2 seule ou la SHP-1 et la SHP-2 sont responsables de la transduction du signal. Nous prévoyons également d'évaluer si l'état de phosphorylation Y248 constitue un mécanisme de régulation de l'état d'interaction PD-1/PD-L1. Pris ensemble, ces résultats indiquent une nouvelle technique permettant d'évaluer l'engagement des points de contrôle immunitaires dans les échantillons de patients. Cette technique pourrait fonctionner en tandem avec d'autres techniques d'IHC quantitatives, telles que l'imagerie par spectrométrie de masse, et pourrait être appliquée à une série de points de contrôle immunitaires. Elle donne naissance à la notion de surveillance immunitaire quantitative, qui pourrait permettre de suivre la protéomique fonctionnelle des patients au fil du temps. En résumé, les résultats de cette étude pluridisciplinaire et donc la mise en œuvre de l'iFRET pour effectuer une surveillance immunitaire quantitative pourraient modifier la façon dont les patients sont sélectionnés pour les immunothérapies et fournir un mécanisme permettant de surveiller leur réponse au traitement.

Mots clés :

FRET/FLIM, PD-1/PD-L1, CTLA-4/CD80, ablation par radiofréquence, surveillance immunitaire quantitative

Title : The Role of Interactive States of Immune Checkpoint Regulators in Cancer: Determined by Quantitative Imaging

Abstract : [4000 caractères maximum]

Immune checkpoints, such as PD-1/PD-L1 and CTLA-4/CD80, are regulatory mechanisms in the immune system designed to promote self-tolerance and avoid autoimmune diseases. A range of cancers modulate these immune checkpoints, by upregulating their cognate ligands, to avoid immune detection and destruction. Immune checkpoint blockade therapies have enhanced cancer therapy in lung and renal cancers as well as melanoma. However, only a small subset of patients experience durable effects, and most acquire primary or secondary resistance. Most patients are stratified for anti-PD-1 or anti-CTLA-4 treatments based on their PD-L1 ligand expression. Ligand expression is currently assessed by traditional immunohistochemistry (IHC) approaches, which are subjective, lack quantitation and a dynamic range. Advances in quantitative IHC have spatially resolved immune checkpoint ligand expression, but this does not correlate with receptor-ligand engagement. We have developed a novel quantitative imaging platform, underpinned by time-resolved Förster resonance energy transfer (FRET) determined by frequency-domain fluorescence lifetime imaging microscopy (FLIM) to spatially quantitate these immune checkpoint interactions at a nanoscopic (<10nm) resolution. This assay is termed immune-FRET (iFRET). We validated the ability of iFRET to measure PD-1/PD-L1 and CTLA-4/CD80 engagements in a cell co-culture assay and then applied iFRET to determine PD-1/PD-L1 interactions in a retrospective study with malignant melanoma and malignant non-small cell lung carcinoma (NSCLC). In both melanoma and NSCLC, it was observed that increased PD-1/PD-L1 interaction state, determined by iFRET, correlated with a worsened overall survival. PD-L1 expression, the current stratification criterion of immunotherapy, failed to correlate with patient outcome. We applied iFRET to PD-1/PD-L1 and CTLA-4/CD80 in a prospective study. A subset of colorectal cancer patients with lung metastases who fail to respond to classical treatments have their metastases treated by radiofrequency ablation (RFA). Between RFA treatments, it has been documented, that an abscopal effect may occur between the treatment of lungs one and two. We therefore applied iFRET to assess these checkpoint interactions in pre- and post-RFA treated lung metastases. Whilst we could not directly report on the mechanisms of an abscopal effect, we detected differential PD-1/PD-L1 and CTLA-4/CD80 interaction patterns within patients, which may be used to predict which therapies a patient would respond to. We also detected a negative correlation between PD-1/PD-L1 interaction and intratumoral CD3⁺ density. Critically, neither checkpoint engagement correlated with ligand expression. This could change the paradigm of current

immune oncology and the rationale behind selecting patient treatments. Lastly, we sought to apply iFRET and CRISPR/Cas12 to probe the intracellular mechanisms by which the ITSM of PD-1 effects its negative effects. We generated Y248A and Y248E mutations in the ITSM of PD-1 and plan to probe if SHP-2 alone or SHP-1 and SHP-2 are responsible for signal transduction. We also plan to assess whether Y248 phosphorylation state poses a regulatory mechanism by which to regulate PD-1/PD-L1 interaction state. Taken together, these results indicate a novel technique by which to assess immune checkpoint engagement in patient samples. This could work in tandem with other quantitative IHC techniques, such as imaging mass spectrometry (IMS) and may be applied to a range of immune checkpoints. This gives rise to the notion of quantitative immune surveyance which may monitor the functional proteomics of patients over time. To summarise, the results from this multi-disciplinary investigation and thus the implementation of iFRET to carry out quantitative immune surveyance may change the way patients are selected for immunotherapies and may provide a mechanism by which to monitor their response to treatment.

Keywords :

FRET/FLIM, PD-1/PD-L1, CTLA-4/CD80, Radiofrequency Ablation, Quantitative Immune Surveyance

Statement of Originality

The entirety of Chapter 3 is composed from the research article “High PD-1/PD-L1 Checkpoint Interaction Infers Tumour Selection and Therapeutic Sensitivity to Anti-PD-1/PD-L1 Treatment” Sánchez-Magraner and Miles et al., 2020. Data presented in Figures 3.3 and 3.4 were produced by Dr. Lissete Sánchez-Magraner and Katriona Withers (MPharmacol placement student, University of Bath). The work presented in Figure 3.5 was carried out by Claire L. Baker (MPharmacol placement student, University of Bath). Labelling and acquisition of samples and data analysis for the results in Figures 3.6 – 3.10 was carried out by myself. Figures 3.1 and 3.2 and Tables 3.1, 3.2 and 3.3 were produced by myself. I took a leading role in manuscript preparation, writing, proofing and corrections.

Some patient samples from Chapter 4 were run on our mfFLIM platform by Christopher Applebee (MSc Engineer, Cell Biophysics Laboratory) and Sandra del Castillo (placement student, University of the-Basque Country (UPV/EHU)).

T-lymphocyte infiltration labelling, presented in Chapter 4, was performed by Professor Franck Pagès team, at the Hôpital Européen Georges-Pompidou (Hôpitaux Universitaires Paris-Ouest).

Statement of Confidentiality

The results in Chapter 4 are strictly confidential and therefore must not be disclosed or redistributed under any circumstances.

Acknowledgements

The journey of a thesis is not one of translating research from the workbench to a document, but a journey in which the mind and determination of a scientist evolves. My deepest and most profound gratitude is reserved for my thesis supervisor Banafshé Larijani. Without the initial backing and support of Banafshé, I would never have picked up a pipette after the second year of my pharmacology degree. Banafshe's support and continual guidance has shaped the way I think and the respect I now hold for science and research. Her knowledge and supervision of my masters and doctoral studies have been critical in my completion of these studies. My co-supervisor Antoine Italiano (Institut Bergonié, Université de Bordeaux) is deeply thanked for his guidance and support throughout my doctoral studies. Enormous thanks are given to Jean Palussière (Institut Bergonié) for his passion to deepen the molecular understanding of radiotherapies has been a cornerstone of this PhD, with his guidance and help being critical for its completion. Steve Ward (University of Bath) has provided invaluable guidance, support, teaching, and insight into multiple aspects of this doctoral thesis. Without his insight into the immune system and its complexities I would still be drowning in abbreviations and signalling crosstalk! Alicia Alonso (Universidad del País Vasco (UPV/EHU)) has endured storms of emails from me throughout this PhD, and reminded, without fail, every year of my PhD, that I have to re-enrol at the university. One would think after two years the message would sink in! Alicia has been a rock throughout my PhD, and I am forever grateful for her help and support.

Due to the extremely collaborative nature of my PhD, I am fortunate enough to be writing such a long acknowledgements section where help, guidance, friendship, and support have been given by so many. Firstly I must thank those I have had the opportunities to work with in the Cell Biophysics Laboratory. Christopher Applebee will forever be a friend and ranked amongst my closest and most valuable colleagues. Never without ample amount of support, questionable humour, and red wine, without Chris I am certain that this PhD will not have reached completion. Throughout my masters degree and subsequent PhD studies, I have had the pleasure of working with a range of masters students. Charlie Evans, Sam Packham-Walsh, Claire Baker, David Adegbite, Chloe Thomson, and Emmeline Tregembo are colleagues whom I enjoyed working with and enjoyed their support and friendship throughout my studies. Claire Baker and Kat Withers are given particular thanks for their work and contributions that led to the development of the work that went into Chapter 3. Régine Dazzoni and Marta Gutierrez Lete also provided copious help, teaching and support throughout my studies and without this I would not have the skill set required to complete a doctorate.

I must thank everyone within my scientific homes in the beautiful Basque Country. Ionan Marigomez

and Manu Soto, the director and co-director respectively of the Plentzia marine station, PiE. PiE, since my first master's placement in 2015, has become a second home to me. All those who work and study within the marine station have never wavered in lending me their full support and friendship, which has ensured I have retained the desire, mental capacity, and determination to complete a PhD. FASTBASE Solutions S.L., the biotechnology spin-off company founded by Banafshé and Peter J Parker (Kings College London) have been instrumental in helping to fund and house my doctoral studies. Particular thanks is given to Lissete Sánchez-Magraner who has provided constant support, guidance and help towards this thesis. I am very thankful to Mary Richardson who has been enormously supportive throughout the entirety of my PhD. I am forever grateful for her personal support which has aided the completion of this thesis. I am deeply thankful to the Basque Government for awarding me the Bikaintek grant (2018-2021) which funded this doctoral work. I am thankful to the Instituto Biofisika and the Department of Biochemistry and Molecular Biology (UPV/EHU) for hosting my doctoral studies and some of the research performed in this thesis.

I was fortunate enough to have the opportunity to work in the laboratory of David Vaux in the Sir William Dunn School of Pathology, Oxford. David's knowledge spreads so far and so deep across a breadth of knowledge that is difficult to parallel. His guidance of the fifth chapter of this thesis has been invaluable and his kind offerings of support across the other chapters is appreciated. Lior Pytowski deserves a special mention, for without his continued support, and copious amounts of patience, intelligence and humour, Chapter 5 would not have made it past a conceptual stage. Zayra Hernandez and Jamie Elwell are deeply thanked for their help throughout my time in Oxford, also helping me to complete a plethora of experiments and teaching me new techniques day after day, particularly in the world of cooking and baking!

I have had the fortune to work with and meet an abundance of renowned scientists throughout my studies. Mentions must go to Vytas Bankaitis (Texas A&M), who has been somewhat of a mentor to me, helping to shape the conceptualisation of my fifth results chapter and constantly helping me to juggle science and the personality which is needed to accomplish science under difficult circumstances. Peter Parker has been a fountain of knowledge and guidance for my studies, regularly offering to meet and go through my work with Banafshe and I in order to leave no stone unturned and to pave the way for ensuring clarity and understanding of complex scientific concepts. Pierre Leboucher is thanked for development and implementation of our automated FLIM algorithm. Without this valuable tool, I would no doubt still be manually acquiring tissue sections. Johan Herz (Lambert Instruments) is thanked for his ongoing support and help with our LI-FLIM hardware and software. Iñaki Lopez (Hospital de Cruces-Osakidetza) is thanked for his help, provision of tissue sections, and collaboration throughout my masters and doctoral studies. Kenton Arkill (University of Nottingham) is thanked for his support and insights and more than required humour. Stefanie S Jeffrey (Stanford University) is thanked for her

medical insights into the results presented in Chapter 4. Franck Pagès (Hôpital Européen Georges-Pompidou) is also thanked, as his immune infiltrate labelling of patient tissue sections has provided key results and scientific opportunities in the latter stages of my studies.

Lastly, I must thank and appreciate those who laid the foundations for my desire to pursue a scientific career. The pharmacology department at the University of Bath were instrumental in teaching me the value of research, science, and integrity. Christine Edmead and Paul Mitchell will always be remembered for their support through my studies.

The last, and by all means deepest thanks must be reserved for my family. My Mum and Dad always instilled in me that one must always push the boundaries of excellence in order to achieve, this has been a mantra that any doctoral student should follow. My aunt Julie has always offered her continued support throughout my life and studies, and I am sure without her support I also would not have reached this milestone. To my Nan, to whom this thesis is dedicated, the philosophy of “you can only ever try your best, if you do that, there is nothing more to worry about” has ensured that excess insanity did not set in throughout these studies. Lastly, to Anne Le Henaff, I offer my deepest and most sincere thanks, as I am sure the completion of this thesis would have been a lot more painful and delayed without her faultless support, humour, compassion, and kindness.

With the fortune of undertaking such a multidisciplinary PhD, I am sure some names may not have made the above list. However, to all I have met throughout my studies, I am grateful. It can be an honest claim that the James Miles who started this PhD in 2018 is not the same James Miles who has written this acknowledgement section in 2021.

Abstract

Immune checkpoints, such as PD-1/PD-L1 and CTLA-4/CD80, are regulatory mechanisms in the immune system designed to promote self-tolerance and avoid autoimmune diseases. A range of cancers modulate these immune checkpoints, by upregulating their cognate ligands, to avoid immune detection and destruction. Immune checkpoint blockade therapies have enhanced cancer therapy in lung and renal cancers as well as melanoma. However, only a small subset of patients experience durable effects, and most acquire primary or secondary resistance. Most patients are stratified for anti-PD-1 or anti-CTLA-4 treatments based on their PD-L1 ligand expression. Ligand expression is currently assessed by traditional immunohistochemistry (IHC) approaches, which are subjective, lack quantitation and a dynamic range. Advances in quantitative IHC have spatially resolved immune checkpoint ligand expression, but this does not correlate with receptor-ligand engagement. We have developed a novel quantitative imaging platform, underpinned by time-resolved Förster resonance energy transfer (FRET) determined by frequency-domain fluorescence lifetime imaging microscopy (FLIM) to spatially quantitate these immune checkpoint interactions at a nanoscopic (<10nm) resolution. This assay is termed immune-FRET (iFRET). We validated the ability of iFRET to measure PD-1/PD-L1 and CTLA-4/CD80 engagements in a cell co-culture assay and then applied iFRET to determine PD-1/PD-L1 interactions in a retrospective study with malignant melanoma and malignant non-small cell lung carcinoma (NSCLC). In both melanoma and NSCLC, it was observed that increased PD-1/PD-L1 interaction state, determined by iFRET, correlated with a worsened overall survival. PD-L1 expression, the current stratification criterion of immunotherapy, failed to correlate with patient outcome. We applied iFRET to PD-1/PD-L1 and CTLA-4/CD80 in a prospective study. A subset of colorectal cancer patients with lung metastases who fail to respond to classical treatments have their metastases treated by radiofrequency ablation (RFA). Between RFA treatments, it has been documented, that an abscopal effect may occur between the treatment of lungs one and two. We therefore applied iFRET to assess these checkpoint interactions in pre- and post-RFA treated lung metastases. Whilst we could not directly report on the mechanisms of an abscopal effect, we detected differential PD-1/PD-L1 and CTLA-4/CD80 interaction patterns within patients, which may be used to predict which therapies a patient would respond to. We also detected a negative correlation between PD-1/PD-L1 interaction and intratumoral CD3⁺ density. Critically, neither checkpoint engagement correlated with ligand expression. This could change the paradigm of current immune oncology and the rationale behind selecting patient treatments. Lastly, we sought to apply iFRET and CRISPR/Cas12 to probe the intracellular mechanisms by which the ITSM of PD-1 effects its negative effects. We generated Y248A and Y248E mutations in the ITSM of PD-1 and plan to probe if SHP-2 alone or SHP-1 and SHP-2 are responsible for signal transduction. We also plan to assess whether Y248 phosphorylation state poses a regulatory mechanism by which to regulate PD-1/PD-L1 interaction state.

Taken together, these results indicate a novel technique by which to assess immune checkpoint engagement in patient samples. This could work in tandem with other quantitative IHC techniques, such as imaging mass spectrometry (IMS) and may be applied to a range of immune checkpoints. This gives rise to the notion of quantitative immune surveyance which may monitor the functional proteomics of patients over time. To summarise, the results from this multi-disciplinary investigation and thus the implementation of iFRET to carry out quantitative immune surveyance may change the way patients are selected for immunotherapies and may provide a mechanism by which to monitor their response to treatment.

Abstract

Les points de contrôle immunitaires, tels que PD-1/PD-L1 et CTLA-4/CD80, sont des mécanismes de régulation du système immunitaire conçus pour favoriser l'autotolérance et éviter les maladies auto-immunes. Une variété de cancers modulent ces points de contrôle immunitaires, en augmentant l'expression de leurs ligands apparentes, afin d'éviter la détection et la destruction immunitaires. Les thérapies de blocage des points de contrôle immunitaires ont amélioré le traitement du cancer dans les cancers du poumon et du rein ainsi que dans le mélanome. Cependant, seul un petit sous-groupe de patients obtient des effets durables et la plupart acquièrent une résistance primaire ou secondaire. La plupart des patients sont stratifiés pour les traitements anti-PD-1 ou anti-CTLA-4 en fonction de l'expression de leur ligand PD-L1. L'expression du ligand est actuellement évaluée par des approches traditionnelles d'immunohistochimie (IHC), qui sont subjectives, manquent de quantification et n'ont pas de gamme dynamique. Les progrès de l'IHC quantitative ont permis de résoudre spatialement l'expression des ligands des points de contrôle immunitaires, mais cela ne correspond pas à l'engagement du récepteur-ligand. Nous avons développé une nouvelle plateforme d'imagerie quantitative, étayée par le transfert d'énergie de résonance de Förster (FRET) résolu dans le temps et déterminé par la microscopie d'imagerie de durée de vie de fluorescence (FLIM) à domaine de fréquence, afin de quantifier spatialement ces interactions de points de contrôle immunitaires à une résolution nanoscopique ($<10\text{nm}$). Ce test est appelé immune-FRET (iFRET). Nous avons validé la capacité de l'iFRET à mesurer les engagements de PD-1/PD-L1 et CTLA-4/CD80 dans un essai de co-culture cellulaire, puis nous avons appliqué l'iFRET pour déterminer les interactions PD-1/PD-L1 dans une étude rétrospective sur le mélanome malin et le cancer du poumon « non à petites cellules » (CPNPC) malin. Dans les mélanomes et les CPNPC, il a été observé que l'augmentation de l'état d'interaction PD-1/PD-L1, déterminée par l'iFRET, était corrélée à une détérioration de la survie globale. L'expression de PD-L1, le critère de stratification actuel de l'immunothérapie, n'a pas permis d'établir une corrélation avec le résultat des patients. Nous avons appliqué l'iFRET à PD-1/PD-L1 et CTLA-4/CD80 dans une étude prospective. Un sous-groupe de patients atteints de cancer colorectal avec des métastases pulmonaires qui ne répondent pas aux traitements classiques voient leurs métastases traitées par ablation par radiofréquence (ARF). Entre les traitements par ARF, il a été documenté qu'un effet abscopal peut se produire entre le traitement des poumons un et deux. Nous avons donc appliqué l'iFRET pour évaluer ces interactions de points de contrôle dans les métastases pulmonaires traitées avant et après l'ARF. Bien que nous n'ayons pas pu rendre compte directement des mécanismes d'un effet abscopal, nous avons détecté des modèles d'interaction PD-1/PD-L1 et CTLA-4/CD80 différentiels chez les patients, qui peuvent être utilisés pour prédire à quelles thérapies un patient répondra. Nous avons également détecté une corrélation négative entre l'interaction PD-1/PD-L1 et la densité CD3^+ intratumorale. De manière critique, aucun des deux points de contrôle

n'était corrélé à l'expression du ligand. Cela pourrait changer le paradigme de l'immuno-oncologie actuelle et le raisonnement derrière la sélection des traitements des patients. Enfin, nous avons cherché à appliquer l'iFRET et CRISPR/Cas12 pour sonder les mécanismes intracellulaires par lesquels le ITSM de PD-1 exerce ses effets négatifs. Nous avons généré des mutations Y248A et Y248E dans l'ITSM de PD-1 et prévoyons de vérifier si la SHP-2 seule ou la SHP-1 et la SHP-2 sont responsables de la transduction du signal. Nous prévoyons également d'évaluer si l'état de phosphorylation Y248 constitue un mécanisme de régulation de l'état d'interaction PD-1/PD-L1. Pris ensemble, ces résultats indiquent une nouvelle technique permettant d'évaluer l'engagement des points de contrôle immunitaires dans les échantillons de patients. Cette technique pourrait fonctionner en tandem avec d'autres techniques d'IHC quantitatives, telles que l'imagerie par spectrométrie de masse, et pourrait être appliquée à une série de points de contrôle immunitaires. Elle donne naissance à la notion de surveillance immunitaire quantitative, qui pourrait permettre de suivre la protéomique fonctionnelle des patients au fil du temps. En résumé, les résultats de cette étude pluridisciplinaire et donc la mise en œuvre de l'iFRET pour effectuer une surveillance immunitaire quantitative pourraient modifier la façon dont les patients sont sélectionnés pour les immunothérapies et fournir un mécanisme permettant de surveiller leur réponse au traitement.

Resumen

Los puntos de control inmunitarios, como PD-1/PD-L1 y CTLA-4/CD80, son mecanismos reguladores del sistema inmunitario, el cual está diseñado para promover la auto-tolerancia y evitar enfermedades autoinmunes. Una serie de cánceres modula estos puntos de control inmunitarios, mediante la regulación al alza de sus ligandos afines, para evitar la detección inmunitaria y su destrucción. Las terapias de bloqueo de puntos de control inmunitario han mejorado la terapia contra el cáncer tanto de pulmón como de riñón y melanomas. Sin embargo, solo un pequeño subgrupo de pacientes experimenta efectos duraderos y la mayoría adquiere resistencia primaria o secundaria. A la mayoría estos pacientes se les selecciona para tratamientos anti-PD-1 o anti-CTLA-4 según su expresión del ligando PD-L1. La expresión del ligando se evalúa actualmente mediante enfoques tradicionales de inmunohistoquímica (IHC), que son subjetivos, carecen de cuantificación y de rango dinámico. Los avances en IHC cuantitativa han resuelto espacialmente la expresión del ligando que es punto de control inmunitario pero esto no se correlaciona con el acoplamiento receptor-ligando. En esta tesis hemos desarrollado una nueva plataforma de imagen cuantitativa, basada en transferencia de energía de resonancia de Förster resuelta en el tiempo (FRET) determinada por medidas de tiempos de vida de la fluorescencia en el dominio de frecuencia (FLIM) de las imágenes de microscopía. Esto nos permite cuantificar espacialmente estas interacciones de puntos de control inmunitarios a una resolución nanoscópica (<10 nm). Este ensayo es denominado inmuno-FRET (iFRET). Hemos validado la capacidad de iFRET para medir PD-1/PD-L1 y las interacciones con CTLA-4/CD80 en un ensayo de co-cultivo de células y posteriormente hemos aplicado iFRET para determinar las interacciones PD-1/PD-L1 en un estudio retrospectivo en melanoma maligno y en cáncer de pulmón de células no pequeñas (NSCLC). Tanto en el melanoma como en el NSCLC, se observó que un aumento del estado de interacción PD-1/PD-L1, determinado por iFRET, se correlacionaba con una peor supervivencia global. La expresión de PD-L1, el criterio de clasificación actual para la inmunoterapia, no mostraba esta correlación con respecto al futuro del paciente.

También hemos aplicado iFRET a PD-1/PD-L1 y CTLA-4/CD80 en un estudio prospectivo. A un subconjunto de pacientes de cáncer colorrectal con metástasis pulmonares que no responden a los tratamientos clásicos se les trataron las metástasis mediante el método de ablación por radiofrecuencia (RFA). En los tratamientos de RFA, se ha documentado un efecto abscopal entre el tratamiento de un pulmón y otro. En este trabajo, hemos aplicado iFRET para evaluar estas interacciones de puntos de control en metástasis pulmonares tratadas antes y después de la RFA. Con los resultados obtenidos, si bien no podemos informar directamente sobre los mecanismos del efecto abscopal, detectamos patrones diferenciales de interacción PD-1/PD-L1 y CTLA-4/CD80 dentro de los pacientes, que se pueden utilizar para predecir a qué terapias responderían. También detectamos una correlación negativa entre Interacción PD-1/PD-L1 y la densidad intratumoral de CD3⁺. Muy importante, no se

observó correlación entre ninguno de los puntos de control con la expresión del ligando. Esto podría cambiar el paradigma de la inmunooncología actual y la justificación de la selección de los tratamientos para los pacientes. Por último, intentamos aplicar iFRET y CRISPR/Cas12 para analizar los mecanismos intracelulares por los cuales el ITSM (immunoreceptor tyrosine-based switching motif) de PD-1 ejerce sus efectos negativos. Hemos generado mutaciones Y248A y Y248E en el ITSM de PD-1, y planeamos investigar si SHP-2 sólo o SHP-1 y SHP-2 conjuntamente son responsables de la transducción de señales. También planeamos evaluar si el estado de fosforilación de Y248 constituye un mecanismo regulador que module el estado de interacción PD-1/PD-L1.

En conjunto, estos resultados permiten validar una técnica novedosa para evaluar en muestras de pacientes la participación de puntos de control inmunológicos. Nuestra técnica podría funcionar conjuntamente con otros métodos de la inmunohistoquímica cuantitativa (IHC), como la imagen por espectrometría de masas (IMS), y podría aplicarse a una variedad de puntos de control inmunitarios.

Esto nos lleva a la noción de vigilancia inmunológica cuantitativa, que permitiría monitorizar la proteómica funcional de pacientes a lo largo del tiempo. En resumen, los resultados de esta investigación multidisciplinar y la implementación de iFRET para llevar a cabo una vigilancia inmunológica cuantitativa pueden cambiar la forma en que se selecciona a los pacientes para su tratamiento mediante inmunoterapias y proporcionar un mecanismo para realizar un seguimiento de su respuesta al tratamiento.

Dedicated to Nan

Table of Contents

Chapter 1 : Introduction	1
1.1 : Cancer: Current Knowledge, Treatment and Prognostics	1
1.2 : An Introduction to the Innate Immune System	4
1.3 : An Introduction to the Adaptive Immune System.....	8
1.4 : How is the Immune System Implicated in Cancer Progression?.....	16
1.4.1 : The Role of the CTLA-4/CD80 Signalling Axis in Cancer.....	18
1.4.2 : The Role of the PD-1/PD-L1 Signalling Axis in Cancer	21
1.5 : Current Approaches to Quantitative Proteomics in Cancer.....	27
1.5.1 : Current Shortcomings of Non-Quantitative Immunohistochemistry.....	27
1.5.2 : Advancements of Quantitative Immunohistochemistry	27
1.5.3 : Quantitative Proteomics Determined by Mass Spectrometry.....	29
1.5.4 : The Unmet Need: The Spatiotemporal Resolution of Functional Proteomics.....	32
1.6 : Förster Resonance Energy Transfer (FRET) Determined by Fluorescence Lifetime Imaging Microscopy (FLIM)	37
1.6.1 : Introduction to FRET	37
1.6.2 : Steady-State vs Time-Resolved FRET	43
1.6.3 : FLIM in the Time-Domain.....	47
1.6.4 : FLIM in the Frequency-Domain	48
1.7 : Aims and Hypotheses.....	51
1.7.1 : Hypotheses	51
1.7.2 : Aims and Objectives	51
Chapter 2 : Materials and Methods	53
2.1 : Buffers and Reagents	53
2.1.1 Buffers.....	53
2.1.2 : Sample Preparation Solutions	53
2.2 : Molecular Biology	57
2.2.1 : Design of CRISPR Cloning Strategy	57
2.2.2 : Genomic DNA Extraction.....	62
2.2.3 : Polymerase Chain reaction.....	62
2.2.4 : Agarose Gel Electrophoresis.....	64
2.2.5 : Gel Extraction and Purification.....	64
2.2.6 : Restriction Digestion.....	65
2.2.7 : Ligation	65

2.2.8 : Gibson Assembly	65
2.2.9 : Bacterial Transformation.....	65
2.2.10 : Fluorescence Activated Cell Sorting	66
2.3 : Cell Biology	67
2.3.1 : General Culture Conditions.....	67
2.3.2 : Cell Passaging and Maintenance	67
2.3.3 : Freezing of Cell Stocks	68
2.3.4 : Transfection	68
2.4 : Förster Resonance Energy Transfer (FRET) Determined by Multiple-Frequency Fluorescence Lifetime Imaging Microscopy (mfFLIM)	70
2.4.1 : Frequency-Domain FLIM Acquisitions	70
2.4.2 : Semi-Automated FLIM Sample Mapping and Acquisition.....	71
2.5 : Two-site Immune-Amplified Förster Resonance Energy Transfer (iFRET) Labelling Assay .	71
2.5.1 : Development and Principles of a Two-Site Assay	71
2.5.2 : iFRET Labelling of Patient Tissue Sections.....	72
2.6 : Data Processing and Statistics.....	80
Chapter 3 : High PD-1/PD-L1 Checkpoint Interaction Infers Tumour Selection and Therapeutic Sensitivity to Anti-PD-1/PD-L1 Treatment.....	82
3.1 : Preface.....	82
3.2 : Introduction.....	82
3.3 : Materials and Methods	85
3.3.1 : Pathology	85
3.3.2 : Antibodies and Reagents.....	88
3.3.3 : Time-resolved Amplified iFRET Detected by FLIM.....	88
3.3.4 : iFRET Assay for PD-1/PD-L1 Interaction in Cell Culture.....	91
3.3.5 : iFRET Assay for CTLA-4/CD80 Interaction in Cell Culture.....	91
3.3.6 : iFRET Assay for PD-1/PD-L1 Interaction in FFPE ccRCC Tissue	92
3.3.7 : iFRET Assay for PD-1/PD-L1 Interaction in FFPE malignant melanoma TMAs	92
3.3.8 : iFRET Assay for PD-1/PD-L1 Interaction in FFPE Metastatic NSCLC.....	92
3.3.9 : Statistical Analysis	93
3.4 : Results.....	93
3.4.1 : Development, Validation and Benchmarking of a Novel Amplified FRET Imaging Assay for Determining Immune Checkpoint Interaction in ex-vivo Assays.....	93
3.4.2 : PD-L1 Expression Does Not Correspond to Interaction Status of PD-1 and PD-L1 in ccRCC	99
3.4.3 : PD-1/PD-L1 Interaction State is Indicative of Patient Outcome in Malignant Melanoma	99

3.4.4 : Lower PD-1/PD-L1 Interaction States Correlation with Worsened Overall and Progression-Free Survival in Metastatic NSCLC.....	104
3.4.5 : Discussion	107
Chapter 4 : The Quantification of PD-1/PD-L1 and CTLA-4/CD80 Interactions in Radiofrequency-Ablated Lung Metastases: Determined by Time-Resolved immune-FRET	110
4.1 : Preface.....	110
4.2 : Introduction.....	110
4.3 : Results.....	117
4.3.1 : CTLA-4/CD80 antibody concentration optimisation in tissue microarray.....	118
4.3.2 : Quantification of CTLA-4/CD80 and PD-1/PD-L1 interactions in pre-RFA treatment lung metastases.....	121
4.3.3 : Quantification of CTLA-4/CD80 and PD-1/PD-L1 interactions in post-RFA treatment lung metastases.....	125
4.3.4 : Immune Checkpoint Ligand Expression Does Not Correlate with Immune Checkpoint Engagement.....	127
4.3.5 : Correlation of immune checkpoint engagement with CD3 ⁺ and CD8 ⁺ T-lymphocyte infiltration.....	129
4.4 : Discussion	133
Chapter 5 : The Elucidation of Programmed Death Receptor 1 (PD-1) Activation Dynamics at Tyrosine-248 of the Immunoreceptor Tyrosine-based Switch Motif (ITSM)	138
5.1 : Introduction.....	138
5.2 : Results.....	145
5.2.1 : Creation of CRISPR Guides and Repair Templates.....	145
5.2.2 : Creation of <i>PDCDI</i> Y248-Specific CRISPR Guides.....	147
5.2.3 : Creation of single-stranded Y ₂₄₈ A and Y ₂₄₈ E Point Mutation Repair Templates with Microhomology Arms.....	147
5.2.4 : Creation of Donor Repair Templates with Full-Length Homology Arms.....	147
5.2.5 : Transfection into Leukemic Cell Lines	150
5.3 : Discussion	155
Chapter 6 : Discussion	160
6.1 : Summary of Results	160
6.1.1 : PD-1/PD-L1 Checkpoint Interaction State is Predictive of Patient Outcome in Malignant Melanoma and Metastatic Non-Small Cell Lung Carcinoma.....	160
6.1.2 : iFRET Can Detect Differential Checkpoint Interactions within RFA-Treated Patients..	161
6.1.3 : CRISPR/Cas12 Coupled to aFRET and iFRET May Elucidate the Intracellular Signalling Dynamics of PD-1 upon PD-L1 Ligation.....	161
6.2 : Future Perspectives	164
6.2.1 : Unravelling the Intracellular Signalling Dynamics of PD-1 and CTLA-4	164

6.2.2 : Assessment of CTLA-4/CD86 and PD-1/PD-L2	164
6.2.3 : Simultaneous Functional Spatial Mapping of Multiple Immune Checkpoints: iFRET and Imaging Mass Spectrometry as Complementary Techniques.....	167
Chapter 7 : References	174
Appendix.....	189

List of Tables

Table 2.1: List of Antibodies.....	54
Table 2.2: List of Reagents.....	55
Table 2.3: List of Oligonucleotides.....	58
Table 2.4: List of Enzymes.....	60
Table 2.5: List of Plasmids.....	60
Table 2.6: List of Molecular Cloning Kits.....	61
Table 2.7: List of Eukaryotic Cell Lines.....	61
Table 2.8: PCR reaction steps outlining the required temperatures, times, and number of cycles.....	64
Table 2.9: FuGENE HD transfection reagent:DNA ratios tested.....	69
Table 2.10: Primary antibody dilutions used for labelling the donor and acceptor sites of cell and FFPE patient samples, respectively.....	73
Table 2.11: Secondary F(ab') ₂ fragment dilutions used for the labelling of the donor and acceptor primary antibodies, respectively.....	74
Table 2.12: List of Clinical Parameters for Malignant Melanoma Patients.....	79
Table 2.13: List of Clinical Parameters for NSCLC Patients.....	80
Table 3.1: List of clinical parameters - malignant melanoma.....	86
Table 3.2: List of clinical parameters - NSCLC.....	87
Table 3.3: FRET efficiency can be used to calculate receptor-ligand distance.....	95
Table 4.1: FRET efficiency correlates with receptor-ligand distance.....	122
Table 4.2: Median interaction states vs intratumoral lymphocyte density.....	131
Table 4.3: Upper quartile interaction state vs intratumoral lymphocyte density.....	132

List of Equations

Equation 1-1: FRET Efficiency I.....	37
Equation 1-2: FRET Efficiency II.	38
Equation 1-3: Overlap Integral.....	40
Equation 1-4: k^2 Orientation Factor.....	40
Equation 1-5: Relationship between k^2, n, R_0	41
Equation 1-6: Decrease in Donor Fluorescence.	43
Equation 1-7: Correted excitation spectra after FRET.	43
Equation 1-8: Absorption Spectrum.	43
Equation 1-9: Increased Acceptor Fluorescence afteer FRET.	44
Equation 1-10: Measure of the Decay of Donor Fluorescence.	44
Equation 1-11: ϕ_T FRET Efficiency.	44
Equation 1-12: Distance Between Two Chromophores.	45
Equation 1-13: Time Resolution of FRET I.	45
Equation 1-14: Time Resolution of FRET II.	45
Equation 1-15: Amplitude-Averaged Decay.	45
Equation 1-16: Calculation of Monoexponential Decay I.	47
Equation 1-17: Calculation of Monoexpontneital Decay II.	47
Equation 1-18: Calculation of Lifetime in the Frequency Domain.	48
Equation 1-19: Calculation of Phase Shift.	48
Equation 1-20: Calculation of Modulation Ratio.	48
Equation 3-1: Calculation of FRET Efficiency.....	89

List of Figures

Figure 1.1: The Hallmarks of Cancer:	2
Figure 1.2: Balance of pro- and anti-inflammatory cytokines.	5
Figure 1.3: Summary of innate immune cells.....	7
Figure 1.4: TCR engagement invokes a cascade of lymphocyte signalling events.....	9
Figure 1.5: CD8 ⁺ cells retain adaptive immune memory upon clearance of an infection.....	11
Figure 1.6: Differential cytokine exposure results in Th lymphocyte differentiation.	13
Figure 1.7: Tregs can exert their immunosuppressive function in multiple ways.....	15
Figure 1.8: The crystal structure of CTLA-4 and CD80.	17
Figure 1.9: The three mechanisms by which CTLA-4 exerts its immunosuppressive functions.....	20
Figure 1.10: The crystal structure of the extracellular domain of PD-1.....	22
Figure 1.11: PD-1/PD-L1 engagement results in the recruitment of SHP-2 to the pY ₂₄₈ residue of the ITSM of PD-1.....	24
Figure 1.12: Linear structures of SHP-1 and SHP-2.	26
Figure 1.13: MALDI-MS allows for the spatial resolution of biomarker abundance within a tissue section.....	31
Figure 1.14: Time resolved FRET unravels the activation dynamics of PKB.	34
Figure 1.15: aFRET quantifies biomarker activation state which is predictive of patient outcome. ...	36
Figure 1.16: Jablonski diagram indicating the Coulombic interactions that underpin resonance energy transfer.....	39
Figure 1.17: Excitation/emission spectrum from ATTO488 and Alexa594.	42
Figure 1.18: Intensity decay curve for time-domain FLIM.....	46
Figure 1.19: Sinusoidally modulated light is the excitation source for frequency-domain FLIM.....	50
Figure 2.1: Overview of the polymerase chain reaction.....	63
Figure 2.2: Tyramide Signal Amplification is Used to Conjugate the Acceptor Chromophore to the Sample.	75
Figure 2.3: iFRET Labelling Workflow.	76
Figure 3.1: Scale Bar and iFRET Labelling Schematic.....	84
Figure 3.2: Schematics of TSA, mfFLIM and Förster Radius.	90
Figure 3.3: iFRET detects and quantifies PD-1/PD-L1 interaction between CHO K1 and Jurkat cells.	94
Figure 3.4: iFRET precisely determines CTLA-4/CD80 interaction between Raji and Jurkat cells. ...	96
Figure 3.5: PLA detects proximity between PD-1 and PD-L1 but does not report on interaction.....	98
Figure 3.6: iFRET detects heterogeneity of PD-1 and PD-L1 interaction in FFPE ccRCC.....	100

Figure 3.7: PD-L1 expression does not correlate with PD-1/PD-L1 interaction state in malignant melanoma.....	101
Figure 3.8: PD-1/PD-L1 interaction state predicts patient outcome in malignant melanoma, where PD-L1 expression fails to do so.....	103
Figure 3.9: iFRET quantifies PD-1/PD-L1 interaction state in metastatic NSCLC alongside inter and intra patient heterogeneity. A) FLIM images show intensity and lifetime maps of a FFPE metastatic NSCLC sample.....	105
Figure 3.10: Lower PD-1/PD-L1 interaction correlates to a significantly worsened patient survival in metastatic NSCLC.	106
Figure 4.1: Overview of radiofrequency ablation of lung metastases.	112
Figure 4.2: The three mechanisms by which CTLA-4 exerts its immunosuppressive functions.....	114
Figure 4.3: iFRET labelling schematic.....	116
Figure 4.4: iFRET detects CTLA-4/CD80 interaction in FFPE sections for the first time.....	119
Figure 4.5: iFRET quantifies high and low CTLA-4/CD80 interaction states in lung metastases, detecting inter and intratumoral heterogeneity.....	120
Figure 4.6: iFRET detects intra and intertumoral heterogeneity in both CTLA-4/CD80 and PD-1/PD-L1 interactions in metastases from lung one (pre-RFA).	123
Figure 4.7: iFRET detects intra and intertumoral heterogeneity in both CTLA-4/CD80 and PD-1/PD-L1 interactions in metastases from lung two (post-RFA).....	124
Figure 4.8: iFRET quantifies high and low PD-1/PD-L1 interaction states in lung metastases, detecting inter and intratumoral heterogeneity.....	126
Figure 4.9: Checkpoint interaction does not correlate with ligand expression in RFA-treated metastases.	128
Figure 4.10: Median PD-1/PD-L1 interaction state negatively correlates with intratumoral CD3 ⁺ and CD8 ⁺ density in metastases from lung one (pre RFA).	130
Figure 4.11: CD3 ⁺ and CD8 ⁺ intratumoral density may not correlate with immune checkpoint interaction due to the presence of naïve T lymphocytes or the presence of other checkpoint interactions.....	136
Figure 5.1: PD-1/PD-L1 engagement results in phosphorylation of Y ₂₄₈ of the ITSM of PD-1.....	140
Figure 5.2: Linear structures of SHP-1 and SHP-2.	141
Figure 5.3: An overview of CRISPR/Cas9 for gene editing.	143
Figure 5.4: A pAsCpf1 (Cas12) guide plasmid was created which contains a guide sequence homologous to the 20 amino acids that follow the Y ₂₄₈ locus.....	146
Figure 5.5: Sanger sequencing analysis confirms the creation of the Y ₂₄₈ A insert.	148
Figure 5.6: Sanger sequencing analysis confirms the creation of the Y ₂₄₈ E insert.	149

Figure 5.7: The Y ₂₄₈ A donor repair template with full-length homology arms was successfully cloned: confirmed by Sanger sequencing analysis.	151
Figure 5.8: The Y ₂₄₈ E donor repair template with full-length homology arms was successfully cloned: confirmed by Sanger sequencing analysis.	152
Figure 5.9: Representative images show high transfection cytotoxicity when transfecting MOLT-4 cells with lipid-based or electroporation-based transfection.	154
Figure 5.10: Predicted SHP-1/PD-1 interactions.	157
Figure 6.1: Increased PD-L2 mRNA expression significantly correlates with an improved OS in NSCLC.	163
Figure 6.2: Decreased mRNA CD86 expression significantly correlates with a worsened OS in NSCLC.	166
Figure 6.3: Median LAG-3 mRNA expression significantly correlates with a worsened clinical outcome in NSCLC.	168
Figure 6.4: Median TIM-3 mRNA expression significantly correlates with a worsened clinical outcome in NSCLC.	169
Figure 6.5: Median TIGIT mRNA expression does not correlate with clinical outcome in NSCLC.	170
Figure 6.6: Median VISTA mRNA expression correlates with an improved clinical outcome in NSCLC.	171
Figure 6.7: Routine patient screening with iFRET and IMS may change the paradigm of current immunotherapy prescriptions.	173

Abbreviations

aFRET - Amplified FRET	HER - Human epidermal growth factor receptor
AP-1 - Activator protein 1	HNSCC - head and neck squamous cell carcinomas
APC - antigen presenting cells	HRP - horseradish peroxidase
BRET - Bioluminescence resonance energy transfer	HSP - heat shock protein
BSA - bovine serum albumin	iCARD - Improved catalysed reporter deposition
Cas - CRISPR associated system	IFNγ - interferon gamma
ccRCC - clear-cell renal cell carcinoma	iFRET - Immune FRET
CD - cluster of differentiation	Ig - immunoglobulin
CD3 - T-lymphocyte	IgE - Immunoglobulin E
CD4 - T-helper lymphocyte	IgG - immunoglobulin G
CD8 - cytotoxic T-lymphocyte	IgG1 - Immunoglobulin G1
CLRs - C-type lectin receptors	IgSF - immunoglobulin superfamily
CO₂ - carbon dioxide	IHC - immunohistochemistry
CRC - colorectal cancer	IL - interleukin
CRISPR - Clustered Regularly Interspaced Short Palindromic Repeats	IL2R - IL-2 receptor
CT - computed tomography	IMS - imaging mass spectrometry
CTLA-4 - cytotoxic T-cell lymphocyte-associated protein 4	IP₃ - 1,4,5-triphosphate
CytoF - cytometry by time-of-flight	IPEX - Immune dysregulation polyendocrinopathy enteropathy X-linked
DAG - Diacylglycerol	irAEs - Immune-related adverse effects
DAPI - 4',6-diamidino-2-phenylindole	ITAM - Immune tyrosine-based activation motifs
DMD - Digital micromirror device	ITIM - immunoreceptor tyrosine-based inhibition motif
DMEM - Dulbecco's modified Eagle's medium	ITSM - immunoreceptor tyrosine-based switching motif
DMSO - Dimethylsulfoxide	JAK/STAT - Janus kinase/signal transducer and activator of transcription
DNA - deoxyribonucleic acid	LAG-3 - Lymphocyte activation gene-3
dNTP - deoxynucleoside triphosphates	LAT - linker for activation of T cells
DSB - double strand break	LB - Lysogeny broth
DSP - Digital spatial profiling	LI - Lambert Instruments
EDTA - Ethylenediaminetetraacetic acid	LRR - Leucine rich repeat
Ef(%) - FRET efficiency	mAb - monoclonal antibody
EGFP - Enhanced green fluorescent protein	MALDI - Matrix assisted laser desorption ionisation
ELISA - Enzyme-linked immunosorbent assay	mfFLIM - multiple-frequency FLIM
F(ab')₂ - fragment antibody	MHC - major histocompatibility complex
FACS - fluorescence activated cell sorting	mNG - mNeon Green
FBS - foetal bovine serum	mRNA - messenger ribonucleic acid
FDA - Food and Drug Administration	MS - Mass spectrometry
FFPE - formalin-fixed paraffin-embedded	MSS - microsatellite stable
FITC - Fluorescein isothiocyanate	MSTS - multi-site tumour sampling
FLIM - Fluorescence lifetime imaging microscopy	NFAT - Nuclear factor of activated T-cells
FOXP3 - Forkhead P3	NFκB - Nuclear factor kappa-light-chain-enhancer of activated B-cells
FRET - Förster resonance energy transfer	NGS - Next generation sequencing
GADS - Grb2-related adaptor downstream of Shc	NK - Natural killer
gDNA - genomic DNA	NLRs - Containing receptors
GFP - green fluorescent protein	NMR - Nuclear Magnetic Resonance
GRB2 - Growth factor receptor-bound protein 2	
H&E - haematoxylin and eosin	
H₂O₂ - hydrogen peroxide	
HAVCR2 - hepatitis A virus cellular receptor 2	

NOD - Nucleotide-binding oligomerisation domain
NSCLC – non-small cell lung cancer
P/S - penicillin-streptomycin
pAb – polyclonal antibody
PAM – protospacer adjacent motif
PAMPs - Pathogen associated molecular patterns
PBS – phosphate-buffered saline
PBST – phosphate-buffered saline with Tween20
PCR – polymerase chain reaction
PD-1 – programmed death receptor 1
PDB - Protein Data Bank
PDCD1 – Programmed cell death protein 1
PDGF - Platelet-derived growth factor
PDK1 - Phosphorylates phosphoinositide-dependant kinase 1
PD-L1 – programmed death ligand 1
PE - Phosphatidylethanolamine
PFA – paraformaldehyde
PH - Pleckstrin-homology
PKB - Protein kinase B
PKC – protein kinase C
PKC θ - Protein kinase C theta
PLA - proximity ligation assay
PLA – proximity ligation assay
PLC γ 1 - Phospholipase C gamma 1
PNK – Polynucleotide Kinase
PRR - Pattern recognition receptors
PTEN - Phosphatase and tensin homolog
PTKs - Protein tyrosine kinases
PTP - Protein tyrosine phosphatase
qIHC - Quantitative IHC
RB - Retinoblastoma-associated
RCC – renal cell carcinoma
RFA – radiofrequency ablation
RFP - Red fluorescence protein
RIG-1 - Retinoic acid-inducible gene 1
RLRs - Like receptors

RNA – ribonucleic acid
ROI – Return on Investment
RPMI – Roswell Park Memorial Institute
SCLC – small cell lung carcinoma
SEM – standard error of the mean
SH2 – Scr homology 2
SHP-1 – SH2-domain containing tyrosine phosphatases-1
SHP-2 – SH-2 domain containing tyrosine phosphatases-2
SILAC - Stable isotope labelling in amino acid cell culture
SOC – Super Optimal broth with Catabolic repression
STAT3 - Signal Transducer And Activator Of Transcription 3
TAA – tumour associated antigen
TAE - Tris-acetate-EDTA
TCR - T-cell receptor
TCSPC - Time-correlated single-photon counting
 τ **D** – donor lifetime
 τ **DA** – donor-acceptor lifetime
TIGIT - T cell immunoreceptor with Ig and ITIM domains
TIM-3 –T-cell immunoglobulin mucin-3
TLRs - Toll-like receptors
TMA – tumour microarray
TMT - Tandem mass tag
TNF - Tumour necrosis factor
TOF - Time of flight
TRAIL - Tumour necrosis factor-related apoptosis-inducing ligand
Tregs - Regulatory T-lymphocytes
TRITC – Tetramethylrhodamine
TSA – tyramide signal amplification
UV - Ultraviolet
VISTA - V-domain Ig suppressor of T cell activation
ZAP-70 - zeta-chain associated protein kinase 70

Chapter 1: Introduction

1.1: Cancer: Current Knowledge, Treatment and Prognostics

Cancer is the leading cause of death worldwide, accounting for nearly ten million deaths globally in 2020. In 2020, female breast cancer was the most commonly diagnosed cancer worldwide (2.26 million cases), followed by lung cancer (2.21 million cases). Lung cancer accounted for the highest number of worldwide cancer deaths in 2020 (1.80 million deaths) followed by liver and stomach cancer (0.83 million and 0.77 million deaths respectively) (Ferlay et al., 2021). As the leading cause of death worldwide, it is crucial that the underpinnings of cancer development and progression are well understood. The hallmarks of cancer outline a set of biological capabilities cancer cells exhibit in order to form malignant tumours. Six hallmarks were first defined by Douglas Hanahan and Robert Weinberg in 2000 (Hanahan and Weinberg, 2000). In the subsequent decade, four new hallmarks have been added to this list. The 10 hallmarks in total are discussed below and summarised in [Figure 1.1](#)

Potentially the most central attribute of a cancer cell is the ability to sustain chronic proliferation. This gives rise to the first hallmark **sustaining proliferative signalling** (Hanahan and Weinberg, 2011). Normal cells carefully regulate the production and release of growth-promoting signals and carefully regulate a cell's progression through the cell cycle. However, cancer cells can dysregulate these processes in several ways. This can be achieved by, improper growth factor production and response, mutation-induced constitutive activation of kinases or a lack of activity from negative feedback regulators, such as phosphatase and tensin homolog (PTEN) (Hanahan and Weinberg, 2011). In addition to sustaining proliferative signalling, cancer cells must **evade growth suppressors**, which are in place to prevent malignancies from forming. Tumour suppressors are known to counteract proliferative signals and are dysregulated in a range of neoplasia; the retinoblastoma-associated (RB) and p53 proteins are notable examples of these. The RB protein largely responds to extracellular signals and determines if a cell should progress through the cell cycle. The p53 protein largely responds to intracellular signals and may halt the cell cycle in order to allow the cell to undergo repair in response to “alarm signals”. If required, the p53 protein may also promote apoptosis. The prominence of p53 mutations is large, with over 50% of cancers harbouring a p53 mutation (Perri et al., 2016). In keeping with the evasion of growth suppressors, cancer cells are also able to **resist cell death**. This can involve resisting the extrinsic apoptotic pathway (i.e., the Fas ligand/Fas receptor) or the intrinsic apoptotic pathway (e.g., the activation of caspases 8 and 9). Moreover, normal cells may undergo cellular growth and replication a limited number of times. Cancer cells can **enable replicative immortality**, thus allowing them to undergo unlimited replicative cycles. Furthermore, cancer cells **induce angiogenesis** to increase the supply of nutrients to the cells. Maybe the most recognised clinical hallmark of cancer

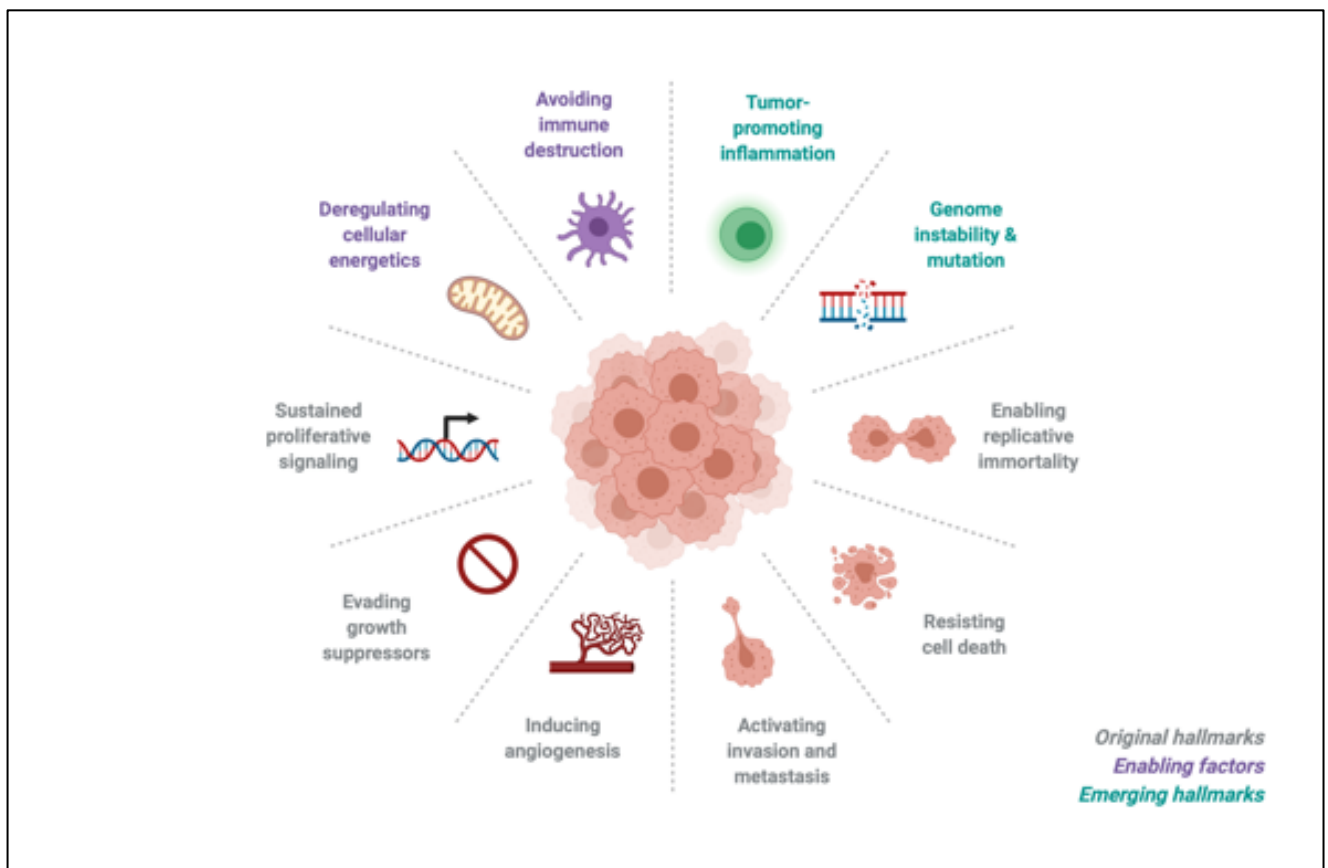


Figure 1.1: The Hallmarks of Cancer: The original six hallmarks of cancer were outlined by Hanahan and Weinberg in 2000. These included the ability of cancer cells to enable replicative immortality, resist cell death, activate invasion and metastasis, induce angiogenesis, evade growth suppressors and sustain proliferative signalling. In 2011, four new hallmarks were added to this list, including genome instability and mutation, dysregulating cellular energetics, tumour promoting inflammation and evading immune destruction.

is its ability to **activate invasion and metastasis**. This is facilitated by a number of transformations, notably by the loss of E-cadherin which is crucial in maintaining quiescence and ordered epithelial cell sheets. Increased expression of E-cadherin is listed as an antagonist of invasion and metastasis. These are the original hallmarks of cancer that were described by Hanahan and Weinberg in 2000. In 2011, four new hallmarks were identified: **dysregulating cellular energetics, genome instability and mutation, tumour-promoting inflammation** and **avoiding immune destruction**. The avoidance of immune destruction has led to a new focus in cancer therapies, with the spotlight falling on the concept of enabling the immune system to specifically target and destroy cancer cells. The immune system is in a constant state of immune surveillance, monitoring cells and tissues and naturally attacking nascent tumours, late-stage tumours and micro metastases. Therefore, the formation of a tumour indicates that to some degree, these cells have avoided the natural host defence in order to survive. Prior to dissecting the mechanisms by which neoplasia can avoid immune detection, it would be pertinent to introduce the immune system and its key components and functions.

1.2: An Introduction to the Innate Immune System

The immune system comprises of an assortment of cells, chemical messengers and processes that function to protect the host from foreign antigens. Foreign antigens may comprise of microbes (bacteria or fungi as examples), viruses, toxins and neoplastic cells (Marshall et al., 2018). The immune system has two lines of defence. The first line of defence is known as the innate immune system and will be introduced here. The second line of defence is the adaptive immune system, which is outlined in Section 1.3. The innate immune system comprises of four defensive barriers: anatomical barriers, (e.g., skin, or mucosal membranes), physiological barriers (e.g., temperature and chemical mediators), endocytic and phagocytic barriers (resulting in cell death) and inflammatory barriers. The innate immune system can recognise pathogens using pattern recognition receptors (PRRs). There are four major classes of PRR: Toll-like receptors (TLRs); nucleotide-binding oligomerisation domain (NOD)- leucine rich repeat (LRR)-containing receptors (NLRs); retinoic acid-inducible gene 1 (RIG-1)-like receptors (RLRs); and the C-type lectin receptors (CLRs) (Amarante-Mendes et al., 2018). This allows for a limited range of immune cells to identify a wide range of pathogens, all of which share common structures known as pathogen associated molecular patterns (PAMPs) (such as lipopolysaccharides) (Marshall et al., 2018). A key feature of innate immunity is a rapid recruitment of immune cells to sites of infection and inflammation. This is achieved through the production of cytokines and chemokines. Cytokines are small, secreted proteins which may be either pro-inflammatory or anti-inflammatory (Figure 1.2). Cytokines can act on the cells that secreted them in an autocrine manner, or act on nearby cells in a paracrine manner (Zhang and An, 2007). Key inflammatory cytokines released in the early innate immune response include tumour necrosis factor (TNF) and interleukins (IL) one and six (IL-1 and IL-6).

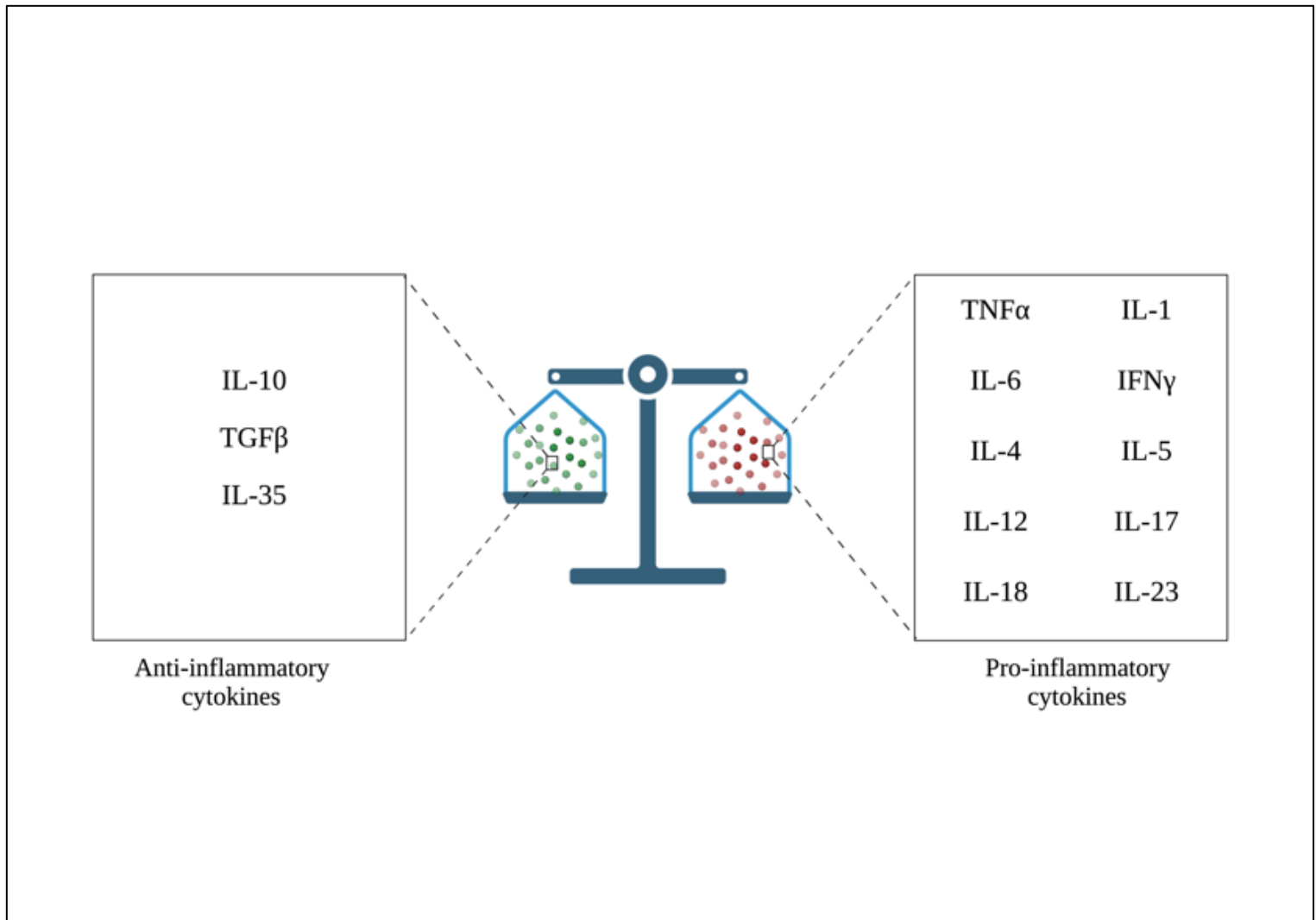
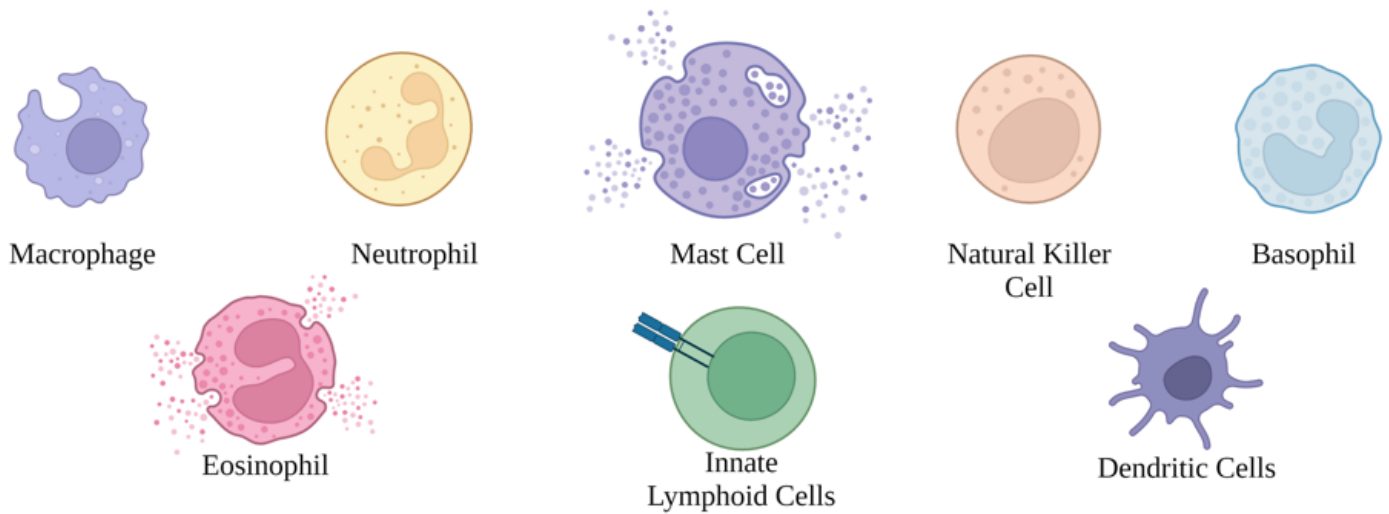


Figure 1.2: Balance of pro- and anti-inflammatory cytokines. Cytokines are small proteins that are secreted from a range of immune cells. In the immune system there is a balance between pro- and anti-inflammatory cytokines. Here, some of these cytokines are listed and categorised as either pro- or anti-inflammatory. IL-10, TGF β and IL-35 exert anti-inflammatory effects on the immune system. TNF α , IL-1, IL-4, IL-5, IL-6, IL-12, IL-17, IL-18, IL-23 and IFN γ exert pro-inflammatory effects on the immune system.

Chemokines (whose name derives from chemotactic cytokines) are also small secreted proteins that induce signal response in cells through G-protein coupled heptahelical chemokine receptors. Their function is to induce the migration of cells, often white blood cells, to sites of infection and inflammation (Hughes and Nibbs, 2018). The signalling between, and migration of, the cells that make up the innate immune system are critical for its efficient function. The cells that make up the innate immune system consist of phagocytes, mast cells, dendritic cells, natural killer (NK) cells, basophils, eosinophils, and innate lymphoid cells (Figure 1.3). Phagocytes, which are further subdivided into macrophages or neutrophils, are responsible for phagocytosis (from the ancient Greek *phagein*, to eat, and *ctye*, cell). Phagocytosis involves the engulfment and subsequent digestion of foreign antigens. Neutrophils which contain digestive granules, are short lived, whereas macrophages are long-lived and play a role in antigen presentation to the adaptive immune system. Mast cells are important in the induction of acute inflammatory response by the release of inflammatory mediators such as histamine. These usually exist in connective tissue near blood vessels and are also involved in physiological homeostatic functions such as vasodilation regulation and angiogenesis (Krystel-Whittemore et al., 2016). Dendritic cells are a class of specialised antigen presenting cell (APC) and act as key messengers between the innate and adaptive immune response (Marshall et al., 2018). Alongside their antigen presenting roles, dendritic cells are also involved in the phagocytosis of foreign antigens. NK cells play an important role in tumour rejection, releasing perforins and granzymes which induce apoptosis in targeted cells. Moreover, NK cells are a source of interferon gamma (IFN γ) which mobilises APCs. Basophils are found in the circulation and can also release inflammatory mediators such as histamine. Eosinophils are granulocytes which again can release inflammatory mediators and can destroy foreign bodies too large for phagocytosis (such as parasites). Innate lymphoid cells are the innate counterpart of T-lymphocytes (which are found in the adaptive immune system) which lack antigen-specific receptors (Panda and Colonna, 2019). These cells secrete effector cytokines and guide immune response to the site of specific antigens, thus helping to regulate the innate immune response.

Whilst the innate immune system is a complex series of chemical messengers and effector cells that can deal with a range of foreign antigens, it lacks memory. The ability to remember an invading body to invoke a more rapid immune response upon re-exposure is a hallmark of the adaptive immune system.

Cells of the Innate Immune System



Principles of the Innate Immune Response

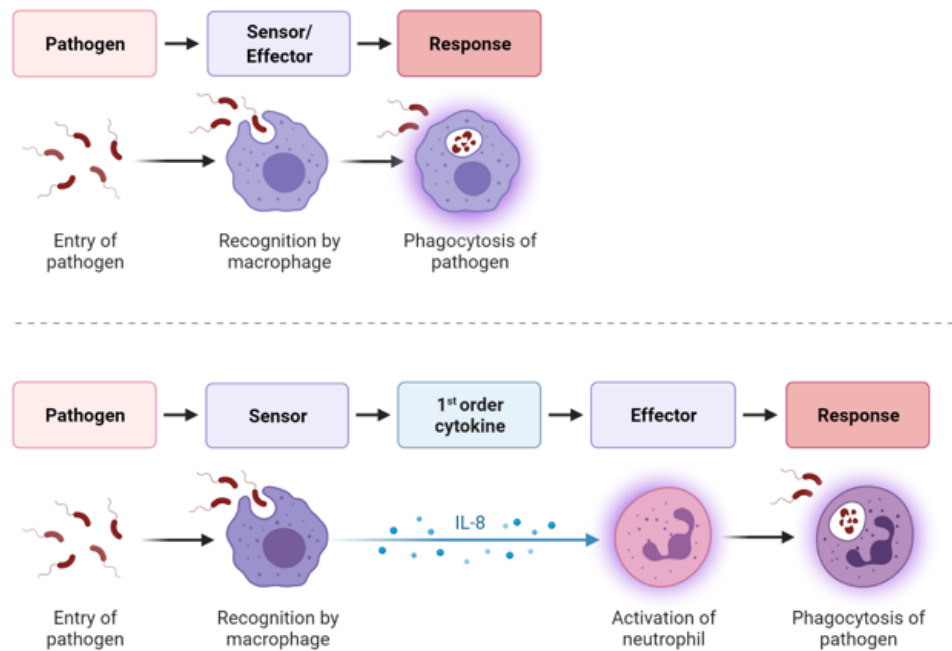


Figure 1.3: Summary of innate immune cells. **Top panel:** The innate immune system comprises of a range of cells such as: macrophages, neutrophils, mast cells, natural killer cells, basophils, eosinophils, innate lymphoid cells, and dendritic cells. Both macrophages and neutrophils are known as phagocytes. Dendritic cells are a class of professional antigen presenting cell and are key in priming the adaptive immune response. **Bottom panel:** An example workflow of the innate immune system. The innate immune system senses or detects common pathogenic patterns (such as lipopolysaccharide) which results in the phagocytosis of that pathogen or antigen. Sometimes a macrophage can directly phagocytose a pathogen. Other times it will release pro-inflammatory cytokines such as IL-8 to recruit further phagocytes, such as neutrophils, to phagocytose the pathogen.

1.3: An Introduction to the Adaptive Immune System

The adaptive immune system works in conjunction with the innate immune system and is crucial when the innate immune response is unable to eliminate a foreign antigen. The primary role of the adaptive immune system involves the recognition of specific non-self-antigens and the development of an immunological memory (Marshall et al., 2018). The three major classes of cells involved in adaptive immunity are APCs, T-lymphocytes (also known as T-cells) and B-lymphocytes (also known as B-cells). T-lymphocytes are derived from haemopoietic stem cells in the bone marrow which migrate to and mature in the thymus. Once matured, these cells express a unique antigen binding receptor known as the T-cell receptor (TCR). To recognise and respond to an antigen, the antigen must be presented to the T-lymphocyte by an APC. The APCs responsible for this are often dendritic cells but may also be macrophages or B-lymphocytes. The APCs express proteins that form a major histocompatibility complex (MHC). There are two classes of MHC, class I, which presents endogenous peptides to cytotoxic T-lymphocytes, and class II, which present exogenous peptides to helper T-lymphocytes (Marshall et al., 2018, Wieczorek et al., 2017). Endogenous peptides are fragments of antigen that arise intracellularly when a cell has been infected, for example by a virus. Exogenous peptides arise extracellularly and are formed from phagocytosed foreign bodies. The statistical chance of a T-lymphocyte meeting an APC with the correct antigen presented is increased by the circulation of T-lymphocytes through the blood and lymphatic systems as well as their accumulation in lymph nodes.

The TCR complex is formed from TCR α/β heterodimers and their hydrophobic interactions with CD3 subunits (CD3 subunits include γ , δ , ϵ or ζ) (Hwang et al., 2020). The TCR α/β heterodimer recognises the antigen presented by the MHC and triggers the recruitment and activation of several protein tyrosine kinases (PTKs). These PTKs include Lck, Fyn and Zeta-chain-associated protein kinase 70 (ZAP-70). Studies have indicated that Fyn is dispensable for TCR signalling whereas Lck is not (Groves et al., 1996). Once bound to a peptide-MHC, the TCR results in the recruitment of CD45 (a tyrosine phosphatase) which removes the inhibitory **Y₅₀₅**¹ phosphorylation of Lck. Lck then phosphorylates the immune tyrosine-based activation motifs (ITAM) of CD3 subunits in complex with TCR α/β . These phosphorylated ITAMs serve as docking sites for ZAP-70 which binds to the ITAM via a Src-homology-2 (SH-2) interaction and is itself phosphorylated by Lck or Fyn (Zhang et al., 1998). ZAP-70 phosphorylates the adapter protein, linker for activation of T-cells (LAT), which results in the recruitment and activation of phospholipase C γ 1 (PLC γ 1). PLC γ 1 synthesises inositol 1,4,5-triphosphate (IP₃) and diacylglycerol (DAG) from PtdIns(4,5)P₂. IP₃ mobilises cytosolic Ca²⁺ from intracellular stores (Schmidt et al., 2012).

¹ To aid in the differentiation of amino acid sequences, cell surface (e.g., CD) markers and acronyms, amino acid sequences are written in bold.

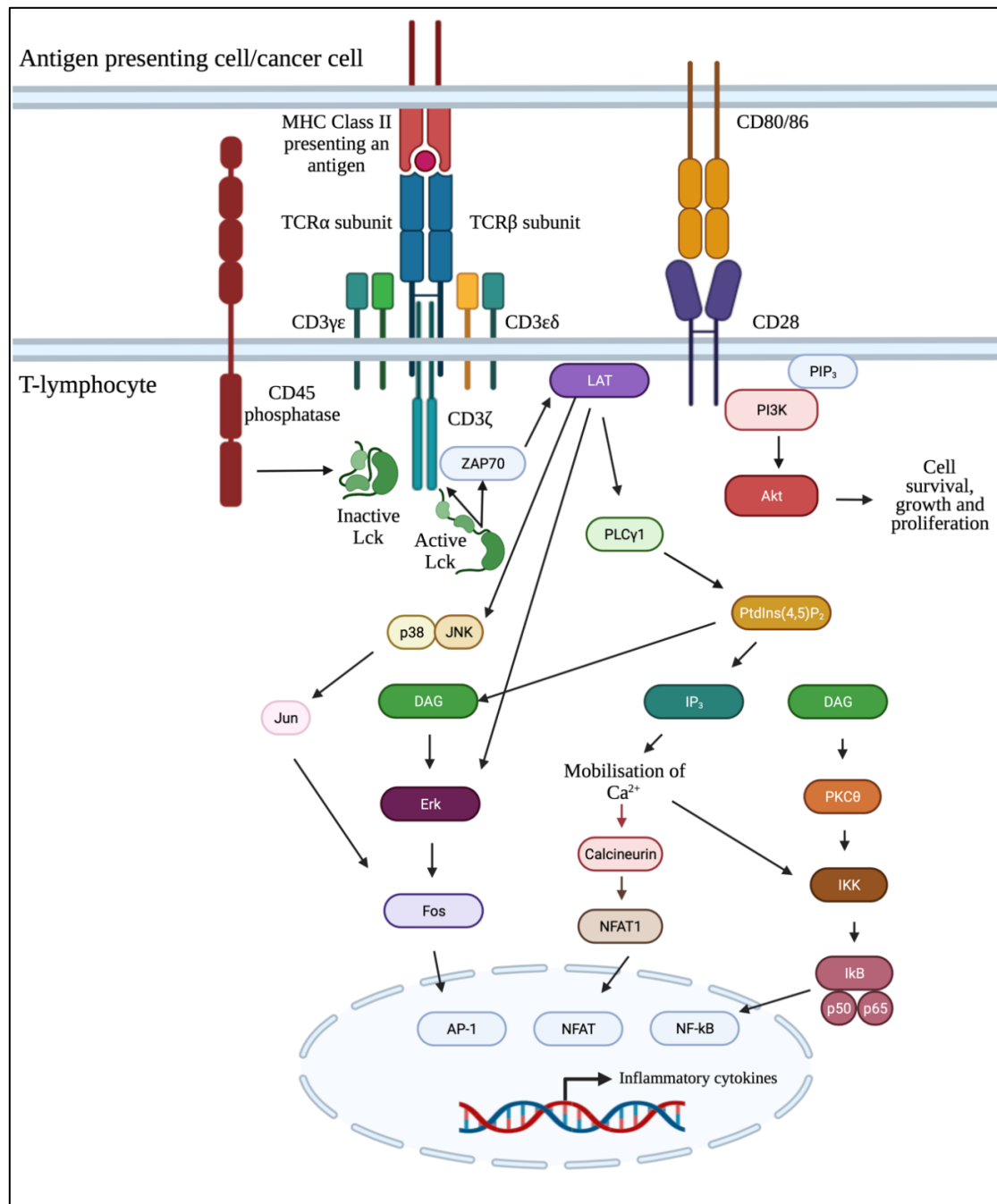


Figure 1.4: TCR engagement invokes a cascade of lymphocyte signalling events. An intricate and complex cascade of signalling occurs upon TCR ligation with an MHC class II molecule. In a T-lymphocyte, the TCR is formed of an α/β heterodimer which hydrophobically interacts with CD3 subunits (here CD3 $\gamma\epsilon$, CD3 $\epsilon\delta$ and CD3 ζ). Ligation of the TCR with an MHC complex presenting an antigen recruits the kinases Lck and ZAP-70 to the TCR, as well as the transmembrane phosphatase CD45. CD45 dephosphorylates the inhibitory phosphorylation of Lck, rendering it active. Lck phosphorylates the ITAM of the TCR which docks ZAP-70. Lck then phosphorylates ZAP-70. ZAP-70 activates the adapter protein LAT, which subsequently activates PLC γ 1 and Erk. PLC γ 1 activation results in the formation of DAG and IP $_3$. IP $_3$ acts to increase intracellular calcium concentration which results in activation of the NFAT and NF κ B transcription factors. DAG results in Erk activation (which activates AP-1 via Fos) and activation of NF κ B (via PKC θ , IKK and I κ B). For full activation of a T-lymphocyte, CD28 ligation with CD80/86 is required. CD28 activation also results in PKC θ activation via recruitment of PDK1 (not shown). (Modified from Schmidt et al., 2012).

However, TCR ligation alone fails to result in full activation of T-lymphocytes. For full activation to occur, a co-stimulatory signal is also required, and this often propagates from the co-stimulatory receptor CD28 (Figure 1.4). CD28 is expressed on approximately 80% of CD4⁺ lymphocytes and 50% of CD8⁺ lymphocytes (Esensten et al., 2016). CD28 is a 220 amino acid protein which exhibits a 44kDa glycosylated, disulphide-linked homodimer structure at the cell surface. Two ligands are known to bind to CD28; CD80 (also known as B7.1) and CD86 (also known as B7.2). Both ligands comprise of single V-set and C1-set IgSF (immunoglobulin superfamily) domains. The interaction of these ligands occurs at the ⁹⁹**MYPPPY**¹⁰⁵ motif within the V-set domain of the receptor (Esensten et al., 2016). The two ligands originated from a gene duplication in early mammalian evolution, however significant sequence divergence means that the two ligands now only share 26% amino acid sequence identity (Freeman et al., 1993). Bioluminescence resonance energy transfer (BRET) has shown that, at the cell surface, CD80 is present as a non-covalent dimer whereas CD86 is present as a monomer (James et al., 2006). Moreover, CD80^{-/-} mice are able to invoke almost normal humoral and cytotoxic T-lymphocyte responses to antigens compared to wildtype mice. However CD86^{-/-} mice fail to undergo antibody class switching and exhibit impaired cytotoxic T-lymphocyte response and proliferation (Halliday et al., 2020). Whilst both ligands have a higher affinity towards a competing receptor (CTLA-4, discussed in Section 1.4.1), the relative bias of CD80 towards CTLA-4 impairs its function as a ligand for CD28, resulting in CD86 being the preferred ligand for CD28 (Halliday et al., 2020).

Once CD28 is ligated to either CD80 or CD86, a cascade of intracellular T-lymphocyte signalling is evoked. The membrane proximal **YMN**M and distal **PYAP** motifs are known to dock a range of kinases and adaptor proteins via SH2 or SH3 interactions. One significant event is the phosphorylation of cytoplasmic tyrosine domains of CD28 by Lck. Lck then docks at the **PYAP** motif and phosphorylates phosphoinositide-dependant kinase 1 (PDK1) at **Y9**. PDK1 then phosphorylates protein kinase C theta (PKCθ) whose signalling activates the transcription factors: nuclear factor kappa-light-chain-enhancer of activated B-cells (NFκB); activator protein 1 (AP-1) and nuclear factor of activated T-cells (NFAT) (Esensten et al., 2016) (Figure 1.4). The promoters of many cytokines contain NFAT-AP1 binding domains which greatly enhances their transcription upon TCR/CD28 mediated activation of NFAT and AP-1 (Schmidt et al., 2012). Additionally, the adaptor proteins GRB2 (growth factor receptor-bound protein 2) and GADS (Grb2-related adaptor downstream of Shc) are recruited to CD28 and result in the activation of the Ras signalling cascade. Upon this activation, a T-lymphocyte undergoes proliferation and secretes inflammatory cytokines to transmit the immune response. However, the immune response that is mounted is formed from a range of T-lymphocyte subsets.

Presentation of an antigen by an MHC class I molecule on an APC or cancer cell will differentiate a naïve cytotoxic T-lymphocyte (CD8⁺ lymphocyte) into an effector cytotoxic T-lymphocyte. CD8⁺ effector lymphocytes are involved in the destruction of infected cells and neoplastic cells. Cell destruction is achieved through the release of perforin and granzyme (Figure 1.5). Perforin is a glycoprotein that forms pores in cell membranes, resulting in cell death (Osińska et al., 2014). Granzymes are a family of serine proteases stored in the granules of cytotoxic T-lymphocytes whose activity also result in targeted cell death (Boivin et al., 2009). After an infection has been resolved, the majority of CD8⁺ effector lymphocytes die and are phagocytosed. Critically, some of the lymphocytes are retained as memory lymphocytes which, upon reinfection with the same antigen, rapidly differentiate back into effector lymphocytes (Figure 1.5).

Another subset of T-lymphocytes are helper T-lymphocytes, or CD4⁺ lymphocytes. Whilst these cells lack an innate ability to destroy target cells, they are key in mediating the immune response by their targeted cytokine release. The three most frequent subsets of CD4⁺ lymphocytes are: Th1, Th2 and Th17. Upon activation by an MHC class II APC, Th1 lymphocytes secrete IFN γ which activates the bactericidal activities of macrophages. Th1 lymphocytes also secrete TNF α (Figure 1.6). Moreover, cytokines secreted from Th1 lymphocytes increase the ability of B-lymphocytes (discussed below) to synthesise opsonising antibodies (which increase phagocyte efficacy). Th2 lymphocytes typically release IL-4, IL-5, IL-9 and IL-13 upon activation. This is linked with the expansion of immunoglobulin E (IgE) synthesising B-lymphocytes (Zhu et al., 2010) (Figure 1.6). Moreover, the secretion of these interleukins results in the recruitment of mast cells and eosinophils. Upon activation, Th17 lymphocytes secrete IL-17, which is linked to ongoing inflammation, particularly in chronic infection, and IL-22 (Zhu et al., 2010) (Figure 1.6). As seen with CD8⁺ lymphocytes, upon the resolution of an infection, the majority of CD4⁺ cells will die and be cleared, however a subset will remain as CD4⁺ memory cells.

Alongside the diverse range of functions of T-lymphocytes, a second category of lymphocyte, the B-lymphocytes, also exist. B-lymphocytes also arise from haemopoietic stem cells; however, they undergo maturation in the bone marrow before migrating. Upon maturation these lymphocytes express a unique antigen-binding receptor and can recognise antigens without APCs (Marshall et al., 2018). The primary function of B-lymphocytes is antibody production, although in some instances B-lymphocytes may also act as APCs. When activated by an antigen complimentary to the antigen specific receptor of a B-lymphocyte, B-lymphocytes proliferate and differentiate into plasma cells or memory cells. Plasma cells are short-lived cells which produce antibodies in large quantities and secrete them into the circulation. After being secreted, antibodies bind to foreign antigens and mark them for destruction; often through complement activation, opsonisation or phagocytosis (Hart et al., 2004). Memory B-lymphocytes continue to circulate and express antigen-binding receptors. These can rapidly differentiate into plasma cells upon reinfection.

T lymphocyte activation and differentiation

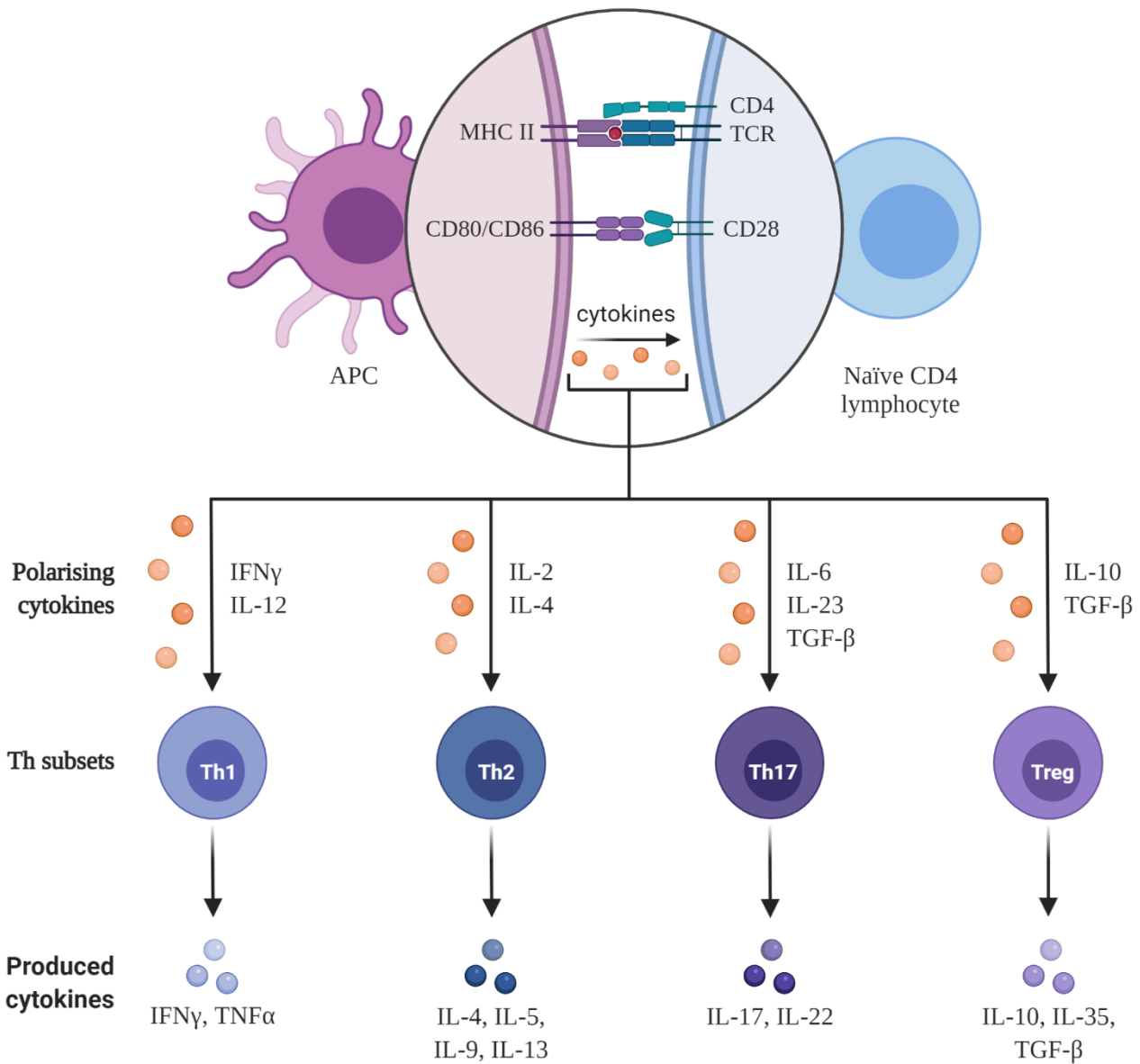


Figure 1.6: Differential cytokine exposure results in Th lymphocyte differentiation. Upon exposure to IFN γ and IL-12, naïve CD4⁺ lymphocytes differentiate into Th1 lymphocytes. Th1 lymphocytes secrete IFN γ and TNF α . IL-2 or IL-4 exposure differentiates naïve CD4⁺ lymphocytes into Th2 lymphocytes. These can secrete IL-4, IL-5, IL-9 and IL-13. IL-6, IL-23 and TGF β exposure differentiates naïve CD4⁺ lymphocytes into Th17 lymphocytes. These lymphocytes secrete IL-22 and IL-17, which is linked to chronic infection. IL-10 and TGF β exposure causes CD4⁺ lymphocytes to differentiate into Treg lymphocytes. Tregs exert immunosuppressive functions and secrete the anti-inflammatory cytokines IL-10, IL-35 and TGF β .

Whilst a rapid and efficacious immune response is critical in tackling infection and removing foreign antigens from the body, abhorrent immune activation results in a range of pathologies. Therefore, a tight regulation of immune activation is required. A subset of CD4⁺ T-lymphocytes play an important role in immune regulation. Regulatory T-lymphocytes (Tregs) are an immunosuppressive subpopulation of CD4⁺ lymphocytes that constitute approximately 5-10% of peripheral CD4⁺ lymphocytes (Hatzioannou et al., 2021). The hallmark of a Treg lymphocyte is expression of the forkhead P3 (FOXP3) transcription factor, CD25^{high} and IL-2 receptor alpha (IL2R α) (Sharma and Rudra, 2019, Saleh and Elkord, 2019). FOXP3 expression is pivotal in maintaining correct immune activation, with males who bear a loss of function mutation to the *FOXP3* gene exhibiting immune dysregulation polyendocrinopathy enteropathy X-linked (IPEX) syndrome (Bennett et al., 2001). Similarly in mice, male mice hemizygous for an X-linked frame shift in *FOXP3* exhibit a scurfy phenotype. This manifests as an expansion and hyperactivation of CD4⁺ lymphocytes resulting in multi-organ failure fatality within 16 to 25 days (Brunkow et al., 2001). FOXP3 can act either as an activator of transcription (when bound to the transcription factors RELA, IKZF2 and KAT5) or a repressor of transcription (when bound to the transcription factors YY1, IKZF3 or the histone methyltransferase EZH2) (Hatzioannou et al., 2021).

Alongside FOXP3 expression, Tregs also express a range of co-inhibitory molecules and co-stimulatory molecules. To exert their suppressive functions, Tregs themselves must be TCR-activated in the presence of IL-2. However CD28 co-stimulation is dispensable (Schmidt et al., 2012). Literature has suggested there are multiple mechanisms by which Tregs exert their immunosuppressive effect including: immunosuppressive cytokine production (Figure 1.6) cytolysis of conventional T-lymphocytes; metabolic disruption; and suppression of the maturation and function of APCs (Figure 1.7). Immunosuppressive cytokines (outlined in Figure 1.2) can result in a downregulation of immune activation. Treg IL-10 production results in the reduction of IFN γ -induced activation of APCs. Moreover IL-10 secretion leads to a reduction of IFN γ secretion from CD8⁺ lymphocytes and downregulation of MHC II on tumour-associated macrophages. IL35 secretion from Treg lymphocytes can lead to cell cycle arrest via the JAK/STAT (Janus kinase/signal transducer and activator of transcription) pathway, reducing T-lymphocyte proliferation (Hatzioannou et al., 2021). Cytolysis can be induced in CD4⁺, CD8⁺, and B-lymphocytes via the secretion of granzyme by Treg lymphocytes in a perforin dependant or independent manner (Hatzioannou et al., 2021). Moreover, Tregs may express tumour necrosis factor-related apoptosis-inducing ligand (TRAIL), which upon binding to the death receptor on target cells results in apoptosis and downregulation of the immune system. Tregs expressing the IL2R consume IL-2 which negatively regulates CD4⁺ and CD8⁺ lymphocytes (Schmidt et al., 2012) (Figure 1.7). High CD25 expression on Tregs in the tumour microenvironment also leads to depletion of IL-2 which reduces CD4⁺ and CD8⁺ activation and induces their apoptosis.

Mechanisms of Treg mediated immune suppression

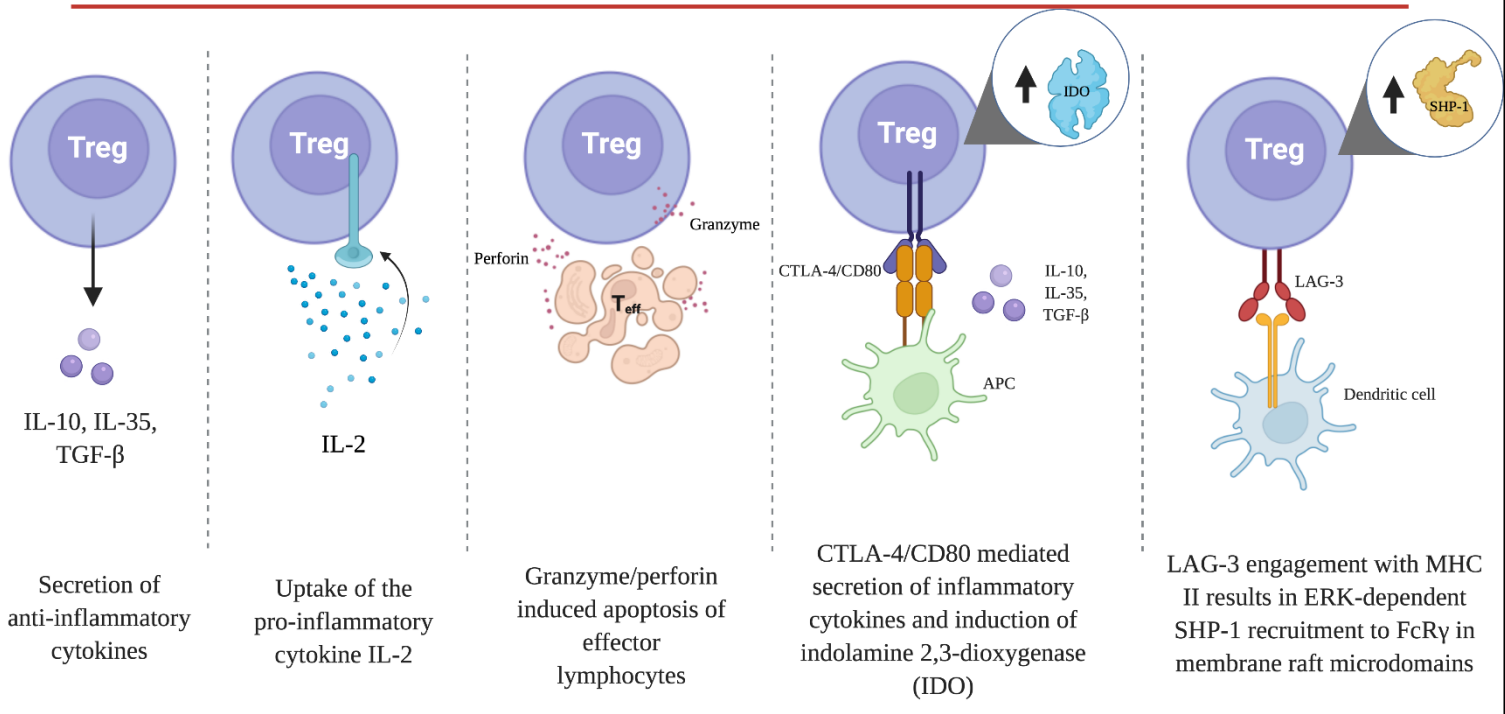


Figure 1.7: Tregs can exert their immunosuppressive function in multiple ways. They can secrete anti-inflammatory cytokines such as IL-10, IL-35 and TGFβ. Moreover, their expression of the IL2Rα chain allows for the mopping up of the pro-inflammatory cytokine IL-2, thus reducing the activation signals available for CD4⁺ and CD8⁺ lymphocytes. Tregs can directly induce apoptosis in CD4⁺ and CD8⁺ cells via the release of granzyme and perforin in the presence of these lymphocytes. CTLA-4 engagement with CD80 can increase the secretion of anti-inflammatory cytokines from Tregs and can also induce indolamine 2,3 dioxygenase (IDO) in Tregs. LAG-3 engagement with MHC class II on a dendritic cell may induce the Erk-dependant recruitment of the phosphatase SHP-1 to FcRγ in membrane microdomains.

1.4: How is the Immune System Implicated in Cancer Progression?

As stated by Hanahan and Weinberg, immune evasion is a hallmark of cancer, and there is a plethora of mechanisms by which this is achieved. The bone marrow, blood, spleen and draining lymph nodes form a communication network throughout neoplastic development and result in changes to immune phenotype. Haematopoiesis within the bone-marrow becomes skewed and results in an expansion of immature neutrophils and monocytes. A severe disruption of haemopoiesis is experienced in tumour-burdened patients. Haemopoietic stem cells and progenitor cells proliferate and differentiate into monocytic and granulocytic lineages which results in peripheral expansion of immature immunosuppressive neutrophils, monocytes and macrophages (Hiam-Galvez et al., 2021). A pan-cancer study identified that multipotent progenitors, granulocyte monocyte progenitors and haematopoietic stem cells were elevated in the blood of breast, cervical, liver, lung, ovarian, oesophageal and gastrointestinal cancer patients (Wu et al., 2014). Moreover, increased neutrophil frequency has been correlated with a poor prognosis in mesothelioma, renal cell carcinoma, pancreatic cancer, colorectal carcinoma, non-small cell lung carcinoma (NSCLC), hepatocellular carcinoma and gastroesophageal cancer (Templeton et al., 2014). Dendritic cell levels are also perturbed in cancer, with a decrease in peripheral blood dendritic cells seen in ovarian, prostate, breast, lung, renal and head and neck squamous cell cancers as well as melanoma (Hiam-Galvez et al., 2021). Lymphopenia is observed in several cancers (e.g., breast, sarcoma, lymphoma) and circulating T-lymphocytes in breast, lung and cervical cancer patients experience reduced TCR diversity. Treg lymphocytes show an expansion in the periphery and invasion into the tumour, eliciting immunosuppressive effects, alongside IL-10 secreting regulatory B-lymphocytes. Natural killer cells from breast cancer patients are shown to have dysregulated phenotypes with decreased expression of the activating receptors NKp30, NKG2D, DNAM-1 and CD16. Moreover, NK cells in breast cancer patients may also experience increased inhibitory receptor (NKG2A) expression (Mamessier et al., 2011). To conclude, it is now known that a systemic corruption of the organisation of the immune system occurs in the neoplastic development and progression of a range of tumour types (Hiam-Galvez et al., 2021).

A major mechanism by which cancers can evade immune attack is by the dampening down of T-lymphocyte response towards cancer cells. This may be in part elicited by a cancer cells downregulation of MHC class I and neoantigens on its cell surface (Saleh and Elkord, 2019). Additionally, the identification of co-inhibitory molecules on the cell surface of T-lymphocytes has provided an insight into how cancers may avoid T-lymphocyte-mediated destruction. The role of these co-inhibitory molecules, known as immune checkpoints, is to control the balance between T-lymphocyte tolerance and activation. Cancer cells are now known to hijack these pathways, by providing the cognate co-inhibitory ligands for these receptors, thus reducing T-lymphocyte activation in the tumour microenvironment.

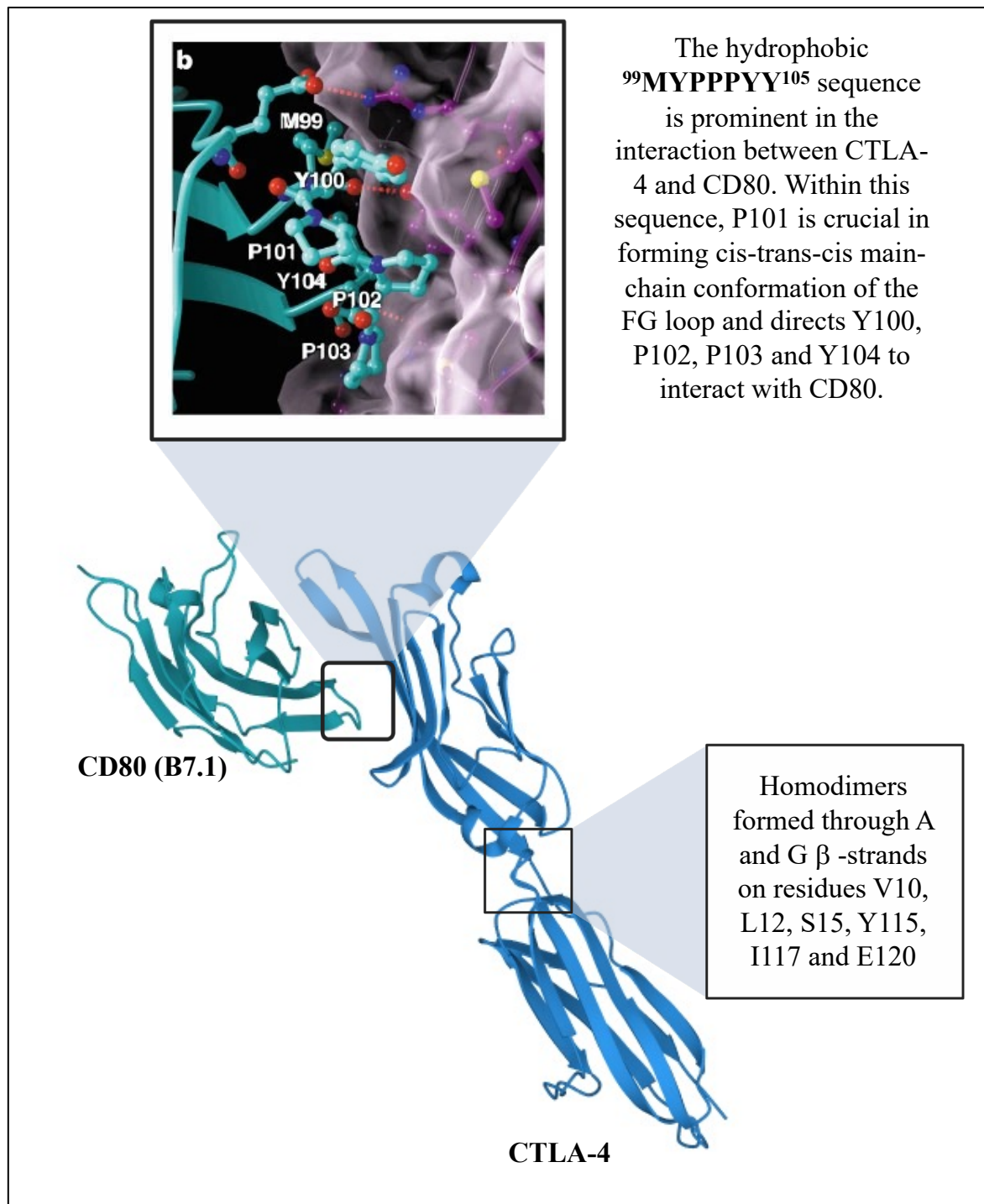


Figure 1.8: The crystal structure of CTLA-4 and CD80. The resolution of the displayed crystal structure (PDB ID: 1I8L) resolution is 3.0Å. CTLA-4 comprises of a single V-set domain and forms homodimers through A and G β -strands on residues: V₁₀, L₁₂, S₁₅, Y₁₁₅, I₁₁₇ and E₁₂₀. This creates an interface that is largely hydrophobic. CTLA-4 binds to its cognate ligand, CD80 or CD86 by the GFCC' face of CTLA-4 and CD80 V-set domain. Contacts are made between the ligand and receptor on the ⁹⁹MYPPPY¹⁰⁵ sequence of CTLA-4. *CTLA-4/CD80 binding zoom box modified from Stamper et al., 2001.*

Two major immune checkpoint receptors are the cytotoxic T-cell associated protein-4 (CTLA-4) and the programmed death receptor 1 (PD-1). Drugs aimed at blocking the interaction of these receptors with their cognate ligands are increasingly used in cancer therapy, particularly in malignant melanoma and lung cancer (Ma et al., 2021). The mechanism of signal transduction of these two checkpoints, alongside their targeting in cancer are discussed in Sections 1.4.2 and 1.4.3. Whilst these two co-inhibitory molecules are prominent, other molecules exist such as: T-cell immunoreceptor with Ig and ITIM (Immunoreceptor Tyrosine-based inhibition motif) domains (TIGIT); V-domain Ig suppressor of T-cell activation (VISTA); T-cell immunoglobulin mucin 3 (TIM-3) and lymphocyte activation gene-3 (LAG-3).

1.4.1: The Role of the CTLA-4/CD80 Signalling Axis in Cancer

The CTLA-4 pathway provides host protection against autoimmune diseases by downregulating adaptive immune system activation. CTLA-4 is a homolog of the co-stimulatory molecule CD28 (discussed in Section 1.3). CTLA-4 comprises of a single V-set domain and human CTLA-4 monomers interact through A and G β -strand residues (**V₁₀**, **L₁₂**, **S₁₅**, **Y₁₁₅**, **I₁₁₇** and **E₁₂₀**) (Figure 1.8, resolution 3.0Å). This creates an interface that is largely hydrophobic except for reciprocal interchain hydrogen bonds between **S₁₅** and main-chain nitrogen of **E₁₂₀**. Binding of CTLA-4 to CD80, one of its cognate ligands, is facilitated by the GFCC' face of CTLA-4 and CD80 V-set domains with an angle of approximately 90° between the two β -sheets (Stamper et al., 2001). Interatomic contacts are made between 13 residues of CTLA-4 and CD80, respectively. The hydrophobic ⁹⁹**MYPPPY**¹⁰⁵ sequence is prominent in the interaction between CTLA-4 and CD80. Within this sequence, **P₁₀₁** is crucial in forming cis-trans-cis main-chain conformation of the FG loop and directs **Y₁₀₀**, **P₁₀₂**, **P₁₀₃** and **Y₁₀₄** to interact with CD80. Alanine substitutions of any residues in the ⁹⁹**MYPPPY**¹⁰⁵ sequence act to reduce or abolish CTLA-4/CD80 interactions (Stamper et al., 2001). Whilst CD28 and CTLA-4 share similar structures, their function and signalling dynamics drastically differ. Whereas CD28 is constitutively expressed at the plasma membrane of T-lymphocytes and propagates T-lymphocyte activation, CTLA-4 surface expression is induced upon T-lymphocyte activation and is constitutively expressed in Tregs. Approximately 90% of CTLA-4 is located in intracellular vesicles and upon surface expression, CTLA-4 is typically internalised. It has been shown that depletion of the **YKVM** motif of CTLA-4 inhibits receptor internalisation, which is mediated by the clathrin adaptor AP-2 (Verma et al., 2017). An experiment by Quershi et al., 2012, labelled CHO cells with anti-CTLA-4 phosphatidylethanolamine (PE) at 4°C to detect cell-surface CTLA-4 expression. Cells were then warmed to 37°C for different times, transferred on ice and subsequently probed with a chromophore-conjugated secondary antibody. This revealed the proportion of cell surface CTLA-4 remaining. It was seen that the majority of cell surface CTLA-4 was internalised within five minutes. The data from this study, alongside the truncation of the **YKVM** motif, indicate that CLTA-4 is rapidly

internalised in a ligand independent manner via its **YKVM** motif (Qureshi et al., 2012).

CTLA-4 and CD28 compete for the same ligands CD80 and CD86, however CTLA-4 has an increased binding affinity compared to CD28 (Buchbinder and Desai, 2016, Parry et al., 2005). It is thought that the dynamic ratio of CD28/CD80/6 and CTLA-4/CD80/6 binding determines whether a T-lymphocyte will become activated or enter an anergic state, with CTLA-4 being able to outcompete CD28 and thus prevent co-stimulation of T-lymphocytes (Stumpf et al., 2014).

It is also known that the kinases Fyn, Lck and ZAP-70 are constitutively activated in CTLA-4^{-/-} mice, indicating an inhibition of TCR proximal events by CTLA-4. Moreover, immunoprecipitation analysis has shown the tyrosine protein phosphatase SYP (now known as SHP-2) to be a binding partner to the cytoplasmic tail of CTLA-4 (Marengère et al., 1996). Furthermore, a study by Stumpf et al., 2015 has shown that the intracellular **Y₂₀₁** residue of CTLA-4 may contribute to T-lymphocyte signalling. A point mutated CTLA-4 (**Y₂₀₁V**) led to increased CTLA-4 expression on T-lymphocytes and a Th2 bias upon activation. However, homeostatic functions of T-lymphocytes were not altered in mice up to eight weeks of age. A study assessing experimental autoimmune encephalomyelitis in these mice showed that increased disease severity in **Y₂₀₁V** mice is due to impairment of Tregs. This indicates that the intracellular signalling of CTLA-4 plays a more prominent role in this subset of lymphocytes (Stumpf et al., 2014). A third mechanism by which CTLA-4 can induce a downregulation is through its aforementioned endocytosis. When CTLA-4 undergoes internalisation, it can “strip” its cognate ligand from an antigen presenting cell in a process known as trans-endocytosis. The internalised ligand is then degraded (Qureshi et al., 2011). This provides an additional, cell extrinsic, means by which CD28 is deprived of CD80/CD86 interaction. The mechanisms by which CTLA-4 provides an inhibitory immune signal are summarised in Figure 1.9.

Due to the considerable roles in which CTLA-4 can repress the immune system, combined with the immune evasion hallmark of cancer, it is to be expected that it has been explored as a promising anti-cancer target. Ipilimumab is a recombinant human immunoglobulin G1 (IgG1) monoclonal antibody designed by Bristol Meyer Squibb. Ipilimumab binds to CTLA-4 at its ⁹⁹**MYPPPY**¹⁰⁵ motif, blocking its interaction with its cognate ligands. In 2011, the Food and Drug Administration (FDA) approved ipilimumab for use in late-stage metastatic melanoma. In the study that led to its approval, ipilimumab extended the life of late-stage melanoma patients from an average of 6.5 months to an average of 10 months. Since 2011, Ipilimumab has subsequently been licenced for the treatment of NSCLC, mesothelioma, ovarian, breast, prostate, and urothelial cancers. Whilst a subset of patients respond to treatment, some patients show no response to this treatment.

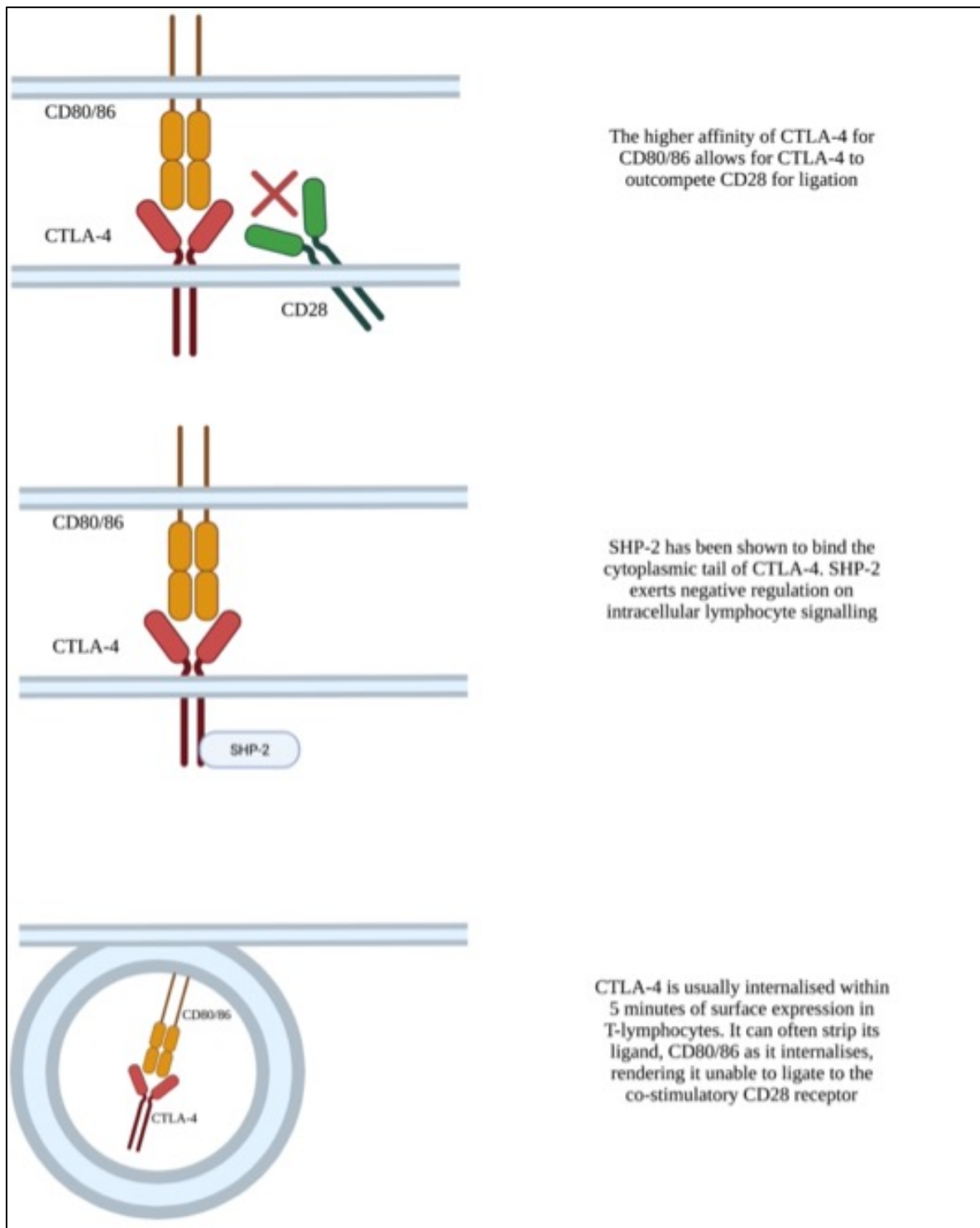


Figure 1.9: The three mechanisms by which CTLA-4 exerts its immunosuppressive functions. CTLA-4 can exert an immunosuppressive signal on the immune system in three ways. **Top panel)** CTLA-4 has a higher affinity for the ligand CD80/86 than the co-stimulatory CD28 receptor. Therefore CTLA-4 can outcompete CD28 and result in a negative immune response. **Middle panel)** Studies have shown that the cytoplasmic tail of CTLA-4 recruits the phosphatase SHP-2, which dephosphorylates kinases proximal to the TCR, thus reducing T-lymphocyte activation (Marengère et al., 1996). **Bottom Panel)** CTLA-4 is usually internalised within 5 minutes of T-lymphocyte surface expression. It can strip the ligand CD80/86 upon internalisation from the antigen presenting cell, meaning it cannot ligate to the co-stimulatory CD28 receptor Qureshi et al., 2011).

Moreover, ipilimumab treatment results in immune-related adverse effects (irAEs) in up to 65% of patients. These commonly affect the skin, gastrointestinal tract and endocrine organs, although irAEs have been recorded in almost all other organs (Rowshanravan et al., 2018).

Despite the efficacy shown with this treatment, increased efficacy may arise when targeting other immune checkpoints alongside CTLA-4. Currently, the only other immune checkpoint for which therapeutic blocking antibodies have been approved is the programmed death receptor (PD-1) / programmed death ligand (PD-L1) (PD-1/PD-L1).

1.4.2: The Role of the PD-1/PD-L1 Signalling Axis in Cancer

PD-1 is a 228 amino acid membrane protein receptor with a canonical immunoglobulin (Ig)-like extracellular domain (Zak et al., 2017). PD-1 is expressed on a subset of thymocytes, such as activated T- and B-lymphocytes, monocytes, dendritic cells, and tumour-infiltrating lymphocytes (Sun et al., 2015, Sheppard et al., 2004). When inflammatory cytokines such as IL-1 or IL-6 or TNF α are secreted in the adaptive immune response, PD-L1 expression is induced in the surrounding tissue. When bound to PD-1, this can lead to immune tolerance, whereby the immune system is unable to mount an immune response, even in the presence of antigens and stimulatory signals (Mahoney et al., 2015). This results in peripheral tolerance and, alongside the CTLA-4/CD80 checkpoint, provides a negative feedback mechanism to maintain immune system homeostasis.

Figure 1.10A illustrates the crystal structure of the extracellular IgV of a high-PD-L1 affinity PD-1 mutant (**A₁₃₂L**) obtained by X-ray diffraction (Lázár-Molnár et al., 2017). This structure has been deposited on the Protein Data Bank (PDB) with the ID 3RRQ with a resolution of 2.10Å. Other extracellular-domain PD-1 structures have also been deposited, 1NPU and 2M2D, which were obtained by X-ray diffraction and Nuclear Magnetic Resonance (NMR) spectroscopy respectively (Zhang et al., 2004, Cheng et al., 2013). In the study carried out by Lázár-Molnár et al., 2017, diffraction-quality crystals were unobtainable for wild-type PD-1, however the **A₁₃₂L** mutant yields important data on the structure of the extracellular domain of PD-1. The structure is typical of IgV domain topology with the front and back β -sheets forming a two-layered β -sandwich which is stabilised by a disulphide bond between **C₅₄** and **C₁₂₃** on the B and F strands, respectively.

Figure 1.10B highlights the interatomic contacts formed between murine PD-1 and human PD-L1 when crystallised together. PD-1/PD-L1 interactions occur at their V-domain A'GFCC' β -sheets, forming a pair of V-domains in a Fv-like structure (Lin et al., 2008). Eighty-seven interatomic contacts are formed between 18 murine PD-1 residues and 14 human PD-L1 residues. Fifteen of these residues are identical to human residues, those that differ being **M₆₄** (**V₆₄** in human), **N₆₈** (**Y₆₈** in human) and **V₉₀** (**G₉₀** in human).

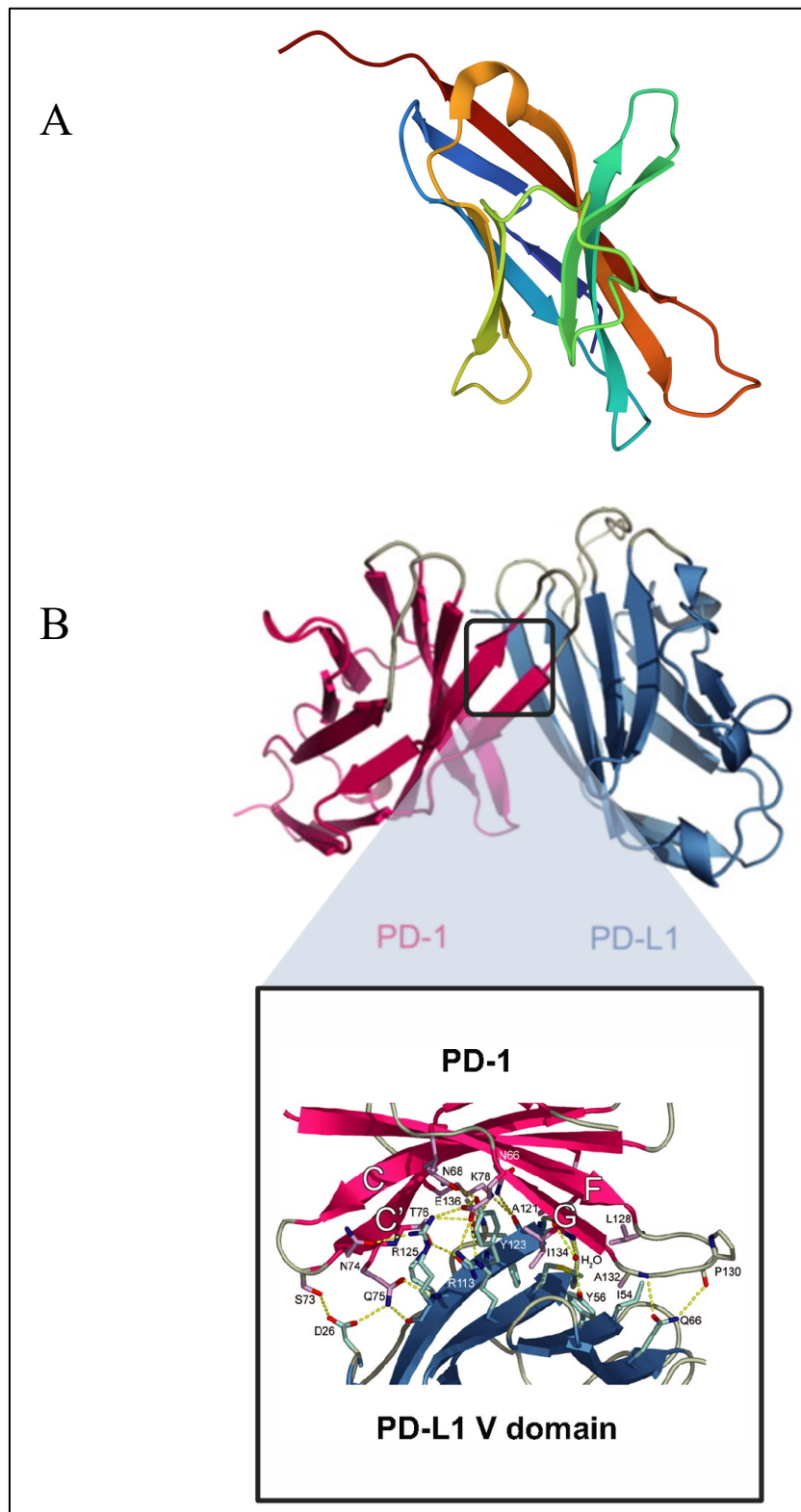


Figure 1.10: The crystal structure of the extracellular domain of PD-1. **A)** The crystal structure of the extracellular domain of PD-1 reveals a typical IgV domain topology with the front and back β -sheets forming a two-layered β -sandwich which is stabilised by a disulphide bond between C54 and C123 on the B and F strands, respectively. The intracellular domain of PD-1 which does not have a resolved crystal structure is responsible for the intracellular signal transduction of the PD-1 pathway. **B)** 87 interatomic contacts are formed between the murine PD-1 and human PD-L1 crystalised by Yin-wei Lin et al., 2008 (using a 4Å cut-off). This forms a buried surface area of 1870Å². Modified from Yin-wei Lin et al., 2008.

Of these differences, **M₆₄** and **V₉₀** result in smaller or absent amino acid side chains so would minimally affect the binding interface. The resulting buried surface area of this binding interface is 1820Å², which is larger than the binding surface of CTLA-4/CD80 (approximately 1200 Å²). Surface plasmon resonance indicates a K_d of approximately 8μM between murine PD-1 and human PD-L1 (Lin et al., 2008).

Steady-state (intensity-based) Förster resonance energy transfer (FRET) analysis performed by Zhang et al., 2004 has shown that PD-1 exists in a monomeric state both in solution and at the cell surface. Whilst the extracellular domain of PD-1 has been crystallised, the intracellular domain has not. It is the intracellular domain of PD-1, the cytoplasmic tail, which is responsible for effecting PD-1 signal transduction (Zhang et al., 2004). The cytoplasmic portion of the PD-1 receptor contains an N-terminal sequence **VDYGEI** forming an Immunoreceptor Tyrosine-based Inhibition Motif (ITIM), defined as **V/I/LxYxxL**, which recruits SH2 domain containing phosphatases. The cytoplasmic tail of PD-1 also contains a C-terminal sequence **TEYATI**, forming an Immunoreceptor Tyrosine-based Switch Motif (ITSM), defined as **TxYxxL** (Boussiotis, 2016, Yokosuka et al., 2012).

PD-1 is phosphorylated on two tyrosines of its cytoplasmic domain (**Y₂₂₃** and **Y₂₄₈**) after its interaction with PD-L1. These residues are located in the ITIM and ITSM respectively (Boussiotis, 2016, Yokosuka et al., 2012). Directed mutagenesis studies have shown that phosphorylation of residue 248 is crucial for PD-1 signalling, and the proteins Lck and Fyn, but not ZAP-70, have been suggested to be responsible for the modification of this amino acid (Figure 1.11) (Patsoukis et al., 2020). Subsequent deactivation of the T-lymphocyte is mediated in several ways. Firstly, upon the binding of PD-L1 to PD-1, downstream of the PD-1 receptor, there is an activation and recruitment of the SH2 domain containing tyrosine phosphatases-1 and 2 (SHP-1 and SHP-2 respectively) (Figure 1.11). SHP phosphatases are responsible for the dephosphorylation of tyrosine residues. SHP-1 and SHP-2 have a high sequence identity with both phosphatases containing an N-terminus SH2 domain, followed by a catalytic Protein Tyrosine Phosphatase (PTP) domain and a C-terminal SH2 domain (Figure 1.12) (Craggs and Kellie, 2001). When inactive, SHP-1 adopts a closed conformation whereby the N-SH2 domain binds the PTP domain.

This has been confirmed in crystal structures of tail-truncated SHP-1 and SHP-2 (Hof et al., 1998, Yang et al., 2003). SHP-1 is predominantly expressed in haemopoietic cells and is primarily a negative regulator of signalling pathways in T-lymphocytes (Yang et al., 2003). SHP-2 however is ubiquitously expressed and activated by a range of signalling molecules such as hormones, cytokines, growth factors and MHC-antigen complexes (Hof et al., 1998, Wang et al., 2011).

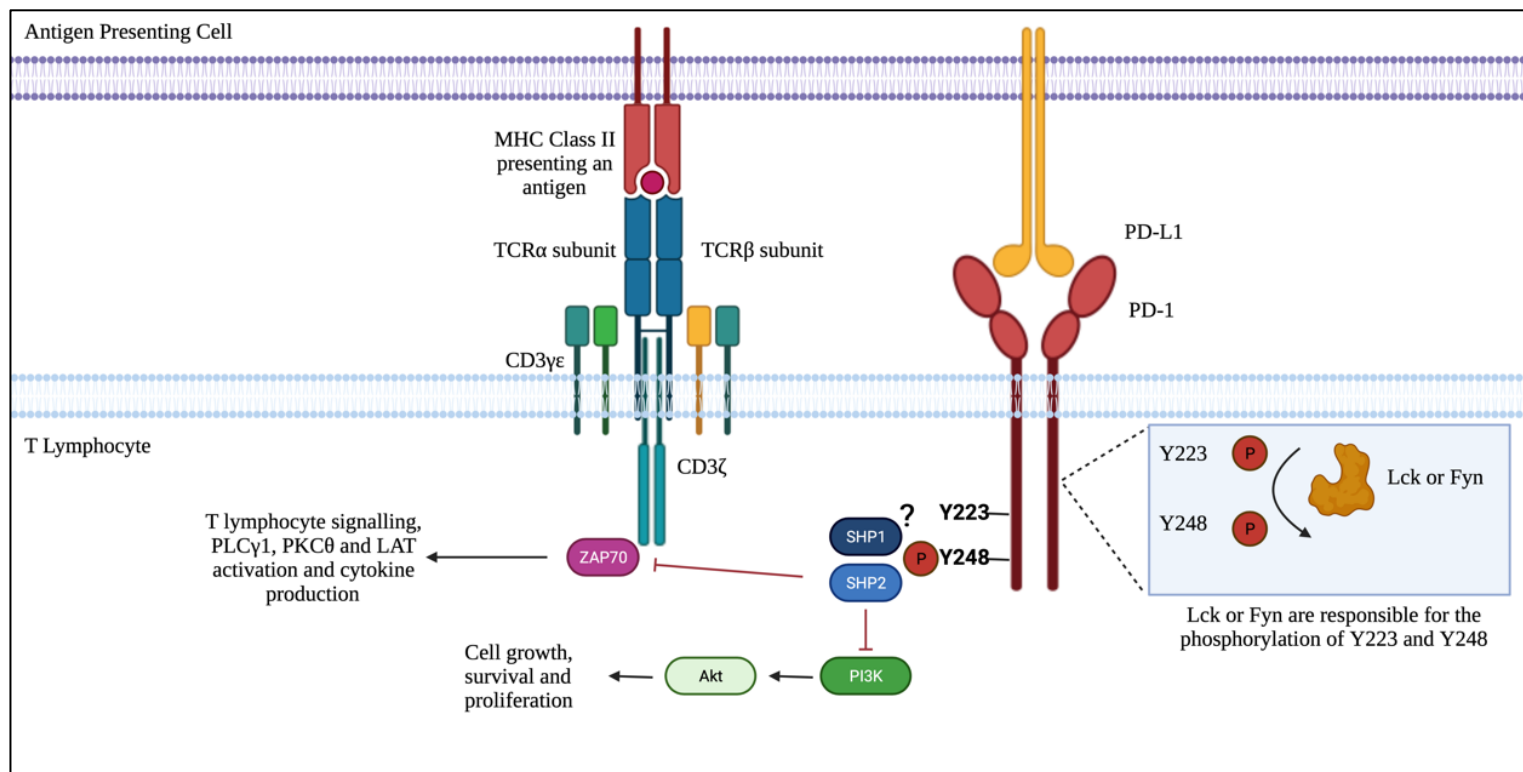


Figure 1.11: PD-1/PD-L1 engagement results in the recruitment of SHP-2 to the pY₂₄₈ residue of the ITSM of PD-1. Upon binding of PD-L1, (presented by a cancer cell or antigen presenting cell (APC)) and PD-1, present on the T-lymphocyte, a series of signalling events occur to attenuate T-lymphocyte signalling (refer to Figure 1.4). The interaction of receptor and ligand results in the phosphorylation of Y₂₂₃ and Y₂₄₈, located on the ITIM and ITSM of PD-1, respectively. These phosphorylation events are likely to be carried out by Lck or Fyn. Upon phosphorylation of Y₂₄₈, SHP-2 is recruited via its SH-2 domain. This results in the inhibition of the PI3K/Akt signalling pathway, resulting in reduced cell growth, survival, and proliferation. Also attenuated by SHP-2 is T-lymphocyte activation and IL-2 production, this results from a dephosphorylation of ZAP70, located on the CD3 ζ chain. What remains poorly understood is to identify whether SHP-1 does bind to the pY₂₄₈ residue. Furthermore, if binding should occur, the activation state, and role of SHP-1 downstream of PD-1 remains unknown.

The PD-1/PD-L1 signalling axis is becoming increasingly targeted in cancer therapies. In 2014, the FDA approved nivolumab, a monoclonal antibody against the PD-1 receptor for the treatment of advanced melanoma. This was expanded to lung cancer, chiefly NSCLC, in March 2015. Since then, nivolumab has been licenced for the treatment of metastatic renal cell carcinoma (2015), Hodgkin's lymphoma (2016), head and neck cancer (2016) and hepatocellular carcinoma (2017), amongst other indications. Another PD-1 blocking antibody, pembrolizumab, was approved in 2014 for the treatment of advanced melanoma and has since been licenced for the treatment of a range of cancers. As well as PD-1, the ligand, PD-L1 is also targeted in some cancers, with atezolizumab gaining FDA approval for the treatment of urothelial carcinoma in 2016.

Often, patients are selected for checkpoint blockade therapies (against CTLA-4/CD80 or PD-1/PD-L1) based on the expression of the PD-L1 ligand in the tumour (Madonna et al., 2018). This has several critical limitations. Firstly, PD-L1 is not the cognate ligand for CTLA-4, thus highlighting the lack of a predictive biomarker for CTLA-4/CD80 therapeutic intervention (Madonna et al., 2018). Secondly, ligand expression does not report on receptor-ligand interactions. Studies have shown that PD-L1 expression does correlate with PD-1 blockade, with PD-L1 negative patients often experiencing therapeutic benefit from these therapies (Nunes-Xavier et al., 2019, Sánchez-Magraner et al., 2020, Davis and Patel, 2019). This could also highlight a mechanism by which patients prematurely acquire secondary resistance, through the incorrect prescription of immune checkpoint blockades based on ligand expression profiling.

Two approaches could be enlisted to elucidate a predictive biomarker for therapies against CTLA-4/CD80 and PD-1/PD-L1. The first would be to identify a biomarker using spatial quantitative immunohistochemistry, although this would still not report on the functional state of an immune checkpoint. The second would be to elucidate a functional biomarker, which is also quantifiable and spatially resolved, in order to predict patient response to therapy and to aid patient stratification.

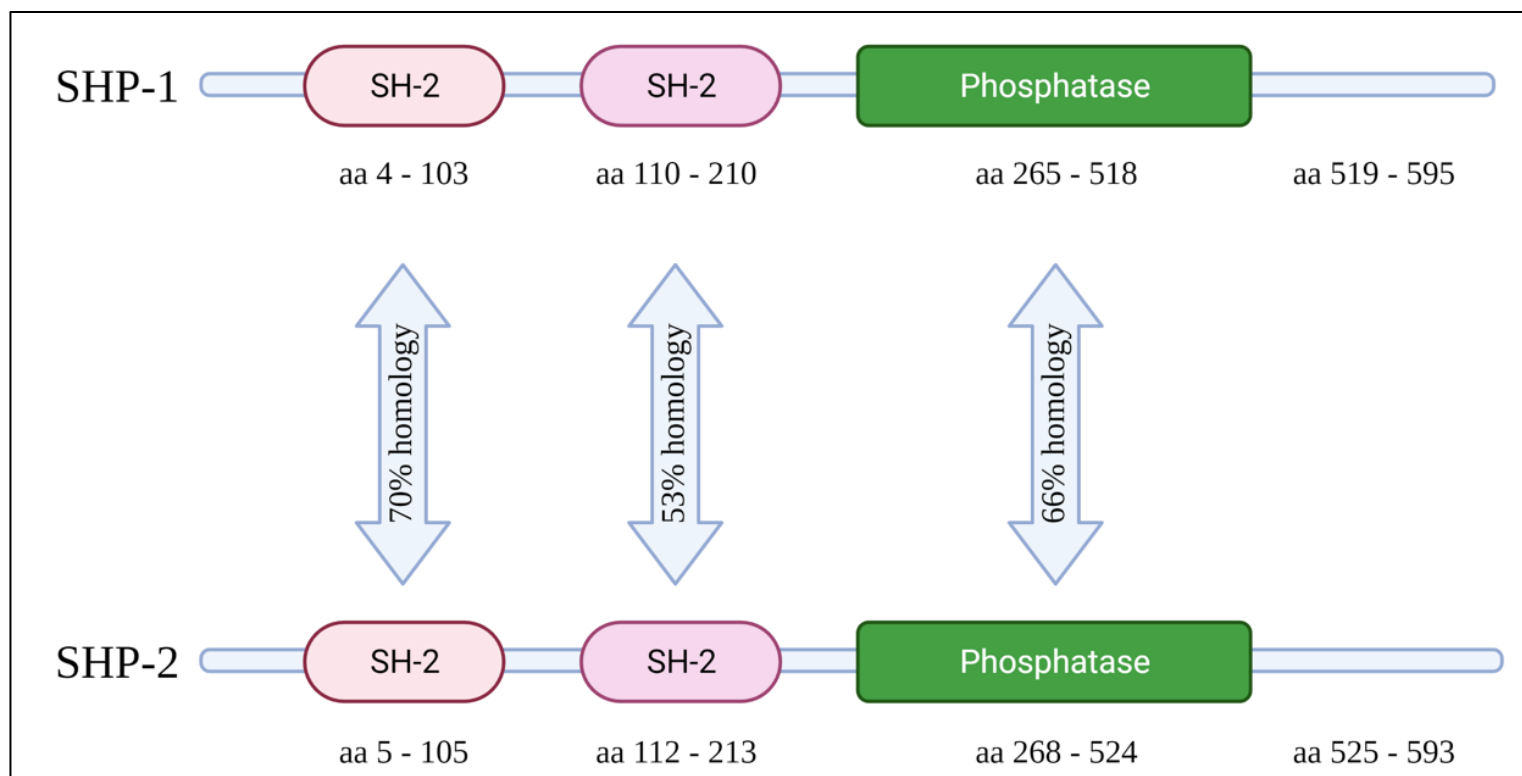


Figure 1.12: Linear structures of SHP-1 and SHP-2. SHP-1 and SHP-2 are protein tyrosine phosphatases that share a high sequence homology. Both phosphatases contain an N-terminus SH2 domain, followed by a catalytic Protein Tyrosine Phosphatase (PTP) domain and a C-terminal SH2 domain.

1.5: Current Approaches to Quantitative Proteomics in Cancer

1.5.1: Current Shortcomings of Non-Quantitative Immunohistochemistry

Immunohistochemistry (IHC) has long been the gold standard for detecting the expression of a target protein in tissue samples. Developed in 1941, the first instance of IHC was the detection of pneumococcus using an anti-pneumococcus antibody conjugated to β -anthryl-carbamide (Coons et al., 1941). IHC involves detecting a target protein via the detection of antigen-specific antibodies which are often conjugated to fluorescent probes, bioluminescent probes or colorogenic substrates (Wang et al., 2020). Whilst immunohistochemistry has become a routine process, there are several advantages and disadvantages associated to the technique. The technique has become a low-cost routine process which is able to inform a user on the expression of a protein or biomarker in a section of formalin-fixed paraffin-embedded (FFPE) tissue. However, the use of antibodies, even monoclonal antibodies, which are more expensive but inherently more antigen-specific, can lead to non-specific binding. When utilising a one-site assay (an assay labelling one probe at a time) such as IHC, the introduction of non-specific binding can result in the generation of false results and reduces the spatial resolution obtainable from a sample. Furthermore, the assessment of IHC-stained sections is subject to operator bias. For example, a pathologist assessing the expression profile of a given biomarker may score with a binary (positive or negative) system, use a narrow grading system (grading expression from 0-4, for example), or look at the percentage of positively stained cells within a sample (Bishop et al., 2018). Therefore, the results obtained could vary drastically between operators. As an example, this has culminated in, different laboratories offering different diagnoses when the same patient tissue was tested (Jensen et al., 2017). Thus, if protein or biomarker expression is to be determined in a sample, it must be carried out in a quantitative, rather than qualitative, manner which preserves the spatial resolution of a sample.

1.5.2: Advancements of Quantitative Immunohistochemistry

The hallmark of quantitative IHC (qIHC) is the ability to accurately determine the spatial resolution of a biomarker and quantify its expression, preferable in a manner free from operator bias. A study by Jensen et al., 2017, created a qIHC platform which was able to quantify human epidermal growth factor receptor 2 (HER2) expression in cell lines and breast cancer tissue sections. The qIHC technique utilises improved catalysed reporter deposition (iCARD), which is comprised of five steps, the first two being largely identical to normal IHC experiments. Firstly, a sample is labelled with a primary antibody which binds to the target biomarker (HER2 in this instance). This is in turn labelled with a secondary antibody which is conjugated to horseradish peroxidase (HRP). However, only a pre-determined fraction of the secondary antibody applied is labelled to HRP. HRP catalyses the deposition of a reporter (a phenol

conjugated to a detectable label such as fluorescein isothiocyanate (FITC)) which is added alongside a cross-linking co-substrate. A F(Ab') fragment conjugated to alkaline phosphatase is added and binds to the deposited cross-linker and substrate (Lohse et al., 2014). This causes a chromogenic amplification and the creation of a red dot. This results in an assay whereby the number of red dots produced in a sample is representative of the number of HER2 receptors in the sample. This assay was compared to ELISA (enzyme-linked immunosorbent assay) and flow cytometry to rank five breast cancer cell lines in order of HER2 expression. qIHC reported the same ranking of HER2 expressing cell lines as both ELISA and flow cytometry. When applied to 44 breast cancer sections, qIHC was able to count the number of dots per cell, reporting on the number of HER2 receptors per cell. Whilst IHC and qIHC were both in concordance in the HER2 expression of these samples, IHC ranks HER2 expression as 0, 1⁺, 2⁺ or 3⁺. This demonstrates an incredibly low dynamic range which is overcome by qIHC (Jensen et al., 2017). In the 3⁺ category, qIHC could further detect and stratify differences in HER2 expression between patients. One of the advantages of this system is the ability to alter the ratio of conjugated and unconjugated secondary antibody to allow for the detection of high or low expression biomarkers. Furthermore, dot counting can be coupled to an automated counting algorithm to remove operator bias from the analysis. Whilst qIHC demonstrates an improved dynamic range and reduction in operator bias, it is still inherently dependant on antibody specificity and only reports on biomarker expression, albeit in a spatial manner. Moreover, the assay outlined here is capable only of exposing the expression profile of a single biomarker at a time.

To combat the lack of simultaneous biomarker detection in qIHC, a multiplexed immunofluorescence approach could be utilised. The Vectra Polaris multispectral imaging platform (Akoya Bioscience) allows for a user to stain a regular FFPE section with up to nine probes (conjugated to different chromophores) and allows for a fully automated slide scan to reveal the spatial resolution of these biomarkers simultaneously. NanoString technologies have increased the advancement of qIHC further by introducing Digital Spatial Profiling (DSP). DSP involves labelling an FFPE section or tissue microarrays (TMAs), or frozen tissue section, with up to four fluorescently labelled primary antibodies. The choice of antibody is free and allows for a user to stain for tissue morphology or markers of interest. The slide is also labelled with a number of primary antibodies conjugated to indexing oligonucleotides which are conjugated to the antibody via an ultraviolet (UV) cleavable linker. The section is then loaded into a GeoMx digital spatial profiler (Nanostring Technologies), and the four fluorescent channels are used to construct a digital image of the sample (Merritt et al., 2020). The user can create a region of interest (either manually or automatically) and a digital micromirror device (DMD) directs UV light to specifically illuminate the region of interest. The UV light cleaves the linker and releases the oligonucleotides which are collected by microcapillary aspiration and then digitally counted (using the nCounter system or next generation sequencing (NGS)) (Merritt et al., 2020). This allows for the

collection of a vast amount of spatial expression profiles from a single tissue sample. Moreover, DSP couples a high dynamic range and high sensitivity with a platform that does not require complex instrumentation. Furthermore, this platform is capable of being run by non-specialised personnel which is significant when translating research science to clinical applications.

Therefore, the remaining shortcomings of current quantitative proteomics are the following: 1) one-site antibody-based detection methods are inherently sensitive to non-specific binding of probe antibodies; 2) whilst being spatially resolved, current qIHC techniques fail to report on post-translational modifications and therefore do not report on biomarker functional states. This is critical as it is biomarker functionality that drives disease progression, and not solely biomarker expression.

1.5.3: Quantitative Proteomics Determined by Mass Spectrometry

Proteomics refers to the analysis of all proteins in a living system and includes the description and identification of protein post-translational modifications. Mass spectrometry (MS) is often central to proteomic experiments and is able to identify and quantify proteins in a sample as well as reporting on their post-translational modifications (Guerrera and Kleiner, 2005). Unlike IHC-based techniques, MS can quantify biomarker abundance in a spatial manner without the reliance of antibody-based detection. This overcomes the non-specificity issues that often plague IHC methodologies. The ability of MS-based approaches to report on post-translational modifications is crucial in the analysis of biomarkers.

Mass spectrometers consist of three fundamental components: an ion source, a mass analyser, and an ion detector (Guerrera and Kleiner, 2005, Sinha and Mann, 2020). Briefly, a routine workflow for utilising MS for proteomics is to isolate proteins from a sample and digest them with a sequence-specific enzyme such as trypsin. The complex mixture of peptides is separated, often by reverse phase chromatography, and turned into the gaseous ion phase, frequently by electrospray ionisation. Next, the mass analyser, such as a quadrupole, is used to direct ions of choice (separated by their mass (m) over charge (z) ratio) into the detector. This displays the m/z spectra for a given analysed peptide. Tandem MS is the process by which analysed peptides are further fragmented and analysed. This is often carried out in a data dependent manner, that is, a list of m/z peaks from analysed peptides is created, often ranked in order of abundance. The mass analyser selects one ion in turn (based on the order of the created list). Peptides are fragmented by collision—induced dissociation, the process of accelerating ions through an electrical field into an inert gas (such as helium, nitrogen or argon) which fragments the peptide ion (Sinha and Mann, 2020). Fragment ions are analysed by MS (MS analysis of a fragmented ion is known as MS/MS or MS^2) and yield greater information of protein structure and amino acid sequence.

Tandem MS can be used in proteomics to report on changes in protein abundance between samples (such as disease vs control samples). For example, stable isotope labelling in amino acid cell culture (SILAC) can be used to measure relative change in protein abundance in two different cell cultures. Cells are grown in two different culture media with either light or heavy amino acids (heavy being ^{13}C lysine or ^{15}N arginine) for at least five division cycles (Chen et al., 2015). This allows for the incorporation of heavy-isotope amino acids in synthesised proteins. One cell culture is then perturbed, for example to mimic a disease state, and MS/MS used to compare the target protein(s) from each cell population (either comparing changes to abundance or post-translational modifications for example). This allows for the quantification of change in biomarker expression or structure between control and disease states. Methods that utilise multiplexed isobaric labelling such as tandem mass tag (TMT) allow for the relative quantitation of proteins in multiple samples at the MS^2 level (Macklin et al., 2020). Whilst these MS applications yield vast proteomic data, they lack a spatial resolution and due to sample digestion and separation, result in sample destruction. Matrix assisted laser desorption ionisation (MALDI) coupled to time of flight (TOF) allow for the spatial resolution of samples when coupled to MS.

MALDI imaging MS (IMS) is a technique capable of quantifying the relative abundance and spatial resolution of proteins, peptides and lipids with a lateral resolution as low as $10\mu\text{M}$ (Schwamborn et al., 2017). Here, samples (FFPE tissue samples for example) are mounted on a slide and covered in a low molecular weight UV absorbing compounding known as a matrix. Next, a laser (often a 337nm laser) is used to desorb and ionise the analytes that are now mixed with the matrix (the matrix aids the desorption and ionisation) and the resulting ionised analytes are analysed by MS (Figure 1.13). The laser raster scans the sample and in some instruments laser adjustments can be as low as $1\mu\text{m}$ (Norris and Caprioli, 2013). This allows for the simultaneous quantitation of multiple biomarkers within a sample which can be spatially resolved and correlated to histopathology and tissue structure.

It is clear that MS-based approaches can overcome the shortcomings of IHC-based approaches, despite the recent advances in the field of the latter. However, whilst reporting on post-translational modifications, MS quantifies biomarker expression in a spatial manner. It is true that proteins are the effectors that drive a host of pathologies, but it is their functionalities that confer disease progression. Therefore, it is crucial that biomarker evaluation is, at least in part, quantitated from a functional standpoint in a manner that preserves a high spatial resolution.

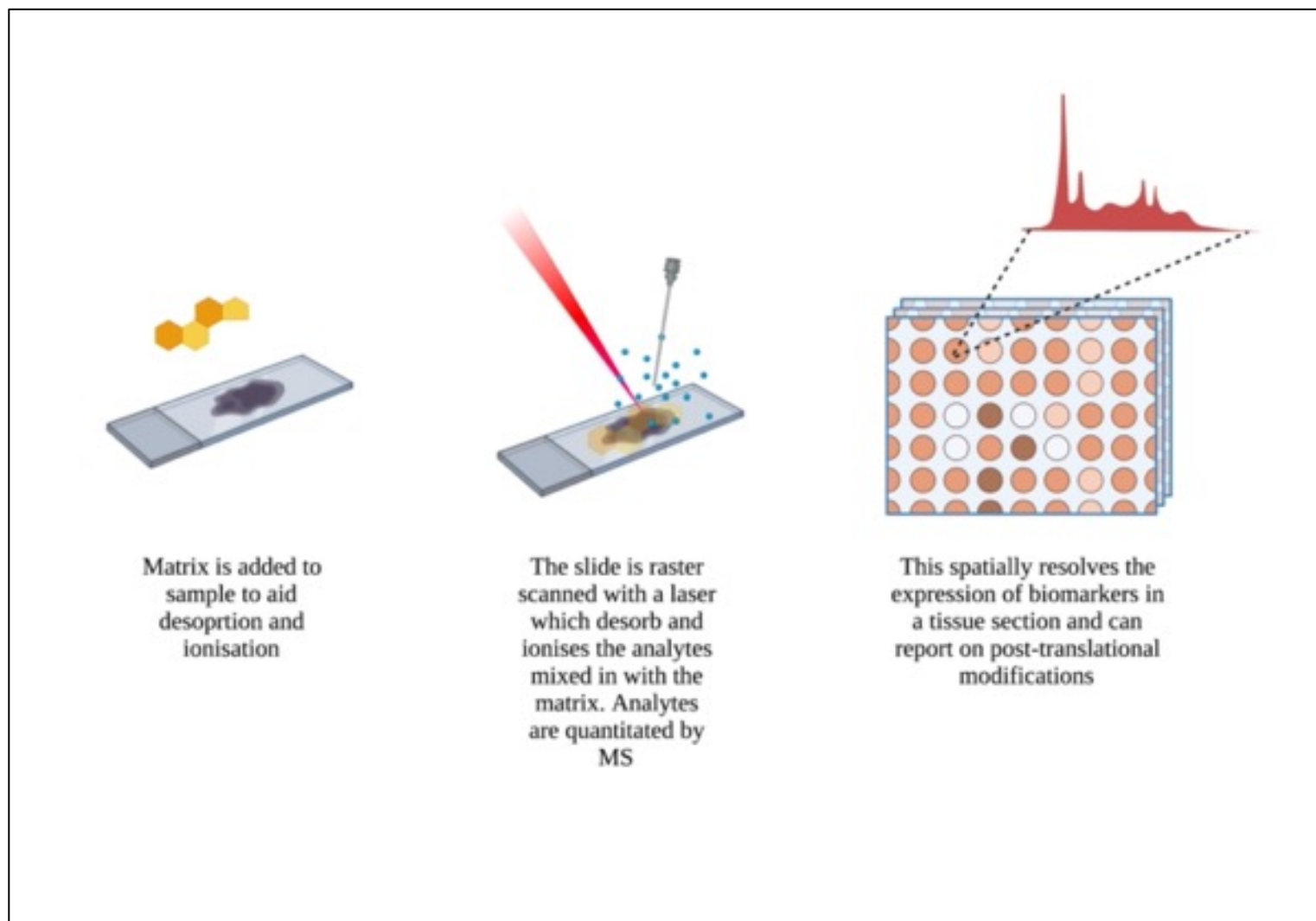


Figure 1.13: MALDI-MS allows for the spatial resolution of biomarker abundance within a tissue section. MALDI imaging MS quantifies the abundance and spatial resolution of biomarkers in a tissue section. A UV absorbing matrix is added to the sample to aid with desorption and ionisation. A UV laser is directed to the tissue and results in the release of ionised analytes. These are quantified by MS and spatially resolved on the tissue. The laser raster scans the section to build an image of biomarker abundance across a tissue section.

1.5.4: The Unmet Need: The Spatiotemporal Resolution of Functional Proteomics

Whilst qIHC has evolved to report on spatial biomarker expression in a high-plex manner, and MS is able to showcase the spatial expression of functional protein groups, a system in which protein (biomarker) functionality can be assessed *in-situ* is required. A two-site labelling assay, coupled to the detection of Förster Resonance Energy Transfer (FRET) has been developed which is able to quantify biomarker expression and functionality in a spatiotemporal manner. Whilst this subsection will outline the development and applications of a two-site assay coupled to FRET, Section 1.6 will introduce and explain FRET in detail. For the purpose of these case studies, FRET involves the transfer of energy from a donor chromophore to an acceptor chromophore, providing the chromophores are within 10nm. IHC is an example of a one-site assay whereby one probe at a time is resolved using an antibody (coupled to a detectable probe such as a chromophore or fluorescent dye) within a sample. As discussed above, non-specific antibody binding within a sample cannot be excluded (Veeriah et al., 2014). A two-site (coincidence) assay has been developed which labels a biomarker on two distinct sites using species-specific primary antibodies. These are then resolved with species-specific F(ab')₂ fragments conjugated to either a donor or acceptor chromophore. When the chromophores are within 10nm, resonance energy transfer occurs from the donor chromophore to the acceptor chromophore. Thus, in this assay, FRET may act as a 'chemical ruler', quantifying distances of 1-10nm in biological systems (Atkins and de Paula, 2009).

A notable achievement of this assay was its ability to determine the activation dynamics of the AGC kinase, protein kinase B (PKB, also known as Akt). Frequently dysregulated in a range of cancers, PKB signal transduction is responsible for cell proliferation, growth, survival, malignant transformations and chemoresistance (Song et al., 2005, Hill and Hemmings, 2002). It was thought that PKB activation was achieved through its recruitment to the plasma membrane, via an interaction of its pleckstrin-homology (PH) domain with PtdIns(3,4,5)P₃. The membrane-bound kinase was thought to be phosphorylated by PDK1, which is also recruited to PtdIns(3,4,5)P₃ at the plasma membrane. This phosphorylation event occurs at threonine-308 (T₃₀₈) in the T-loop of the protein. A secondary phosphorylation event, located on serine-473 (S₄₇₃) within the C-terminus of the kinase, leads to full kinase activation (Calleja et al., 2007). However, the intracellular dynamics by which PDK1 and PKB interacted, remained unknown. Calleja et al., utilised FRET to determine this interaction. The authors constructed two fusion proteins by encoding enhanced green fluorescent protein (EGFP) to the N-terminus of PDK1 and encoding red fluorescent protein (RFP) to the N terminus of PKB α . Here, EGFP acts as the donor chromophore and RFP as the acceptor. The detection of FRET between the two chromophores indicated that, under basal conditions, PKB and PDK1 formed a complex in the cytoplasm. Upon cell stimulation with platelet-derived growth factor (PDGF), the PKB-PDK1 complex translocates to the plasma membrane. The authors also sought to elucidate the mechanism by which PKB makes its T₃₀₈ residue accessible to

phosphorylation by PDK1. Two reporter PKB constructs were created: PKB tagged with green fluorescent protein (GFP) (donor) on the N-terminus and PKB tagged with GFP on the N-terminus and RFP (acceptor) on the C-terminus. It was seen under basal conditions that chromophores were held within 10nm (i.e., FRET was occurring between the donor and acceptor chromophore), indicating the protein was in a “closed, *PH in*” conformation. When stimulated with PDGF, FRET was no longer detected, indicating the chromophores were >10nm apart. This was termed the “open, *PH out*” confirmation, rendering **T₃₀₈** accessible for phosphorylation by PDK1 (Figure 1.14).

The role of a two-site FRET assay is not solely useful in cell signalling research but has also identified predictive biomarkers for clinical utility. In 2014, Veeriah et al., used the two-site assay to label PKB with a pan-Akt and **pT₃₀₈** primary antibodies. The **pT₃₀₈** labels the phosphorylated **T₃₀₈** site of PKB which is a marker of its activation state. The primary antibodies were in turn labelled with species-specific F(ab')₂ fragments. Pan-Akt was labelled with a F(ab')₂-fragment conjugated to ORG488 (donor chromophore) and **pT₃₀₈** labelled with a F(ab')₂-fragment conjugated to HRP-Alexa594 (acceptor chromophore). Here, an enzymatic (tyramide signal amplification) reaction was used to bind the acceptor chromophore to the F(ab')₂ fragment, thus increasing the signal-to-noise ratio of the assay. The resultant assay was named amplified FRET (aFRET). Thus, in this study, aFRET would report on the activation state of PKB, with a higher FRET signal reporting on a higher activation state of PKB. When correlated with overall survival in breast carcinoma, it was seen that higher PKB activation significantly correlated with a worsened overall survival. Crucially, **pT₃₀₈** expression levels did not correlate with patient outcome, indicating that the expression of activated Akt alone was not sufficient to predict patient survival (Figure 1.15) (Veeriah et al., 2014). In 2017, Miles et al., applied the same labelling assay to assess PKB activation state in clear-cell renal cell carcinoma. Again, PKB activation state correlated with a worsened patient outcome whereas **pT₃₀₈** expression did not (Figure 1.15) (Miles et al., 2017).

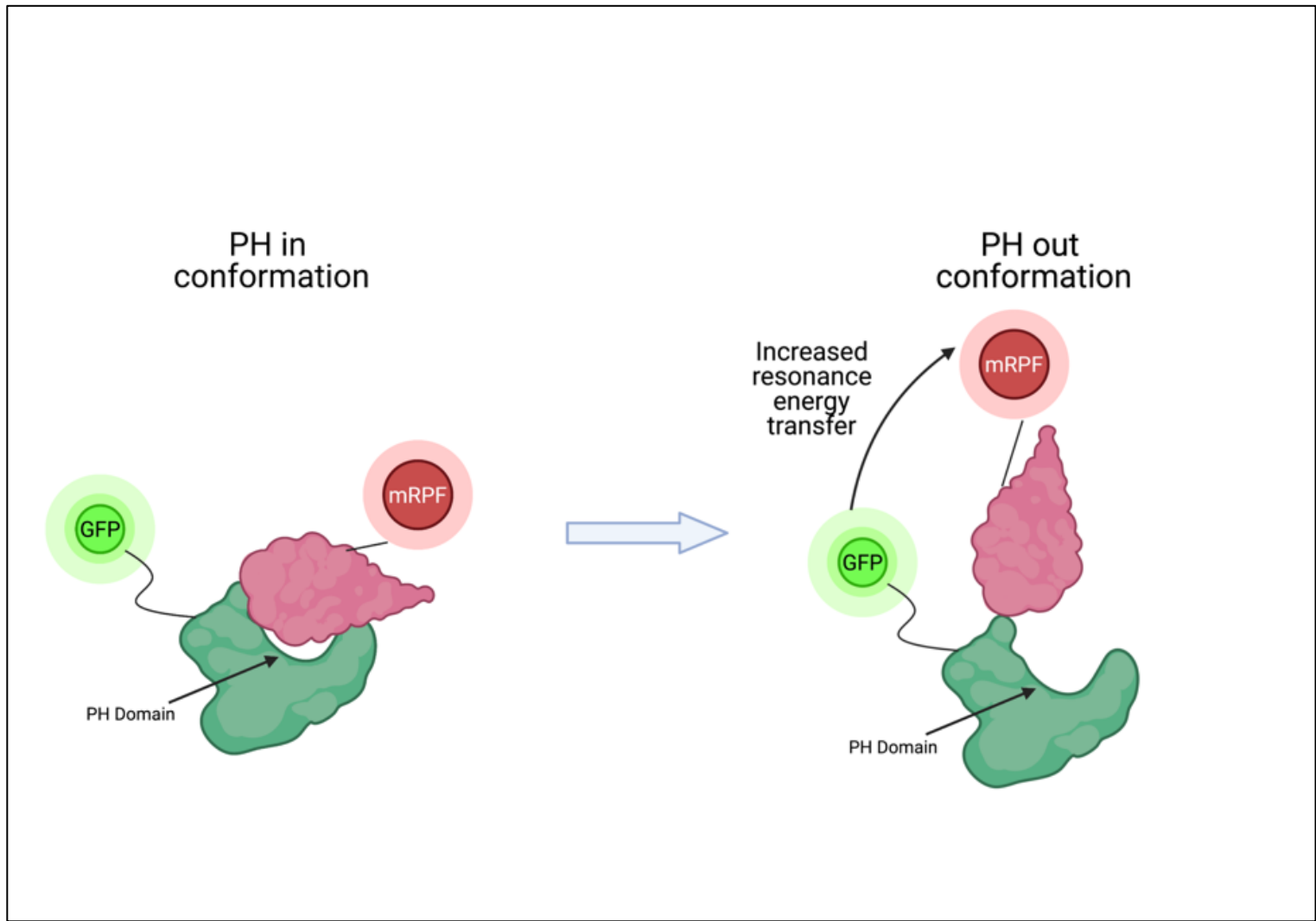
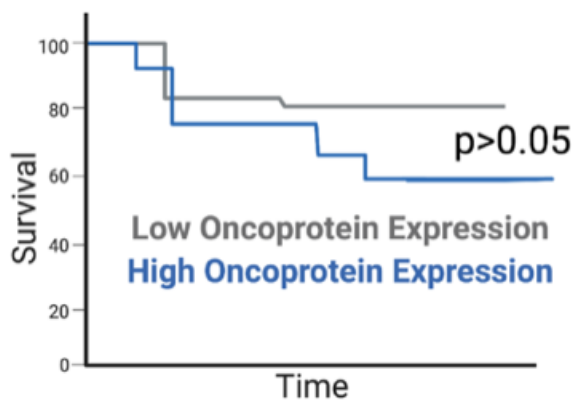


Figure 1.14: Time resolved FRET unravels the activation dynamics of PKB. When inactive, PKB/Akt is held in a closed conformation whereby GFP and mRFP, tagged to N and C termini respectively, are within 10nm. In this conformation, the PH domain is not accessible and therefore cannot be phosphorylated by PDK1. Upon translocation to the plasma membrane, PKB/Akt undergoes a conformational change, making the PH domain accessible to PDK1. In this open, “*PH out*” conformation, GFP and mRFP are brought to closer proximity, therefore the FRET efficiency observed between them is increased in this conformation. *Calleja et al., 2007.*

Therefore, it can be seen that biomarker functionality (the activation state of PKB in this instance) can be predictive of patient outcome and survival in cancer, whereas biomarker expression is not. Moreover, the measurement of distances of 1-10nm result in an assay with a high dynamic range, which is lacking in non-quantitative IHC. Other techniques to perform intracellular or indeed intercellular measurements are available, such as the proximity ligation assay (PLA). However, PLA has a working distance of up to 40nm. This reports on proximity alone and cannot report on direct interactions and associates such as aFRET (Söderberg et al., 2008). Coupled to fluorescence lifetime imaging microscopy (FLIM), aFRET can be spatially resolved in tissue. The two-stie coincidence assay relies on the binding of two primary antibodies to a target. This makes the assay more robust against the non-specific binding events that plague traditional IHC. Whilst only reporting on one biomarker at a time, aFRET can overcome the issues experienced in traditional IHC and can combine the spatial resolution of IMS with a highly dynamic functional readout that holds significant clinical utility. Moreover, this assay can be manipulated to target virtually any biomarker for which commercial primary antibodies exist. Therefore, aFRET could be utilised to measure checkpoint interactions in cancer which may ultimately be predictive of patient outcome and response. Prior to hypothesising the utility aFRET may hold in the domain of immune oncology, it is crucial to explain the photophysical events that underpin FRET and FLIM.

Survival vs Oncoprotein Expression



Survival vs Oncoprotein Activation

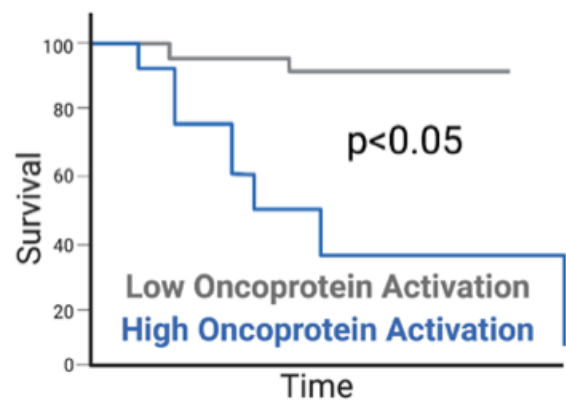


Figure 1.15: aFRET quantifies biomarker activation state which is predictive of patient outcome. When using IHC to assess oncoprotein expression, expression levels of proteins do not correlate to patient survival. This is in part due to the insensitive and subjective nature of IHC assays. Two-site amplified FRET/FLIM assesses oncoprotein activation, whereby oncoprotein activation correlates survival and can predict patient outcome in a range of solid neoplasia.

1.6: Förster Resonance Energy Transfer (FRET) Determined by Fluorescence Lifetime Imaging Microscopy (FLIM)

1.6.1: Introduction to FRET

Förster resonance energy transfer (FRET) was first documented in the 1940s by Theodore Förster (Förster, 1946). FRET is a photophysical event which involves the non-radiative transfer of energy from a one chromophore (termed the donor) to another (termed the acceptor) via long-range dipole-dipole coupling (Bastiaens and Squire, 1999, Förster, 1946, Lakowicz, 2002). This transfer of energy only occurs when chromophores are between 1-10nm (10-100Å) apart. Unlike Dexter energy transfer, which involves the transfer of an electron from an excited donor to an acceptor, FRET involves the transfer of electronic energy from the donor to the acceptor (Valeur and Berberan-Santos, 2013). It is the transfer of energy via the Coulombic interactions between electrons that allows FRET to operate over 10-100Å (whereas the transfer of an electron in Dexter energy transfer occurs at distances of 10Å or less). For FRET to occur, the donor chromophore absorbs a photon from an excitation light source. This excites an electron from the ground state (S_0) which upon relaxation settles in the lowest excited singlet state (S_1). If the acceptor chromophore is within 10nm, the energy released when the electron returns to the ground state may simultaneously excite an electron in the acceptor chromophore. Upon relaxation of this electron from the S_1 to S_0 state, the energy emitted by this relaxation is in the form of a photon; providing no other quenching states exist (Figure 1.16).

FRET efficiency (E) is the quantum yield of energy transfer transition, that is, the fraction of energy that is transferred per donor excitation event. FRET efficiency is calculated using the following equation:

$$E = \frac{k_{ET}}{k_f + k_{ET} + \sum k_i}$$

Equation 1-1

Here, k_{ET} is the rate of FRET, k_f is the rate of radiative relaxation and k_i are the rates of non-radiative relaxation. Within a point dipole-dipole approximation, the FRET efficiency (E) can also be used to calculate the distance between the donor and acceptor chromophores using the following equation:

$$E = \frac{1}{1 + \left(\frac{r}{R_0}\right)^6}$$

Equation 1-2

Here, r is the distance between the two chromophores and R_0 (known as the Förster radius) is the distance between the chromophores at which the FRET efficiency is 50%.

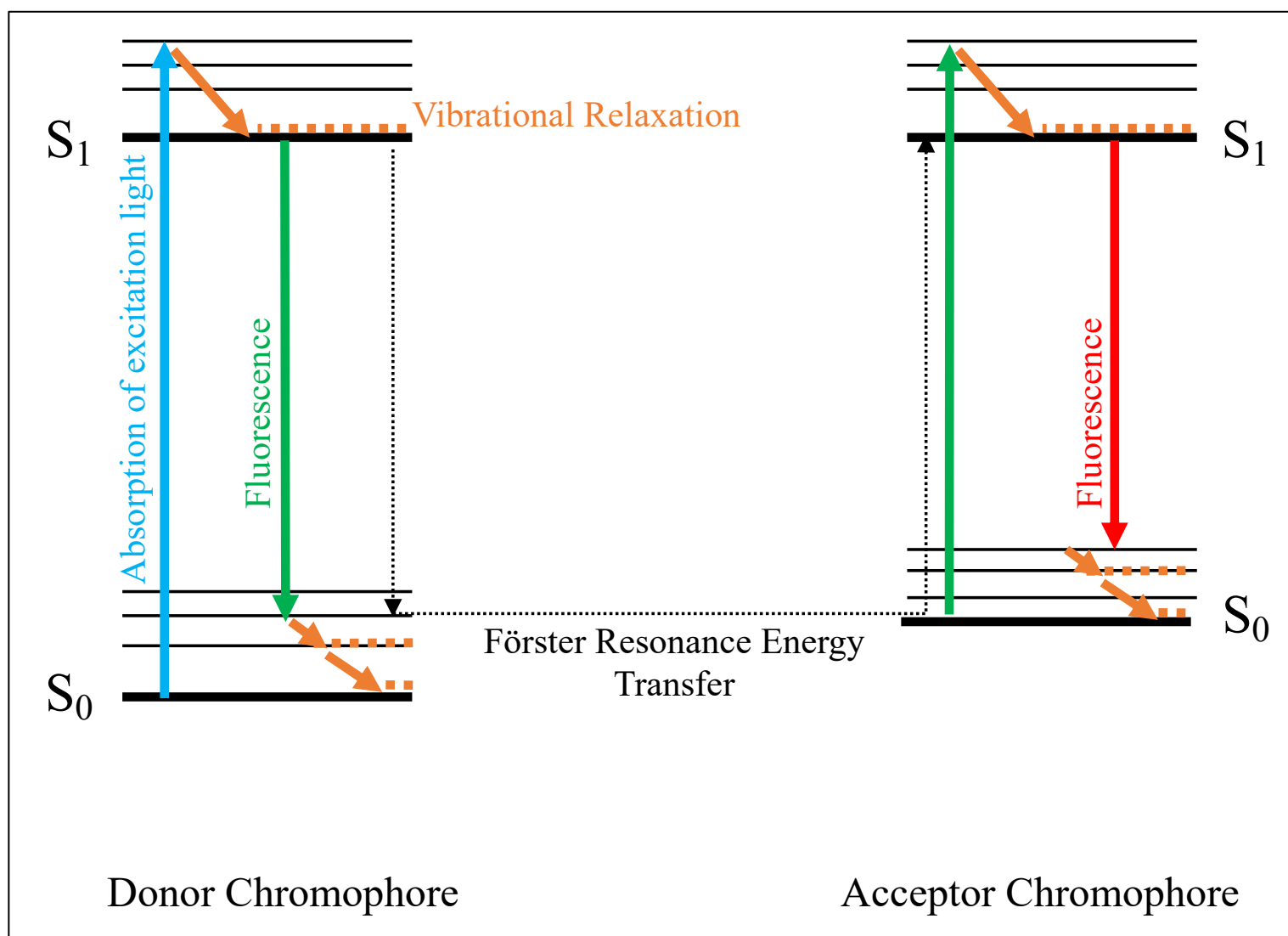


Figure 1.16: Jablonski diagram indicating the Coulombic interactions that underpin resonance energy transfer. A Jablonski diagram highlights the resonance energy transfer that occurs in FRET. When the donor chromophore absorbs a photon of excitation source, at an equal or greater energy, an electron is excited to a higher energy state. The electron undergoes vibrational relaxation to the S_1 energy level by a non-radiative process known as internal conversion. Fluorescence decay is a radiative process where an electron drops to the ground state via the emission of a photon. If the donor chromophore is within 10nm of the acceptor, rather than the release of a photon from the donor, the energy released is absorbed by the acceptor chromophore, which in turn excites an electron within the acceptor chromophore. Upon relaxation of this electron back to the ground state, a photon ($h\nu$) is released from the acceptor chromophore.

For FRET to occur, the donor and acceptor chromophores must have suitable overlapping spectroscopic properties. This means that within the donor, several vibronic transitions have practically the same energy as the acceptor (Valeur and Berberan-Santos, 2013). The donor chromophore should be selected to have a good ability to absorb and emit photons. That is, it should have a high extinction coefficient and high quantum yield. The overlap of the donor emission spectrum and acceptor absorption spectrum means that the energy lost from the donor upon deexcitation should excite the acceptor. With a higher overlap of these spectra, one can achieve a higher efficiency of energy transfer. The overlap integral, J , calculates that overlap between the donor and acceptor spectra:

$$J = \int_0^{\infty} F_D(\lambda) \epsilon_A(\lambda) \lambda^4 d\lambda$$

Equation 1-3

Here, F_D represents the normalised emission spectrum of the donor, ϵ_A stands for the molar absorption coefficient of the acceptor, and λ is the wavelength. The required overlap of donor and acceptor chromophores is outlined with a spectrum in Figure 1.17. The efficiency of energy transfer is also relative to the emission transition dipole of the donor, and the absorption dipole of the acceptor. k^2 is the orientation parameter and quantitates the interaction between two dipole moments. Values of k^2 can theoretically range from 0 (perpendicular dipoles) to 4 (collinear dipoles). FRET may only occur when dipoles are in a non-perpendicular orientation (Valeur and Berberan-Santos, 2013). k^2 is calculated using the following equation:

$$k^2 = (\cos\theta_T \cdot 3\cos\theta_0\cos\theta_A)^2 = (\sin\theta_0\sin\theta_A\cos\phi \cdot 2\cos\theta_0\sin\theta_A)^2$$

Equation 1-4

k^2 is equal to 1 when the two transition dipoles are parallel. In a system where the donor and acceptor chromophores are permitted to rotate freely, k^2 is assumed to be $\frac{2}{3}$.

A high R_0 result in a high FRET efficiency (i.e., 50% FRET efficiency occurs when the chromophores are farther away). R_0 is a function of the quantum yield of the donor chromophore (ϕ_D), the spectral overlap of the donor and acceptor chromophores (J , calculated above) and is directly related to the transition dipole orientation (k^2) and refractive index of the medium (n). The following equation outlines this relationship:

$$(R_0)^6 \propto k^2 \phi_D J(\lambda) n^{-4}$$

Equation 1-5

The FRET efficiency can be calculated by three steady state methods (intensity-based) or time-resolved methods (Valeur and Berberan-Santos, 2013).

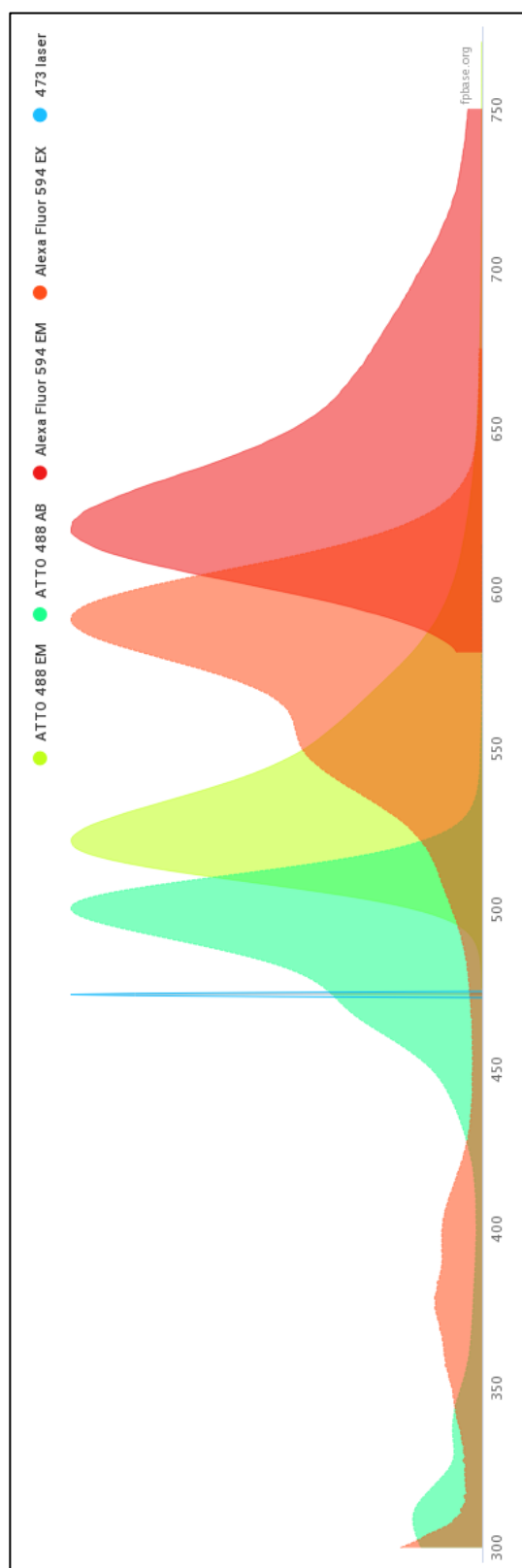


Figure 1.17: Excitation/emission spectrum from ATTO488 and Alexa594. For FRET to occur, a suitable chromophore pair must be selected for use in experiments. Here, the donor chromophore, ATTO488 has an emission spectrum that overlaps with the excitation spectrum of the acceptor chromophore, Alexa594. Therefore, upon excitation of ATTO488 (in this case with the 473nm laser indicated), the non-radiative transfer of energy may occur providing the chromophores are with 10nm of each other. Importantly, the 473nm laser excitation source does not directly excite the acceptor chromophore.

1.6.2: Steady-State vs Time-Resolved FRET

Intensity-based or steady-state FRET is calculated by measuring changes in either donor or acceptor fluorescence intensity. The FRET efficiency can be resolved by three methods:

- 1) **Decrease in donor fluorescence:** Transfer of energy from the donor to the acceptor chromophore results in a reduction of the quantum yield of the donor. The FRET efficiency is calculated using the following equation:

$$\phi_T = 1 - \frac{\phi_D}{\phi_D^0}$$

Equation 1-6

Here, ϕ_D^0 and ϕ_D are the quantum yields of the donor in the absence and presence of the acceptor, respectively.

- 2) **Comparison between the absorption spectrum and excitation spectrum (observed through acceptor fluorescence):** If complete transfer occurs (i.e., FRET efficiency ϕ_T is 1, then the excitation band corresponding to donor excitation is lower than the absorption band. The corrected excitation spectrum is calculated as follows, where C is the instrumental factor constant:

$$I_A(\lambda, \lambda_A^{em}) = C\phi_A[A_A(\lambda) + A_D(\lambda)\phi_T]$$

Equation 1-7

The absorption spectrum is:

$$A(\lambda) = A_A(\lambda) + A_D(\lambda)$$

Equation 1-8

- 3) **Increase in acceptor fluorescence:** The fluorescence of the acceptor chromophore is increased upon energy transfer, thus measuring the ratio of acceptor fluorescence in the absence and presence energy transfer (i.e., the absence or presence of the donor chromophore) yields the efficiency of energy transfer:

$$\phi_T = \frac{A_A(\lambda_D)}{A_D(\lambda_D)} \left[\frac{I_A(\lambda_D, \lambda_A^{em})}{I_D^0(\lambda_D, \lambda_A^{em})} - 1 \right]$$

Equation 1-9

It should be noted, that whilst straightforward, method (1) cannot be utilised when using a donor with a very low quantum yield. Moreover, steady-state measurements of FRET are dependent on the light path and chromophore concentration (Wouters and Bastiaens, 2000). Therefore, steady-state measurements should only be performed when the stoichiometry of the donor and acceptor chromophores is 1. Time-resolved measurements report directly on FRET and are independent of light path and chromophore concentration (Wouters and Bastiaens, 2000). One method to time-resolve transfer efficiency is:

- 1) **Measure decay of donor fluorescence:** If the donor fluorescence decay is monoexponential, then the transfer rate constant (k_T) can be measured as follows:

$$\frac{1}{\tau_D} = \frac{1}{\tau_D^0} + k_T$$

Equation 1-10

Here, τ_D^0 and τ_D are the decay times (lifetimes) of the donor in the absence and presence of resonance energy transfer (i.e., in the absence or presence of the acceptor chromophore). The transfer (FRET) efficiency can therefore be calculated with the following calculation:

$$\phi_T = 1 - \frac{\tau_D}{\tau_D^0}$$

Equation 1-11

And the chromophore distance can then be calculated with the following equation:

$$r = \frac{R_0}{\left(\frac{\tau_D^0}{\tau_D}\right)^{\frac{1}{6}}}$$

Equation 1-12

Time-resolution of FRET efficiency can assess whether the decay in the absence and presence of the acceptor is monoexponential or not. If a non-monoexponential donor decay exists in the absence of the acceptor, this is likely reporting on heterogeneity of the donor chromophore microenvironment. This can then be empirically modelled as a sum of exponentials and used to calculate the transfer efficiency using the average donor decay times in the absence and presence of the acceptor using the following two equations:

$$i_D(t) = \sum_i \alpha_i \exp\left(\frac{-t}{\tau_i}\right)$$

Equation 1-13

$$\phi_T = 1 - \frac{\langle \tau_D \rangle}{\langle \tau_D^0 \rangle}$$

Equation 1-14

The amplitude-averaged decay times are defined as:

$$\langle \tau \rangle = \frac{\sum_i \alpha_i \tau_i}{\sum_i \alpha_i}$$

Equation 1-15

This approach to measure fluorescence decay of the donor is valid providing the decay is not too far from a monoexponential.

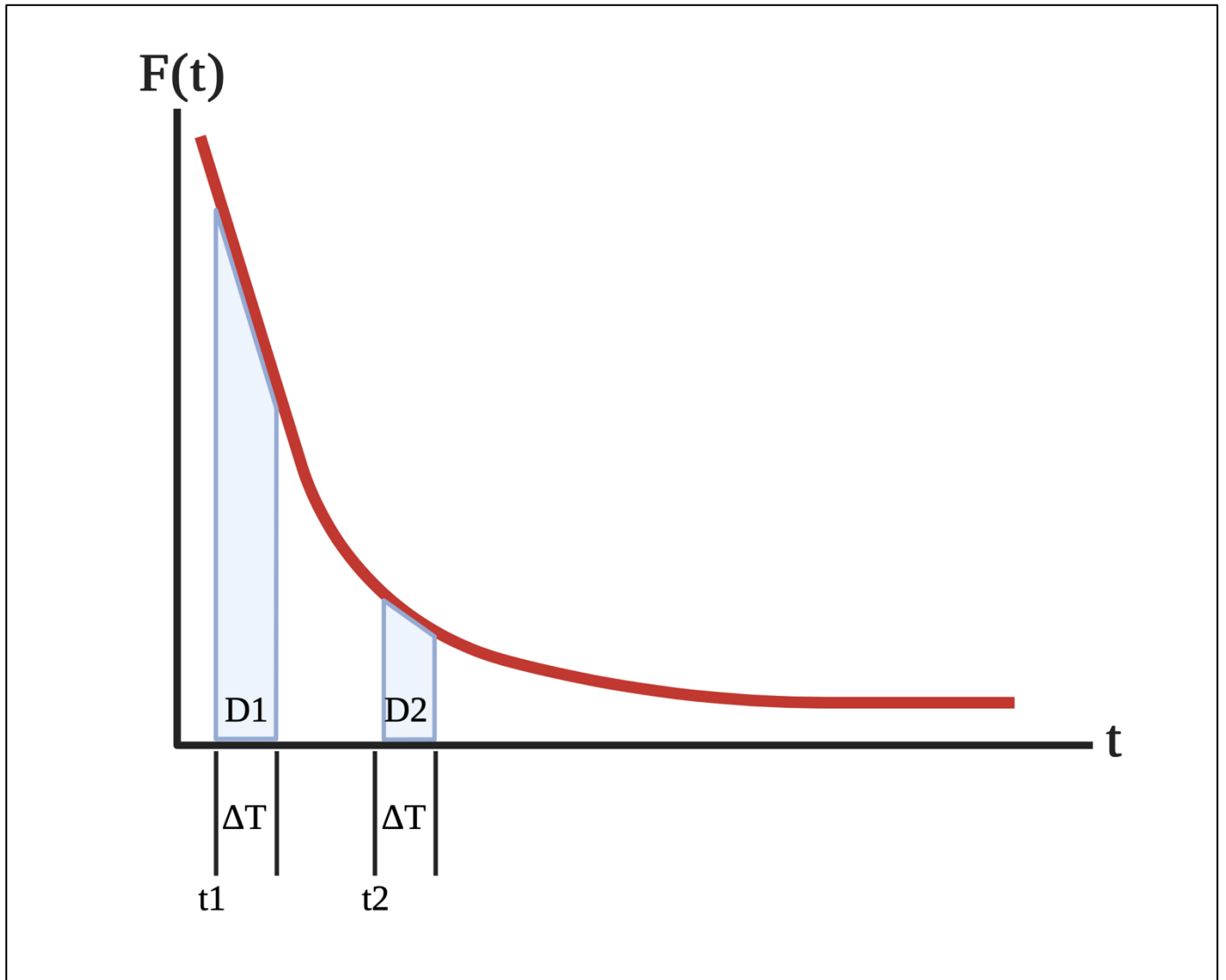


Figure 1.18: Intensity decay curve for time-domain FLIM. At time t_D after an excitation light pulse, a sampling gate pulse is applied to the photocathode of the intensifier. This allows for the detection of fluorescence at various time delays. For a monoexponential decay, two delay times are sufficient to calculate the fluorescence. These times, t_1 and t_2 , are used alongside the corresponding fluorescence signals D_1 and D_2 .

When working with time-resolved FRET measurements, FLIM can be used to spatially measure changes in the excited-state lifetime of a chromophore.

1.6.3: FLIM in the Time-Domain

Time-domain measurements of fluorescence decay are typically performed using fast-gated single-photon counting detectors and a pulsed light (often laser) source which pulses at frequencies of 15kHz to 2MHz (Lakowicz, 2002). The use of a short light pulse (which is short in comparison to the lifetime of the chromophore) allows for the recording of the exponential decay of the fluorescence intensity of the chromophore (Bastiaens and Squire, 1999). This can be measured directly (by gated detection or pulse sampling) or using time-resolved electronics. Time-resolved electronics, such as time-correlated single-photon counting (TCSPC) measure the time between the excitation photon of the laser reaching the sample and the emission photon of the chromophore reaching the detector. This determines a photons time of arrival, which is converted into an analogue voltage using a time-amplitude converter circuit. These counted photons are binned in a histogram as a function of time to measure the number of photons emitted over time, thus giving a readout of fluorescence decay. In typical TCSPC systems, at high photon count rates, most photons will not be measured due to the “dead-time” of the instrument. This leads to an effect known as photon pile-up which can skew the resulting lifetime histogram. To avoid this, a low photon count is required which is ideally less than 10% of the excitation repetition rate.

Within a gated image intensifier, at time t_D after the excitation light pulse, a sampling gate pulse, Δt , is applied to the photocathode of the intensifier. This allows for the detection of fluorescence at various time delays. For a monoexponential decay, with the form $\alpha \exp(\frac{-t}{\tau})$, two delay times are sufficient to calculate the fluorescence. These times, t_1 and t_2 , are used alongside the corresponding fluorescence signals D_1 and D_2 , calculated below:

$$D_1 = \int_{t_1}^{t_1+\Delta t} \alpha \exp(\frac{-t}{\tau}) dt$$

Equation 1-16

$$D_2 = \int_{t_2}^{t_2+\Delta t} \alpha \exp(\frac{-t}{\tau}) dt$$

Equation 1-17

Using t_1 , t_2 , D_1 and D_2 , (Figure 1.18) the resulting lifetime can be calculated using:

$$\tau = \frac{t_2 - t_1}{\ln\left(\frac{D_1}{D_2}\right)}$$

Equation 1-18

The need for just four parameters allows for lifetime images and results to be calculated quickly, although the time resolution of the gated image intensifier (often around 3ns) is not sufficient for fast decaying probes. If pixel-by-pixel deconvolution is needed for the resulting image, excessively long computational times may arise. Frequency domain FLIM allows for the faster calculation and acquisition of lifetime events.

1.6.4: FLIM in the Frequency-Domain

In the frequency domain, the optics and detection system are coupled to a continuous wave laser that is acousto-optically modulated. The lifetime of a chromophore may also be measured by exciting the chromophore with sinusoidally modulated light, that is, light whose intensity varies sinusoidally with time (Figure 1.19) (Lakowicz, 2002). Upon excitation with modulated light, the chromophore will emit sinusoidal wave at the same frequency but with a delay in phase and reduction in modulation. This is calculated against a known fluorescence reference (Figure 1.19) (E Gratton et al., 1984, Valeur and Berberan-Santos, 2013). In a homodyne system, the modulation frequency of the image intensifier and excitation source is the same (Valeur and Berberan-Santos, 2013). For monoexponential decays, the lifetime of a chromophore can be calculated by either determining the phase shift or modulation ratio (ϕ or M respectively) using the following equations:

$$\tau_\phi = \frac{1}{\omega} \tan^{-1} \phi$$

Equation 1-19

$$\tau_M = \frac{1}{\omega} \left(\frac{1}{M^2} \right)^{\frac{1}{2}}$$

Equation 1-20

Here, ω is the angular frequency ($2\pi f$).

The description of FRET determined by FLIM outlined here, coupled with the literature review above indicate that FRET/FLIM holds the potential to make precise biological measurements, acting as a “chemical ruler” which exhibits a high dynamic range and sensitivity.

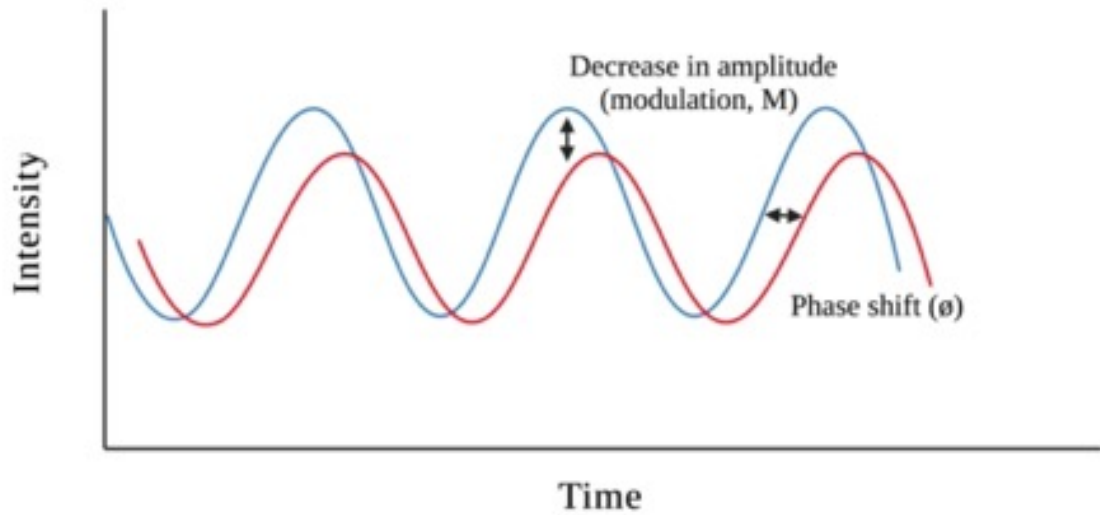


Figure 1.19: Sinusoidally modulated light is the excitation source for frequency-domain FLIM. In the frequency domain, a continuous wave laser is sinusoidally modulated using an acousto-optical modulator. Once excited with sinusoidally modulated light, a chromophore will emit sinusoidal wave of the same frequency but with a reduced amplitude (demodulation) and a delay in phase (phase shift). Both the demodulation and phase shift can be used to calculate the lifetime of a chromophore.

1.7: Aims and Hypotheses

The literature reviewed here has identified that, whilst the therapeutic targeting of the immune checkpoints CTLA-4/CD80 and PD-1/PD-L1 (either with mono- or dual-therapies) is efficacious, it is often prescribed to an incorrectly stratified patient subset. The use of ligand expression to predict patients that should be prescribed these immunotherapies is insufficient, as multiple studies have shown that biomarker functionality, as opposed to expression, correlates with patient outcome (Miles et al., 2017, Veeriah et al., 2014, Kong et al., 2006, Sánchez-Magraner et al., 2020). It is thought that aFRET could successfully be applied to immune oncology (and subsequently termed immune-FRET, (iFRET) for the detection of intercellular interactions, and remain aFRET for intracellular applications) and employed to measure receptor-ligand interactions in cancer, which would be predictive of patient outcome, rather than ligand expression.

Whilst the emergence of qIHC and advancements in IMS have allowed for the spatial quantification of biomarker expression, they fail to report on biomarker functionality. We propose that iFRET can be used to quantitatively measure, at a nanometre resolution, CTLA-4/CD80 and PD-1/PD-L1 interactions in solid cancer samples. We acknowledge the high-plex capabilities of IMS and qIHC, but we predict that the quantitation of the functionality of a single biomarker at a time confers more biologically relevant data than a large volume of expressional analyses.

Therefore, the following aims and hypotheses are proposed:

1.7.1: Hypotheses

- 1) iFRET will quantitatively measure CTLA-4/CD80 and PD-1/PD-L1 interaction states in a range of solid tumours and correlate with patient survival. The analysis of ligand expression (CD80 or PD-L1) will not correlate with patient outcome.
- 2) iFRET will determine the evolution of checkpoint interaction states in radiofrequency-ablated lung metastases and elucidate the mechanism by which an abscopal effect occurs.
- 3) iFRET, coupled with aFRET, will quantitatively confirm that PD-1/PD-L1 signal transduction is in part mediated by the phosphatase SHP-2. iFRET and aFRET will identify SHP-1 as a signal transducer of the PD-1 receptor.

1.7.2: Aims and Objectives

- 1) **Chapter 3:** To establish iFRET as a two-site assay capable of measuring intercellular PD-1/PD-L1 and CTLA-4/CD80 interactions in a cell co-culture model. To validate PD-1/PD-L1 interaction states in solid tumour samples in retrospective malignant melanoma and NSCLC studies.

- 2) **Chapter 4:** To use the established iFRET assay to assess the evolution of CTLA-4/CD80 and PD-1/PD-L1 interaction states in metastatic lung samples pre- and post-treatment with radiofrequency ablation. This will identify if these checkpoints play a role in an immune-mediated abscopal effect. This study will be prospective with a future opportunity to correlate checkpoint interaction with patient survival when available.
- 3) **Chapter 5:** Use iFRET and aFRET to confirm if the interaction of PD-1 and PD-L1 results in the recruitment of SHP-2 to the Y₂₄₈ residue of PD-1. iFRET and aFRET will then elucidate whether SHP-1 is a binding partner of the Y₂₄₈ residue of SHP-1. CRISPR/Cas12 will be used to create modified cell lines in which the 248 residue is mutated to be a phospho-inactive (Y₂₄₈A) or phospho-mimetic (Y₂₄₈E) residue, thus reporting on the significance of this phosphorylation event after receptor ligation with PD-L1.

Chapter 2: Materials and Methods

2.1: Buffers and Reagents

Please see Table 2.1 for list a of antibodies used.

2.1.1 Buffers

TAE Buffer (10X, pH 7.4): 24.2g tris-base, 1.86g ethylenediaminetetraacetic acid (EDTA) and acetic acid to adjust pH.

Lysogeny Broth (LB): 20g of LB in 1L of ddH₂O.

Phosphate Buffered Saline (10X, pH 7.4): 1.37M NaCl, 27mM KCl, 100mM Na₂HPO₄, 18mM KH₂PO₄ made up to 1L in distilled water.

DNA Loading Buffer (10X): 200mg bromophenol blue, 90mL glycerol, make up to 120mL with water.

2.1.2: Sample Preparation Solutions

Bovine Serum Albumin: 1mg/mL in 1X PBS.

Sodium Borohydride Solution: 1mg/mL of sodium borohydride in 1X PBS.

Rhodamine B (50uM): 1.2mg rhodamine B in 50mL of distilled water. Used as fluorescence lifetime imaging reference.

Please see Table 2.2 for complete list of reagents used.

Table 2.1: List of Antibodies.

Name	Description	Host Species	Catalogue Number	Source
1. α PD-1	Primary monoclonal antibody	Mouse	ab52587	Abcam
2. α PD-L1	Primary monoclonal antibody	Rabbit	ab205921	
3. α CTLA-4	Primary monoclonal antibody	Mouse	ab19792	
4. α CTLA-4	Primary polyclonal antibody	Rabbit	MBS2522916	
5. Ipilimumab	Blocks CTLA-4/CD80 interactions	-	JA1020	Promega
6. J1201	Blocks PD-1/PD-L1 interactions	-	J1201	
7. AffiniPure F(ab') ₂ Fragment Donkey Anti-Mouse IgG (H+L)	Secondary F(ab') ₂ fragment to label mouse primary antibodies (α PD-1/ α CTLA-4)	Donkey	715-006-150	Jackson ImmunoResearch
8. Peroxidase AffiniPure F(ab') ₂ Fragment Donkey Anti-Rabbit IgG (H+L)	Secondary F(ab') ₂ fragment conjugated to horseradish peroxidase. For labelling of rabbit primary antibodies (α PD-L1/ α CD80)	Donkey	711-036-152	

Table 2.2: List of Reagents.

Name	Description	Catalogue Number	Source
Heat-inactivated foetal bovine serum	Cell growth medium supplement	A3840001	ThermoFisher Scientific
Gibco DMEM high glucose with GlutaMax	Complete growth medium for HeLa cells	10569010	
Gibco RPMI1640	Complete growth medium for Jurkat and MOLT-4 cells	21875034	
Penicillin/Streptomycin	Cell growth medium supplement	15140148	
Pierce endogenous peroxidase suppressor	Quenches endogenous intracellular peroxidases to prevent premature activation of tyramide signal amplification step	35000	
TSA signal amplification Kit	Allows for the labelling and amplification of the acceptor chromophore, Alexa594 to the acceptor site of samples	T20950	
TSA SuperBoost kit*		B40925	
Prolong Diamond anti-fade mount	Glycerol-based mount which protects against photobleaching in the visible and near infrared spectra	P36970	
Prolong Glass antifade mount **	Glycerol-based mount which protects against photobleaching in the visible and near infrared spectra with a refractive index of 1.52, resulting in enhanced imaging resolution	P36980	Sigma Aldrich
ATTO488 NHS ester	Donor chromophore, subsequently conjugated to AffiniPure F(ab') ₂ fragment donkey anti-mouse IgG	41698-1MG-F	
Sodium borohydride	Reduces the autofluorescence of samples caused by fixative agents	45,288-2	
Rhodamine B	Reference for mFLLIM system with a defined lifetime of 1.840ns	234141-10G	
Hydrophobic PAP pen	For drawing a hydrophobic barrier around sample tissue on a slide	Z377821-1EA	

Bovine serum albumin	Prevents non-specific labelling and binding of antibodies	A2153-100G	
----------------------	---	------------	--

* TSA signal amplification kit (T20950) was used for all results presented in Chapter 3. Thermofisher Scientific discontinued this product which was subsequently replaced with TSA SuperBoost kit (B40925). Optimisations were performed to ensure consistent fluorescence intensities and lifetimes were achieved when moving from the old product to new.

** The samples presented in Chapter 3 were cured with Prolong Diamond antifade mount. Prior to the experiments carried out in Chapter 4, Thermofisher released a new mount, Prolong Glass, with a higher refractive index (1.52) and increased photobleaching protection. Therefore, Prolong Glass was adopted for experiments presented in Chapter 4.

2.2: Molecular Biology

2.2.1: Design of CRISPR Cloning Strategy

For a list of oligonucleotides, enzymes and plasmids used, please see Tables 2.3, 2.4 and 2.5 respectively). CRISPR (Clustered Regularly Interspaced Short Palindromic Repeats) guides were created and inserted into a vector plasmid coding for *Cpf1*, Cas12. These guides were designed to specifically recognise a sequence of DNA 19bp from the site that was modified. pAsCpf1(TYCV)(BB) (**pY₂₁₁**) was a gift from Feng Zhang (Addgene plasmid # 89352; <http://n2t.net/addgene:89352>; RRID: Addgene_89352). The oligonucleotides 1 and 2 (see Table 2.3) were annealed to create the guide sequence insert. Subsequently, the plasmid was opened by restriction digestion with BbsI prior to the insertion of the guide sequence, CTAGGAAAGACAATGGTGGC, which corresponds to amino acids A₂₄₉ to S₂₅₅ of programme cell death protein 1 (*PDCDI*). The guide sequence was inserted after the U6 promoter of the plasmid.

To create donor-repair template inserts, oligonucleotides 5&6 and 7&8 were used to create **Y₂₄₈A** and **Y₂₄₈E** mutations, respectively. These oligonucleotides also contained 9bp micro-homology arms complimentary to the sequence that flanks the **Y₂₄₈** locus of the *PDCDI* gene. One oligonucleotide of each pair (oligonucleotides 5 and 7) was phosphorylated on the 5' end using the T4 polynucleotide kinase (PNK) kit from New England Biolabs as per the manufacturers instruction (please see Table 2.6 for a list of molecular cloning kits used). Oligonucleotides 5&6 and 7&8 were annealed. The annealed primers were amplified using genomic DNA (gDNA) as a template with mNeonGreen (mNG) so as to incorporate the positive selection marker into the insert sequence. λ exonuclease digestion was carried out which creates single stranded inserts and increases homology-directed repair.

Additionally, a full-length homology arm approach was undertaken. 956bp homology arms were created by carrying out a polymerase chain reaction (PCR) with gDNA using primers 15-20. This product was inserted into an opened vector plasmid, by Gibson Assembly, which also coded for the positive selection marker mNG.

To complete the above cloning strategy, a range of molecular cloning techniques: gDNA extraction, PCR, restriction digestion, ligation, Gibson assembly and bacterial transformation were carried out. These techniques are explained in detail below.

Table 2.3: List of Oligonucleotides.

Name	Sequence	Length	Tm	Description
1. gRNA pY211 A1_1	CTAGGAAAGACAATGGTGGC	20	-	
2. gRNA pY211 A2_2	GCCACCATTGTCTTTCCTAG	20	-	
3. gRNA pY211 B1_3	GCTAGGAAAGACAATGGTGG	20	-	
4. gRNA pY211 B2_4	CCACCATTGTCTTTCCTAGC	20	-	
5. <i>PDCDI</i> 248Ala Fw	TGAGCAGACGGAGGCCAAGAGCAACTCGGT CGC	33	63 then 72	Create donor template Y₂₄₈A with micro-homology arms
6. <i>PDCDI</i> 248Ala Rev	AGACAATGGTGGCGGCCCGTCGTGTAGATAA CTACG	36		
7. <i>PDCDI</i> 248Glu Fw	TGAGCAGACGGAGGAGAAGAGCAACTCGGT CGC	33	63 then 72	Create donor template Y₂₄₈A with micro-homology arms
8. <i>PDCDI</i> 248Glu Rev	AGACAATGGTGGCCTCCCGTCGTGTAGATAA CTACG	36		
9 <i>PDCDI</i> Fw gDNA	GGTGTCCCCAGATCACACAG	20	68	Amplify genomic DNA to check insertion after transfection
10 <i>PDCDI</i> Rev gDNA	CTCCTGAGGAAATGCGCTGA	20		
11 <i>PDCDI</i> Fw gDNA	GTGGGACAGCTCAGGGTAAG	20	69	Amplify genomic DNA to check insertion after transfection
12 <i>PDCDI</i> Rev gDNA	TCCTGAGGAAATGCGCTGAC	20		
13 <i>PDCDI</i> Fw gDNA	GTGGTGTCCCCAGATCACAC	20	69	Amplify genomic DNA to check insertion after transfection
14 <i>PDCDI</i> Rev gDNA	GAACACTGGTGGCCAAGGAA	20		
15 <i>PDCDI</i> Fw DNA	AGGGACATTTTCAGAGGGGGA	20	69	Create full length homology arms to be inserted in pBluescript
16 <i>PDCDI</i> Rev DNA	AAGGCCATCTCCAACCAGC	19		

17 <i>PDCDI</i> Fw DNA	GGGGACATTGAGCCAGAGAG	20	69	Create full length homology arms to be inserted in pBluescript
18 <i>PDCDI</i> Rev DNA	CCCCAAGTTCAGGCAGGAG	19		
19 <i>PDCDI</i> Fw DNA	GGGTGGGCTTGGTCATTTCT	20	69	Create full length homology arms to be inserted in pBluescript
20 <i>PDCDI</i> Rev DNA	TCCAAGGCCATCTCCAACCA	20		
21 Open pBS Fw	TGGTTGGAGATGGCCTTGGAATATCGAATTC CTGCAGCC	39	63 then 72	Open pBluescript prior to insertion of homology arms
22 Open pBS Rev	AGAAATGACCAAGCCCACCCCAAGCTTATCG ATACCGTCG	40		
23 Open pBS Fw	GCCACCATTGTCTTTCCTAGC	21	66	Open pBluescript prior to insertion of mNeonGreen and point mutations
24 Open pBS Rev	CTCCGTCTGCTCAGGG	16		
25 gRNA WT 7732_A	agatTGAGCAGACGGAGTATGCCA	20	-	Guide RNA for <i>PDCDI</i> in wild type Jurkats
26 gRNA WT 7732_B	aaaaTGGCATACTCCGTCTGCTCA	20	-	
27 gRNA WT 7749_A	agatCCACCATTGTCTTTCCTAGC	20	-	Guide RNA for <i>PDCDI</i> in wild type Jurkats
28 gRNA WT 7749_B	aaaaGCTAGGAAAGACAATGGTGG	20	-	
29 Open pBS Fw	GCCACCATTGTCTTTCCTAGCGGAATG	27	72	Open pBluescript prior to insertion of mNeonGreen and point mutations
30 Open pBS Rev	TACTCCGTCTGCTCAGGGACACAG	24		
31 Open pBS Fw	TGTCTTTCCTAGCGGAATGGGCAC	24	72	Open pBluescript prior to insertion of mNeonGreen and point mutations
32 Open pBS Rev	GCATACTCCGTCTGCTCAGGGAC	23		
33 Open pBS Fw	GGACTATGGGGAGCTGGATTTCAGT	26	72	Open pBluescript prior to insertion of mNeonGreen and point mutations
34 Open pBS Rev	CTGAGGGGTCCTCCTTCTTTGAGGA	25		

Table 2.4: List of Enzymes.

Name	Type	Source
1. Q5® High-Fidelity DNA polymerase	DNA polymerase	New England Biolabs
2. T4 DNA ligase	DNA ligase	
3. T7 DNA ligase		
4. T4 polynucleotide kinase	5' kinase	
5. DpnI	Parental digestion	
6. BsaI	Type II restriction enzyme	
7. ScaI		
8. BbsI		
9. BamH1		
10. XhoI		

Table 2.5: List of Plasmids.

Name	Description	Source
1. 329 Dig2	Opened pBlueScript vector digested with BamHI and XhoI	Vaux Laboratory, Oxford, United Kingdom
2. pBlueScript	Un-opened pBlueScript vector	Vaux Laboratory, Oxford, United Kingdom
3. pAsCpfI(TYCV)(BB) (pY211)	Expresses humanised AsCpfI TYCV PAM variant	Deposited by Feng Zhang on Addgene

Table 2.6: List of Molecular Cloning Kits.

Name	Description	Source
1. Q5® High Fidelity polymerase kit	High fidelity polymerase with accompanying buffer	New England Biolabs
2. Monarch ® DNA gel extraction kit	Facilitates DNA product extraction and purification from agarose gel	
3. Monarch® plasmid miniprep kit	Purification of product plasmid from transformed <i>E. coli</i> colonies	

Table 2.7: List of Eukaryotic Cell Lines.

Name	Description	Source
1. Jurkat Clone E6	Immortalised human leukemic cell line	ATCC and Vaux Laboratory, Oxford, United Kingdom
2. MOLT-4	Immortalised human leukemic cell line	ATCC and Vaux Laboratory, Oxford, United Kingdom
3. HeLa	Immortalised human cervical cancer cell line	Vaux Laboratory, Oxford, United Kingdom

2.2.2: Genomic DNA Extraction

The Monarch® genomic DNA purification kit was used following the manufacturers protocol (New England Biolabs). 1×10^6 cells were pelleted by centrifugation at 1000g for 1 minute and resuspended in cold PBS by pipetting up and down. 1 μ L of Proteinase K and 3 μ L of RNase A were added to the resuspended pellet and briefly vortexed to ensure proper mixing and dispersal. 100 μ L of cell lysis buffer was added and vortexed immediately and thoroughly. The sample was incubated for five minutes at 56°C in a heat block with periodic vortexing (approximately vortexed for 3 seconds every 1 minute).

400 μ L of gDNA binding buffer was added to the sample and mixed thoroughly by pulse vortexing. This solution was transferred to a gDNA purification column inserted into a collection tube. The sample was centrifuged for 3 minutes at 1000g to bind the gDNA and then for a further 1 minute at maximum speed (16000g). The flow through was discarded and column transferred to a new collection tube. 500 μ L of gDNA wash buffer was added and centrifuged for 1 minute at 1000g. The flow was discarded. This washing step was repeated once more. The column was placed in a DNase-free 1.5mL microfuge tube and 100 μ L of pre-heated (60°C) nuclease-free water was added to elute the gDNA. The water was left for 1 minute at room temperature before being spun at maximum speed 16000g. The sample concentration was quantified using a NanoDrop ND1000 spectrophotometer. Samples were sent for Sanger Sequencing to confirm the correct DNA sequence was extracted with no mutations present.

2.2.3: Polymerase Chain reaction

The polymerase chain reaction (PCR) is a temperature dependant enzymatic reaction which is used to amplify genetic sequences of interest. For a PCR reaction, template DNA (which contains the sequence of interest), heat-stable polymerase, deoxynucleoside triphosphates (dNTPs) and forward and reverse primers are required. The primers are designed to hybridise to sequences that flank either side of the target sequence. These primers should be designed to be specific to this sequence only to avoid off-target binding and the subsequent creation of unwanted product sequences. For every PCR reaction, 1ng of template DNA was combined with both forward and reverse primers (0.5 μ M), Q5 polymerase, Q5 polymerase buffer, dNTPs (200 μ M) and betaine solution (5 μ L). The total reaction volume was 25 μ L. The reaction tube was placed in an Eppendorf MasterCycler. Annealing temperatures were selected by introducing the sequence of each primer used into the NEB Tm Calculator. An extension time of 30 seconds per 1000bp was used with 35 cycles. Table 2.8 outlines the temperatures and times of each stage of the PCR reaction and the workflow is shown schematically in Figure 2.1

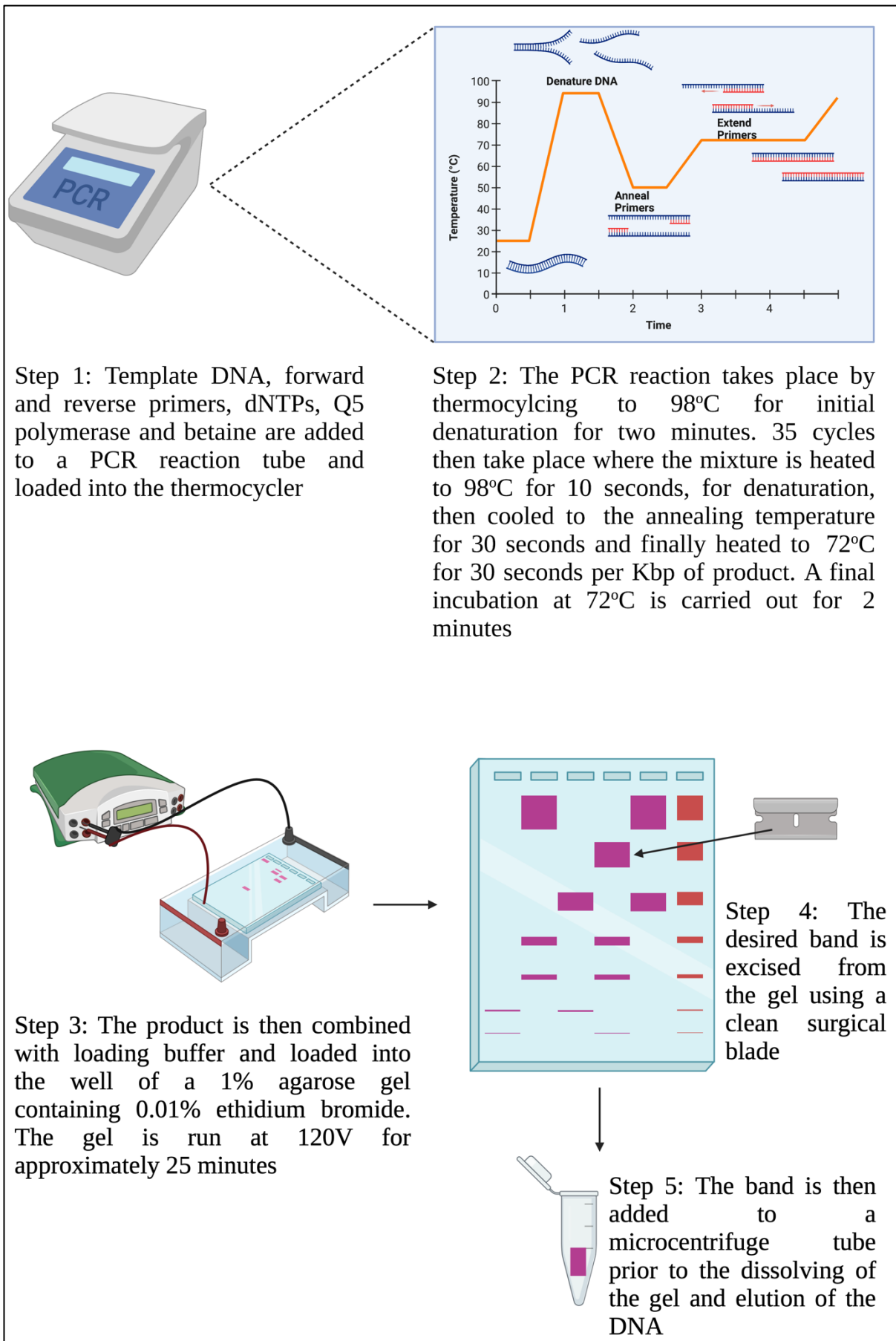


Figure 2.1: Overview of the polymerase chain reaction. In the first step, template DNA, primers, dNTPs, polymerase, buffer and betaine are added to a reaction tube and placed in a thermocycler. The PCR reaction denatures the DNA at 98°C for 2 minutes. 35 cycles then take place whereby the mixture is heated and cooled as shown to allow for denaturation, annealing and extension. The PCR product is visualised on an agarose gel containing ethidium bromide under UV light. The product band is excised from the gel. The gel is dissolved, and the DNA is purified and eluted.

Table 2.8: PCR reaction steps outlining the required temperatures, times, and number of cycles.

Step	Temperature (°C)	Time	Number of Cycles
Initial denaturation	98	2.5 minutes	1
Denaturation	98	10 seconds	35
Prime Annealing	T _m	30 seconds	
Elongation	72	30 seconds per 1Kbp	
Final Elongation	72	2.5 minutes	1
Hold	4	∞	-

2.2.4: Agarose Gel Electrophoresis

PCR products were combined with loading buffer (2.5µL of 10X loading buffer in a 25µL reaction) and pipetted into the well of a 1% w/v agarose gel (agarose and 1X tris-acetate-EDTA (TAE) buffer). Ethidium bromide solution was added to the gel prior to casting at a final concentration of 0.01% v/v. A 1Kbp DNA ladder was added to the gel. The gel was submerged into an electrophoresis tank containing 1X TAE buffer and run for approximately 25 minutes (dependant of product size) at 120V. DNA bands were visualised in an ultraviolet (UV) transilluminator.

2.2.5: Gel Extraction and Purification

Correct product bands were excised from the gel using a clean surgical blade and put into a 1.5mL microfuge tube. The Monarch® DNA gel extraction kit from New England Biolabs was used. The excised band was weighed, and 4 volumes of gel dissolving buffer were added to the slice (i.e., 400µL buffer per 100mg of excised gel). This was incubated at 50°C until the gel was completely dissolved. The product was run through a separation column and centrifuged for 1 minute. 200µL of DNA wash buffer was added to the column and spun for 1 minute. This was repeated once. The column was transferred to a new 1.5mL microcentrifuge tube and 7µL of nuclease-free water added. The column was left for 1 minute before being spun to elute the DNA.

The eluted DNA was quantified using a NanoDrop ND-1000 spectrophotometer. Samples were sent for Sanger Sequencing to confirm the correct DNA sequence was present in the plasmid with no mutations

present.

2.2.6: Restriction Digestion

Restriction digestion allows for the insertion of a target sequence into a vector. Restriction digestion was carried out for the guide plasmid and guide sequence insert. Both the guide sequence (annealed and amplified primers 1 and 2) and the vector plasmid (pAsCpf1(TYCV)(BB) (pY211)) were digested with BbsI. BbsI digests the DNA and creates blunt ends on both the insert and vector which are complementary to each other. The vector or insert were incubated at 37°C with the appropriate restriction enzyme for 30 minutes in a thermocycler. DpnI digestion was carried out to digest any unreacted starting material. Digested products were then separated on an agarose gel, excised, and purified as described above.

2.2.7: Ligation

The digested insert and vector were incubated with T4 ligase which binds the insert into the vector at the desired site. The ligation is carried out for 1 hour at 37°C in a thermocycler. A negative control was carried out whereby only the digested vector was incubated with ligase to assess the ability of the vector to self-ligate. The product was plated on pre-warmed ampicillin agar plates and grown overnight in an incubator at 37°C.

2.2.8: Gibson Assembly

For the full-length homology arm donor-repair template, Gibson assembly was used to anneal desired linear inserts into opened vector. The vector plasmid, pBlueScript, was opened by PCR using primers 21 and 22 prior to the insertion of the homology arms. The homology arms, created by a PCR with gDNA and primers 15-20, were inserted into the plasmid by Gibson assembly. For each Gibson Assembly, 15ng of vector was used and the amount of DNA in fmoles calculated. Twice this amount of insert was added and combined with 2µl of Gibson assembly master mix (New England Biolabs) and ddH₂O up to a final volume of 4µl. The samples were then incubated at 50°C for 30 minutes.

To insert the **Y₂₄₈A**-mNG or **Y₂₄₈E**-mNG sequences into the pBlueScript containing full-length homology arms (vector), the vector was opened by PCR using primers 23 and 24. The inserts were inserted into the vector using Gibson assembly as described above.

2.2.9: Bacterial Transformation

The ligated or assembled products, and their respective controls, were then transformed into competent *E. coli*. For each transformation, 50µL of 5a competent *E. coli* was incubated with 2µL of DNA

(assembled product or control) and incubated on ice for 30 minutes. The bacteria were heat-shocked for 30 seconds at 42°C and returned to ice for 2 minutes. The bacteria were incubated with 950µL of super optimal broth with catabolite repression (SOC) at 37°C for 1 hour. Bacteria were subsequently spread onto pre-warmed ampicillin agar plates and incubated overnight at 37°C. The next day, colonies were inoculated into 10mL of ampicillin-lysogeny broth (LB) and incubated at 37°C for 12-16 hours on an orbital shaker. Cultured bacteria were purified with a Monarch® miniprep kit (New England Biolabs). 3mL of bacteria were pelleted by a 30 second centrifugation and subsequently resuspended in 200µL of plasmid resuspension buffer. Plasmid lysis buffer was added at room temperature for 1 minute prior to the addition of 400µL of plasmid neutralisation buffer and a further 2-minute incubation at room temperature. The lysates were centrifuged for 5 minutes, and the supernatant transferred to a separation column and subsequently spun for 1 minute. The immobilised plasmid was washed twice with plasmid wash buffers before being eluted into 50µL of endonuclease-free water.

Plasmid concentrations were quantified by using a NanoDrop ND-1000 spectrophotometer. Samples were sent for Sanger Sequencing to confirm the correct DNA sequence was present in the plasmid with no mutations present. Bacterial stocks were prepared by mixing equal volumes of cultured medium and 50% glycerol in a cryotube and then stored at -80°C.

2.2.10: Fluorescence Activated Cell Sorting

Post-transfection (see Section 2.3.1, Cell Transfection), cells were sorted by fluorescence activated cell sorting (FACS). Cells were sorted on a BD FACS Aria III (BD Biosciences, San Jose, CA, USA) run with BD FACSDiva™ Software version 8.0.2 (BD Biosciences). Cells were single sorted into a 96-well plate containing pre-conditioned media (RPMI1640) if 488nm fluorescence was 1000 times brighter than control (non-transfected) cells. Cells also had to have positive nuclear (DAPI) staining to confirm cell viability to be eligible for sorting.

2.3: Cell Biology

2.3.1: General Culture Conditions

The cell lines used are listed and described in Table 2.7. Jurkat and MOLT-4 cells were grown in RPMI 1640 media containing 10% foetal bovine serum (FBS) and 1% penicillin-streptomycin (P/S). HeLa cells were cultured in Dulbecco's modified Eagle's medium (DMEM) containing 10% FBS and 1% P/S. Cells were grown in T75 flasks (75cm² surface area with a working volume of 12-15mL) in an aseptic incubator at 37°C with 5% carbon dioxide (CO₂). Cells remained under aseptic conditions at all times. This meant cells were worked on (manipulated, passaged, transfected) in a category two laminar flow hood which is cleaned before and after every use with 70% ethanol. Once a week, the flow hood was irradiated with UV light for 1 hour to maintain sterility.

2.3.2: Cell Passaging and Maintenance

Jurkat and MOLT-4 cells are non-adherent leukemic cell lines. To maintain a viable cell number in the flask, cells were homogenised by pipetting up and down with a serological pipette and then approximately 50% (6mL) of the cell solution was discarded by aspiration. 6mL of fresh pre-warmed RPMI1640 (10% FBS and 1% P/S) was added to facilitate new cell growth. This was repeated twice a week (typically on a Monday and Wednesday). Once a week cells were homogenised by pipetting and transferred to a 15mL falcon tube (to allow for easy access to the cells using a Gilson pipette). 10μL of cells were transferred to a Neubauer haemocytometer cell counting chamber and the number of cells counted under a brightfield microscope. The number of cells per mL of media was calculated and 1x10⁵ cells transferred to a new falcon tube. Cells were centrifuged for 5 minutes at 300g, and the supernatant (consisting of old media) was discarded. The 1x10⁵ cell pellet was resuspended in 12mL of fresh pre-warmed RPMI1640 and transferred to a new sterile T75 flask. Cells were returned to the incubator at 37°C with 5% CO₂.

For the passaging of HeLa cells, which are adherent cervical cancer cells, trypsinisation was carried out. Typically, 2-3 times a week, and prior to cell confluence reaching 80%, flasks containing HeLa cells had their growth medium removed by aspiration. Cells were washed with 10-12mL of room temperature 1X PBS which was subsequently aspirated. This is performed to remove traces of growth media which contains proteins which inactivate Trypsin-EDTA. 1mL of Trypsin-EDTA was added to the cells and incubated at room temperature until the cells had detached (typically within 5 minutes). Cells were resuspended in 6mL of fresh pre-warmed DMEM. To maintain a desired and optimum confluency of cells, a dilution of 1 in 12 was used. This means of the 6mL of resuspended cells, 0.5mL was removed and added to new T75 flasks containing 11.5mL of fresh pre-warmed DMEM. Cells were returned to the incubator at 37°C with 5% CO₂.

2.3.3: Freezing of Cell Stocks

To maintain a biobank of cells, stocks were replenished when required. To carry this out adherent cells were trypsinised as described above (this step is not required for non-adherent cells). Cells were centrifuged at 300g for 5 minutes and the supernatant discarded. The pellet was resuspended in 1mL of cold freezing medium (90% FBS, 10% dimethylsulfoxide (DMSO)). Cells were transferred to a cryovial and immediately transferred to a -20°C freezer overnight. Cells were transferred to a -80°C freezer for short to medium term storage. For long term storage, cryovials of cells were stored in liquid nitrogen.

2.3.4: Transfection

2.3.4.1: Lipofectamine 2000 Transfection:

Lipofectamine 2000 transfection was carried out as per the manufacturers protocol. In a 24 well plate, 4×10^5 Jurkat or MOLT-4 cells were plated per well in serum-free RPMI1640 media. As Jurkat and MOLT-4 cells are non-adherent, cells can be plated and transfected on the same day. 250ng of guide and 250ng of donor repair template were diluted in 50µL of OptiMEM and gently mixed. In a separate Eppendorf, 1µL of Lipofectamine 2000 transfection reagent was mixed with 50µL of OptiMEM. This mixture was left for 5 minutes at room temperature. The two solutions (OptiMEM-DNA and OptiMEM-Lipofectamine) were combined gently and left to incubate at room temperature for 20 minutes. The total volume (100µL) of this mixture was added to each well to be transfected. Cells were returned to the incubator and cultured at 37°C with 5% CO₂ for 16 hours. Media was changed for complete growth media and cells returned to the incubator for a further 24 hours.

2.3.4.2: Lipofectamine 3000 Transfection:

Lipofectamine 3000 transfection was carried out as per the manufacturers protocol. In a 24 well plate, 4×10^5 Jurkat or MOLT-4 cells were plated per well in serum-free RPMI1640 media. As Jurkat and MOLT-4 cells are non-adherent, cells can be plated and transfected on the same day. 250ng of guide and 250ng of donor repair template were diluted in 25µL of OptiMEM alongside 1µL of P3000 reagent and gently mixed. In a separate Eppendorf, 1.5µL of Lipofectamine 3000 transfection reagent was mixed with 25µL of OptiMEM. The two solutions (OptiMEM-DNA and OptiMEM-Lipofectamine) were combined gently and left to incubate at room temperature for 15 minutes. The total volume (50µL) of this mixture was then added to each well to be transfected. Cells were returned to the incubator and cultured at 37°C with 5% CO₂ for 16 hours. Media was changed for complete growth media and cells returned to the incubator for a further 24 hours. For the transfection of HeLa cells, the above protocol was used, however cells were seeded in DMEM the day before transfection to allow for cell adherence. Cell media was changed for serum-free DMEM at the time of transfection.

2.3.4.3: FuGENE HD Transfection:

The FuGENE HD transfection kit has been published to transfect “difficult to transfect” cell lines, such as Jurkat cells. Transfection was carried out using FuGENE HD as per the manufacturer’s instructions, trialling differing ratios of transfection reagent to DNA shown below in Table 2.9. Cells were plated in RPMI1640 on the day of transfection with 1×10^5 cells plated per well of a 96-well plate. DNA was diluted in OptiMEM to $2 \mu\text{g}/\mu\text{L}$. The appropriate amount of FuGENE HD transfection reagent was added (Table 2.9) and incubated for 15 minutes at room temperature. $5 \mu\text{L}$ of this mixture was added to each well to be transfected and cells returned to the incubator for 48 hours.

Table 2.9: FuGENE HD transfection reagent:DNA ratios tested.

Transfection Reagent	DNA
1	1
1.5	1
2	1
2.5	1
3	1
3.5	1
4	1
4.5	1
5	1
5.5	1
6	1
6.5	1
7	1
7.5	1
8	1

2.3.4.4: Electroporation

An Amaxa Nucleofector II was used for the electroporation transfection of HeLa and MOLT-4 cells. A 24 well plate was prepared by adding $1000 \mu\text{L}$ of complete growth medium to all wells to be transfected (DMEM for HeLa cells and RPMI1640 for MOLT-4 cells). The plate was transferred to an incubator at 37°C with 5% CO_2 . For MOLT-4 cells, 1×10^6 cells were pelleted by centrifugation for 4 minutes at 300g. Cells were resuspended in $100 \mu\text{L}$ of room-temperature Nucleofector[®] solution. $1 \mu\text{g}$ of plasmid DNA was added (500ng of guide plasmid DNA and 500ng of donor repair template). The solutions were transferred into a certified cuvette with the solution confirmed to be covering the bottom of the cuvette with no air bubbles present. The cuvette was inserted into the nucleofector device, and the C-05 program run. This program is designed for MOLT-4 cells and listed on the manufacturer’s website. After the program completed, $500 \mu\text{L}$ of pre-equilibrated medium from the plate was added to the

cuvette and the sample transferred to the plate. Cells were incubated for 48 hours at 37°C and 5% CO₂ prior to visualisation to confirm transfection.

For HeLa cell transfection, cells were trypsinised from their flask and 1×10^5 cells pelleted by centrifugation for four minutes at 300g. Prior to this, 1000µL of DMEM was added to each well of a 24-well plate to be transfected and the plate returned to an incubator at 37°C and 5% CO₂. Cells were resuspended in 100µL of room-temperature Nucleofector® solution. 1µg of plasmid DNA was added (500ng of guide plasmid DNA and 500ng of donor repair template). The solutions were transferred into a certified cuvette with the solution confirmed to be covering the bottom of the cuvette with no air bubbles present. The cuvette was inserted into the nucleofector device and either the O-05 (high viability) or I-13 (high expression) program was run. These are specific HeLa cells transfection programmes recommended by the manufacturer. 500µL of pre-equilibrated medium was added to each cuvette transfected and cells returned to the 24 well plate. Cells were incubated for 48 hours at 37°C and 5% CO₂ prior to visualisation to confirm transfection.

2.4: Förster Resonance Energy Transfer (FRET) Determined by Multiple-Frequency Fluorescence Lifetime Imaging Microscopy (mfFLIM)

For a comprehensive introduction to Förster resonance energy transfer (FRET) and fluorescence lifetime imaging microscopy (FLIM), please refer to Section 1.6. We have utilised time-resolved FRET which directly measures the lifetime of a donor chromophore in the absence and presence of an acceptor chromophore. Unlike steady-state FRET (which assesses changes in either donor or acceptor intensity and is dependent on chromophore concentration) time-resolved FRET is independent of chromophore concentration, as lifetime is an intrinsic property of a chromophore. We have determined our time-resolved FRET measurements using FLIM in the frequency-domain. This allows for the quick calculation of chromophore lifetime.

2.4.1: Frequency-Domain FLIM Acquisitions

The FLIM acquisitions were performed on a Nikon Eclipse Ti inverted widefield microscope equipped with a 20X objective (Nikon S Plan Fluor, NA 0.45). The excitation source was a modulated Omicron diode (LDM473-TA) laser which excites at 473nm. The modulation frequency was 40MHz with a peak power of 30mW. The detector was a Lambert Instruments LI² CAM which was also modulated at 40MHz, creating a homodyne system (where both the detector and excitation source are modulated at the same frequency).

For FLIM acquisitions, Lambert Instruments LI-FLIM software was used. During FLIM acquisitions, 16 phase images were generated (each 22.5° apart) in pseudo-random order to minimise potential

photobleaching. Each FLIM measurement is calibrated against a reference lifetime (1.840ns) made from a freshly prepared 50 μ M solution of Rhodamine B. An exposure time of 1000ms was used for all tissue samples acquired, and a 300ms exposure time used for cell experiments. The LI-FLIM software calculates the average donor intensity of a sample, both the phase and modulation lifetimes, and their respective standard deviations. However, an algorithm designed and created by Pierre Leboucher was utilised for all experiments which allows for semi-automated FLIM acquisitions with minimal user supervision.

2.4.2: Semi-Automated FLIM Sample Mapping and Acquisition

The hardware and software described above were controlled using a custom-made software called FLIM 2019, designed by Pierre Leboucher. This software allows a user to create a mapping file, which records regions of interest within a sample slide to be analysed. This mapping file contains the X, Y, Z coordinates of all the regions of interest selected by the user. The software can then enter acquisition mode, where all recorded points in a mapping file were sequentially analysed by the FLIM platform, with the resulting data exported to a CSV file. The FLIM 2019 software contains an algorithm that automatically excludes data below a predefined and universally applied threshold by applying a region of interest to a sample image using the active contours method (Chapter 3 and (Veeriah et al., 2014)). The data from all pixels outside this region of interest are not analysed. The algorithm detects the signal-to-noise ratio of the sample and only pixels with a signal-to-noise ratio of at least four are included in the ROI (Region of Interest) for analysis. The use of this software reduces the need for operator supervision and input, thus reducing operator bias. The reduction of operator bias occurs when analysing results, as regions of interest are designated based on signal-to-noise ratios rather than user subjectivity.

2.5: Two-site Immune-Amplified Förster Resonance Energy Transfer (iFRET) Labelling Assay

2.5.1: Development and Principles of a Two-Site Assay

The current gold-standard of biomarker analysis in patient tumour samples has historically been immunohistochemistry (IHC). Whilst this has shifted towards quantitative IHC (qIHC), IHC methodologies are prone to non-specific binding of target antibodies and can be skewed by operator bias and subjectivity (Kong et al., 2006, Veeriah et al., 2014, Miles et al., 2017, Sánchez-Magraner et al., 2020). This is an inherent problem that is true of one-site assays, i.e., assays that detect one antigen site at a time using chromophore-conjugated antibodies. This led to the development of a two-site assay. A two-site (coincident) assay simultaneously labels a single protein on two distinct sites, or two separate proteins on distinct sites, with donor- and acceptor-conjugated probes (Kong et al., 2006, Veeriah et al.,

2014). This allows for the detection of FRET between the chromophores which results in FRET acting as a “chemical ruler,” measuring distances of 1-10nm to report on biomarker functional states.

Initial attempts to create the two-site assay utilised primary antibodies against the desired antigen sites that were directly conjugated to chromophores. This led to the presence of multiple chromophores at the antigen recognition site, which negatively affects antibody-antigen binding. This limited the maximum obtainable signal to the number of chromophores an antibody can bind to before experiencing a reduction of antibody-antigen binding. There was also an inherent cost associated to this approach due to the large amount of primary antibody required for chromophore conjugation (Veeriah et al., 2014). An attempt was made to overcome these limitations by detecting the bound primary antibodies with chromophore-conjugated secondary antibodies. Due to the dimensions of a secondary IgG antibody (150-180kDa), this results in the conjugated chromophores being above the critical FRET distance of 10nm. The authors creating this assay used $F(ab')_2$ fragments conjugated to donor and acceptor chromophores rather than secondary antibodies. This has several advantages such as: the critical FRET distance of 10nm being maintained due to their smaller size of 50-100kDa; they penetrate cells and tissues more easily; the lack of Fc region results in the abolishment of non-specific binding to Fc receptors within samples (Veeriah et al., 2014). Moreover, the authors of Veeriah et al., exploited a tyramide signal amplification (TSA) step to increase the signal-to-noise ratio of the sample (detailed in Section 2.5.2.4).

The two-site assay, coupled to a TSA step can be applied to any biomarker (e.g., Akt, STAT3), or biomarker pair (e.g., human epidermal growth factor receptor (HER) 2/HER3, programmed death receptor 1(PD-1)/programmed death ligand (PD-L1), cytotoxic T-lymphocyte associated protein 4 (CTLA-4)/CD80) that can be targeted by antibodies in a species-specific manner. In the labelling set-up used here, the donor, either PD-1 or CTLA-4 was labelled with an anti-mouse antibody against the extracellular domain. The acceptor, either PD-L1 or CD80, was labelled with an anti-rabbit primary antibody, against the extracellular domain. In turn, the donor antibodies were labelled with $F(ab')_2$ fragments conjugated to ATTO488, the donor chromophore, and the acceptor antibodies labelled with $F(ab')_2$ -HRP (horseradish peroxidase) fragments. TSA (see Section 2.5.2.3) was used to conjugate the acceptor chromophore, Alexa594, to the $F(ab')_2$ -HRP.

2.5.2: iFRET Labelling of Patient Tissue Sections

2.5.2.1: Antigen Retrieval and Primary Antibody Labelling of Tissue Sections

Two consecutive formalin-fixed paraffin-embedded (FFPE) tissue sections were mounted onto two separate glass microscope slides to allow for donor-only and donor-acceptor labelling for all patient samples. Samples then underwent dewaxing and antigen retrieval using Envision Flex retrieval solution

(pH 9) in a Dako PT-Link instrument. In this process, slides are heated to 95°C for 20 minutes. Remaining paraffin was removed by washing 3 times with PBS in a coplin jar with gentle agitation using an orbital shaker. A hydrophobic border was drawn around the tissue on slides using a PAP pen. Samples were treated with fresh effervescent 1mg/ml NaBH₄ for 10 minutes to reduce autofluorescence caused by fixative agents. Samples were washed 3 times with PBS. Two drops of Pierce endogenous peroxidase suppressor were added to the samples and the slides were incubated for 30 minutes at room temperature in a humidified tray. The humidified tray was created by adding tissue paper moistened with water to the bottom of a large plastic tray with a tight-fitting lid. This prevented samples from drying out. After the 30 minute incubation with peroxidase suppressor the slides were washed with PBS 3 times in coplin jars with gentle agitation. Samples were then incubated for 1 hour with 1% (10mg/ml) bovine serum albumin (BSA) to prevent the non-specific binding of labelling antibodies. Samples were then labelled with primary antibodies using the concentrations shown in Table 2.10. Donor-only slides were incubated with the donor primary antibody (α PD-1 or α CTLA-4) and donor-acceptor slides were incubated with both the donor primary antibody and acceptor primary antibody (α PD-L1 or α CD80). Slides were incubated overnight at 4°C.

Table 2.10: Primary antibody dilutions used for labelling the donor and acceptor sites of cell and FFPE patient samples, respectively.

<u>Biomarker</u>	<u>Donor-Only</u>	<u>Donor-Acceptor</u>
PD-1/PD-L1	α PD-1 (1:100)	α PD-1 (1:100) and α PD-L1 (1:500)
CTLA-4/CD80	α CTLA-4 (1:100)	α CTLA-4 (1:100) and α CD80 (1:500)

2.5.2.2: Secondary Antibody Labelling

Samples were removed from the refrigerator and washed three times with 0.02% Tween20 in PBS (PBST). Secondary F(ab')₂ fragments were added to the donor-only and donor-acceptor samples as outlined in Table 2.11. Samples were incubated in a humidified tray in the dark for 2 hours at room temperature. Slides were washed 3 times with 0.02% PBST in coplin jars. Donor-only slides were then washed once with PBS in a coplin jar and mounted with Prolong Diamond (Chapter 3) or Prolong Glass (Chapter 4). Donor-acceptor slides underwent tyramide signal amplification (see Section 2.5.2.4). The edges of the donor-only slides were then sealed using clear nail varnish. Prior to the experiments carried out in Chapter 4, Thermofisher Scientific released anew mountant, Prolong Glass, with a higher refractive index, of 1.52, and increased photobleaching protection. Therefore, Prolong Glass was adopted for experiments presented in Chapter 4.

Table 2.11: Secondary F(ab')₂ fragment dilutions used for the labelling of the donor and acceptor primary antibodies, respectively.

<u>Experiment</u>	<u>Donor-Only</u>	<u>Donor-Acceptor</u>
ccRCC, malignant melanoma and NSCLC tissue sections (Chapter 3)	ATTO488 conjugated-F(ab') ₂ donkey anti-mouse (1:100)	ATTO488 conjugated-F(ab') ₂ donkey anti-mouse (1:100)
		Peroxidase conjugated-F(ab') ₂ donkey anti-rabbit (1:200)
RFA-treated lung metastases (Chapter 4)	ATTO488 conjugated-F(ab') ₂ donkey anti-mouse (1:50)	ATTO488 conjugated-F(ab') ₂ donkey anti-mouse (1:50)
		Peroxidase conjugated-F(ab') ₂ donkey anti-rabbit (1:200)

2.5.2.3: Tyramide Signal Amplification

To detect the signal of a sample with good precision and overcome autofluorescence, especially in fixed tissue samples, a signal-to-noise ratio of at least four must be observed. To achieve this, tyramide signal amplification was carried out on donor-acceptor slides. The purpose of tyramide signal amplification was to visualise the acceptor secondary F(ab')₂-HRP fragments as well as to amplify the acceptor labelling, thus increase the signal-to-noise ratio. Briefly, the reaction involves adding tyramide-Alexa594 to the samples in the presence of hydrogen peroxide. Tyramide-Alexa594 is a phenol ring with an Alexa594 chromophore at the para position to the hydroxyl group. The hydrogen peroxide, in the presence of HRP (labelling the acceptor antibody), causes the formation of a free radical on the phenol ring of the tyramide, which subsequently reacts and covalently binds to nearby tyrosine residues in the sample (on the F(ab')₂ fragment). This is summarised schematically in Figure 2.2. The tyramide signal amplification was performed for 20 minutes at room temperature in the dark. Slides were washed 3 times with 0.02% PBST in coplin jars before a final PBS wash. Lastly, slides were mounted with Prolong Diamond (Chapter 3), or Prolong Glass (Chapter 4) and the edges of the slides sealed with clear nail varnish.

The entire labelling workflow is outlined schematically in Figure 2.3.

Tyramide Signal Amplification increases the signal-to-noise ratio of the sample

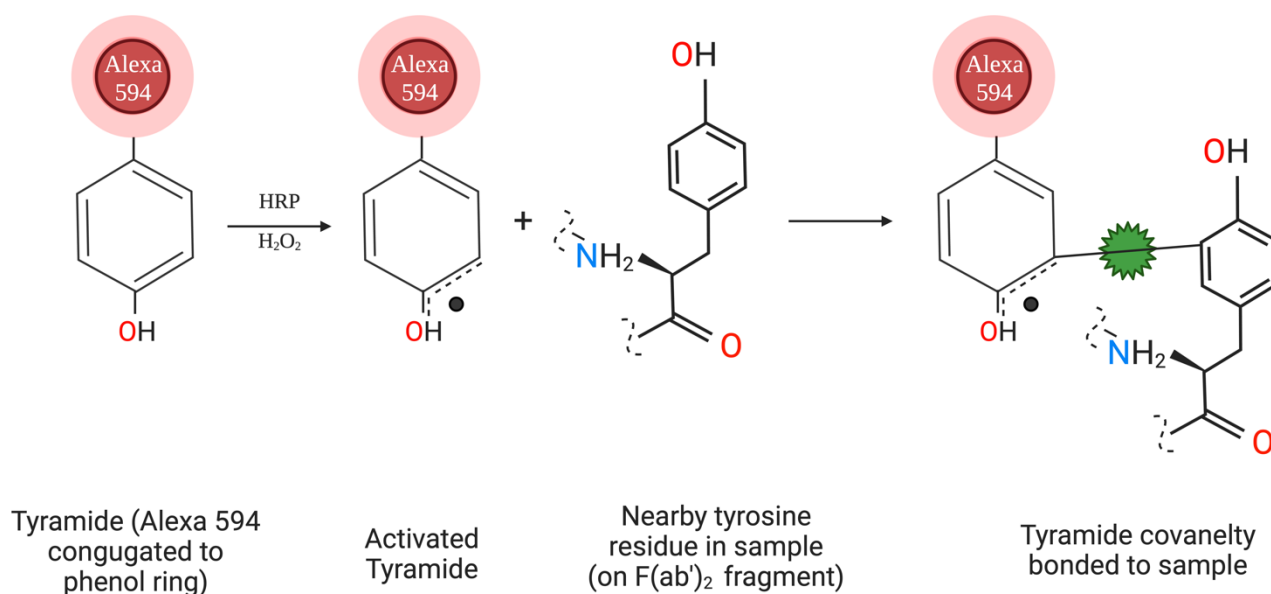


Figure 2.2: Tyramide Signal Amplification is Used to Conjugate the Acceptor Chromophore to the Sample. To observe a high signal to noise ratio above the autofluorescence signal, tyramide signal amplification is performed on all samples. The donor-acceptor site (PD-L1 or CD80) is labelled with a primary antibody which is labelled with a secondary $F(ab')_2$ fragment conjugated to horseradish peroxidase (HRP). When tyramide (a phenol ring conjugated to Alexa594 at the para position) is added to the sample in the presence of H_2O_2 , a free radical is generated. The tyramide covalently bonds to nearby tyrosine residues in the sample (on the $F(ab')_2$ fragment). An incubation time of 20 minutes is used to prevent non-specific binding of the chromophore to the sample.

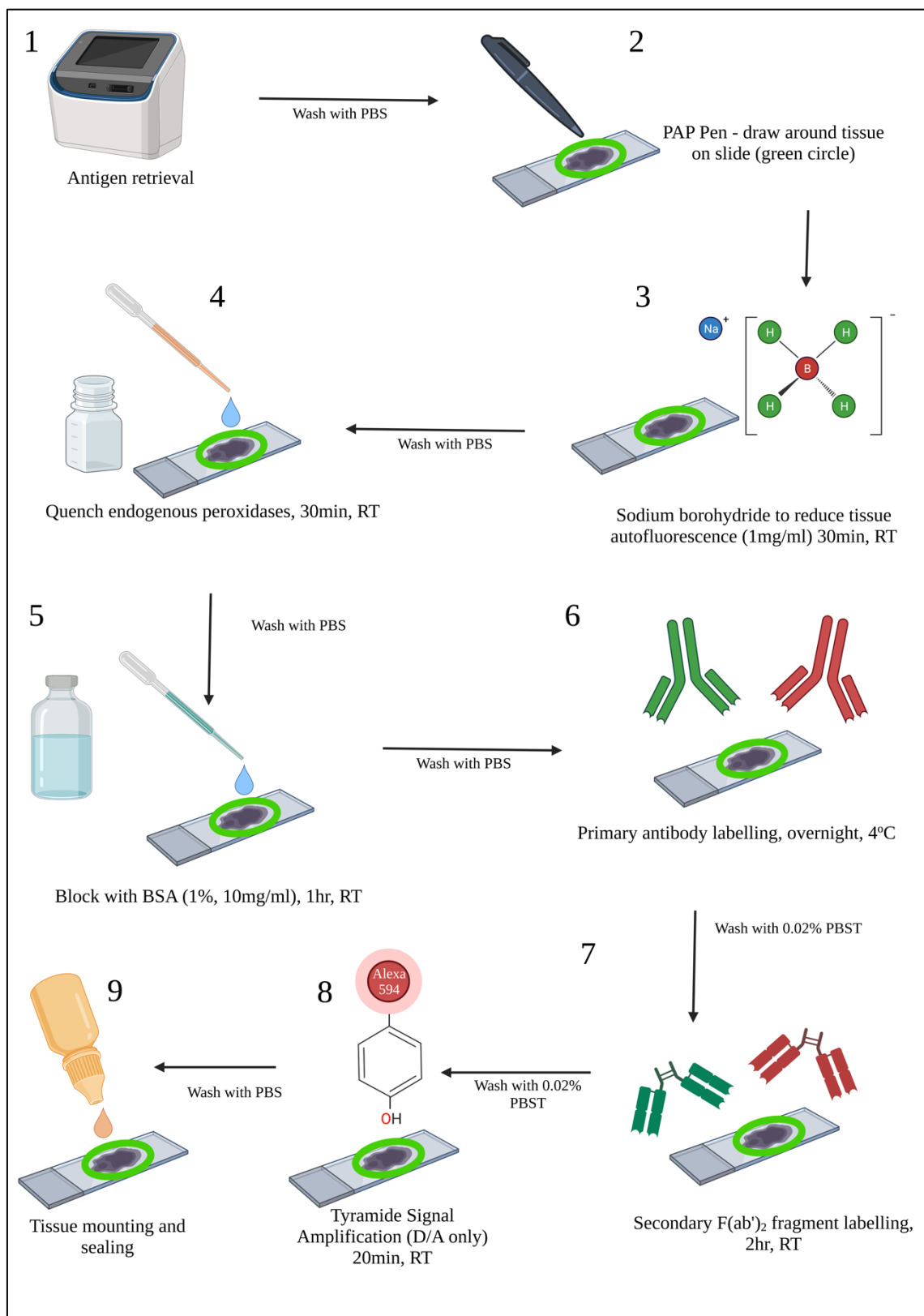


Figure 2.3: iFRET Labelling Workflow: Tissue sections undergo antigen retrieval before the tissue is contained on the slide using a hydrophobic PAP pen. Endogenous peroxidases are quenched, and sodium borohydride is used to reduce tissue autofluorescence. To reduce non-specific binding, slides are blocked with bovine serum albumin before being labelled with primary antibodies overnight. The next day, secondary F(ab')₂ fragments are incubated and tyramide signal amplification carried out to conjugate the acceptor chromophore to the acceptor F(ab')₂-HRP. Slides are mounted with Prolong Diamond or Prolong Glass antifade mount, and a coverslip sealed onto the sample with nail varnish.

2.5.2.4: Pathology

2.5.2.4.1: Clear-cell Renal Cell Carcinoma

Biopsies from patients with clear-cell RCC (ccRCC), diagnosed and treated at the Cruces University Hospital (Barakaldo, Bizkaia, Basque Country, Spain), were graded and staged within the study. All patients gave written informed consent for the potential use of their resected tumours for research. This study was approved by the Ethical and Scientific Committee (CEIC-Euskadi PI2015060). The International Society of Urological Pathology 2013 tumour grading system (Delahunt et al., 2013) was used to assign each sample using routine haematoxylin and eosin (H&E) staining. Tumours were graded and grouped as low (G1/2) and high (G3/4) grade for consistency. To assess PD-L1 expression, a multisite tumour sampling (MSTS) method was used, which samples more areas of a tumour with the aim of overcoming the problems of tissue heterogeneity (López and Cortés, 2017). Samples were determined PD-L1 positive (>1%) or negative (<1%) using the Roche VENTANA PD-L1 (SP142) Assay.

2.5.2.4.2: Malignant Melanoma

Cases of malignant melanoma used in this study were selected from all patients diagnosed with malignant melanoma between June 2003 and February 2017 at Nottingham University Hospital (Nottingham, England, United Kingdom). The main selection criterion was tumours having a Breslow thickness of >1 mm. Patients gave written informed consent for their specimens to be stored and used for research. Patient clinicopathologic data were obtained from Nottingham University Hospital PAS, WinPath, and NotIS databases. Data and specimens were anonymised by using only their designated laboratory case reference. Ethical approval (ACP0000174) was gained from the Nottingham Health Science Biobank Access Committee. A cohort of 176 primary malignant melanoma cases was used for iFRET analysis as tissue microarrays (TMA). Within the TMAs, each patient had one tumour sample. Table 2.12 summarises the clinical parameters of the 176 patients. Tumours were fully surgically excised and FFPE in tissue blocks. Tissue cores of 1mm diameter were selected by studying H&E-stained sections most recently cut from the FFPE tissue block. The location of cores to remove from the tissue block was selected by scanning the slides and using Panoramic Viewer Software (3DHisTech). Cores were removed from the FFPE tissue blocks using the TMA Grand Master (3DHisTech) and arrayed into new paraffin blocks.

2.5.2.4.3: Non-Small Cell Lung Carcinoma

Biopsies from 60 metastatic NSCLC tumours were obtained during interventional radiology procedures from Institut Bergonié (Bordeaux, France; Table 2.13). Thirty-six patients were male and 24 were female, with a median age of 63 years (range, 44–86 years). Performance status was defined with 50

patients given a performance status of ≤ 1 and 10 patients given a status of ≥ 1 . Performance status is a measure of a patients' progress, with a grade of zero being defined as fully active with the patient being able to carry on all pre-disease activities without restriction. A score of 1–3 indicates increasing severity of limitations to daily activities and self-care. A score of 4 is defined as completely disabled and 5 is defined as dead (Oken et al., 1982). The clinical outcome of 40 patients who were treated with either nivolumab (n=37) or pembrolizumab (n=3) was provided and used for Kaplan–Meier survival analysis. Patients' samples were collected between January 2014 and December 2017. This study was approved by the Institutional Review Board of Institut Bergonié (Bordeaux, France). Excised samples were FFPE in tissue blocks prior to being sliced and mounted on microscope slides. For iFRET analysis, three consecutive tissue slices of each patient's sample were provided. One slide for each patient sample was labelled with H&E and a trained pathologist (J.I. Lopez) identified tumoral areas within the sample.

2.5.2.4.4: Radiofrequency-Ablated Lung Metastases

Samples from 16 patients were provided by Dr. Jean Palussière from Institut Bergonié, France. This study was approved by the Institutional Review Board of Institut Bergonié (Bordeaux, France). Excised samples were FFPE in tissue blocks prior to being sliced and mounted on microscope slides. Two slices were provided per-patient prior the radiofrequency ablation procedure being carried out in the first lung. After an interval of one month, prior to the procedure being carried out on the contralateral lung, another two slices were provided per patient ². Of these patients 10 were male and six were female. The lowest age was 64 and the highest age 89. The median age of the 16 patients was 73.2 years. All patients were microsatellite stable (MSS) ³.

² For three patients, no tissue was available from the second radiofrequency ablation procedure.

³ Microsatellite stability not available for one patient.

Table 2.12: List of Clinical Parameters for Malignant Melanoma Patients.

Clinical Parameter		Frequency n (%)
Gender (n= 173)	Male	102 (59.9)
	Female	71 (41.1)
Age at primary diagnosis (n= 172)	<50	30 (17.4)
	50-59	29 (16.9)
	60-69	37 (21.5)
	70-79	36 (21.0)
	≥ 80	40 (23.2)
Stage (n=172)	IA	1 (0.6)
	IB	42 (24.4)
	II	1 (0.6)
	IIA	30 (17.4)
	IIB	27(15.7)
	IIC	17 (9.8)
	III	2 (1.2)
	IIIA	1 (0.6)
	IIIB	2 (1.2)
	IIIC	9 (5.2)
	IIID	2 (1.2)
	IV	38 (22.1)
Site of tumour (n= 172)	Head and Neck	29 (16.9)
	Trunk	19 (11.0)
	Upper Limb(s)	38 (22.1)
	Lower Limb(s)	37 (21.5)
	Pelvic Region	5 (2.9)
	Back	44 (25.6)
Breslow thickness (mm) (n= 172)	<1mm	0.0 (0)
	1-1.9mm	48 (27.9)
	2-3.9mm	69 (40.1)
	4-5.9mm	26 (15.1)
	≥6mm	29 (16.9)
Ulceration (n= 171)	Absent	110 (64.3)
	Present	61 (35.7)
Microsatellites (n=170)	Absent	165 (97.1)
	Present	5 (2.9)
Tumour infiltrating lymphocytes (n= 170)	Absent	39 (22.9)
	Focal	101 (59.4)
	Extensive	30 (17.7)
Local recurrence (n=173)	Absent	157 (90.8)
	Present	16 (9.2)

Table 2.13: List of Clinical Parameters for NSCLC Patients.

Clinical Parameters		Frequency n (%)
Gender (n=60)	Male	36 (60)
	Female	24 (40)
Age (n=60)	44-86 years	Median 63 years
Tumour type (n=60)	Non-small cell lung carcinoma	60 (100)
Performance status (n=60)	≤ 1	50 (83)
	> 1	10 (17)
Previous lines of treatment (n=60)	≤ 1	39 (65)
	> 1	21 (35)
Treatment (n=60)	anti-PD-1 therapy	60 (100)

2.6: Data Processing and Statistics

Statistical analysis and box and whisker plots were performed using Origin Pro8 (Chapter 3) and GraphPad Prism 9 (Chapter 4). Prior to statistical analysis, a Shapiro-Wilk test was used to test result data for normality. The result confirmed that the data did not follow a normal distribution. Therefore, statistical differences were calculated between groups using the Mann–Whitney U test (values indicated on the box and whisker plots). The Mann–Whitney U test is a non-parametric test, thus not assuming a normal distribution of results. Box and whisker plots represent the 25%–75% (box) and the 1–99 (whiskers) ranges. Statistical differences are indicated with $P \leq 0.05$. Kaplan–Meier survival analysis was performed using SPSS. SPSS was also used to calculate Cox Regression for survival analysis to assess which factors (age, sex, tumour stage, and interaction state) were impacting overall survival. For the Kaplan Meier curves in Chapter 3, for NSCLC, patients were ranked in order of their FRET efficiency (interaction status) and split into the two groups, those with the lowest 60% of median FRET efficiencies and those with the highest 40%. For melanoma, patients were split into the highest 20% and lowest 80% of FRET efficiencies. To determine these cut-off points for patients with melanoma and NSCLC, maximally selected rank statistics were performed using the R statistical software (version 3.6.2) and the Maxstat (version 0.7–25) package, which provides several P-value approximations (Lausen and Schumacher, 1992, Hothorn and Lausen, 2003). Maximally selected rank statistics can be used for estimation as well as evaluation of a simple cut-off point mode. The results provided by Maxstat were consistent with the choice of bottom 80% and top 20%, and 60% and 40%, respectively. The log-rank (Mantel–Cox) test was carried out to determine significant differences between the groups. Regression curves plotting intratumoral lymphocyte density vs checkpoint interaction (Chapter 3), were drawn using Microsoft Excel. Spearman’s R^2 correlation coefficients were calculated using GraphPad Prism 9.

Chapter 3: High PD-1/PD-L1 Checkpoint Interaction Infers Tumour Selection and Therapeutic Sensitivity to Anti-PD-1/PD-L1 Treatment

3.1: Preface

The work presented in this chapter is from the manuscript *High PD-1/PD-L1 Checkpoint Interaction Infers Tumour Selection and Therapeutic Sensitivity to Anti-PD-1/PD-L1 Treatment*, Sánchez-Magraner and Miles et al., 2020 (see statement of originality).

3.2: Introduction

Disproportionate immune system activation can result in profound pathologies and there are, therefore, regulatory mechanisms in place to maintain homeostasis (Hanahan and Weinberg, 2017). Interactions referred to as immune checkpoints are critical in this, avoiding immune cell-related collateral damage in pathogenic responses and in suppressing autoimmunity. Inhibitory receptors presented by immune cells, T-lymphocytes in particular, include programmed death receptor-1 (PD-1) and cytotoxic T-lymphocyte antigen-4 (CTLA-4) (Pardoll, 2012, Alsaab et al., 2017). Cancers exploit these physiological mechanisms to avoid immune attack by expressing inhibitory receptor cognate ligands, programmed death ligand-1 (PD-L1) and cluster of differentiation 80/86 (CD80/86) (Hanahan and Weinberg, 2017). The CTLA-4 receptor is a homolog of the immune-activating CD28 receptor, both of which are found on T-lymphocytes and possess CD80 and CD86 as ligand partners (Engelhardt et al., 2006). CTLA-4, however, provides a higher affinity binding site for CD80/86 and interaction with CD80/86 inhibits cell proliferation and IL-2 secretion by T-lymphocytes. The PD-1 immune checkpoint limits later immune responses primarily in peripheral tissue by attenuating T-lymphocyte signalling downstream of the T-cell receptor (TCR) (Okazaki and Honjo, 2006).

There are a number of approved therapeutic mAbs designed to reinstate immune-mediated tumour destruction in immunogenic cancers, by inhibiting the aforementioned immune checkpoint interactions (Mahmoudi and Farokhzad, 2017). In part, through the generation of neoantigens, immunogenicity is strong in non-small cell lung carcinoma (NSCLC), renal cell carcinomas (RCC), melanoma, classical Hodgkin lymphoma, head and neck squamous cell carcinoma, and urothelial carcinoma, all of which show varying degrees of response to immune checkpoint interventions (Mahmoudi and Farokhzad, 2017, Ross and Jones, 2017, Heidegger et al., 2019). Notwithstanding some remarkable successes with immune checkpoint inhibitors, the majority of patients display primary or acquired resistance to treatment (Qin et al., 2019). There is, therefore, an unmet clinical need to identify biomarkers that distinguish potential responders from non-responders to ensure that non-responders are not exposed to the side-effects of these drugs for no therapeutic benefit. The development of different PD-L1

immunohistochemistry (IHC) diagnostics utilising proprietary antibodies has resulted in four Food and Drug Administration (FDA)-approved and CE-*in-vitro* diagnostics-marked assays, each linked to a specific drug and scoring system (Sommer et al., 2020). However, it has become clear that the expression of inhibitory ligands, namely PD-L1, is not an accurate diagnostic marker for use in predicting patient prognosis and response to treatment. A recent study observed that patients with NSCLC demonstrated an increase in response to the anti-PD-1 agent, pembrolizumab, in patients exhibiting a tumour proportion score greater than 50% (Theelen and Baas, 2019). Nevertheless, the response reached only 41% (Roach et al., 2016). Moreover, a different study assessed the efficacy of PD-1 or PD-L1 inhibitors in different neoplasia (primarily lung cancer but also renal cancer and malignant melanoma) in PD-L1- negative and PD-L1- positive cancers. Critically, benefit was seen in patients within the PD-L1-negative group, clearly exposing the failure of PD-L1 expression to determine which patients should receive immune checkpoint inhibitors (Nunes-Xavier et al., 2019).

As immune cell/tumour cell interplay via immune checkpoints is a prominent mechanism for tumour immune evasion and survival, checkpoint interaction status may present a key mechanism-based prognostic and/or predictive biomarker, replacing conventional protein expression readouts for stratifying patients to immune checkpoint interventions. To this end, we have developed and tested an imaging assay that provides a quantitative readout of immune checkpoint interaction between cells. iFRET (immune-FRET) employs a two-site, cell-cell amplified Förster resonance energy transfer (FRET) method, detected by fluorescence lifetime imaging microscopy (FRET/FLIM). Here, iFRET acts as a “chemical ruler,” measuring cell-cell interactions in the range of 1–10 nm. Alternative assays have assessed the PD-1/PD-L1 signalling axis in both cell assays and patient tissue, however, these assays work at a distance greater than that of iFRET (Figure 3.1). Work carried out by Giraldo and colleagues (2018), uses an imaging algorithm that determines when PD-1⁺ and PD-L1⁺ cells are within close proximity (≤ 20 nm) of each other. Such assays investigate distances that reflect proximity over interaction (Giraldo et al., 2018). Johnson and colleagues (2018) also utilised an automated quantitative analysis platform, which again maps cells based on PD-1 and PD-L1 expression profiles. In these assays, the colocalisation of PD-1 and PD-L1-expressing cells (i.e., μ m range) is assumed to be an interaction state (Johnson et al., 2018). Here, the intrinsic distance constraints of iFRET informs on interaction states as receptor and ligand pairs within 1–10 nm of each other; distances exceeding 10 nm are considered to be non-interacting. In this study, we have investigated the application of iFRET in formalin-fixed, paraffin-embedded (FFPE) patient tumour biopsies to assess checkpoint interaction, to understand the relationship of this to ligand expression, and to judge the predictive power of the data in respect of patient response to immune checkpoint interventions.

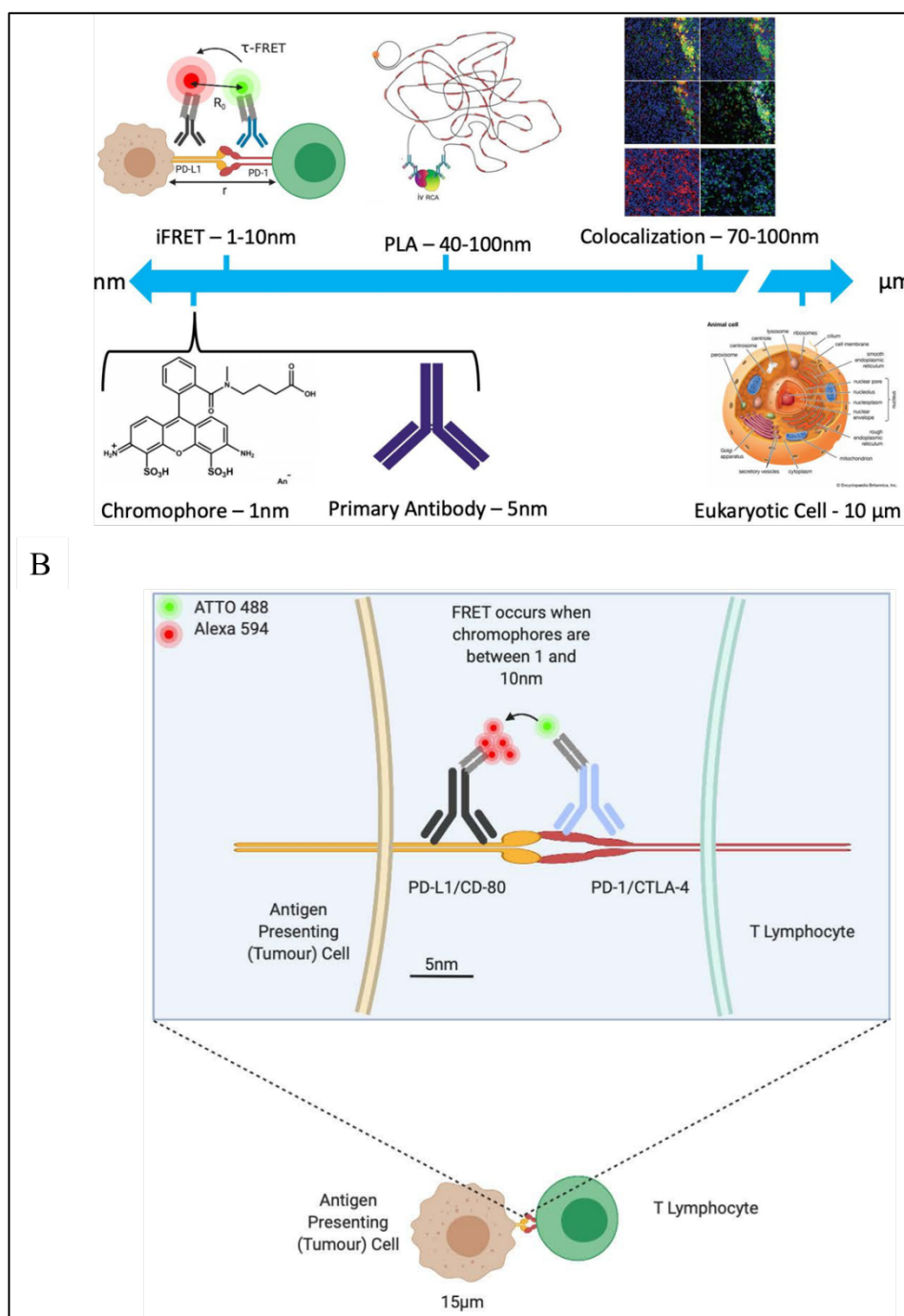


Figure 3.1: Scale Bar and iFRET Labelling Schematic. **A**) Scale bar indicating the working distances of iFRET (1-10nm) compared to the proximity ligation assay (40-100nm) and intensity based colocalisation assays (70-100+ nm). At the distances of 1-10nm, iFRET can determine receptor-ligand interaction as opposed to receptor and ligand being in close proximity. The relative sizes of the chromophores and primary antibodies (1nm and 5nm respectively) are shown. **B**) iFRET uses a two-site assay which determines the interactive states of the immune- checkpoint ligands and receptors. Both the receptor and ligand are labelled with a primary antibody (anti-mouse and anti-rabbit respectively). The anti-mouse primary antibody (detecting CTLA-4 or PD-1) is labelled with a F(ab')₂ fragment conjugated to ATTO488, the donor chromophore. The anti-rabbit antibody (detecting CD80 or PD-L1) is labelled with a F(ab')₂ fragment conjugated to horseradish peroxidase (HRP). Using tyramide signal amplification, the HRP labels the sample with Alexa594 which acts as the acceptor chromophore. FRET can only occur at distances of 1-10nm; the use of secondary F(ab')₂ fragments allows the critical FRET distance of 10nm to be maintained. In the schematic shown here, the ligand and receptor are interacting.

3.3: Materials and Methods

3.3.1: Pathology

3.3.1.1: Clear-cell RCC

Biopsies from patients with clear-cell renal-cell carcinoma (ccRCC), diagnosed and treated at the Cruces University Hospital (Barakaldo, Bizkaia, Spain), were graded and staged within the study. All patients gave written informed consent for the potential use of their resected tumours for research. This study was approved by the Ethical and Scientific Committee (CEIC-Euskadi PI2015060). The International Society of Urological Pathology 2013 tumour grading system (Delahunt et al., 2013) was used to assign each sample using routine haematoxylin and eosin (H&E) staining. Tumours were graded and grouped as low (G1/2) and high (G3/4) grade for consistency. To assess PD-L1 expression, a multisite tumour sampling (MSTS) method was used, which samples more areas of a tumour with the aim of overcoming the problems of tissue heterogeneity (López and Cortés, 2017). Samples were determined PD-L1 positive (>1%) or negative (<1%) using the Roche VENTANA PD-L1 (SP142) Assay.

3.3.1.2: Malignant Melanoma

Cases of malignant melanoma used in this study were selected from all patients diagnosed with malignant melanoma between June 2003 and February 2017 at Nottingham University Hospital (Nottingham, England, United Kingdom). The main selection criterion was tumours having a Breslow thickness of >1 mm. Patients gave written informed consent for their specimens to be stored and used for research. Patient clinicopathologic data were obtained from Nottingham University Hospital PAS, WinPath, and NotIS databases. Data and specimens were anonymised by using only their designated laboratory case reference. Ethical approval (ACP0000174) was gained from the Nottingham Health Science Biobank Access Committee. A cohort of 176 primary malignant melanoma cases was used for iFRET analysis as tissue microarrays (TMA). Within the TMAs, each patient had one tumour sample. Table 3.1 summarises the clinical parameters of the 176 patients. Tumours were fully surgically excised and FFPE in tissue blocks. Tissue cores of 1mm diameter were selected by studying H&E-stained sections most recently cut from the FFPE tissue block. The location of cores to remove from the tissue block was selected by scanning the slides and using Panoramic Viewer Software (3DHiTech). Cores were removed from the FFPE tissue blocks using the TMA Grand Master (3DHiTech) and arrayed into new paraffin blocks.

Table 3.1: List of clinical parameters - malignant melanoma.

Clinical Parameter		Frequency n (%)
Gender (n= 173)	Male	102 (59.9)
	Female	71 (41.1)
Age at primary diagnosis (n= 172)	<50	30 (17.4)
	50-59	29 (16.9)
	60-69	37 (21.5)
	70-79	36 (21.0)
	≥ 80	40 (23.2)
Stage (n=172)	IA	1 (0.6)
	IB	42 (24.4)
	II	1 (0.6)
	IIA	30 (17.4)
	IIB	27(15.7)
	IIC	17 (9.8)
	III	2 (1.2)
	IIIA	1 (0.6)
	IIIB	2 (1.2)
	IIIC	9 (5.2)
	IIID	2 (1.2)
	IV	38 (22.1)
Site of tumour (n= 172)	Head and Neck	29 (16.9)
	Trunk	19 (11.0)
	Upper Limb(s)	38 (22.1)
	Lower Limb(s)	37 (21.5)
	Pelvic Region	5 (2.9)
	Back	44 (25.6)
Breslow thickness (mm) (n= 172)	<1mm	0.0 (0)
	1-1.9mm	48 (27.9)
	2-3.9mm	69 (40.1)
	4-5.9mm	26 (15.1)
	≥6mm	29 (16.9)
Ulceration (n= 171)	Absent	110 (64.3)
	Present	61 (35.7)
Microsatellites (n=170)	Absent	165 (97.1)
	Present	5 (2.9)
Tumour infiltrating lymphocytes (n= 170)	Absent	39 (22.9)
	Focal	101 (59.4)
	Extensive	30 (17.7)
Local recurrence (n=173)	Absent	157 (90.8)
	Present	16 (9.2)

3.3.1.3: Metastatic Non-Small Cell Lung Carcinoma

Biopsies from 60 metastatic NSCLC tumours were obtained during interventional radiology procedures from Institut Bergonié (Bordeaux, France; Table 3.2). Thirty-six patients were male and 24 were female, with a median age of 63 years (range, 44–86 years). Performance status was defined with 50 patients given a performance status of ≤ 1 and 10 patients given a status of ≥ 1 . Performance status is a measure of a patients' progress, with a grade of 0 being defined as fully active with the patient being able to carry on all pre-disease activities without restriction. A score of 1–3 indicates increasing severity of limitations to daily activities and self-care. A score of 4 is defined as completely disabled and 5 is defined as dead (Oken et al., 1982). The clinical outcome of 40 patients who were treated with either nivolumab (n=37) or pembrolizumab (n=3) was provided and used for Kaplan–Meier survival analysis. Patients' samples were collected between January 2014 and December 2017. This study was approved by the Institutional Review Board of Institut Bergonié (Bordeaux, France). Excised samples were FFPE in tissue blocks prior to being sliced and mounted on microscope slides. For iFRET analysis, three consecutive tissue slices of each patient's sample were provided. One slide for each patient sample was labelled with H&E and a trained pathologist (J.I. Lopez) identified tumorous areas within the sample.

Table 3.2: List of clinical parameters - NSCLC.

Clinical Parameters		Frequency n (%)
Gender (n=60)	Male	36 (60)
	Female	24 (40)
Age (n=60)	44-86 years	Median 63 years
Tumour type (n=60)	Non-small cell lung carcinoma	60 (100)
Performance status (n=60)	≤ 1	50 (83)
	> 1	10 (17)
Previous lines of treatment (n=60)	≤ 1	39 (65)
	> 1	21 (35)
Treatment (n=60)	anti-PD-1 therapy	60 (100)

3.3.2: Antibodies and Reagents

Monoclonal antibodies, mouse anti-PD-1 (catalogue no.: ab52587, clone number: NAT105), rabbit anti-PD-L1 (catalogue no.: ab205921, clone number: 28–8), and mouse anti-CTLA-4 (catalogue no.: ab19792, clone number: BNI3) were purchased from Abcam. Rabbit anti-CD80 (catalogue no.: MBS2522916, clone number: MEM-233) was purchased from MyBioSource. The experimental antibody, J1201, which blocks PD-1/PD-L1 interactions was obtained from Promega. Ipilimumab, which blocks CTLA-4/CD80 interactions was also obtained from Promega. Pierce endogenous peroxidase suppressor (35000), Signal amplification kit (T20950), and Prolong Diamond antifade mount (P36970) were obtained from Thermofisher Scientific. AffiniPure F(ab')₂ fragment donkey anti-mouse IgG (immunoglobulin G) and peroxidase-conjugated AffiniPure F(ab')₂ fragment donkey anti-rabbit IgG were purchased from Jackson ImmunoResearch Laboratories. ATTO 488 NHS ester was purchased and conjugated to the AffiniPure F(ab')₂ IgG as described by Veeriah and colleagues (Veeriah et al., 2014). Millicell 8-well plates (PEZGS0816) were purchased from Merck.

3.3.3: Time-resolved Amplified iFRET Detected by FLIM

iFRET relies on a two-site labelling assay, which is illustrated in Figure 3.1(lower panel). Briefly, two primary antibodies are used to detect the receptor and ligand, respectively. These antibodies are then labelled with F(ab')₂ fragments conjugated to the donor chromophore ATTO488 (for the receptor) and horseradish peroxidase (HRP) for the ligand. Tyramide signal amplification is then used to label HRP with the acceptor chromophore, Alexa594 (Figure 3.1, upper panel). The conjugation of the chromophores to F(ab')₂ fragments, which bind to the two primary antibodies, allows the critical FRET distance of 10 nm or less to be maintained and provides the appropriate tool for measuring cell–cell interactions. It should be noted that additional stains, such as DAPI (4',6-diamidino-2-phenylindole), cannot be added to iFRET samples as they disrupt the ability of ATTO488 and Alexa594 to undergo FRET.

Using a semi-automated, high throughput mfFLIM (multiple-frequency FLIM) (FASTBASE Solutions S. L; Figure 3.2, middle panel), a mapping file was created, which mapped each region of interest according to its position on the slide (Veeriah et al., 2014). Phase lifetimes, average intensities, and lifetime images were calculated automatically and translated to an excel spreadsheet. A decrease of donor lifetime (τ_D) in the presence of the acceptor chromophore (τ_{DA}) is indicative of resonance energy transfer. FRET efficiency ($E_f\%$) values were calculated using the following equation, where τ_D and τ_{DA} are the lifetimes of the donor in the absence and presence of the acceptor, respectively.

$$E_f(\%) = \left(1 - \frac{\tau_{DA}}{\tau_D}\right) \cdot 100$$

Equation 3-1

Because of the Förster radius (R_0) of the chromophore pair ATTO488 and Alexa594, the minimum distance that can exist between the chromophores is 5.83 nm (Figure 3.2, lower panel; see Chapter 2). At this distance, energy transfer is maximal and yields a FRET efficiency of 50%.

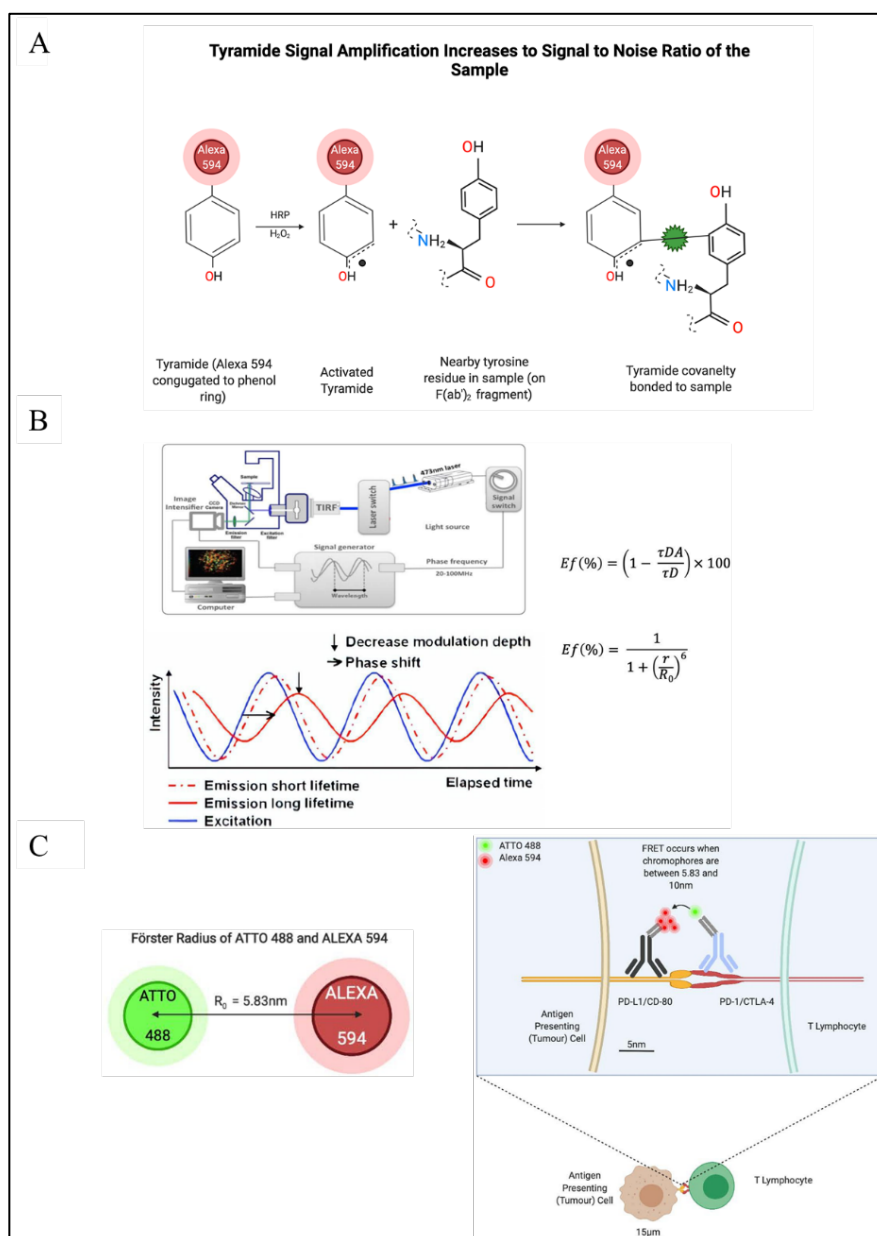


Figure 3.2: Schematics of TSA, mFLIM and Förster Radius. **A)** To observe an elevated signal to noise ratio, tyramide signal amplification is performed on all samples. The donor-acceptor site (PD-L1 or CD80) is labelled with a primary antibody which is labelled with a secondary F(ab')₂ fragment conjugated to horseradish peroxidase (HRP). When tyramide (a phenol ring conjugated to Alexa594 at the para position) is added to the sample in the presence of H₂O₂, a free radical is generated. The tyramide then covalently binds to nearby tyrosine residues in the sample (on the F(ab')₂ fragment). An incubation time of 20 minutes is used to prevent non-specific binding of the chromophore to the sample. **B)** The top panel illustrates the set-up of our mFLIM platform. A 473nm diode laser is the excitation source which is modulated at 40MHz. The LI-FLIM software (Lambert Instruments) calculates average donor lifetime per pixel of the generated image. The lower panel demonstrates how the incident light source (blue) is acousto-optically modulated. The emitted signal from the sample is partially de-modulated and out of phase. Our mFLIM platform measures the phase shift to calculate donor lifetime. The equations given are used to calculate the distance (r) of two-chromophores from the lifetime of the donor alone (D) and the lifetime of the donor in the presence of the acceptor (DA). **C)** Left-hand panel shows the Förster radius (R₀) of ATTO488 and Alexa594 which is 5.83nm. This is the closest distance these two chromophores can be and is measured from the centre of each chromophore. The right-hand panel shows a schematic of the iFRET assay. All objects are drawn to scale, and it can be seen that the transfer of energy from donor to acceptor will only occur if the chromophores are between 5.83nm and 10nm.

3.3.4: iFRET Assay for PD-1/PD-L1 Interaction in Cell Culture

The commercially validated Promega Blockade Bioassay, originally designed to measure the antibody blockade of PD-1/PD-L1 and CTLA-4/CD80 interaction by luminescence, was adapted for an iFRET protocol with the aim of verifying the technique for detecting intercellular interaction of these receptor-ligand pairs. Cells were obtained from the Promega Blockade Bioassay and screened for *Mycoplasma* prior to dispatch. These cells were thawed and directly used in this assay only. PD-L1-expressing CHO-K1 cells were seeded onto Millicell 8-well plates and were incubated at 37°C with 5% CO₂ for 16 hours. The experimental blocking antibody, J1201 (anti-PD-1), was added to four wells at 25 mg/mL final concentration to inhibit receptor–ligand interaction. PD-1-expressing Jurkat cells were subsequently seeded in all wells and the plates were incubated for 20 hours at 37°C with 5% CO₂. The unbound cells were removed, and the plates were washed three times for 5 minutes with PBS before being fixed with 4% paraformaldehyde (PFA) for 12 minutes. The PFA was then removed, and the plates were washed 3 times for 5 minutes with PBS. All samples were incubated with endogenous peroxidase suppressor for 30 minutes at room temperature before being washed with PBS. They were subsequently incubated with 1% (10 mg/mL) BSA for 1 hour at room temperature before further washing with PBS 3 times.

Primary antibody staining was carried out by adding mouse anti-PD-1 (1:100 in BSA), the donor-only (D) readout condition. Meanwhile, the donor plus acceptor (D/A) readout condition was labelled with both anti-PD-1 (1:100) and rabbit anti-PD-L1 (1:500). The plate was incubated overnight at 4°C before being washed twice with PBS containing 0.02% Tween 20 (PBST). Secondary F(ab')₂ fragments were added, the D wells were labelled with anti-mouse F(ab')₂-ATTO488 (1:100) and the D/A wells labelled with F(ab')₂-ATTO488 (1:100) and anti-rabbit F(ab')₂-HRP (1:200). The plate was then incubated for 2 hours at room temperature before being washed twice with PBST and once with PBS. Tyramide signal amplification was performed on the D/A wells for 20 minutes in the dark, via the addition of Alexa594-conjugated tyramide diluted in amplification buffer (1:100) in the presence of 0.15% H₂O₂ (Veeriah et al., 2014, Miles et al., 2017) (Figure 3.2, upper panel). The D/A wells were washed twice with PBST and once with PBS to remove the tyramide. Prolong diamond antifade mount (5 µL) was added to each well before being mounted with a coverslip.

3.3.5: iFRET Assay for CTLA-4/CD80 Interaction in Cell Culture

CTLA-4-expressing Jurkat cells were first seeded onto Millicell 8-well plate, before the blocking antibody, ipilimumab (anti-CTLA-4), was added to four wells at 100 mg/mL final concentration. The CD80-expressing Raji cells were subsequently seeded and incubated for 20 hours at 37°C with 5% CO₂. Unbound cells were removed by PBS washes. The cells were fixed, underwent endogenous peroxidase suppression, and were blocked with BSA as described previously in the PD-1/PD-L1 cell assay. The

primary antibodies were added; D wells were labelled with mouse monoclonal anti-CTLA-4 (1:100) and the D/A wells labelled with both anti-CTLA-4 (1:100) and rabbit polyclonal anti-CD80 (1:100). The rest of the protocol was conducted as described above for the PD-1/PD-L1 single-cell assay.

3.3.6: iFRET Assay for PD-1/PD-L1 Interaction in FFPE ccRCC Tissue

Human ccRCC tissue samples were provided by Cruces University Hospital (Barakaldo, Bizkaia, Spain). Consecutive cross-sections of tissues were mounted on separate slides to allow D and D/A antibody labelling. Samples were obtained from 22 patients, from which, five consecutive tissue section slides were provided. Of the five samples, two were available for D and two for D/A staining, while the remaining section was analysed using H&E staining to determine regions of immune infiltration. IHC with PD-L1 (SP-142, Ventana) was performed in Benchmark Ultra (Ventana) Immunostainers following the specific protocol recommended by the manufacturer. For iFRET sample preparation, antigen retrieval was carried out using Envision Flex solution, pH 9, and a PT-Link Instrument (Dako), where the slides were heated to 95°C for 20 minutes. Remaining paraffin was removed by PBS washes before containing tissue areas with a hydrophobic PAP pen border. One to two drops per slide of endogenous peroxidase suppressor were added and the slides were incubated in a humidified tray for 30 minutes at room temperature. The slides were then blocked with BSA, and D slides were labelled with anti-PD-1, while D/A slides were labelled with anti-PD-1 plus anti-PD-L1, following the previously described cell assay protocol.

3.3.7: iFRET Assay for PD-1/PD-L1 Interaction in FFPE malignant melanoma TMAs

Human malignant melanoma TMAs were provided by Nottingham University Hospital (Nottingham, England, United Kingdom). Consecutive cross-sections of tissues were mounted on separate slides to allow D and D/A antibody labelling. Samples from 176 patients, with two consecutive tissue section slides per patient were provided. Of the two samples, one was available for D and one for D/A staining. The primary antibodies used were anti-PD-1 and anti-PD-L1 following the same protocol as the FFPE RCC tissue above.

3.3.8: iFRET Assay for PD-1/PD-L1 Interaction in FFPE Metastatic NSCLC

Human metastatic NSCLC tissue slices were provided by Institut Bergonié (Bordeaux, France). Consecutive cross-sections of tissues were mounted on separate slides to allow D and D/A antibody labelling. Samples from 40 patients, with two consecutive tissue section slides per patient were provided. Of the two samples, one was available for D and one for D/A staining. The primary antibodies used were anti-PD-1 and anti-PD-L1 following the same protocol as the FFPE ccRCC tissue above.

3.3.9: Statistical Analysis

Statistical analysis and box and whisker plots were performed using Origin Pro8. Statistical differences were calculated between groups using the Mann–Whitney U test (values indicated on the box and whisker plots). The Mann–Whitney U test is a non-parametric test, thus not assuming a normal distribution of results. Box and whisker plots represent the 25%–75% (box) and the 1–99 (whiskers) ranges. Statistical differences are indicated with $P \leq 0.05$. Kaplan–Meier survival analysis was performed using SPSS. SPSS was also used to calculate Cox regression for survival analysis to assess which factors (age, sex, tumour stage, and interaction state) were impacting overall survival. For NSCLC, patients were ranked in order of their median FRET efficiency (interaction status) and split into the two groups, those with the lowest 60% of median FRET efficiencies and those with the highest 40%. For melanoma, patients were split into the highest 20% and lowest 80% of mean FRET efficiencies. To determine these cut-off points for patients with melanoma and NSCLC, maximally selected rank statistics were performed using the R statistical software (version 3.6.2) and the maxstat (version 0.7–25) package, which provides several P-value approximations (Lausen and Schumacher, 1992, Hothorn and Lausen, 2003). Maximally selected rank statistics can be used for estimation as well as evaluation of a simple cut-off point mode. The results provided by maxstat were consistent with the choice of bottom 80% and top 20%, and 60% and 40%, respectively. The log-rank (Mantel–Cox) test was carried out to determine significant differences between the groups.

3.4: Results

3.4.1: Development, Validation and Benchmarking of a Novel Amplified FRET Imaging Assay for Determining Immune Checkpoint Interaction in ex-vivo Assays

The iFRET assay used to measure the immune checkpoint interaction state is based on time-resolved FRET. Here, FRET acts as a “chemical ruler,” measuring distances of 1–10 nm, which are the same order of magnitude as cell surface interactions. The maximum FRET efficiency value permitted is 50%. Our definition of interaction is distances under 10 nm, as opposed to proximity ligation assay (PLA), which detects distances of tens of nm and colocalisation assays, which range from 100 nm up to 20 μ m (Figure 3.2, upper panel) (Söderberg et al., 2008, Giraldo et al., 2018).

To develop and validate iFRET for the measurement of immune checkpoint interactions, two antibodies (Promega) were employed; J1201, an experimental antibody for blocking PD-1/PD-L1 interactions, and ipilimumab, for blocking CTLA-4/CD-80 interactions. These antibodies were used to verify iFRET as a technique for detecting the intercellular interaction of these ligand-receptor pairs. These antibodies and cell lines were chosen as they were components from a commercially available validated assay.

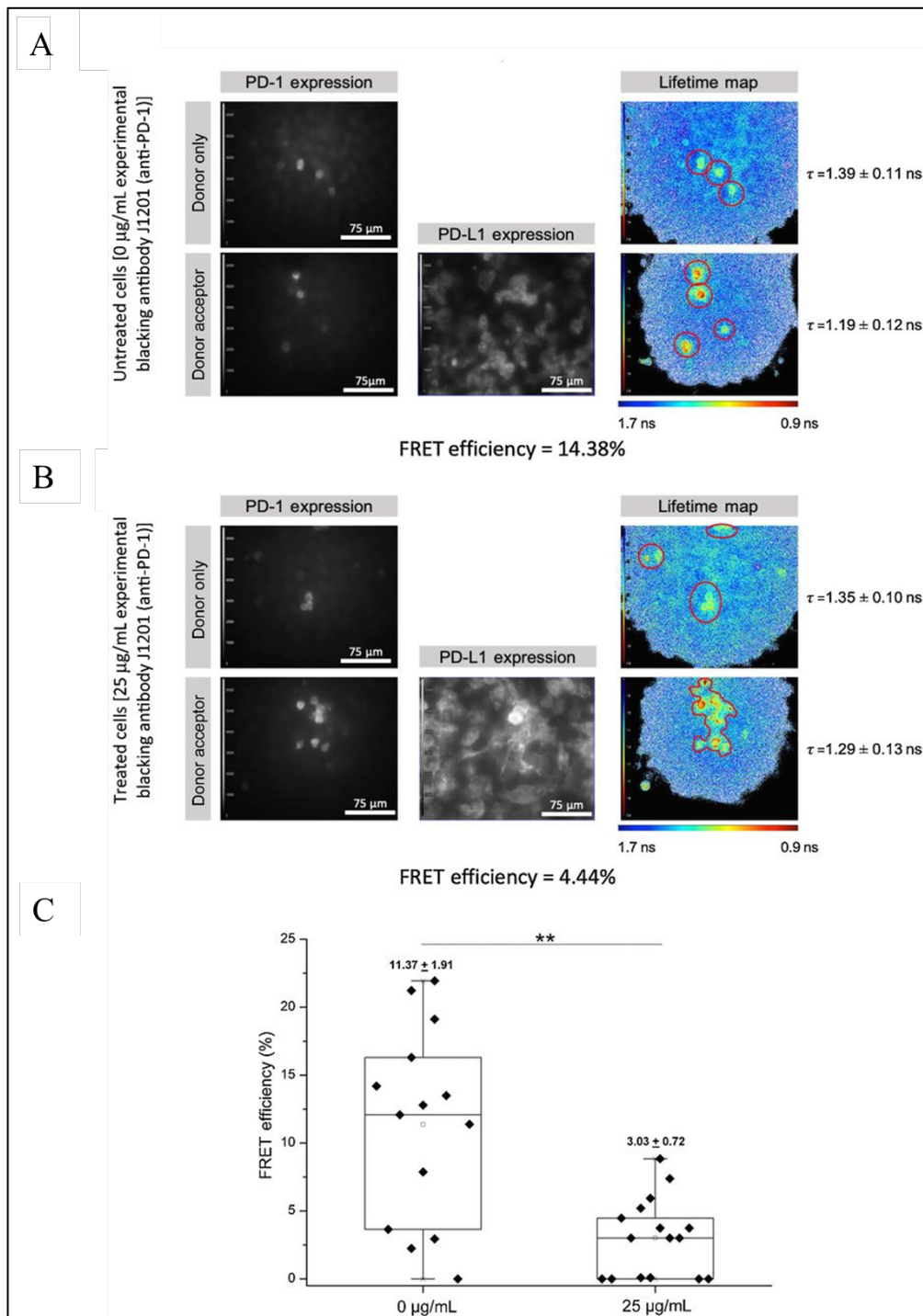


Figure 3.3: iFRET detects and quantifies PD-1/PD-L1 interaction between CHO K1 and Jurkat cells. **A)** FLIM images consist of grayscale expression maps indicating PD-1 expression (donor, ATTO488) and PD-L1 expression (acceptor, Alexa594). Pseudocolour lifetime maps indicate the lifetime of the donor alone and lifetime of the donor in the presence of the acceptor. A lifetime decrease from $1.39 \pm 0.11 \text{ ns}$ to $1.19 \pm 0.12 \text{ ns}$ yields a FRET efficiency of 14.38% in untreated cells. **B)** When treated with 25 $\mu\text{g/mL}$ J1201 (experimental anti-PD1 blocking antibody), the donor lifetime decreased from $1.35 \pm 0.10 \text{ ns}$ to $1.29 \pm 0.13 \text{ ns}$. This gives a FRET efficiency of 4.44%, indicating a significant reduction of PD-1/PD-L1 interaction. **C)** Box and whisker plot compares FRET efficiency values in the absence and presence of experimental blocking antibody, J1201 (25 $\mu\text{g/mL}$). Each point on the graph represents one region of interest, which may contain between five and 25 cells. Mean FRET efficiencies \pm SEM are indicated. Mann–Whitney U analysis determined statistical differences between treated and untreated cells. **, $P = 0.004$.

Figure 3.3 illustrates the intercellular interaction of PD-1 and PD-L1, on Jurkat and CHO-K1 cells, using iFRET. Cells were not permeabilised and therefore, the observable interaction was that of two membrane-bound, extracellular proteins. The FLIM images provided in the following figures consist of pseudocolour lifetime maps, which represent lower lifetimes (red) and higher lifetimes (blue). Also provided are grayscale intensity maps, which indicate donor (PD-1 or CTLA-4) expression and acceptor (PD-L1 or CD80) expression. In untreated cells, a lifetime decrease from 1.39 ± 0.11 ns to 1.19 ± 0.12 ns was detected, resulting in a FRET efficiency of 14.38% (Figure 3.3, upper panel). FRET efficiency is correlated to molecular distance; Table 3.3 indicates the range of receptor–ligand distances obtained for the following results. In cells treated with 25 mg/mL of experimental blocking antibody, J1201, the lifetime reduced from 1.35 ± 0.10 ns to 1.29 ± 0.13 ns, yielding a FRET efficiency of 4.44% (Figure 3.3, middle panel). iFRET signal was not observed when either of the primary staining antibody was omitted. Moreover, when each cell type was analysed alone, no interaction state was detected. The findings indicate that the decrease in donor lifetime reflected by the high FRET efficiency was due to the specific interaction of PD-1 and PD-L1, which was attenuated in the presence of J1201. In both cases, intensity maps confirm the presence of the donor, PD-1 and acceptor, PD-L1. In Figure 3.3, lower panel, a box and whisker plot compares FRET efficiency values in the absence and presence of experimental blocking antibody, J1201 (25 mg/mL). Each point on the graph represents one region of interest, which may contain between five and 25 cells. Mean FRET efficiencies SEM (standard error of the mean) are indicated. Mann–Whitney U analysis determined statistical differences between treated and untreated cells (**, $P=0.004$). Table 3.3 indicates how the FRET efficiencies of each figure correlate to a nanoscopic receptor-ligand interaction.

Table 3.3: FRET efficiency can be used to calculate receptor-ligand distance.

Result	FRET Efficiency (%)	Receptor-Ligand Distance (nm)
Figure 4C (i)	14.38	7.85
Figure 4C (ii)	4.44	9.78
Figure 4D (i)	26.02	6.94
Figure 4D (ii)	3.88	9.95
Figure 4F (i)	17.28	7.57
Figure 4G (ii)	3.50	>10
Figure 4G (iii)	26.20	6.93
Figure 4I (i)	27.64	6.80

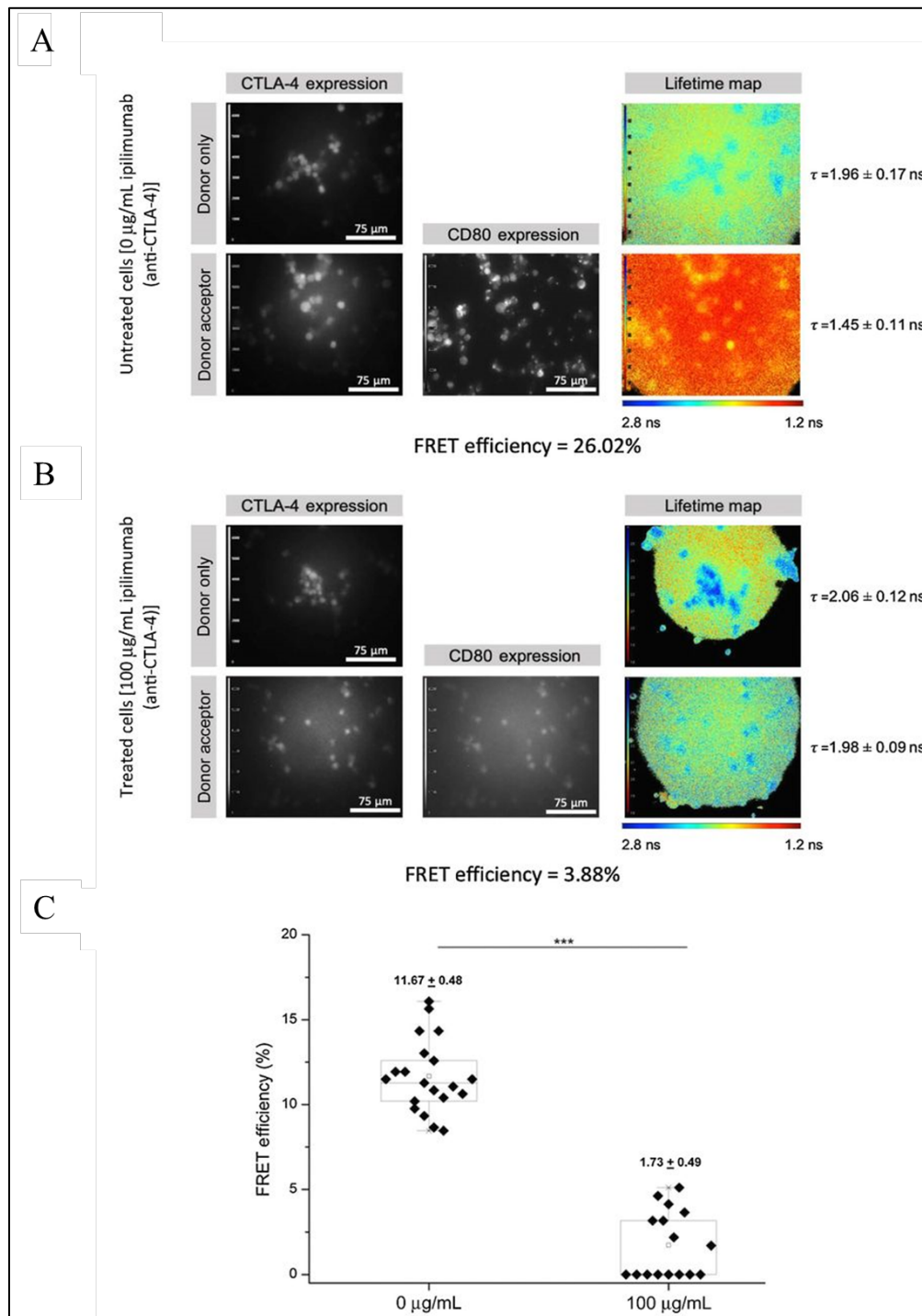


Figure 3.4: iFRET precisely determines CTLA-4/CD80 interaction between Raji and Jurkat cells. **A)** In untreated Raji and Jurkat cells, the donor lifetime decreased from 1.96 ± 0.17 ns alone to 1.45 ± 0.11 ns in the presence of the acceptor. This gives a FRET efficiency of 26.02%. **B)** When treated with 100 μg ipilimumab, donor lifetime decreased from 2.06 ± 0.12 ns to 1.98 ± 0.09 ns. This results in a FRET efficiency of 3.88%. **C)** Box and whisker plot compares FRET efficiency values in the absence and presence of 100 $\mu\text{g/mL}$ ipilimumab. Each point on the graph represents one region of interest, which may contain between five and 25 cells. Mann–Whitney U analysis determined statistical differences between treated and untreated cells. ***, $P = 3.27 \times 10^{-7}$.

Intercellular CTLA-4 and CD80 interactions, in Jurkat and Raji cells, were also assessed using iFRET (Figure 3.4). Here, in the absence of the blocking antibody, ipilimumab, donor lifetime decreased from 1.96 ± 0.17 ns to 1.45 ± 0.11 ns in the presence of the acceptor. This resulted in a FRET efficiency of 26.02% (Figure 3.4, upper panel). When ipilimumab was added at 100 mg/mL, the donor lifetime decreased from 2.06 ± 0.12 ns to 1.98 ± 0.09 ns, resulting in a FRET efficiency of 3.88% (Figure 3.4, middle panel). Intensity maps confirm the expression of CTLA-4 (donor) and CD-80 (acceptor). Box and whisker plot (Figure 3.4, lower panel) compares FRET efficiency values in the absence and presence of 100 mg/mL ipilimumab. Each point on the graph represents one region of interest, which may contain between five and 25 cells. Mann-Whitney U analysis determined statistical differences between treated and untreated cells (***, $P=3.27 \times 10^{-7}$).

To benchmark the effectiveness of the iFRET assay in clinically relevant settings, we compared the assay with a PLA, which in principle can also visualise PD-1 and PD-L1 within proximities of approximately 40 nm. To achieve this comparison, iFRET and PLA were run on sequential ccRCC tissue sections from the same tissue block. Prior to the investigation, samples were determined PD-L1 positive (>1%) or negative (<1%) using the Roche VENTANA PD-L1 (SP142) assay.

PLA allowed the qualitative visualization of PD-1 and PD-L1 within close proximity (Figure 3.5, upper panel). The PD-L1–positive ccRCC sample labelled with anti-PD-1, anti-PD-L1, and PLA / probes produced measurable PLA signals, albeit comparatively weak signals. Furthermore, PLA signals were observed across both experimental and control groups (normal renal tissue), possibly due to PLA only determining close proximity (up to 40 nm) as opposed to direct interaction (≤ 10 nm), limiting the specificity of the assay (Debaize et al., 2017).

The box and whisker plots show the interaction states in the PD-L1–positive and PD-L1–negative groups. In the PD-L1-negative group, PLA failed to detect an interaction, whereas iFRET detected two areas of significant interaction (Figure 3.5 lower panel). These observations suggest that iFRET provides greater sensitivity and specificity than PLA, allowing the identification of tumour-mediated immune suppression in patients otherwise considered as PD-L1 negative.

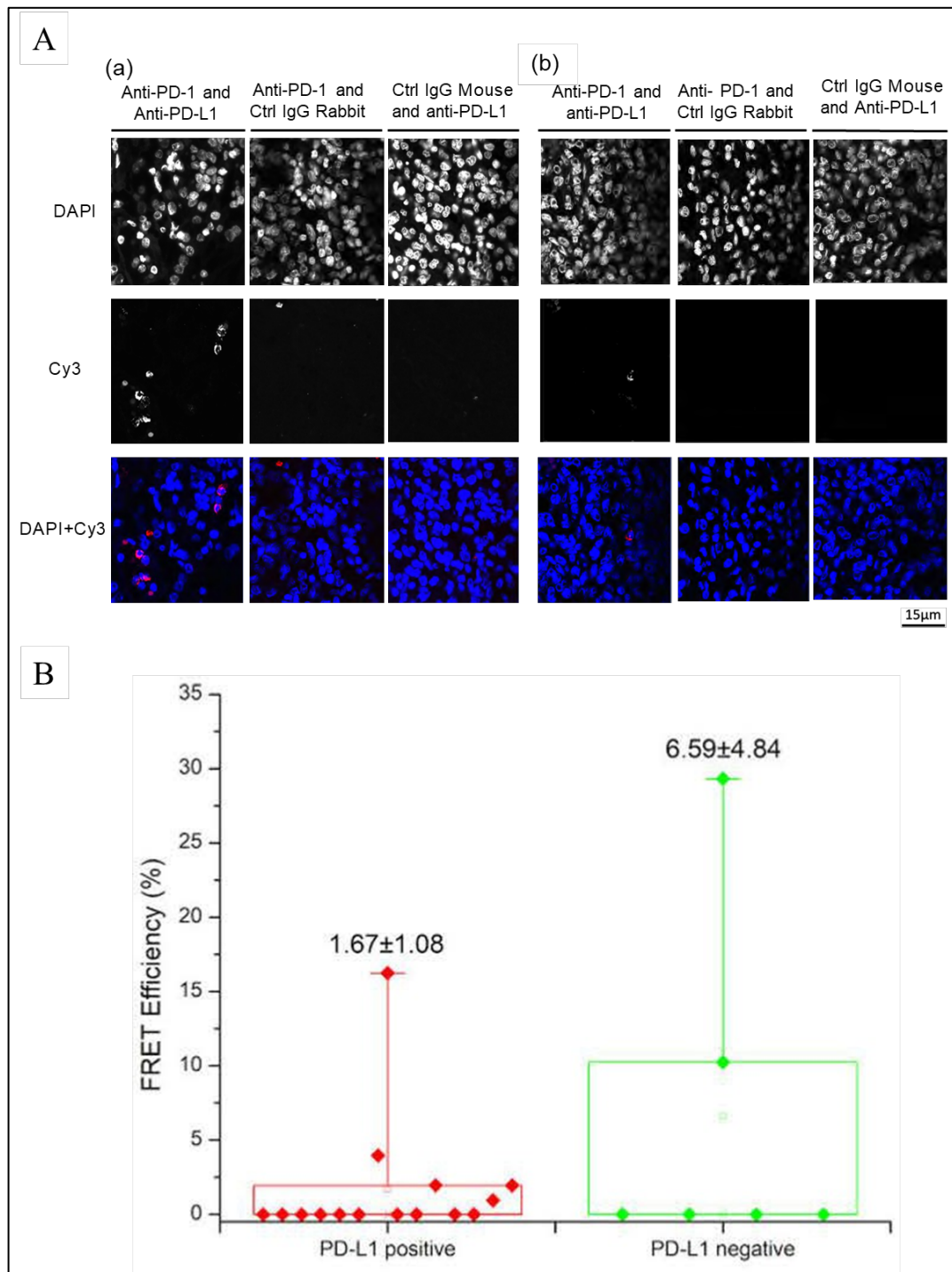


Figure 3.5: PLA detects proximity between PD-1 and PD-L1 but does not report on interaction. **A)** Visualisation of PD-1 and PD-L1 colocalisation in PD-L1 positive (**a**) and PD-L1 negative (**b**) fixed ccRCC samples using PLA. Samples were labelled with primary antibodies against PD-1 and PD-L1 and secondary PLA probes. Negative controls were included whereby PD-L1 and PD-1 primary antibodies were replaced with non-specific rabbit IgG and mouse IgG antibodies, respectively. Rolling circle amplification (RCA) products and nuclei were labelled with Cy3 and DAPI, respectively. 30 images were acquired for the PD-L1 positive section stained with both PD-1 and PD-L1 antibodies and 15 for each control. Five images were acquired for each PD-L1 negative condition. **B)** PD-1 and PD-L1 interaction status determined by iFRET in fixed ccRCC patient samples. Box and Whisker plots represent the FRET efficiency values for PD-L1 positive and PD-L1 negative tissue samples. The mean values \pm SEM are indicated, and the median is represented by the midline. It is seen that a number of patients who would be labelled PD-L1 negative had high PD-1/PD-L1 interaction states. Conversely, 10 patients who were deemed PD-L1 positive elicited no PD-1/PD-L1 interaction state.

3.4.2: PD-L1 Expression Does Not Correspond to Interaction Status of PD-1 and PD-L1 in ccRCC

Following iFRET optimisation and benchmarking, we assessed the interaction of PD-1 and PD-L1 in the subsequent FFPE ccRCC tissue sections from the above cohort of patients with as yet unknown outcomes. The series included samples from 22 patients considered as PD-L1 negative (<1%) or positive (>1%), as determined using the Roche VENTANA PD-L1 (SP142) assay and MSTs. Three regions of interest per patient sample were analysed and the mean FRET efficiency for each patient was calculated. Across these patients, mean FRET efficiencies varied from 0.17% to 14.1%, indicating iFRET is able to quantitatively detect the heterogeneity of PD-1 and PD-L1 interaction states in patients. Figure 3.6, upper panel, shows a sample with a donor lifetime decrease from 1.91 ± 0.18 ns to 1.58 ± 0.19 ns. This resulted in a FRET efficiency of 17.28%. Notably, PD-L1 expression, classified by MSTs, did not correlate with the interaction status of PD-1 and PD-L1 as determined by iFRET (Figure 3.6, lower panel). Crucially, iFRET detected significant interaction states in 11 of the 12 PD-L1-negative patients, a functional state that was not detected by conventional IHC methods. Conversely, one PD-L1-positive patient showed a minimal interaction state (Figure 3.6, lower panel).

3.4.3: PD-1/PD-L1 Interaction State is Indicative of Patient Outcome in Malignant Melanoma

After analysing PD-1/PD-L1 interaction in ccRCC tissue, the interaction status in 176 patients with malignant melanoma with known outcomes was assessed. The cohort, which consisted of treated and untreated patients, was predominantly male with a split of 102 males/71 females and a mean age of 66.1 years. Twenty-five percent of patients had stage I tumours, 43.5% had stage II tumours, 9.4% had stage III tumours, and 22.1% had stage IV tumours. Tumour-infiltrating lymphocytes were absent in 39 patients, and 101 patients had focal infiltration with 30 patients experiencing extensive infiltration (Table 3.1). Of the 176 patients, 148 were untreated, 14 received immunotherapies (nivolumab, pembrolizumab, or ipilimumab), and 14 received non-immune therapies (radiotherapy, chemotherapy, or small-molecule inhibitors, e.g., vemurafenib, trametinib, and dabrafenib).

Figure 3.7, upper panel, shows the H&E staining of a primary cutaneous malignant melanoma. The tiles on the left show the H&E staining of patient 390, a non-ulcerated tumour sample with no tumour-infiltrating lymphocytes, this patient had a FRET efficiency of 3.50%. The upper tile shows a 5x magnification with the lack of ulceration circled, and subsequent 10x magnifications show the lack of tumour-infiltrating lymphocytes. The tiles on the right show patient 131, with high tumour-infiltrating lymphocytes. This patient had a FRET efficiency of 26.20%. The top tile here shows a 5x magnification indicating the tumour-infiltrating lymphocytes (black circled area) and tumour ulceration (blue circle).

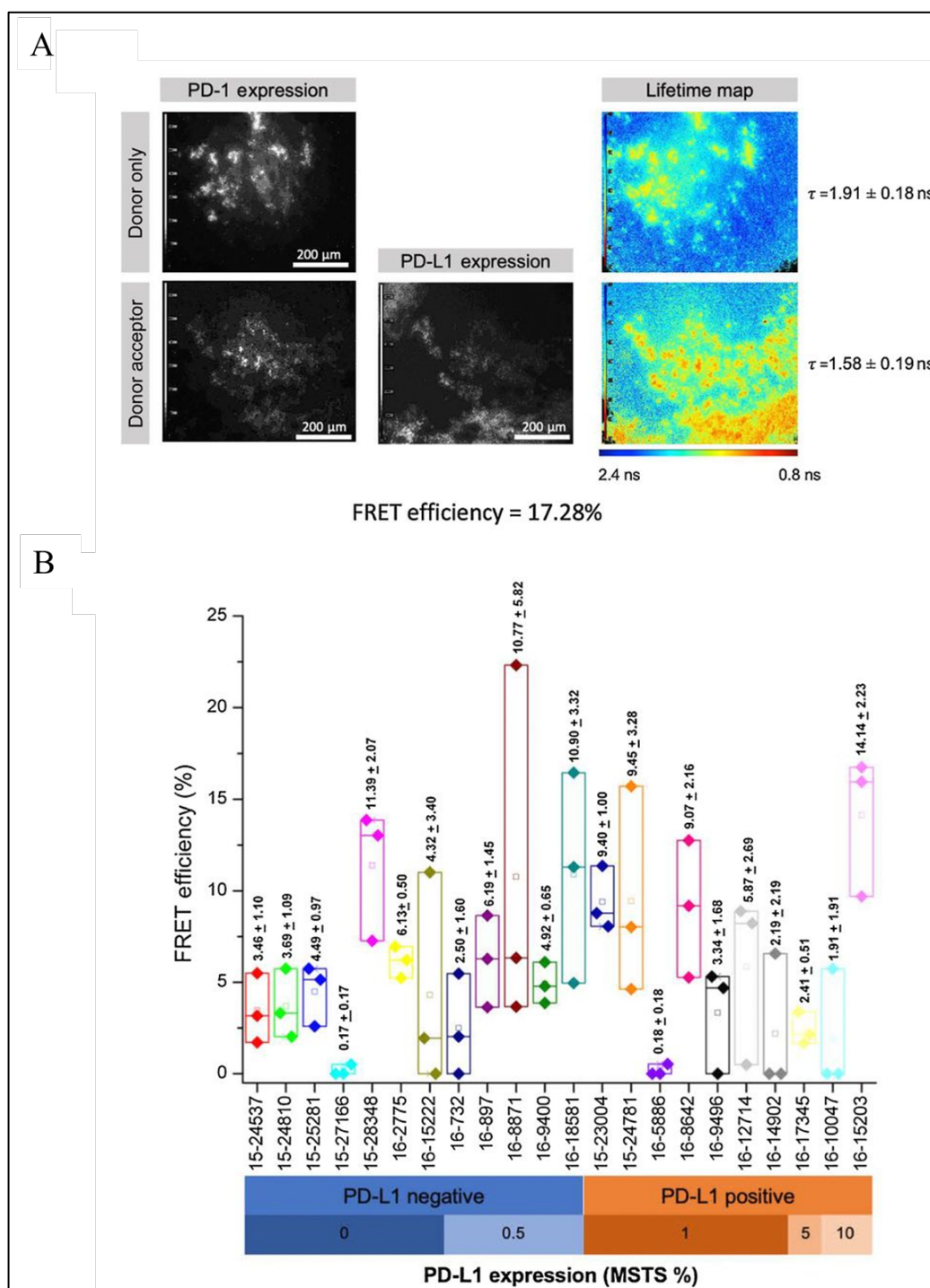


Figure 3.6: iFRET detects heterogeneity of PD-1 and PD-L1 interaction in FFPE ccRCC. A) Intensity images and lifetime maps (pseudocolour scale) of FFPE human ccRCC patient sample 16-15203. A decrease in donor lifetime from 1.91 ± 0.18 ns alone to 1.58 ± 0.19 ns in the presence of the acceptor gives a FRET efficiency of 17.28%. **B)** Box and whisker plots show the interaction state of each patient in either the PD-L1–negative or PD-L1–positive group. Here, iFRET identified that 11 of the 12 PD-L1–negative patients had a significant interaction state. Conversely, one patient in the PD-L1–positive group exhibited no interaction state.

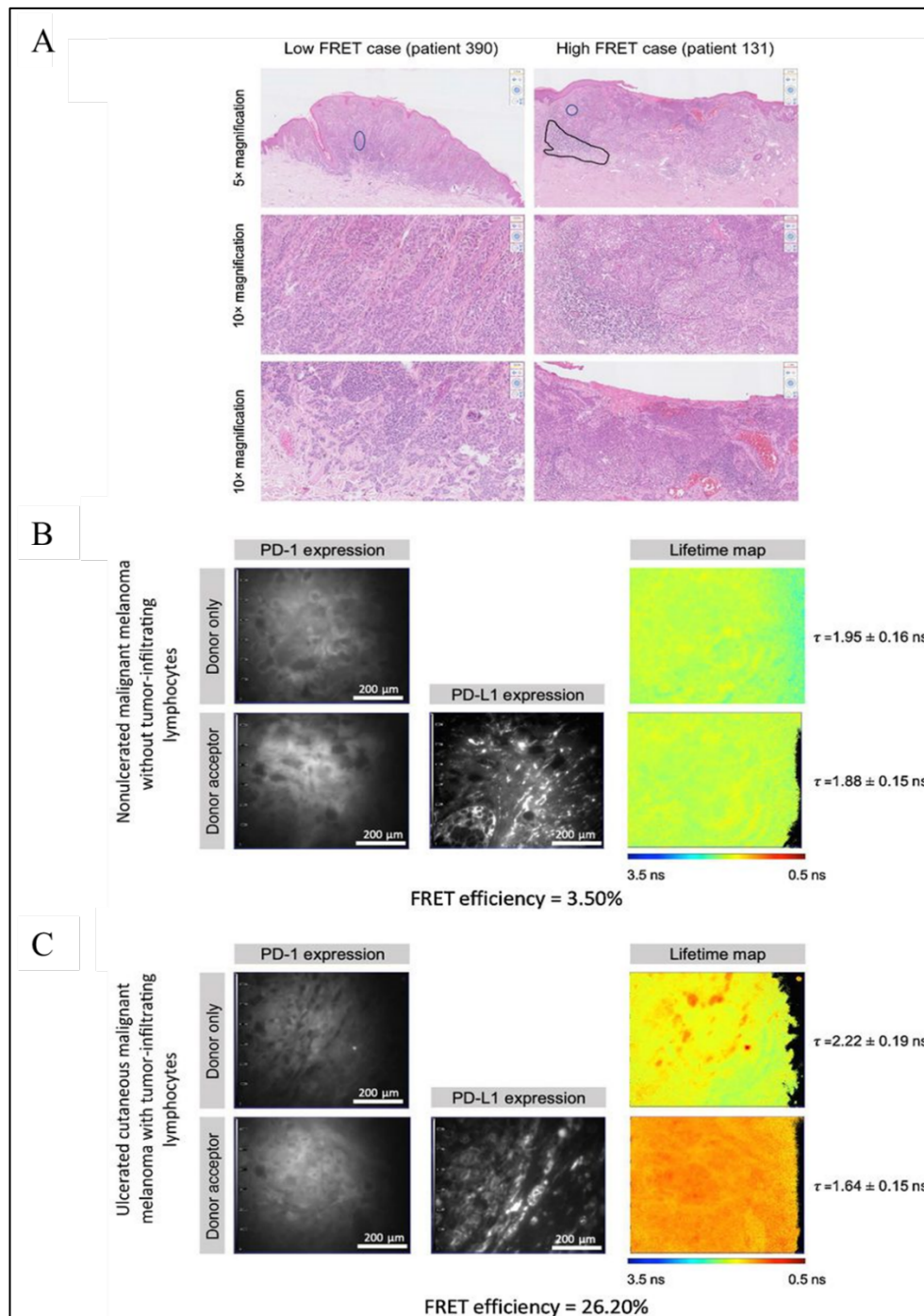


Figure 3.7: PD-L1 expression does not correlate with PD-1/PD-L1 interaction state in malignant melanoma. **A)** The H&E staining of the sample of patient 390 with a FRET efficiency of 3.50% (left). A scanning view of the non-ulcerated (blue circle) tumour at 5x magnification, with the subsequent images showing high power (magnification, 10x) images of the tumour, highlighting a lack of tumour-infiltrating leukocytes (top). The H&E staining of patient 131 with a FRET efficiency of 26.20% (right). A scanning view of the tumour with the tumour-infiltrating leukocytes shown (black marked area) and tumour ulceration (blue circle; top). Tumour leukocyte infiltration (middle) and tumour ulceration (bottom) at a magnification of 10x. **B)** FLIM images show a melanoma with a low PD-1/PD-L1 interaction state. Expression images, based on PD-1 or PD-L1 intensity, show the presence of the receptor and ligand, however, the lifetime map shows no change in pseudocolour, indicating a lifetime change from 1.95 ± 0.16 ns to 1.88 ± 0.15 ns and thus, no interaction state. **C)** FLIM images show a melanoma sample with a high PD-1/PD-L1 interaction state. Again, the expression maps show the presence of PD-1 and PD-L1 as in (A), however, the change in pseudocolour represents a change in lifetime from 2.22 ± 0.19 ns to 1.64 ± 0.15 ns, indicating a high interaction state.

The subsequent middle and bottom panels show 10x magnifications of lymphocyte infiltration and tumour ulceration, respectively. The middle panel of Figure 3.7 shows FLIM images from the sample of patient 390, where intensity maps illustrate the expression of PD-1 and PD-L1. Here, the pseudocolour scale runs from 3.5 ns (blue) to 0.5 ns (red). Despite a high expression of PD-L1 in this patient's sample, a low change in donor lifetime was observed; donor lifetime alone was 1.95 ± 0.16 ns and slightly decreased to 1.88 ± 0.15 ns in the presence of the acceptor. The resulting FRET efficiency was 3.50%. Conversely, Figure 3.7, lower panel, shows the sample of patient 131. As observed in the sample of patient 390, patient 131's sample demonstrated a prominent level of PD-L1 expression. However, unlike patient 390, patient 131 displayed a high interaction state between ligand and receptor, with the donor lifetime decreasing from 2.22 ± 0.19 ns to 1.64 ± 0.15 ns when in the presence of the acceptor, with a resulting FRET efficiency of 26.20%. These results reinforce the hypothesis that PD-L1 expression does not correlate with PD-1/PD-L1 interaction.

The interaction state was assessed with respect to clinical PD-L1 expression scores for 159 of the 176 patients in this cohort (PD-L1 scores were not available for the remaining 17 patients). Figure 3.7, upper panel, shows the lack of correlation between clinical PD-L1 expression scores and interaction state determined by iFRET. Here, the clinical IHC images of patient 390 (bottom) and patient 131 (top) are shown. As this was performed on a TMA, each patient had one FRET efficiency value, with each point of the box and whisker plot representing one patient's FRET efficiency. Of the 117 patients who were stratified as being PD-L1 negative, 58 showed a PD-1/PD-L1 interaction state; a functional state not detected by conventional IHC methods. Of the 42 patients who were in the PD-L1-positive group, 19 showed no interaction despite the presence of the ligand.

We then correlated PD-1/PD-L1 interaction state with patient survival. The cohorts were ranked in order of their FRET efficiency values and sorted into the following categories: those with the lowest 80% of FRET efficiencies and those with the highest 20%. In the middle panel of Figure 3.8, Kaplan–Meier survival analysis revealed that those with the lowest 80% of FRET efficiencies had a significantly worse outcome than those with the highest 20% (log-rank Mantel-Cox, $P=0.05$). Cox regression for survival analysis revealed PD-1/PD-L1 interaction was the only significant factor impacting overall survival ($P=0.019$). We then sought to apply Kaplan–Meier analysis to correlate the clinical PD-L1 scores with patient outcome. In Figure 3.8, lower panel, there is no significant difference in outcome between the PD-L1⁺ and PD-L1⁻ patients (log-rank Mantel-Cox, $P=0.87$). This illustrates that iFRET is more informative on patient outcome than conventional IHC approaches reporting ligand expression.

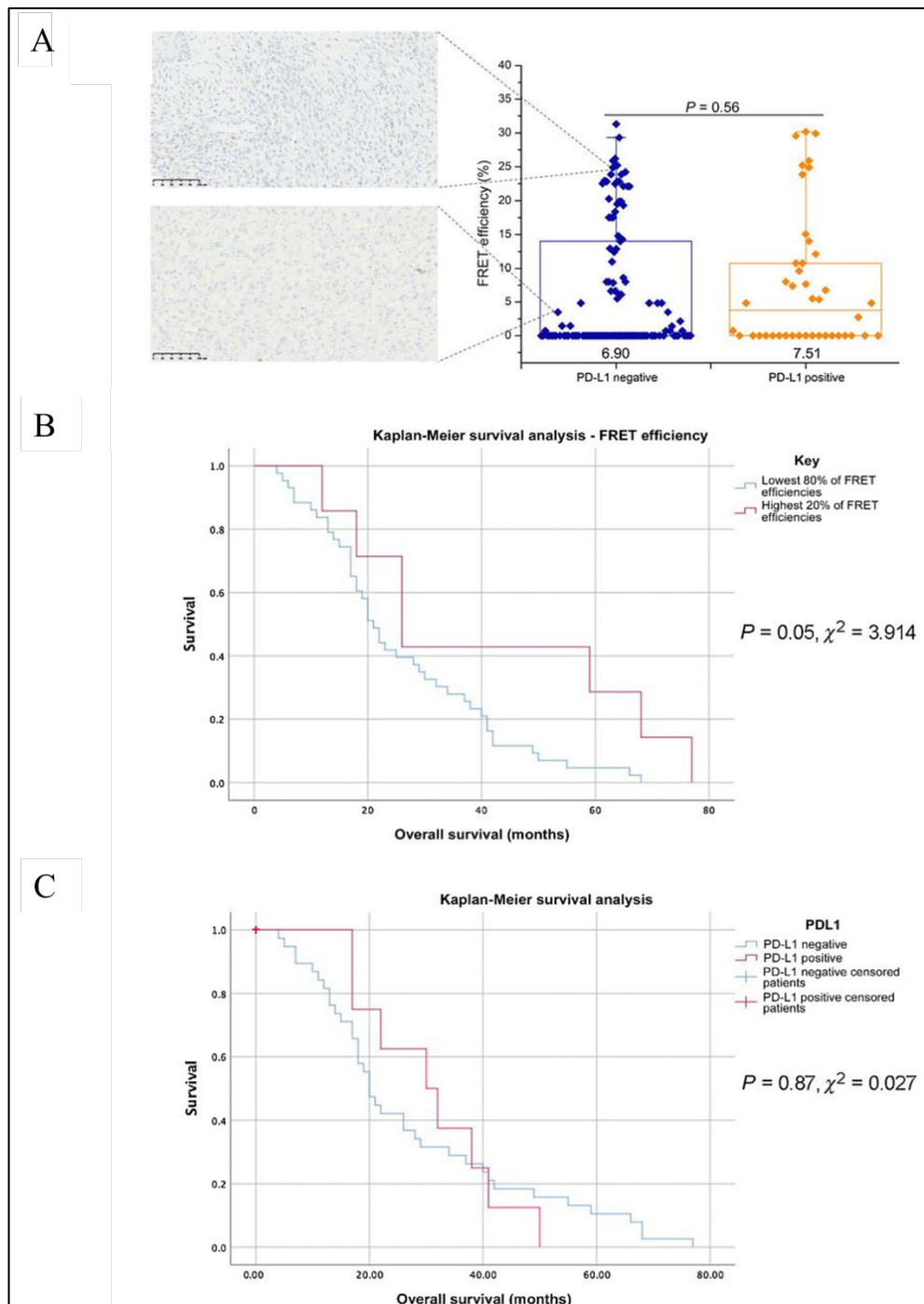


Figure 3.8: PD-1/PD-L1 interaction state predicts patient outcome in malignant melanoma, where PD-L1 expression fails to do so. A) PD-L1 was labelled and patients' clinical PD-L1 expressions were determined as PD-L1 negative or PD-L1 positive. PD-L1 expression status was correlated with interaction state. Within the patients' assessed as PD-L1 negative, iFRET determined 58 patients that showed an interaction state, with 59 patients in the PD-L1-negative group showing no interaction state. Conversely, in those patients clinically stratified as PD-L1 positive, iFRET determined that 19 of 42 patients showed no interaction state. The IHC PD-L1 images of patients 390 and 131 with FRET efficiencies of 3.50% and 26.2%, respectively, are shown. **B)** Kaplan–Meier survival analyses comparing patients with the highest 20% of FRET efficiencies and those with the lowest 80% ($n = 176$). Those with a lower PD-1/PD-L1 interaction state (lower FRET efficiency) had an improved overall survival compared with those with a higher interaction state (log-rank Mantel–Cox, $P = 0.05$), underpinning the ability of iFRET to predict patient outcome. Clinical PD-L1 scores defined patients as being PD-L1 positive or PD-L1 negative. Kaplan–Meier analysis detected no significant difference in patient outcome when correlated with PD-L1 expression (log-rank Mantel–Cox, $P = 0.87$), exhibiting that PD-L1 expression levels fail to predict patient outcome.

3.4.4: Lower PD-1/PD-L1 Interaction States Correlation with Worsened Overall and Progression-Free Survival in Metastatic NSCLC

Next, in an outcome blinded study, we applied iFRET to samples from patients with metastatic NSCLC. A statistical power calculation indicated that, to obtain results with at least 80% significance, a sample number of >30 was required, hence we tested 60 FFPE samples, all from anti-PD-1 post-treatment patients. Of these 60 patients, 40 had clinical follow-up and outcome and were used to create Kaplan–Meier survival plots. The cohort comprised of 36 males and 24 females with an age range of 44–86 years (median age, 63 years; Table 3.2). Performance status was defined, and 50 patients had a performance status of ≤ 1 and 10 patients had a status of >1 (see Chapter 2).

Pathologist assessment highlighted regions of interest within each sample by identifying tumours and regions of immune cell infiltration for each sample. To analyse the whole region of interest within a patient sample, multiple subregions were analysed for PD-1/PD-L1 interaction state, resulting in a range of FRET efficiencies for each patient. Figure 3.9, upper panel, shows FLIM images demonstrating that as in other tumour settings (see above), PD-1 and PD-L1 expression levels do not correlate with interaction state. The pseudocolour scale (ranging from 1.0 ns to 2.7 ns) illustrates a donor lifetime decrease from 1.99 ± 0.17 ns to 1.44 ± 0.14 ns yielding a FRET efficiency of 27.64%. The lower panel of Figure 3.9 is a box and whisker plot, where each plot represents one patient. Each plot represents all the FRET efficiency values obtained for each patient, with the median value written above each plot. The highest median FRET efficiency value was 29.90% and the lowest being 0.00%. The box and whisker diagram demonstrates the ability of iFRET to quantify inter- and intra-patient heterogeneity of PD-1/PD-L1 interactions in metastatic NSCLC (Figure 3.9, lower panel).

The survival data of 40 patients were subsequently analysed and correlated to each patient's FRET efficiency, indicating their PD-1/PD-L1 interaction state. Patients were then ranked in order of their median FRET efficiency and split into the following two groups: those with the highest 40% of median FRET efficiencies and those with the lowest 60% of median FRET efficiencies. Kaplan-Meier survival analysis demonstrated that for these anti-PD-1-treated patients, those with the lowest 60% median FRET efficiency values, and therefore, a lower PD-1/PD-L1 interaction state, had a significant worsened overall survival ($P=0.05$; Figure 3.10, upper panel). When analysing PD-L1 expression (indicated by acceptor intensity), Kaplan-Meier analysis failed to determine a difference between those with a high PD-L1 expression and those with a low PD-L1 expression ($P=0.97$; Figure 3.10, lower panel). This again shows the shortcomings of using PD-L1 expression levels to determine patient outcome.

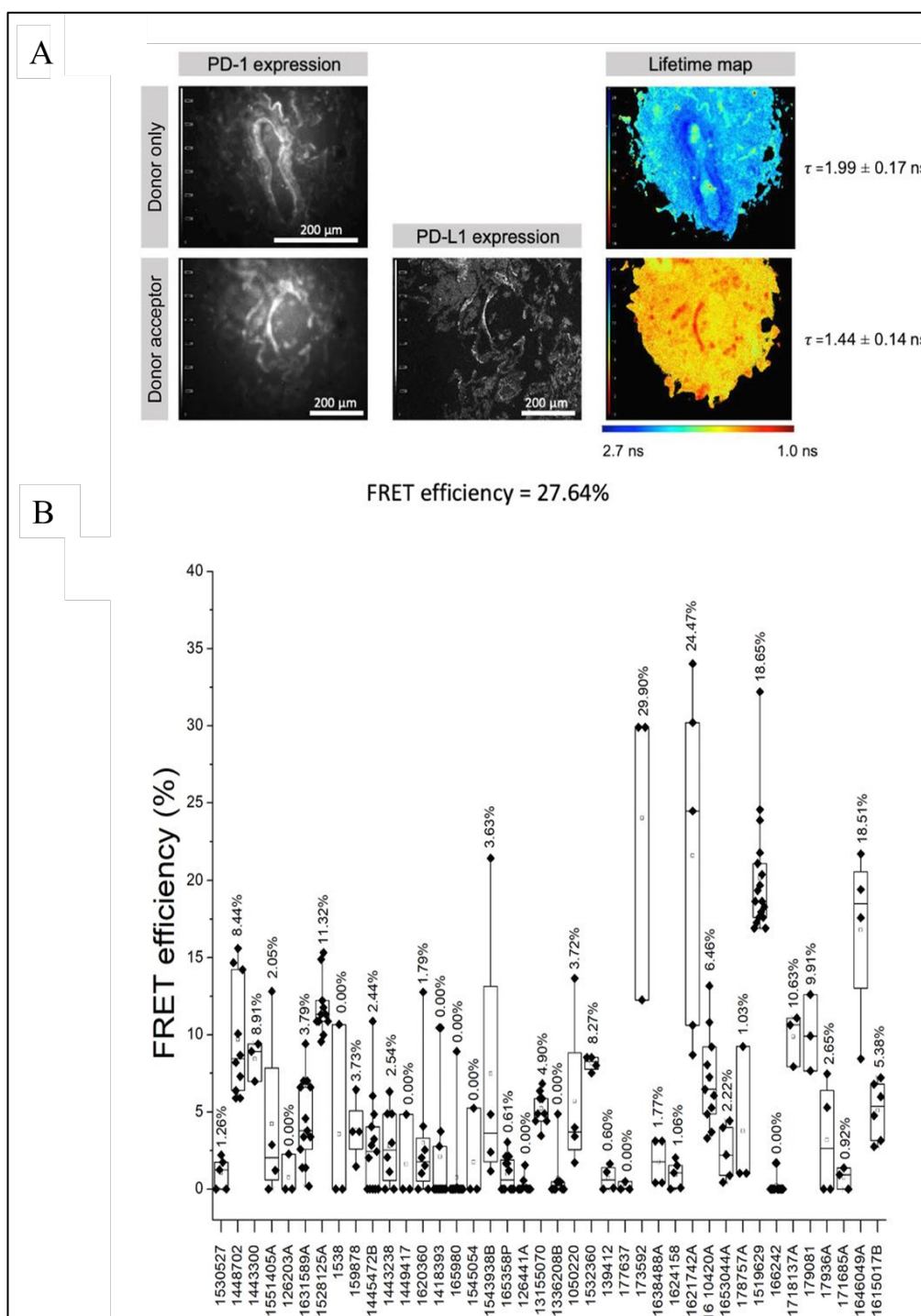


Figure 3.9: iFRET quantifies PD-1/PD-L1 interaction state in metastatic NSCLC alongside inter and intra patient heterogeneity. **A)** FLIM images show intensity and lifetime maps of a FFPE metastatic NSCLC sample. Intensity images show PD-1 and PD-L1 expressions, respectively. The pseudocolour scale illustrates a donor lifetime decrease from 1.99 ± 0.17 ns to 1.44 ± 0.14 ns, yielding a FRET efficiency of 27.64%. **B)** Box and whisker plots quantify the interaction states observed, with each plot representing the interaction states detected within each patient sample. Values above each plot represent the median FRET efficiency value for each patient sample. The highest median FRET efficiency value observed was 29.90% and the lowest 0.00%. iFRET not only quantifies interpatient heterogeneity but also intra-patient heterogeneity.

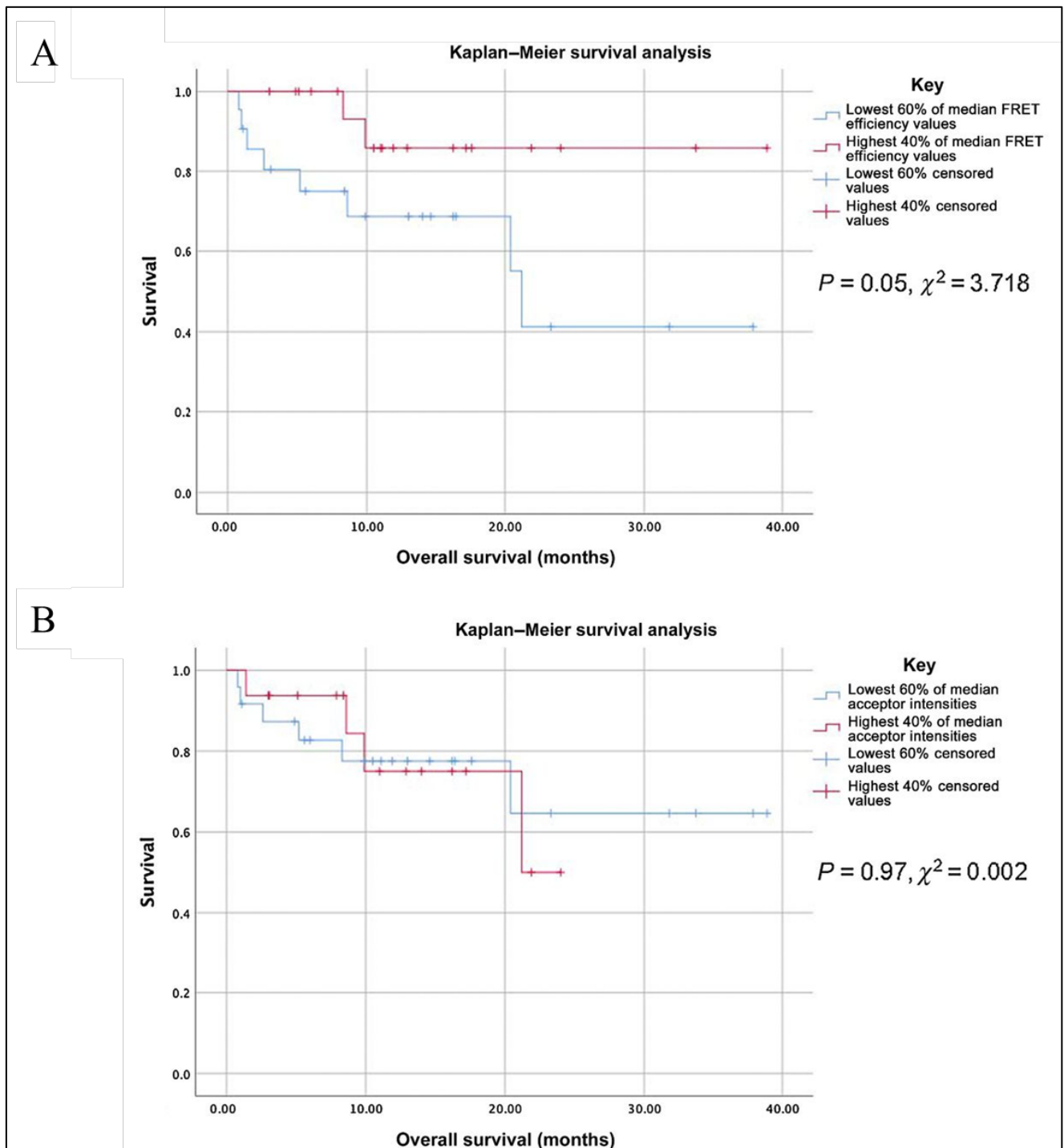


Figure 3.10: Lower PD-1/PD-L1 interaction correlates to a significantly worsened patient survival in metastatic NSCLC. **A)** Anti-PD-1 post-treatment patients were ranked by their mean FRET efficiency value and grouped into the following: the lowest 60% of median FRET efficiencies and the highest 40% of median FRET efficiencies. Those with the lowest 60% of median FRET efficiencies had a significantly ($P = 0.05$) worsened overall survival. **B)** Patients were ranked by their PD-L1 expression (acceptor intensity) and split into the lowest 60% of median acceptor intensities and the highest 40%. Kaplan–Meier survival analysis was unable to detect a difference between the two groups (log-rank Mantel–Cox, $P = 0.97$).

3.4.5: Discussion

This study has demonstrated the application of iFRET to detect intercellular receptor-ligand interactions. The method combines a two-site, time-resolved FRET assay and signal amplification, with a tissue preparation time identical to that of IHC approaches. The high throughput frequency domain FRET/FLIM imaging platform allowed mapping and automated acquisition of data from both cell cultures and arrayed tissue samples, thereby creating a straightforward procedure for non-specialised personnel (see Chapter 2). The automatic detection of regions of interest within the acquisition process significantly reduced operator bias. This assay measures receptor–ligand distances of 1–10 nm and determines interaction as any distance that falls within this range. Currently, alternative assays have utilised PD-1 and PD-L1 expression to determine receptor–ligand proximity. Tumeh and colleagues, 2014, have applied an assay that determines the presence of PD-1 and PD-L1 in close proximity to be an interaction (Tumeh et al., 2014). However, the working distances of intensity colocalisation assays are far greater (70 nm–20 mm) than that of iFRET. Moreover, when expression readouts were used in the pathologies assessed here, PD-L1 expression did not correlate with interaction state or patient outcome.

The iFRET methodology was exemplified for assessing the interaction status of two immune checkpoint pairs, PD-1/PD-L1 and CTLA-4/CD80, in single-cell assays and biopsy tissue samples from patients with ccRCC, primary malignant melanoma, and metastatic NSCLC. The initial validation of the method in single-cell coculture assays, where manipulation of receptor-ligand interactions can be specifically suppressed, has provided the confidence to assess these complexes in patient biopsies. The additional controls with respect to the use of secondary labelled reagents only, without the presence of primary antibodies, adds further control to this two-site assay.

Comparison of iFRET with PLA provided evidence that the latter did not perform as well in these settings in identifying interaction. By its very design, the iFRET methodology elaborated here provides both a measure of receptor-ligand interaction and the spatial resolution of this interaction. Importantly, this is readily achieved in routinely fixed samples from patient biopsies, offering great promise in being able to inform on the more detailed behaviour of these interactions and their distribution within pathologic settings. This is well illustrated here with the observed heterogeneity seen not simply between patient biopsies, but within individual biopsies reflected in the spread of FRET efficiencies across regions of interest for individual patients. This heterogeneity may reflect differential patterns of reprogramming of the tumour microenvironment playing out in modified immune suppressive ligand presentation and/or variability in the degree of immune cell infiltration.

A lack of correlation between the extent of PD-1/PD-L1 interaction state and the expression levels of these two proteins was evident in ccRCC, malignant melanoma, and metastatic NSCLC cohorts. In both

melanoma and NSCLC, it was shown that PD-L1 expression levels were unable to predict patient outcome. This questions current protocols that rely on IHC PD-L1 expression levels to predict patient outcome and, thus, have implications for the use of simple expression levels to stratify patients for treatment. Moreover, in patients with ccRCC, high interaction states were observed in patients who would otherwise be labelled as PD-L1 negative. Blockade of interaction would be predicted to be effective in contexts where elevated levels of interaction occur and is by inference responsible for the immune privileged state of the tumour. Hence, interaction would a priori be a criterion for treatment.

To examine the potential impact of this approach further, a unique cohort of patients with metastatic NSCLC was studied. The cohort of patients from which the FFPE samples were derived were all treated with anti-PD-1 monotherapies and had full clinical follow-up and outcomes. Within this cohort, iFRET has shown the potential for a high versus low PD-1/PD-L1 interaction state to be utilised as a predictive clinical biomarker posttreatment. Conceptually, it is surmised that a high degree of PD-1/PD-L1 interaction infers tumour selection in patients, indicating that the patient's tumour may be reliant on PD-1/PD-L1 interaction to facilitate immune evasion. It is precisely this group of patients that would be expected to respond to immune checkpoint inhibition.

As these were post-treatment samples from responsive patients with metastatic NSCLC, it was questioned why a high level of PD-1/PD-L1 interaction state might be observed. The pharmacodynamics of immune checkpoint disruption as a measure of target interaction have not been monitored to date. As such, it is not known whether blockade of checkpoint interaction needs to be either sustained or complete. The working hypothesis derived from this dataset is that interaction is likely incomplete and as such, a threshold level of T-lymphocyte complex disengagement is sufficient to trigger the observed responses to intervention. It will be informative in a suitable setting to monitor complex disengagement as a function of time following treatment.

Those patients with low interaction and therefore, worsened survival, may nevertheless benefit from alternative immune therapies. These tumours may evade the immune system by dysregulating CTLA-4/CD80 or other inhibitory interactions. Furthermore, no tumour will discretely dysregulate one pathway, in fact, a tumour may evolve to evade host immune response by modulating multiple pathways simultaneously, indicating a patient group who would benefit from dual checkpoint inhibitor therapies (Autio et al., 2020, Intlekofer and Thompson, 2013).

iFRET can be exploited to monitor other intercellular protein interactions and there are ongoing developments designed to capture related immune modulatory interactions pertinent to cancer and emerging cancer treatments. This provides the potential for iFRET to become a useful predictive tool informing on the nature of the tumour immune-privileged state. While single-region analysis has here provided insight into treatment responses, multiregional analysis may provide a more comprehensive

view. Furthermore, as a principle, it is clear that this approach has capabilities beyond immune–tumour cell interactions and the broader uptake of the approach promises to be informative in many research (e.g., axon guidance) and clinical (e.g., angiopathies) settings.

The exemplification of iFRET in tumour settings opens up exciting and powerful new opportunities to move beyond the cataloguing of cell phenotypes *in-situ* and add functional attributes to our patient data inventory, impacting clinical decisions. This is a routine parameter for small-molecule inhibitors targeted at driver mutations, and we suggest it should become a routine for these more complex biotherapeutic interventions.

Chapter 4: The Quantification of PD-1/PD-L1 and CTLA-4/CD80 Interactions in Radiofrequency-Ablated Lung Metastases: Determined by Time-Resolved immune-FRET

4.1: Preface

The results presented in Section 4.3.5 contain preliminary work carried out by Professor Franck Pagès, Hôpital Européen Georges-Pompidou (Hôpitaux Universitaires Paris-Ouest). Subsequent tissue sections from the biopsies of iFRET (immune-Förster resonance energy transfer) analysed patients were sent to Professor Pagès to stain and analyse for CD3 (T-lymphocyte) and CD8 (cytotoxic T-lymphocyte) infiltration. In Section 4.3.5, these immune infiltration results were correlated with immune checkpoint interaction.

4.2: Introduction

Cancer remains the second largest cause of death in the USA, behind cardiovascular disease. However, metastasis remains the highest cause of cancer deaths (Fares et al., 2020). As an example, one-third of renal-cell carcinoma (RCC) patients will present with metastases at the time of diagnosis, with 60% of total RCC patients eventually developing metastases (Lam et al., 2005). The American Cancer Society lists the lungs as frequent locations of metastases from breast, colon, rectal, head and neck, kidney, testicular and uterine cancers as well as lymphomas. Moreover, lung parenchyma is the second most frequent site of metastases after the liver (Zhu et al., 2008, Hess et al., 2011). Treatments for lung metastases include chemotherapy, radiotherapy and immunotherapies, however surgery is the most effective treatment for patients with isolated pulmonary metastases (Hoffmann et al., 2004). Surgery is often only used if a small number of metastases are present and metastases are confined to the lung (Rama et al., 2009). Therefore, patients with a high number of bilateral tumours, or more advanced metastatic diseases are confined to systemic treatments which can experience drawbacks such as primary or acquired resistance, non-specificity and adverse effects. An advancement of specific therapies to directly target lung cancer metastases will thus increase cancer survival rates by better targeting the leading cause of cancer deaths.

Whilst surgery is an effective treatment of lung metastases, it is an invasive procedure, with inherent associated risks. Two-thirds of patients who are technically eligible for resection make poor surgical candidates due to the presence of comorbidities (Zhu et al., 2008). Furthermore, pulmonary resection results in the removal of otherwise healthy functioning lung tissue alongside any neoplasia. For the treatment of unresectable primary and metastatic lung cancer, the use of radiofrequency ablation (RFA) as a minimally invasive technique has increased and was first performed in lung in humans in 2000 (de

Baère et al., 2015). Compared to surgery, RFA has the advantage of sparing healthy lung tissue and consequently has minimal impact on lung function. Moreover, RFA leads to reduced morbidity, mortality and hospitalisation costs compared to open surgery (Zhu et al., 2008). The RFA procedure requires the patient to be laid in the prone or supine position to allow the clinician to obtain the shortest path to the tumour (de Baere et al., 2006). A multi-tined expandable electrode is introduced through the skin and into the tumour site, guided by computer tomography (CT). The multi-tined electrode is expanded, surrounding the tumour, and obtaining at least a 5mm margin around the tumour (Figure 4.1). A high-frequency (450-550KHz) radiofrequency current is delivered through the electrode and incrementally increased until a major increase in impedance occurs (de Baere et al., 2006). The application of a high-frequency current to the tumour results in localised cellular ionic agitation which results in coagulative necrosis (Zhu et al., 2008). Compared to other tissue types, the lung favours RFA-treatment, with suitable heat-insulation and low electric conductivity allowing for a large ablation per unit of energy applied (de Baère et al., 2015). The procedure results in improved patient outcomes and has success rates comparable to resection without the reduction of lung function (Palussiere et al., 2011). However, in very rare instances, it has been documented that the treatment of one or more tumours by RFA has resulted in a reduction of tumour size in untreated tumours. This phenomenon is known as an abscopal effect. Two case studies have been reported by Rao et al., 2011 depicting this. In the first case study, an RCC patient developed bilateral lung metastases. After conventional treatment failed to control the metastatic disease, two RFA procedures were scheduled, the first on the right lung, and the second on the left lung, four weeks later (Rao et al., 2011). The largest nodule (26mm) in the right lung was targeted by RFA, although subsequent nodules in the right lung were not treated due to the development of a large pneumothorax. The remaining nodules in the right lung were scheduled to be treated four weeks later. When the patient returned for this treatment, a reduction of ground glass opacity was observed around the largest nodule (which had been treated). Surprisingly, the regression of another nodule was observed, which had reduced from 11mm to 9mm. Two other nodules had reduced from 11mm to 10mm and 17mm to 9mm, respectively. One tumour had completely disappeared within the four-week window between treatments (Rao et al., 2011).

The abscopal effect, derived from “*ab*,” away from, and “*scopus*” target, involves a massive antigen release from ablated tumours which polarises an immune response against remaining untreated tumours. This was first observed in 1928 when a nephrectomy procedure resulted in the complete regression of pulmonary metastases (Bumpus, 1928). These antigens, known as Tumour Associated Antigens (TAAs), are taken up by antigen presenting cells such as dendritic cells, and are then presented to CD4⁺ and CD8⁺ effector T-lymphocytes which can polarise an attack against the tumour (Ngwa et al., 2018, Widenmeyer et al., 2011). Heat Shock Proteins (HSPs) have been shown to be a major class of tumour debris that is released upon thermal ablation of tumours. A study by Schueller et al., 2004 identified

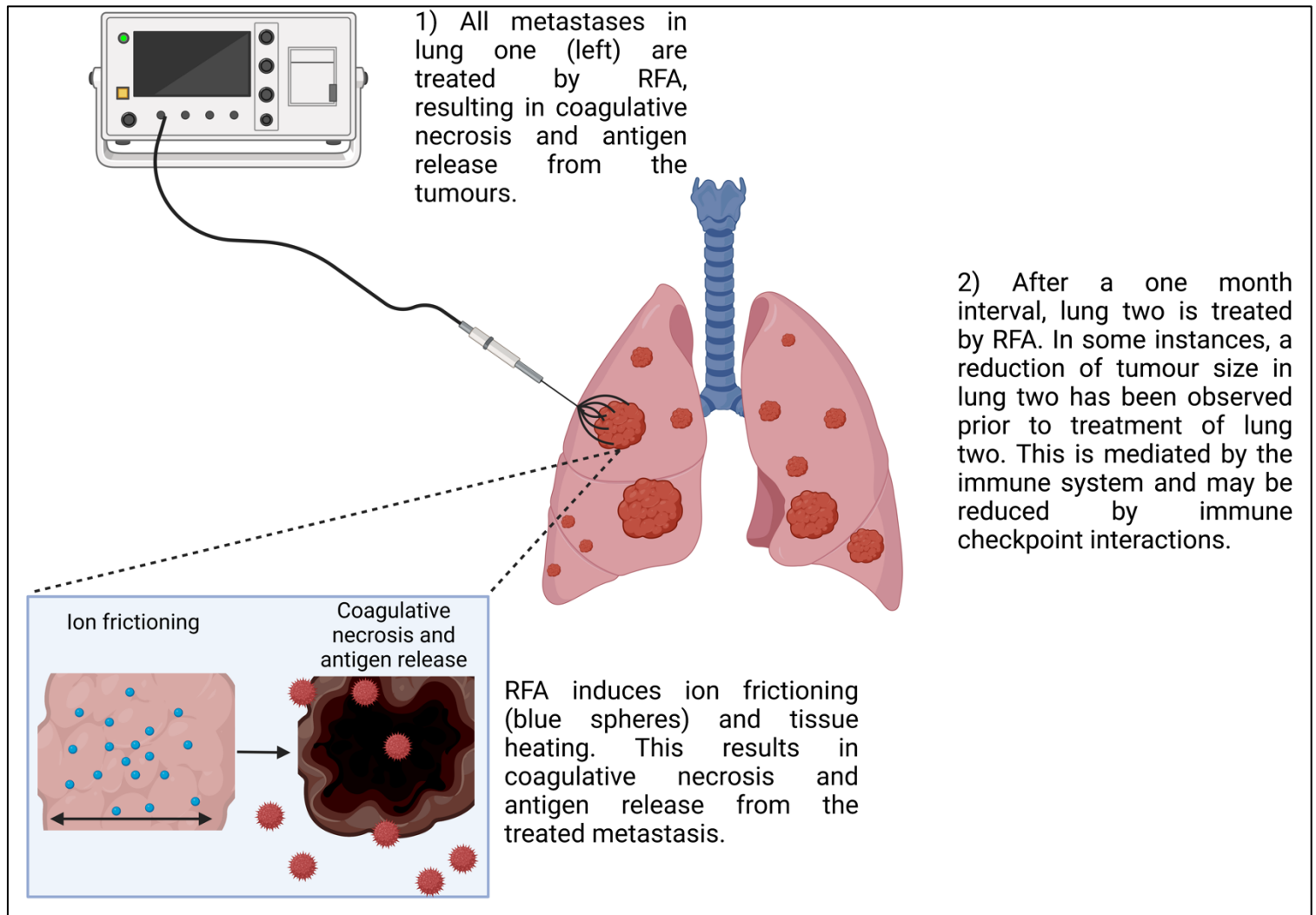


Figure 4.1: Overview of radiofrequency ablation of lung metastases. Radiofrequency ablation (RFA) is able to provide localised treatment to patients with bilateral lung metastases. Firstly (1) all lung metastases in lung number one are treated. The treatment consists of applying a high frequency radiofrequency current to the tumour via a multi-tined electrode. This results in ion fractioning, tissue heating and subsequently coagulative necrosis. This also results in a release of antigen from the tumour. After an interval of one month, the tumours on lung two are treated in the same manner. In rare instances, a reduction in the tumours of lung two has been observed after the treatment of lung one. This is known as an abscopal effect and is thought to be, in part, mediated by the adaptive immune system.

significant increases in HSP70 and HSP90 (HSPs with molecular weights of 70kDa and 90kDa respectively) after ablation of a patient with hepatocellular carcinoma. Immunohistochemistry (IHC) staining revealed RFA induced an increase of HSP70 expression in the cytoplasm and cell surface from 10% to 80%. HSP90 levels increased from 60% pre-ablation to 80% post-ablation (Schueller et al., 2004). Whilst it is known that a large volume of tumour debris is released upon RFA treatment, less is known about changes in immune-cell infiltrates around the metastases to be treated.

Löffler et al., 2019 showed that in a group of patients who received RFA treatment for liver metastases, no drastic change in immune cell infiltrate was detected in distant metastasis (Löffler et al., 2019). However, this may be dependent on the natural immune environment of a tumour microenvironment. Lung metastases are shown to have higher immunophenotype score than brain, bone, or liver metastases. Moreover, lung metastases have higher scores for antigen presentation and effector cells, alongside lower scores for suppressor cells (García-Mulero et al., 2020). This contrasts with liver metastases which exist in a less immunogenic environment. Crucially, the study also highlighted that lung metastases have a higher infiltration of myeloid dendritic cells, which could prove key in antigen presentation of ablated materials to the immune system.

A study by den Brok et al., 2006, identified the prominence of dendritic cells as antigen presenting cells in the abscopal effect mechanism. Firstly, the authors sought to confirm the presence of an abscopal effect in mouse models. B16-OVA tumour-bearing mice exhibited low level protection and a delay in tumour outgrowth when re-challenged with B16-OVA cells after RFA treatment of the initial tumour. This was not exhibited in naïve mice, nor when B16-OVA mice were re-challenged with an unrelated cell line (EL4 thymoma cells) (den Brok et al., 2006). The mechanisms of the abscopal effect are not fully understood or consistently observed between patients and are often weak and partial. A study by Widenmeyer et al., 2011 indicated that out of 49 RFA-treated patients, only 4 had antibody or TAA-reactive CD8⁺ T-lymphocytes, highlighting the weak effect of RFA on the adaptive immune system. Literature suggests that treatment of tumours with RFA combined with immune checkpoint blockade could enhance abscopal effects. Critically, in the study carried out by de Brok et al., 2006, the authors observed that the blockade of the immune checkpoint receptor, cytotoxic T-lymphocyte-associated protein 4 (CTLA-4), in conjunction with RFA treatment enhanced the survival of B16-OVA mice when re-challenged with B16-OVA cells compared to mice given an IgG control. CTLA-4 blockade had no effect on primary tumours or re-challenges when administered alone. Additionally, analysis of T-lymphocytes of these mice treated with both RFA and anti-CTLA-4 revealed increased T-lymphocyte activation as measured by IFN γ (interferon gamma) production (den Brok et al., 2006).

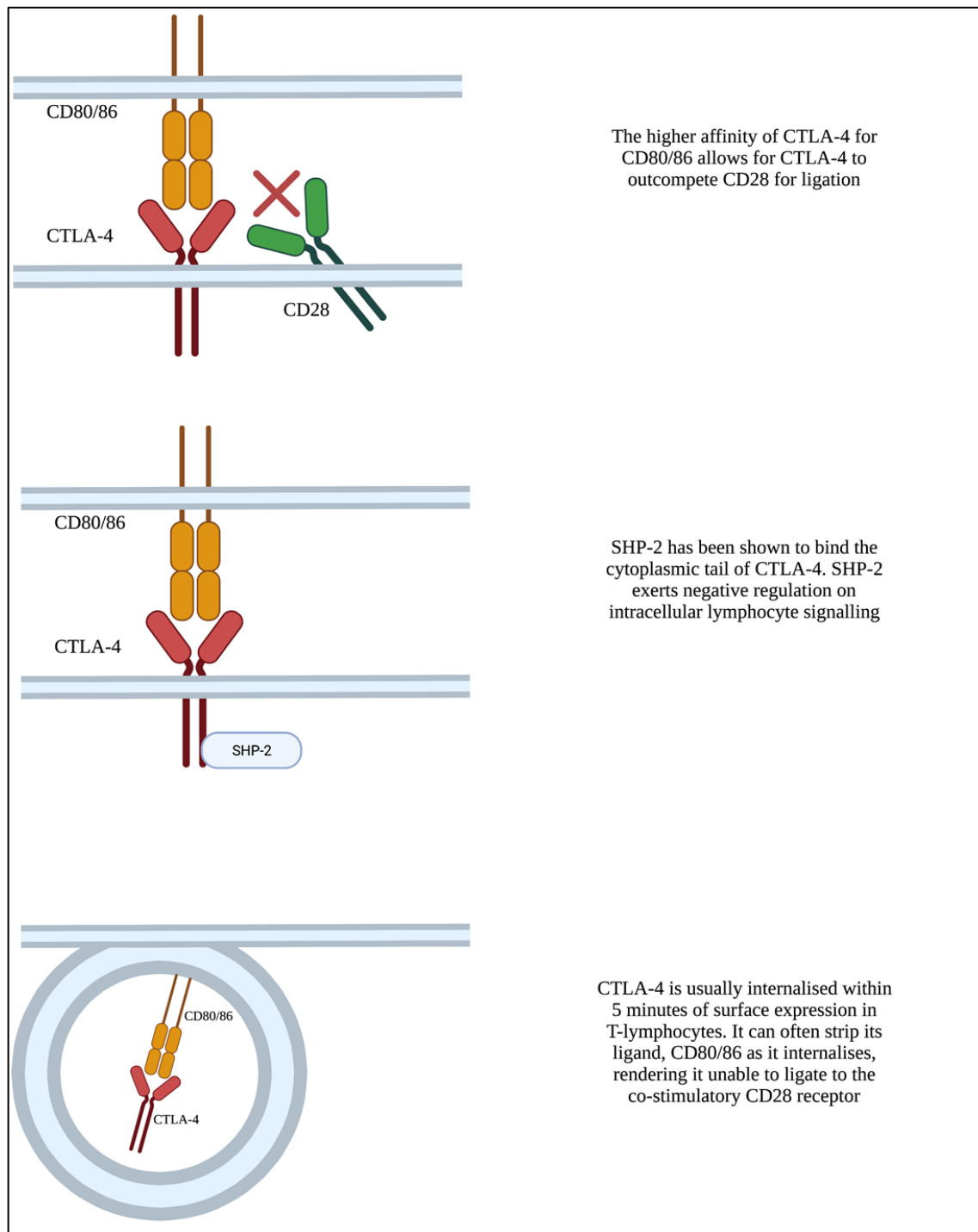


Figure 4.2: The three mechanisms by which CTLA-4 exerts its immunosuppressive functions. **Top panel:** CTLA-4 has a higher affinity for the ligand CD80/86 than the co-stimulatory CD28 receptor. Therefore CTLA-4 can outcompete CD28 and result in a negative immune response. **Middle panel:** Studies have shown that the cytoplasmic tail of CTLA-4 recruits the phosphatase SHP-2, which dephosphorylates kinases proximal to the TCR, thus reducing T-lymphocyte activation (Marengère et al., 1996). **Bottom panel:** CTLA-4 is usually internalised within 5 minutes of T-lymphocyte surface expression. It can strip the ligand CD80/86 upon internalisation from the antigen presenting cell, meaning it cannot ligate to the co-stimulatory CD28 receptor (Qureshi et al., 2011)

The CTLA-4 pathway provides host protection against autoimmune diseases by downregulating adaptive immune system activation. CTLA-4 (structure detailed in Chapter 1, Section 1.4.1) is a homolog of the co-stimulatory molecule cluster of differentiation 28 (CD28). CTLA-4 and CD28 share the same ligands CD80 and CD86 (also known as B7.1 and B7.2, detailed in Section 1.3), however CTLA-4 has an increased binding affinity compared to CD28 (Buchbinder and Desai, 2016, Parry et al., 2005). The mechanisms by which CTLA-4 exerts an immunosuppressive effect on T-lymphocytes is detailed in Section 1.4.1 and outlined diagrammatically in Figure 4.2.

The aims of this chapter were to track the changes in CTLA-4/CD80 and PD-1/PD-L1 (programmed death receptor 1/programmed death ligand 1) interaction states between RFA treatments administered to patients. The rationale to probe CTLA-4/CD80 interactions (as opposed to CTLA-4/CD86) are two-fold. From a technical perspective, a wider range of species-specific (anti-rabbit) monoclonal antibodies were available for CD80 compared to CD86. This resulted in CTLA-4/CD80 interactions being validated in cells first (Chapter 3) as opposed to CTLA-4/CD86. From a biochemical perspective, literature suggests that the increased bias of CD80 towards CTLA-4 impairs its function as a ligand for CD28 (Halliday et al., 2020). We therefore inferred that CTLA-4/CD80 interactions were an appropriate starting point with a view to probe CTLA-4/CD86 interactions in the future (discussed in Chapter 6).

The iFRET (immune-Förster resonance energy transfer) assay was utilised and is described in detail in Chapter 2 and outlined schematically in Figure 4.3. As discussed above, an abscopal effect may be seen when treating patients with RFA. However, in currently treated patient cohorts, instances of this phenomenon when treating lung metastases are rare. The first procedure performed on a patient used RFA to ablate all the metastases in the first lung. The patient was sent home to recover for one month before returning to have the RFA procedure carried out on the contralateral lung. In previous RFA studies carried out at Gustave Roussy hospital, Paris, France, in some patients a partial decrease of tumour size was observed in lung two, after the treatment of lung one as described in the case notes by Rao et al., 2011. This indicated that a weak abscopal effect may be taking place in these patients and gave rationale to study the role and evolution of immune checkpoint interactions in RFA-treated patients. However, it must be reiterated that this phenomenon is rare.

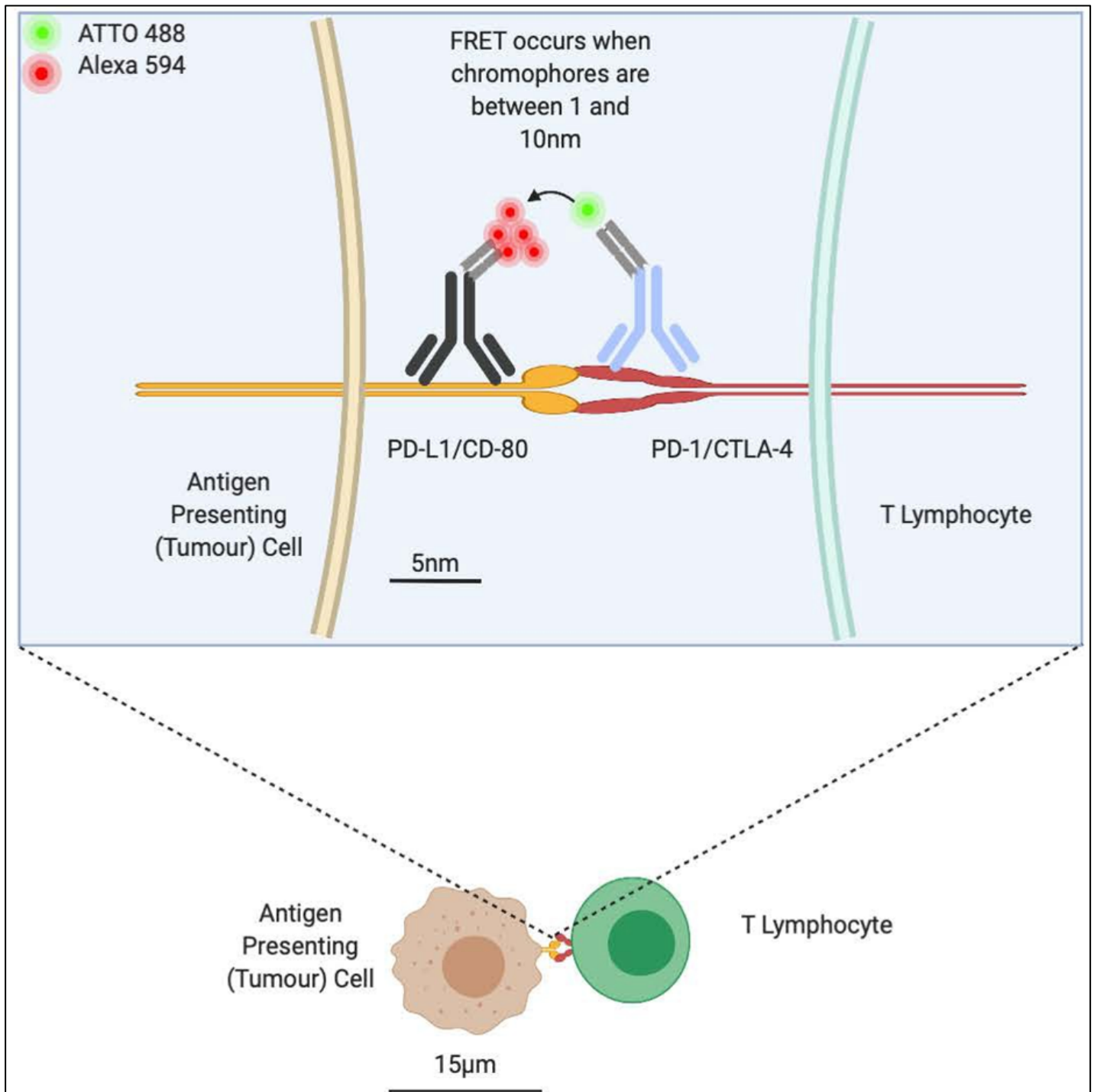


Figure 4.3: iFRET labelling schematic. iFRET utilises a two-site assay which determines the interactive states of the immune checkpoint ligands and receptors. Both the receptor and ligand are labelled with a primary antibody (anti-mouse and anti-rabbit respectively). The anti-mouse primary antibody (detecting CTLA-4 or PD-1) is then labelled with a F(ab')₂ fragment conjugated to ATTO488, the donor chromophore. The anti-rabbit antibody (detecting CD80 or PD-L1) is then labelled with a F(ab')₂ fragment conjugated to horseradish peroxidase (HRP). Using tyramide signal amplification, the HRP labels the sample with Alexa594 which acts as the acceptor chromophore. FRET can only occur at distances of 1-10nm; the use of secondary F(ab')₂ fragments allows the critical FRET distance of 10nm to be maintained. In the schematic shown here, the ligand and receptor are interacting.

4.3: Results

The aforementioned aims of this chapter were to elucidate the evolution in immune checkpoint interactions (CTLA-4/CD80 and PD-1/PD-L1) before RFA-treatment and after RFA-treatment in lung one. The ethical committee and study design, therefore, approved the sectioning of four consecutive tissue slices of a tumour on lung one, prior to RFA treatment. Next, four consecutive sections were taken from a tumour in lung two, after the treatment of lung one, and before the treatment of lung two. Sixteen patients were included in this study. Thirteen of these patients had a biopsy pre- and post-RFA treatment of lung one. The remaining three patients only had a biopsy taken pre-RFA treatment of lung one. This resulted in a total of twenty-nine tissue samples being analysed for both CTLA-4/CD80 and PD-1/PD-L1 analysis. In all results discussed below, RF1 indicates the biopsy pre-RFA treatment of lung one, and RF2 indicates the biopsy of the second lung post-RFA treatment of lung one.

The foundation for this set up was to observe whether a change in interaction state between RFA treatments could identify an evolution of immune-tumour interactions. We also sought to identify whether this could also distinguish patients who would benefit from immune checkpoint inhibition to boost their abscopal effect. However, a shortcoming of this study design was that the observed differences may arise purely from intertumoral heterogeneity, which is that the tumour microenvironment may differ from the tumours in contralateral lungs. Moreover, it was confirmed by Dr Jean Palussière that no abscopal effect was observed in this patient cohort.

Therefore, the aims of the chapter were modified to correlate PD-1/PD-L1 and CTLA-4/CD80 interactions with T-lymphocyte infiltration and to identify patients who may benefit from immune checkpoint inhibition alongside RFA treatment. Despite a lack of clinical level abscopal effect, results were still categorised as pre- and post-RFA treatment for two reasons. Firstly, whilst a clinical abscopal effect was not witnessed, it cannot be ruled out that a change in immune infiltration and activation has taken place. Secondly, the issue of intratumoral heterogeneity may result in the masking of small checkpoint engagement changes if data of pre- and post-treated samples were mixed.

4.3.1: CTLA-4/CD80 antibody concentration optimisation in tissue microarray

The CTLA-4/CD80 labelling antibodies used (Table 2.1, Chapter 2) were validated with our iFRET assay in Chapter 3 (Figure 3.4). In this validation, the labelling antibodies were used to measure CTLA-4/CD80 interaction in a cell co-culture assay. However, these antibodies had not been validated for use in tissue samples. Prior to their use to quantify CTLA-4/CD80 interactions in RFA-treated lung tissue, the concentrations used in the cell assay was verified in tissue. A commercial tumour microarray (TMA) was purchased which contained duplicated cases of common lung cancer types. In total, the TMA contained 150 cores. Two slides were used, one donor-only and one donor-acceptor. The antibody dilutions used were the same as those used in the cell co-culture assay of Chapter 4 (1:100 for both antibodies).

Figure 4.4 highlights the range of FRET efficiencies observed when using the CTLA-4/CD80 antibody pair in these TMAs. Within a box and whisker plot, the box and whiskers represent the 25-75% and 1-99% range of the data, respectively. Each dot represents the average lifetime of all pixels analysed within a given tumour core. A range of FRET efficiencies were observed across the tumour types, which were classified as either non-small cell lung carcinoma (NSCLC) or small-cell lung carcinoma (SCLC). The median FRET efficiency values obtained were 30.62% and 29.19% for the NSCLC and SCLC, respectively. Table 4.1 demonstrates how FRET efficiency correlates with receptor-ligand distances. The highest FRET efficiency observed in the NSCLC and SCLC groups were 42.79% and 36.23% respectively. In both box and whisker plots, a population of high FRET efficiencies are detected; these are values in the upper quartile of the plot. The detection of this upper quartile of data points gave rise to the rationale of correlating the upper quartile of interaction states with immune cell infiltration in Section 5.3.5. No significant differences in CTLA-4/CD80 interaction states were observed between the two groups.

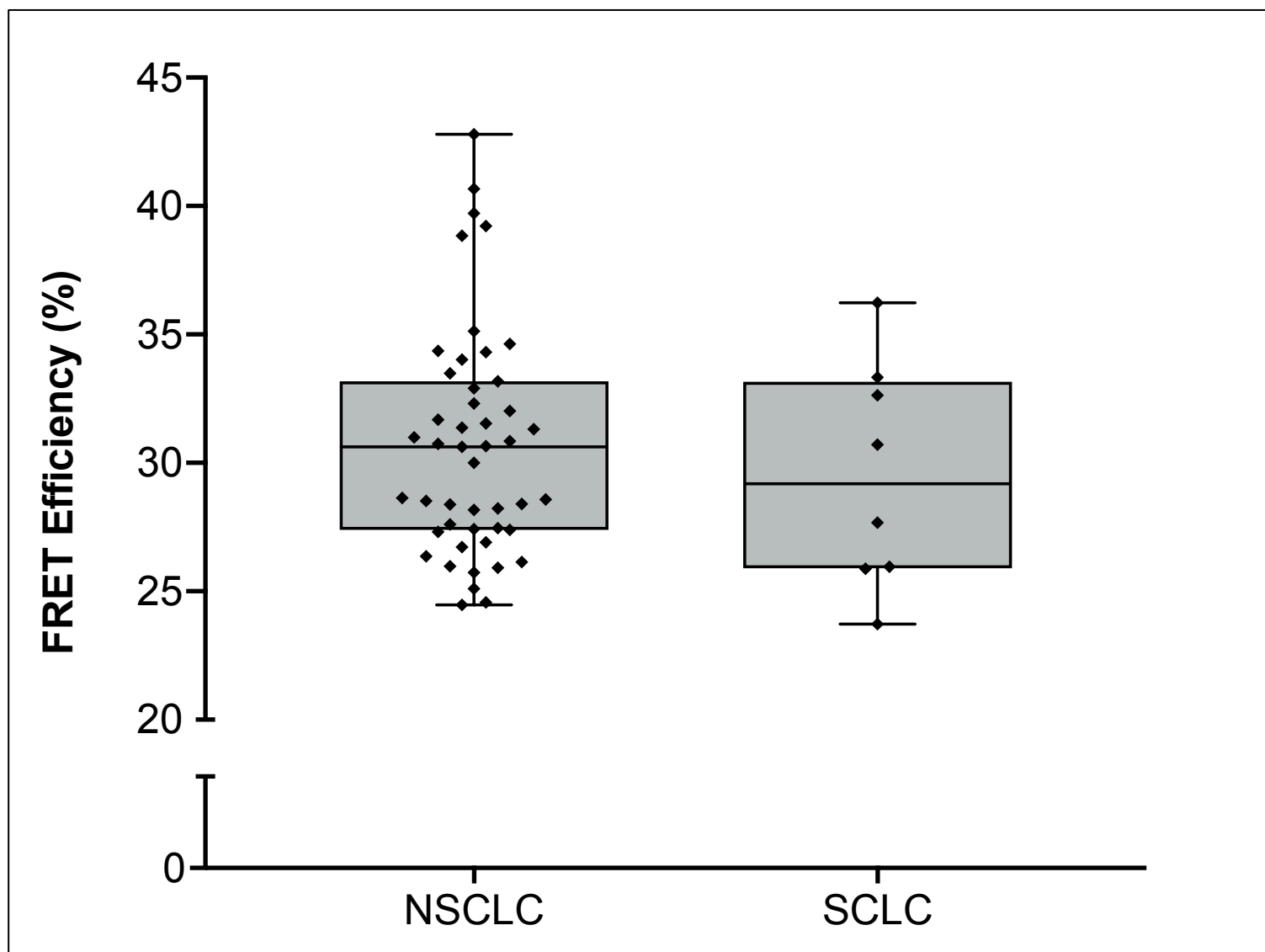


Figure 4.4: iFRET detects CTLA-4/CD80 interaction in FFPE sections for the first time. As the CTLA-4/CD80 antibody dilutions, utilised in the cell co-culture assay in Chapter 3, had not been validated in tissue before, a commercial TMA containing a mix of lung carcinoma samples was used to validate antibody dilutions. The antibody dilutions used were 1:100 for both antibodies. The box and whisker plot has categorised the carcinomas as non-small cell lung carcinoma or small-cell lung carcinoma. Elevated FRET efficiencies were observed across both groups, indicating a CTLA-4/CD80 binding in the analysed samples. The median FRET efficiencies observed were 30.62% and 29.19% for NSCLC and SCLC groups, respectively. A population of high interaction states are observed in the upper quartile of both groups, which may prove to be predictive values if correlated with patient outcome.

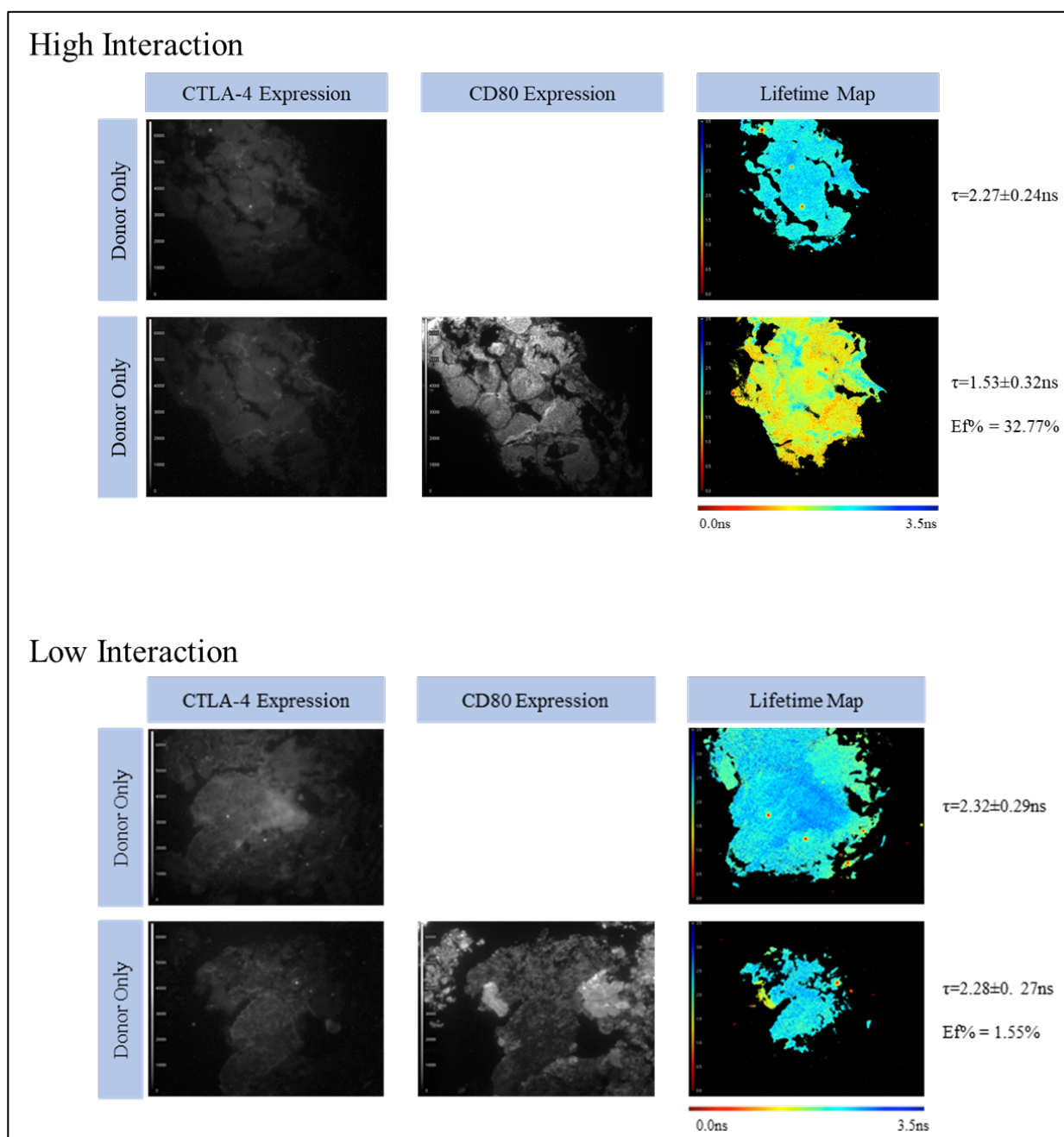


Figure 4.5: iFRET quantifies high and low CTLA-4/CD80 interaction states in lung metastases, detecting inter and intratumoral heterogeneity. Representative FLIM images demonstrating high and low CTLA-4/CD80 interaction states. **Top Panel:** Greyscale images indicate CTLA-4 or CD80 expression in donor-only or donor-acceptor tissue slices for one patient. No difference is observed between CTLA-4 expression between the donor-only and donor-acceptor slides. The lifetime map indicates the mean lifetime per pixel of an image. The donor-only lifetime ($2.27 \pm 0.24 \text{ ns}$) is represented by blue/green in the pseudocolour scale. In the donor-acceptor slide, the lifetime of the donor is reduced to $1.53 \pm 0.32 \text{ ns}$, yielding a FRET efficiency of 32.77%. This is indicative of a high CTLA-4/CD80 interaction state. **Bottom Panel:** Here, a good expression of CTLA-4 and CD80 is observed and no significant differences in expression profiles are seen between the top and bottom panels. The donor-only lifetime is $2.32 \pm 0.29 \text{ ns}$ which is not significantly reduced to $2.28 \pm 0.27 \text{ ns}$ in the presence of the acceptor, hence a low FRET efficiency of 1.55%. This indicates that CTLA-4/CD80 are undergoing little to no interaction in this sample, despite the presence of both receptor and ligand. In both examples, high tissue level coincidence is observed between the donor-only and donor-acceptor slices, meaning that donor lifetime changes are due to the presence of the acceptor chromophore and are not reporting on intratumoral heterogeneity.

Whilst our semi-automated fluorescence lifetime imaging microscopy (FLIM) platform acquired 150 cores per slide, only those with high coincidence between the donor and donor-acceptor, and an appropriate phase lifetime standard deviation, were analysed further and plotted in the box and whisker plot. The two-site coincidence nature of our assay requires a suitable spatial coincidence between the donor and donor-acceptor slide to correctly analyse the spatio-temporal change in donor lifetime in the presence of the acceptor. The signal observed, combined with the range of positive FRET efficiencies indicate that the chosen antibody dilutions, previously used in cells in Chapter 3, were suitable for use in tissue. Therefore, subsequent experiments using pre- and post-RFA treated lung biopsies were analysed with these antibody dilutions.

4.3.2: Quantification of CTLA-4/CD80 and PD-1/PD-L1 interactions in pre-RFA treatment lung metastases

As stated above, the manner in which biopsies of lung metastases were taken did not allow for the tracking of immune checkpoint interactions between RFA treatment cycles. However, as a cellular level abscopal effect may have occurred, albeit not at a clinical level, a decision was made to keep pre-RFA treatment, and post-RFA treatment data separated.

We first determined the interaction state of CTLA-4/CD80 in sixteen lung metastases from lung number one, before the RFA procedure was carried out. One sample (17 RF1) showed a consistently poor signal-to-noise ratio of less than four so was not further analysed for CTLA-4/CD80 interaction or CD80 expression.

Figure 4.5 shows representative FLIM images for patient 10 RF1. The top panel indicates a region of interest with a high CTLA-4/CD80 interaction state. The greyscale images represent CTLA-4 and CD80 expression and the lifetime maps indicate the average donor lifetime of each pixel. The pseudocolour scale runs from 0.00 ns (red) to 3.5 ns (blue). In this example, the lifetime of the donor alone is 2.27 ± 0.24 ns, which was reduced to 1.53 ± 0.32 ns in the presence of the acceptor. This yields a FRET efficiency of 32.77%. In the bottom panel, the donor-only lifetime was 2.32 ± 0.29 ns which was reduced to 2.28 ± 0.27 ns in the presence of the acceptor. This yields a FRET efficiency of 1.55% and indicates an insignificant interaction state (>10 nm). Critically, in both examples, good coincidence was seen between the donor-only and donor-acceptor slides. In both instances, no significant difference was observed in either CTLA-4 or CD80 expression, whereas the interaction state is significantly different in both cases.

All CTLA-4/CD80 interactions quantified from metastases in lung one, prior to RFA treatment, were plotted on a box and whisker plot (Figure 4.6, top panel). The highest interaction state observed was 32.77% in patient 10. The lowest median FRET efficiency, 0.00%, was observed in patients 06 and 09. The highest median interaction state of 22.01% was detected in patient 10.

PD-1/PD-L1 interaction was determined in the same sixteen lung metastases from lung one before the RFA procedure was performed. Figure 4.8 shows representative FLIM images for high and low FRET efficiencies within patient 01. The grayscale images represent PD-1 or PD-L1 expression and the lifetime map shows the donor lifetime, per pixel, of the sample with a pseudocolour scale. In the pseudocolour scale, blue represents a high lifetime (2.5 ns) and red represents a low lifetime (0.0 ns).

Table 4.1: FRET efficiency correlates with receptor-ligand distance.

FRET Efficiency (%)	Receptor-Ligand Distance (nm)
Highest FRET Efficiency: 39.05	6.28
Upper Quartile FRET Efficiency: 12.39	8.08
Median FRET Efficiency: 5.75	9.29
Lower Quartile FRET Efficiency: 0.00	>10nm
Lowest FRET Efficiency: 0.00	>10nm

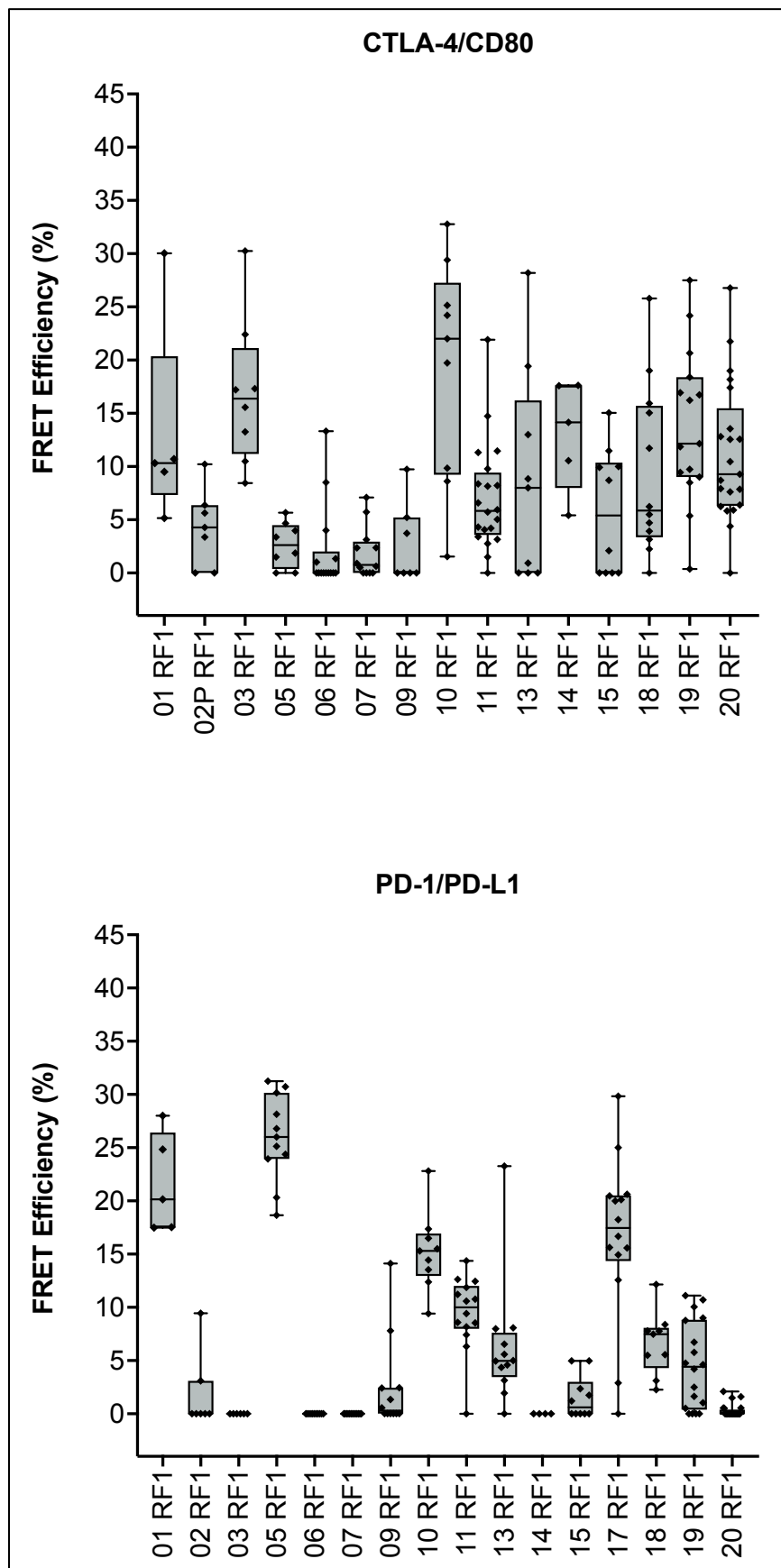


Figure 4.6: iFRET detects intra and intertumoral heterogeneity in both CTLA-4/CD80 and PD-1/PD-L1 interactions in metastases from lung one (pre-RFA). Box and whisker plots show the statistical distribution of all interaction states recorded for CTLA-4/CD80 (**top panel**) and PD-1/PD-L1 (**bottom panel**) in metastases taken from lung one, before RFA was carried out. Boxes represent the 25-75% of the data range and whiskers the 1-99%. Each point represents one region of interest for an analysed patient sample. Note, no data was analysed for CTLA-4/CD80 interactions in patient 17 due to a poor signal-to-noise ratio. Interaction states are generally higher in CTLA-4/CD80 than PD-1/PD-L1 with two patients having no PD-1/PD-L1 interaction across the sample. Some patients have differential interaction profiles for the two pathways. Patient 5 has a low CTLA-4/CD80 interaction and high PD-1/PD-L1 interaction. A contrasting trend is seen in patient 20 who has a significantly higher CTLA-4/CD80 interaction state than PD-1/PD-L1. Some patients, such as patient 13 showed no significant differences between CTLA-4/CD80 and PD-1/PD-L1 interaction states.

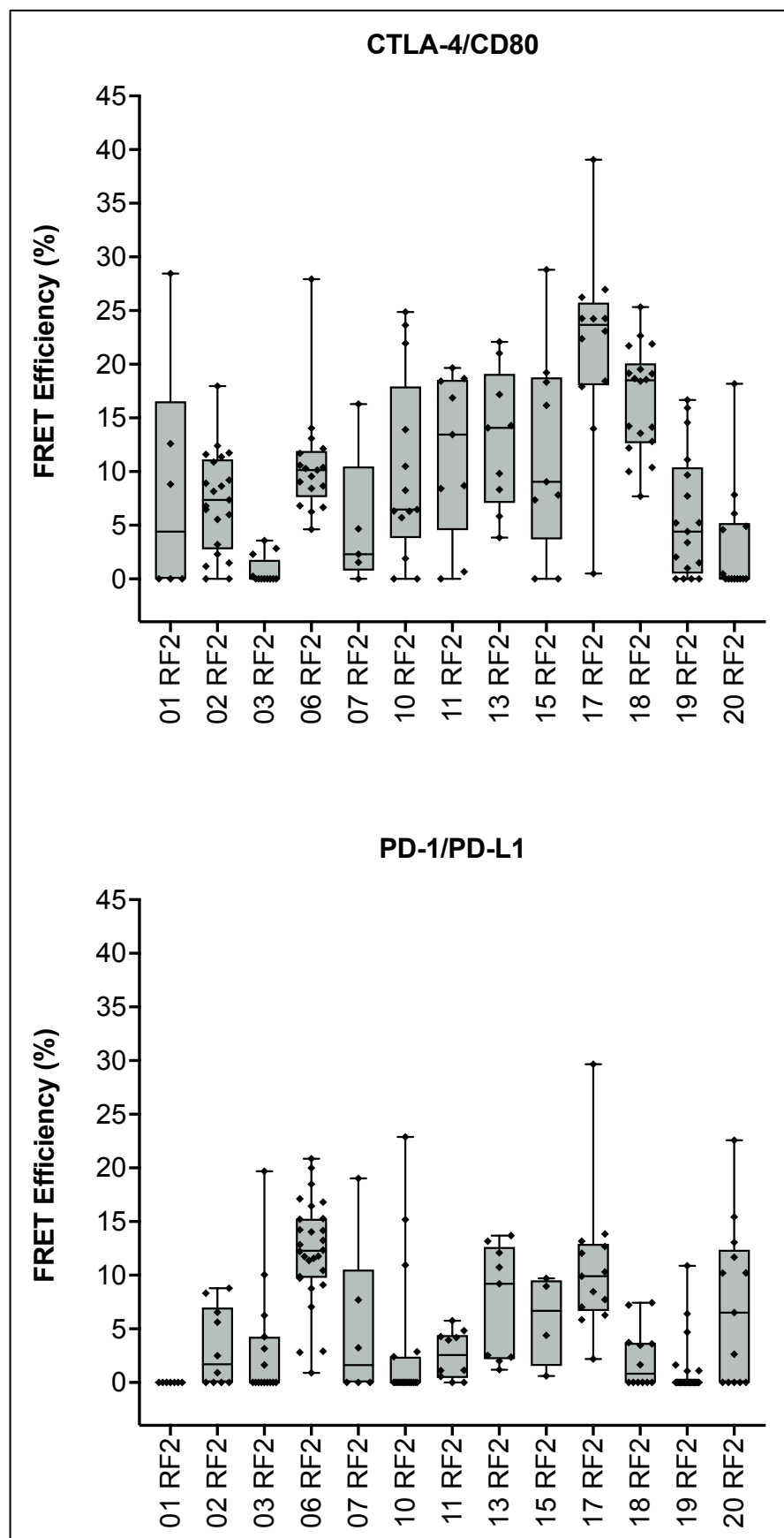


Figure 4.7: iFRET detects intra and intertumoral heterogeneity in both CTLA-4/CD80 and PD-1/PD-L1 interactions in metastases from lung two (post-RFA). Box and whisker plots show the statistical distribution of all interaction states recorded for CTLA-4/CD80 (**top panel**) and PD-1/PD-L1(**bottom panel**) in metastases taken from lung two, after RFA was carried out in lung one. Boxes represent the 25-75% of the data range and whiskers the 1-99%. Each point represents one region of interest for an analysed patient sample. Interaction states are generally higher in CTLA-4/CD80 than PD-1/PD-L1. Some patients have differential interaction profiles for the two pathways. Patient 03 has low CTLA-4/CD80 interaction state and regions of high PD-1/PD-L1 interaction. A contrasting trend is seen in patient 01 who has a significantly higher CTLA-4/CD80 interaction state than PD-1/PD-L1. Some patients, such as patient 06 showed no significant differences between CTLA-4/CD80 and PD-1/PD-L1 interaction states.

In a pre-RFA treatment sample of patient 01, a good donor (PD-1) intensity was seen on both the donor and donor-acceptor slide, with a strong acceptor (PD-L1) expression also seen on the acceptor slide. The donor-only lifetime was 1.61 ± 0.26 ns which was reduced to 1.21 ± 0.31 ns in the presence of the acceptor. This resulted in a FRET efficiency of 24.84%. In a post-RFA treatment sample of patient 01, no PD-1/PD-L1 interaction was observed. Again, a strong PD-1 and PD-L1 expression profile was observed across the sample, however in this instance the donor-only lifetime (1.77 ± 0.19 ns) fails to decrease in the presence of the acceptor, yielding a FRET efficiency of 0.00% (Figure 4.8). Critically, in both FLIM images, tissue coincidence was seen between the donor and donor-acceptor slides. Thus, the resulting lifetime changes are due to changes of the donor lifetime due to the presence of the acceptor chromophore and not due to tissue environmental changes such as polarity and pH.

All PD-1/PD-L1 interaction states were plotted in a box and whisker plot (Figure 4.6, bottom panel). The highest FRET efficiency observed, 31.25%, was in patient 05. The highest median FRET efficiency observed, also in patient 05, was 26.00%. A large degree of intra- and intertumoral heterogeneity was observed across the samples. When comparing the CTLA-4/CD80 and PD-1/PD-L1 interactions, the CTLA-4/CD80 and PD-1/PD-L1 interactions are similar, although more patients have a net zero FRET efficiency in the PD1/PD-L1 group (Figure 4.6). When comparing patients, some changes between the two pathways were detected. Patient 05 has a lower CTLA-4/CD80 interaction state (median FRET efficiency 2.62%) than PD-1/PD-L1 interaction state (median FRET efficiency 26.00%). A contrasting trend is observed with patient 20, with CTLA-4/CD80 interactions being higher (median FRET efficiency 9.28%) than PD-1/PD-L1 interaction (median FRET efficiency 0.00%). Some patients, such as patient 13, showed no significant difference in checkpoint interaction state between CTLA-4/CD80 (median FRET efficiency 8.00%) and PD-1/PD-L1 (median FRET efficiency 4.98%).

4.3.3: Quantification of CTLA-4/CD80 and PD-1/PD-L1 interactions in post-RFA treatment lung metastases

Following the quantification of CTLA-4/CD80 and PD-1/PD-L1 interaction states in the metastases of lung one, pre-RFA treatment, we analysed the immune checkpoint interaction states in biopsies from lung two, post-RFA treatment of lung one. Of the sixteen patients analysed above, thirteen had biopsies taken from lung two, post-RFA treatment of lung one.

Figure 4.7 is a box and whisker plot analysing the CTLA-4/CD80 and PD-1/PD-L1 interaction states observed in the thirteen patients. Here, PD-1/PD-L1 interactions are lower than CTLA-4/CD80 interactions with one PD-1/PD-L1 patient having a net zero FRET efficiency. The highest CTLA-4/CD80 interaction state observed was 39.05% in patient 17. The highest PD-1/PD-L1 interaction observed, also in patient 17, was 29.66%. The highest median FRET efficiency observed in the CTLA-4/CD80 group was 23.66% in patient 17.

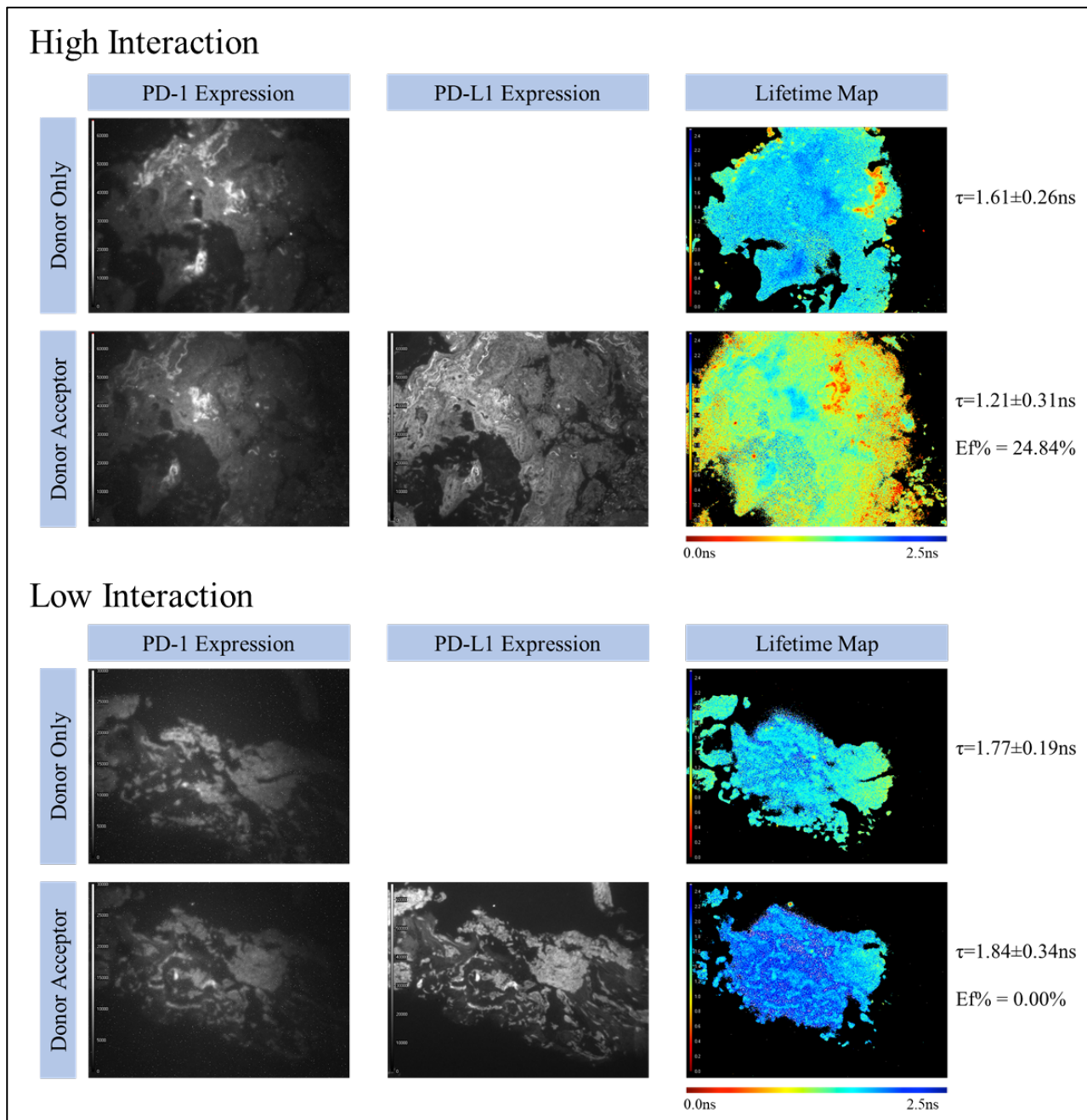


Figure 4.8: iFRET quantifies high and low PD-1/PD-L1 interaction states in lung metastases, detecting inter and intratumoral heterogeneity. Representative FLIM images demonstrating high and low PD-1/PD-L1 interaction states. **Top Panel:** Greyscale images indicate PD-1 or PD-L1 expression in donor-only or donor-acceptor tissue slices for one patient. No difference is observed between PD-1 expression and the donor-only and donor-acceptor slides. The lifetime map indicates the mean lifetime per pixel of an image. The donor-only lifetime ($1.61 \text{ ns} \pm 0.26 \text{ ns}$) is represented by blue/green in the pseudocolour scale. In the donor-acceptor slide, the lifetime of the donor is reduced to $1.21 \pm 0.31 \text{ ns}$, yielding a FRET efficiency of 24.84%. This is indicative of a high PD-1/PD-L1 interaction state. **Bottom Panel:** An elevated expression of PD-1 and PD-L1 is observed and no significant differences in expression profiles are seen between the top and bottom panels. However, the donor-only lifetime here is $1.77 \pm 0.19 \text{ ns}$ which fails to reduce in the presence of the acceptor, giving a FRET efficiency of 0.00%. This indicates that PD-1/PD-L1 are not interacting in this sample, despite the presence of both receptor and ligand. In both examples, high tissue level coincidence is observed between the donor-only and donor-acceptor slices, meaning that donor lifetime changes are due to the presence of the acceptor chromophore and are not reporting on intratumoral heterogeneity.

The highest median FRET efficiency observed in the PD-1/PD-L1 group was 12.28% (8.09nm) in patient 06. Direct patient comparisons revealed that patient 01 had a higher CTLA-4/CD80 interaction state (median FRET efficiency 4.41%) than PD-1/PD-L1 interaction state (median FRET efficiency 0.00%) (Figure 4.7). Patient 03 showed the opposite trend with a lower CTLA-4/CD80 interaction state (median FRET efficiency 0.00%) than PD-1/PD-L1 interaction state (median FRET efficiency 0.00%). Whilst the median values for patient 03 were both 0.00%, the box and whisker plots shows higher PD-1/PD-L1 interactions than CTLA-4/CD80 interactions. This again gave rise to the potential utility of using the upper quartile of interaction states as a correlative value in subsequent results. Patient 06 showed no significant difference between checkpoint interaction states with a similar CTLA-4/CD80 (median FRET efficiency 10.13%) and PD-1/PD-L1 (median FRET efficiency 12.23%) interaction states.

4.3.4: Immune Checkpoint Ligand Expression Does Not Correlate with Immune Checkpoint Engagement

Current attempts to utilise immune checkpoints as predictive biomarkers have relied on ligand expression as assessed by IHC. The results of Chapter 3 identified that PD-L1 expression is not predictive of patient outcome whereas PD-1/PD-L1 interaction state was predictive in malignant melanoma and NSCLC. Whilst no patient outcome was available for these patients (all are alive as this is a prospective study) we aimed to identify if there was a correlation between ligand expression and checkpoint interaction. The first correlations assessed checkpoint interaction versus ligand expression in biopsies from lung one, prior to the RFA-treatment of lung one.

The scatter plots shown in Figure 4.9A, correlated CTLA-4/CD80 interaction and CD80 expression. The x axis measures checkpoint interaction (FRET efficiency) and the y axis measures acceptor chromophore intensity (arbitrary units) as a surrogate of CD80 expression. An r_s value of 0.134, $P=0.632$, indicates no significant correlation between CD80 expression and CTLA-4/CD80 interaction state. Figure 4.9B shows the correlation between PD-1/PD-L1 interaction state, as measured by FRET efficiency, and PD-L1 expression, as measured by acceptor chromophore intensity. An r_s value of -0.211, $P=0.428$, again indicates a lack of correlation between PD-1/PD-L1 interaction state and PD-L1 expression.

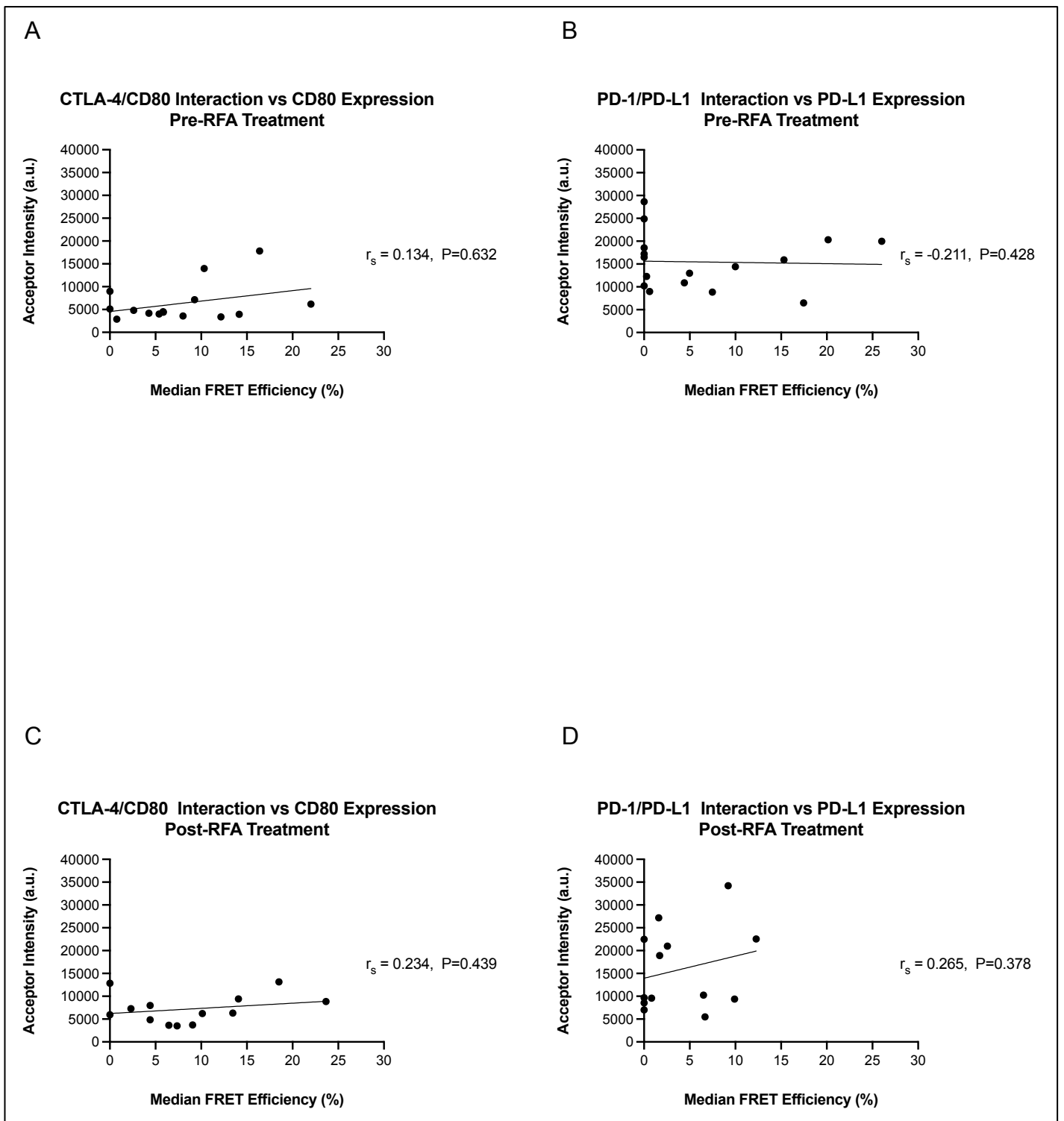


Figure 4.9: Checkpoint interaction does not correlate with ligand expression in RFA-treated metastases. **A)** Scatter plots sought to identify a correlation between CTLA-4/CD80 interaction and CD80 expression in biopsies taken from lung one, before RFA treatment. The x axis plots the median CTLA-4/CD80 FRET efficiency seen per patient and the y axis plots the median acceptor chromophore intensity observed per patient. Acceptor chromophore intensity is used as a surrogate for CD80 expression as it labels the CD80 ligand. An r_s value of 0.134, $P=0.632$ indicates no correlation between CTLA-4/CD80 interaction state and CD80 expression, indicating that CD80 expression would be a poor marker for CTLA-4/CD80 interaction. **B)** Scatter plots identifies a lack of correlation between PD-1/PD-L1 interaction and PD-L1 expression. The median PD-1/PD-L1 FRET efficiency per patient was again plotted against acceptor chromophore intensity, here reporting on PD-L1 expression. An r_s value of -0.211, $P=0.428$, indicates no correlation between PD-1/PD-L1 interaction state and PD-L1 expression. **C)** CTLA-4/CD80 interaction also failed to correlate with CD80 expression in post-RFA treated lung metastases, $r_s=0.234$, $P=0.439$. **D)** In post-RFA treated lung metastases, no correlation was observed between PD-1/PD-L1 interaction and PD-L1 expression, $r_s=0.265$, $P=0.378$. This confirms that ligand expression does not corroborate or predict checkpoint engagement.

Next, we correlated checkpoint interaction and ligand expression in biopsies from lung two, after the RFA-treatment of lung one had been performed. Figure 4.9C correlated CTLA-4/CD80 interaction state with CD80 expression. The correlation was $r_s=0.234$, $P=0.439$, indicating no correlation between CTLA-4/CD80 interaction and CD80 expression. The bottom panel of Figure 4.9D demonstrates that there is no correlation between PD-1/PD-L1 and PD-L1 expression ($r_s=0.265$, $P=0.378$) in the second lung, post-treatment of lung one. Together, the data from this section indicates, as was shown in Chapter 3, that ligand expression does not corroborate immune checkpoint interaction.

4.3.5: Correlation of immune checkpoint engagement with CD3⁺ and CD8⁺ T-lymphocyte infiltration

Whilst an abscopal effect was not observed clinically in this patient cohort, a change in immune-cell infiltration between RFA treatments cannot be ruled out. Therefore, we proceeded to correlate CTLA-4/CD80 and PD-1/PD-L1 interaction states with intratumoral CD3⁺ and CD8⁺ cell infiltration. The following n numbers were available for the immune-infiltration analyses presented below: CTLA-4/CD80 pre-RFA (n=14); PD-1/PD-L1 pre-RFA (n=15); CTLA-4/CD80 post-RFA (n=12); PD-1/PD-L1 post-RFA (n=12).

First, we correlated immune-cell infiltration with checkpoint engagement in biopsies from lung one, prior to its treatment. In the patients who had CD3⁺ data available for lung one, there was no correlation seen between CTLA-4/CD80 interaction and intratumoral CD3⁺ density (cells/mm²) as shown by an r_s value of 0.037, $P=0.900$ (Figure 4.10A). Figure 4.10B shows the correlation between PD-1/PD-L1 interaction state and intratumoral CD3⁺ density. A moderate negative correlation was observed ($r_s=-0.695$, $P=0.006$) between intratumoral CD3⁺ density and PD-1/PD-L1 interaction, indicating that higher interaction states may be observed in tumour regions with lower CD3⁺ infiltration. We then analysed biopsies from lung two, post-treatment of lung one. Here, intratumoral CD3⁺ density did not correlate with CTLA-4/CD80 interaction ($r_s=-0.112$, $P=0.633$) (Appendix 1.1A). PD-1/PD-L1 interaction state also did not correlate with intratumoral CD3⁺ density resulting in an r_s value of 0.155, $P=0.632$ (Appendix 1.1B).

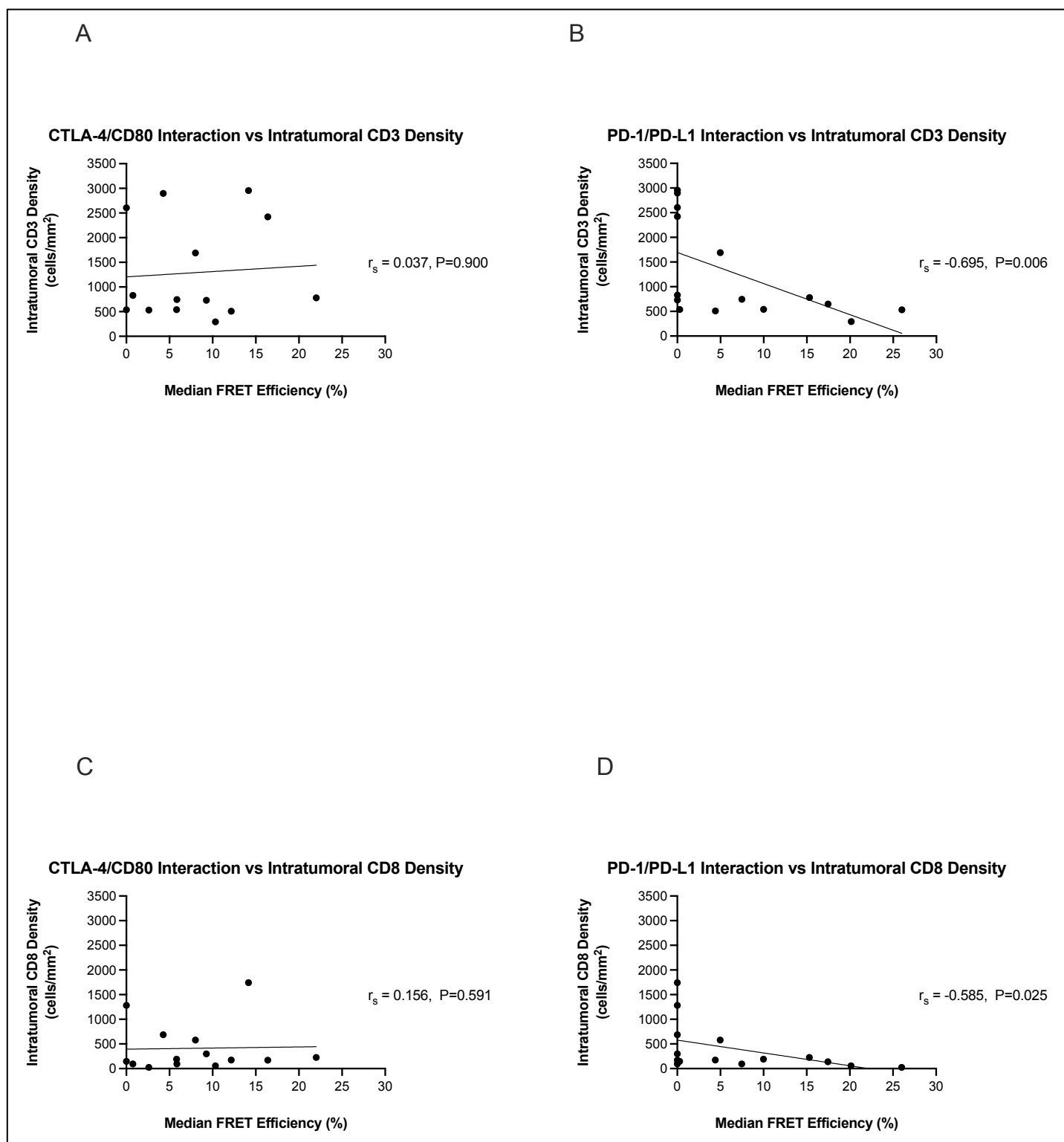


Figure 4.10: Median PD-1/PD-L1 interaction state negatively correlates with intratumoral CD3⁺ and CD8⁺ density in metastases from lung one (pre RFA). **A)** Scatter plots demonstrate a lack of correlation between intratumoral CD3⁺ density (cells/mm²) and median CTLA-4/CD80 interaction ($r_s = 0.037, P=0.900$) in metastases analysed from lung one (pre-RFA). **B)** A moderate negative correlation exists between intratumoral CD3⁺ density and median PD-1/PD-L1 interaction state ($r_s = -0.695, P=0.006$). This indicates, with significance, that higher median PD-1/PD-L1 interaction states are detected in areas with lower intratumoral CD3⁺ density. **C)** No correlation was observed between median CTLA-4/CD80 interaction state and intratumoral CD8⁺ density, $r_s=0.158, P=0.591$. **D)** Intratumoral CD8⁺ density moderately and negatively correlated with median PD-1/PD-L1 interaction state, $r_s=-0.585, P=0.025$. This indicates, with significance, that higher median PD-1/PD-L1 interaction states are detected in areas with lower intratumoral CD8⁺ density.

CD8⁺ infiltration was also measured in the patient biopsies, and we correlated this with intratumoral CD8⁺ density. Figure 4.10C, shows a scatter plot correlating intratumoral CD8⁺ density with CTLA-4/CD80 interaction states. The r_s value obtained was 0.156, $P=0.591$ indicating that there is no correlation between CTLA-4/CD80 interaction and intratumoral CD8⁺ density in biopsies of lung one, prior to RFA treatment. In PD-1/PD-L1 analysed samples, there was a moderate negative correlation between checkpoint interaction and intratumoral CD8⁺ density ($r_s=-0.595$, $P=0.025$) (Figure 4.10D). In biopsies from lung two, after RFA treatment of lung one, no correlations between intratumoral CD8⁺ density and checkpoint interaction were observed. The correlation of CTLA-4/CD80 and intratumoral CD8⁺ density resulting in an r_s value of -0.182, $P=0.573$, indicating no correlation is occurring (Appendix 1.1C). When PD-1/PD-L1 was correlated with intratumoral CD8⁺ density, an r_s value of -0.014, $P=0.973$ was obtained, again indicating no correlation (Appendix 1.1D). All median FRET efficiency correlations are listed in Table 4.2.

Table 4.2: Median interaction states vs intratumoral lymphocyte density.

Correlation	r_s	P
PD-1/PD-L1 RF1 vs intratumoral CD3 density	-0.695	0.006
PD-1/PD-L1 RF2 vs intratumoral CD3 density	0.155	0.632
CTLA-4/CD80 RF1 vs intratumoral CD3 density	0.037	0.900
CTLA-4/CD80 RF2 vs intratumoral CD3 density	-0.112	0.633
PD-1/PD-L1 RF1 vs intratumoral CD8 density	-0.585	0.025
PD-1/PD-L1 RF2 vs intratumoral CD8 density	-0.014	0.973
CTLA-4/CD80 RF1 vs intratumoral CD8 density	0.156	0.591
CTLA-4/CD80 RF2 vs intratumoral CD8 density	-0.182	0.537

As some patient samples had a median FRET efficiency of 0.00%, but still yielded positive interaction states, we postulated that these may correlate with immune cell infiltration and may report on “immune checkpoint hotspots” if the upper quartile of interaction states were used. The results for these correlations are summarised in Table 4.3 and the scatter plots presented in Appendix 1.2 and 1.3. In biopsies from the first lung, intratumoral CD3⁺ density moderately correlated with the upper quartile of PD-1/PD-L1 interaction states ($r_s=-0.714$, $P=0.004$) (Appendix 1.2B). This demonstrates with significance that higher PD-1/PD-L1 interaction states are observed in areas of lower CD3⁺ density. As with the use of median interaction states per patient, CTLA-4/CD80 failed to show correlation between upper quartile interaction state and intratumoral CD3⁺ density ($r_s=0.029$, $P=0.928$). In biopsies from

lung two, after treatment of lung one, no correlation was seen between intratumoral CD3⁺ density and upper quartile CTLA/CD80 or PD-1/PD-L1 interaction states ($r_s=-0.357$, $P=0.192$ and $r_s=0.210$, $P=0.509$ respectively) (Appendix 1.3A-B).

Table 4.3: Upper quartile interaction state vs intratumoral lymphocyte density.

Correlation	r_s	P
PD-1/PD-L1 RF1 vs intratumoral CD3 density	-0.714	0.004
PD-1/PD-L1RF2 vs intratumoral CD3 density	0.210	0.509
CTLA-4/CD80 RF1 vs intratumoral CD3 density	0.029	0.928
CTLA-4/CD80 RF2 vs intratumoral CD3 density	-0.357	0.192
PD-1/PD-L1 RF1 vs intratumoral CD8 density	-0.510	0.054
PD-1/PD-L1 RF2 vs intratumoral CD8 density	-0.046	0.891
CTLA-4/CD80 RF1 vs intratumoral CD8 density	-0.160	0.584
CTLA-4/CD80 RF2 vs intratumoral CD8 density	-0.497	0.104

Intratumoral CD8⁺ density also failed to correlate with upper quartile CTLA-4/CD80 interaction states ($r_s=-0.160$, $P=0.584$) in biopsies from lung one. The upper quartile of PD-1/PD-L1 interaction states moderately correlated with CD8⁺ density, however without statistical significance ($r_s=-0.510$, $P=0.054$) (Appendix 1.2C-D). A lack of correlation was seen in biopsies from lung two with upper quartile CTLA-4/CD80 ($r_s=-0.497$, $P=0.104$) and PD-1/PD-L1 ($r_s=0.046$, $P=0.891$) no correlating to intratumoral CD8⁺ density (Appendix 1.3C-D). All upper quartile correlation results are listed in Table 4.3 and scatter plots presented in Appendixes 1.2 and 1.3.

4.4: Discussion

The aims of this chapter were to elucidate the interaction states of PD-1/PD-L1 and CTLA-4/CD80 in needle biopsies taken from RFA-treated patients. The original aims of the chapter had been to analyse the role of immune checkpoint interaction states pre- and post-RFA treatment. However, the study design did not allow for the removal of intertumoral heterogeneity, a factor that may infer changes in checkpoint interaction status. Also, large intratumor heterogeneity is observed within metastases, highlighting the need for more advance sampling methods to help quantify intratumor heterogeneity (López and Cortés, 2017, Lopez, 2016). Therefore, the aims were modified to assess whether iFRET can detect PD-1/PDL1 and CTLA-4/CD80 interaction states in lung metastasis samples and whether this could be correlated to ligand expression or T-lymphocyte infiltration. The heterogeneity between tumours may present a problem as it has been shown that metastases from colorectal cancer (CRC) are non-uniformly infiltrated with immune lymphocytes (Mlecnik et al., 2018).

The work in this chapter has quantified PD-1/PD-L1 interaction state in lung metastases and directly quantified CTLA-4/CD80 engagement for the first time in any pathology. The novel result is the validation of an assay which can precisely quantify differences in immune checkpoint interaction states between patients. This will aid the correct stratification of patients and result in the precise prescription of immune checkpoint blocking drugs to a correctly stratified patient subset. The results presented in Figure 4.6 and Figure 4.8 highlight the ability of this assay to determine the differences between checkpoint engagements in a single patient. The differences observed between the two pathways could be a result of the biological roles of each checkpoint. The CTLA-4/CD80 checkpoint is more prominent in early immune responses. Contrastingly, PD-1/PD-L1 signalling is associated with later immune response and is linked to T-lymphocyte exhaustion due to chronic antigen exposure, a phenotype often seen in tumour infiltrating lymphocytes (Sansom and Walker, 2019). The increased prominence of PD-1/PD-L1 signalling in the tumour microenvironment could in part explain why no correlations were observed between lymphocyte infiltration and CTLA-4/CD80 checkpoint interaction. Regardless, we have showcased the ability of iFRET to identify which immunotherapies a patient would be likely to respond to (monotherapy vs dual therapy). However, whilst any one tumour may evade host immune response by engaging one immune checkpoint, this does not mean a tumour will fully succumb to a blockade of this checkpoint. The use of a monotherapy against either PD-1/PD-L1 or CTLA-4/CD80 may apply a positive selection pressure to a tumour, resulting in the outgrowth of clones which are able to modulate other immune checkpoints. Therefore, whilst iFRET may currently stratify patients that would respond to initial mono or dual therapies, a continual monitoring of tumour-immune cell interactions would be required to screen for an evolution of immune evasion. Additionally, the initial and simultaneous assessment of several immune checkpoints could yield important data which could further guide patient treatment regimens. Whilst within this cohort of patients, no abscopal effect was

seen, a lack of increase of tumour growth could still indicate that an abscopal effect is taking place.

As also discussed in chapter 4, iFRET is the only assay capable of measuring intercellular interactions in a spatiotemporal manner at distances of 1-10 nm. Competing technologies which claim to assess receptor-ligand interaction (chiefly PD-1/PD-L1 interaction) measure molecule colocalisation which has a working range in the order of micrometres (Giraldo et al., 2018). Furthermore, the correlations calculated above indicate that no statistically significant correlation between checkpoint interaction and ligand expression existed. This, as was seen in chapter 4, is a crucial finding as currently there are no predictive biomarkers for patient response to ipilimumab (Buchbinder and Desai, 2016). Moreover, previous work has indicated that in malignant melanoma and NSCLC, PD-L1 expression does not correlate to patient outcome, whereas PD-1/PD-L1 interaction state does (Sánchez-Magraner et al., 2020). To assess the ability of CTLA-4/CD80 interaction state to predict patient outcome, a large cohort retrospective study must be carried out which uses iFRET to quantify these receptor-ligand interactions. Furthermore, a new study design must be undertaken to address the original aims of this chapter. A study whereby a tumour is biopsied in lung two, prior to RFA-treatment of lung one, and is again biopsied post-RFA treatment of lung one, would allow for the elucidation of the roles of the two checkpoints in abscopal effects.

Whilst ligand expression does not yield useful information on CTLA-4/CD80 interaction, retrospective studies have identified that absolute T-lymphocyte count may be associated with patient response to ipilimumab (Callahan et al., 2013). As there is a documented correlation between T-lymphocyte count and immune checkpoint engagement, we sought to correlate immune checkpoint interactions with CD3⁺ and CD8⁺ intratumoral density. It transpired that PD-1/PD-L1 interactions in pre-RFA treated samples (lung one) significantly negatively correlated to intratumoral CD3⁺ density. This indicated, with significance, that higher checkpoint interaction was observed in areas with lower CD3⁺ density. As CD3⁺ is a global T-lymphocyte marker, this could be in part explained by the following. Not all CD3⁺ infiltrate may be tumour specific, that is, the T-lymphocyte is naïve to tumour specific antigens and thus plays no role in mounting an immune response against the tumour. This could also be coupled to the fact that lung metastases are amongst the most infiltrated metastases and immune infiltrates may be performing other functions, such as response to infection (Figure 4.11) (García-Mulero et al., 2020). A study has shown that metastases with the least immune-cell infiltration correlate with a prolonged survival, thus highlighting the need to investigate these infiltrates further (Mlecnik et al., 2018). Moreover, in this chapter, more distinct subpopulations of T-lymphocyte infiltration should be defined to assess for a correlation with immune checkpoint engagement or abscopal effect. In the preliminary work carried out in this chapter, CD4⁺ (T helper lymphocytes) were not assessed. This could yield important data as CD4⁺ lymphocytes play a critical role in adaptive immunity. Furthermore, once T helper lymphocytes have differentiated from naïve cells to effector cells, their role in targeting cancer

evolves. Whilst effector cells themselves are short lived, a subset of CD4⁺ effector cells form memory against an antigen (Golubovskaya and Wu, 2016). These memory cells, once mobilised, can evoke a more rapid immune response which is also persistent in the absence of antigen and more active compared to initial responses by fresh effector cells. It could therefore be an interesting approach to identify the infiltration of these CD4⁺ memory cells which typically contain the following cell surface marker profile: CD25⁻, CD45RA⁻, CD45RO⁺, CD127⁺ (Golubovskaya and Wu, 2016). The role of CD4⁺ cells in increasing the efficacy of CD8⁺ should also not be underestimated, as studies have shown that CD8⁺ lymphocytes that are primed in the absence of CD4⁺ lymphocytes have a cell intrinsic deficiency in secondary expansion. That is, the T-lymphocyte help is programmed into CD8⁺ lymphocytes (Janssen et al., 2003). CD8⁺ response against tumours is well documented, but as with CD4⁺ lymphocytes, the intratumoral infiltration of more distinct CD8⁺ subpopulations should be analysed to create a more in-depth immune barcode of a tumour. A study by Duhon et al., in 2018 identified two lymphocyte markers which can identify a population of tumour reactive CD8⁺ cells. CD8⁺ lymphocytes which were positive for both integrin α E (CD103) and CD39 were shown to have increased anti-tumour functions. Volcano plot messenger ribonucleic acid (mRNA) comparisons between CD8⁺, CD103⁺ CD39⁺ (termed double positive) and CD8⁺, CD103⁻, CD39⁻ (termed double negative) identified 219 differentially regulated transcripts. Gene set enrichment analysis revealed double positive cells to have an exhausted T-lymphocyte genotype with enriched programme cell death protein 1 (*PDCD1*) (PD-1), *CTLA4* (CTLA-4) and HAVCR2 (TIM-3) (hepatitis A virus cellular receptor 2 (T-cell immunoglobulin mucin-3)) genes.

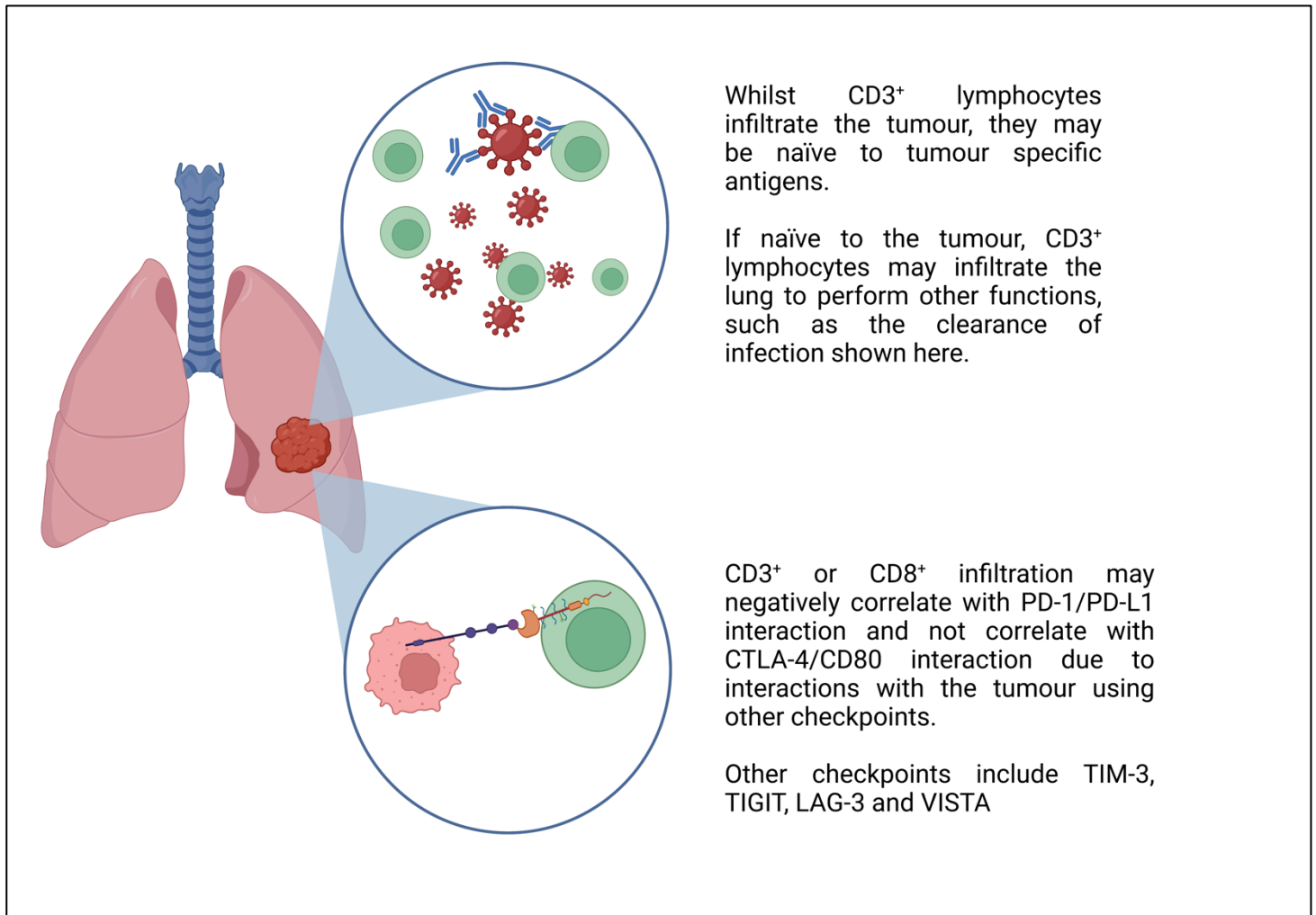


Figure 4.11: $CD3^+$ and $CD8^+$ intratumoral density may not correlate with immune checkpoint interaction due to the presence of naïve T lymphocytes or the presence of other checkpoint interactions. Whilst $CD3^+$ cells infiltrate the tumour, these cells may be naïve to tumour specific antigens. In this case, lymphocyte infiltration will not result in a lymphocyte-mediated attack of the tumour. Additionally, lymphocyte infiltration may report on lymphocytes performing other functions within the lung, such as the clearance of infection. Alternatively, the tumour may evade host immune response by upregulating its interaction with other checkpoints, such as TIM-3, TIGIT, LAG-3 and VISTA. Future studies will be required to identify these interactions.

Flow cytometry reveals that PD-1 expression was higher on the double positive cells and CTLA-4 and TIM-3 were almost exclusively expressed on this subpopulation. Despite exhibiting an exhausted genotype these cells were shown to have an increased cytotoxic potential with a higher frequency of granzyme B positive cells. Crucially the CD8⁺, CD103⁺, CD39⁺ cells showed an increased ability to recognise and kill autologous tumour cells and increased overall survival in HNSCC (head and neck squamous cell carcinomas) patients (Duhon et al., 2018). This study therefore highlights the requirement for distinct T-lymphocyte subsets to be quantified in tumours. Performing this quantification could yield correlations with immune checkpoint engagement, particularly due to the increase in immune checkpoint expression on these cells.

Whilst the CD8⁺, CD103⁺, CD39⁺ cells discussed above exhibited increased expression of the immune checkpoints PD-1, CTLA-4 and TIM-3 (Duhon et al., 2018), the results of this chapter have again shown that checkpoint interaction does not correlate with ligand expression. Therefore, the use of iFRET, coupled with the labelling of this lymphocyte subset will allow for an assessment of how a tumour is evading these efficacious cells and the creation of a patient immune checkpoint signature. This approach should be coupled to advance immune phenotyping, which can be spatially quantified using techniques such as mass imaging CyTOF (cytometry by time-of-flight) (further discussed in Chapter 6).

To summarise, the ability of iFRET to quantify immune checkpoint interactions in patients and determine differences in the dysregulation of different checkpoints will change the paradigm in which immunotherapies are prescribed. Moreover, iFRET has uncovered the need for, and provided the method for advanced quantitative immune surveyance, as opposed to qualitative immune surveyance, of patients which will greatly increase patient access to precision medicine. Other thermal ablative techniques, such as cryoablation and microwave ablation may yield increased antigen release upon tumour treatment. As the microsatellite stability of CRC patients can dictate their response to immunotherapies, this could also yield an opportunity to unravel the functional proteomics that underpin immunotherapy resistance in microsatellite stable (MSS) patients (Wang and Fakih, 2021). iFRET may hold the potential to elucidate different functional immune checkpoint engagement profiles between MSS patients and microsatellite instable (MSI) patients. There could also be a mechanism whereby microsatellite stability underpins an immune-level resistance to abscopal effects. Therefore, the work pioneered in this chapter could also be directly translatable to a range of thermal ablative techniques in a range of tissue types.

Chapter 5: The Elucidation of Programmed Death Receptor 1 (PD-1) Activation Dynamics at Tyrosine-248 of the Immunoreceptor Tyrosine-based Switch Motif (ITSM)

5.1: Introduction

A key component of the adaptive immune response is the ability of the immune cells to remember a previous infection, and thus attack the infecting pathogen sooner when next encountered; a phenomenon known as immunological memory (Beverley, 1991). A crucial element of the adaptive immune response is a group of highly specialised lymphocytes known as T-lymphocytes. Once a T-lymphocyte has recognised an antigen, presented by an antigen presenting cell's (APCs) major histocompatibility complex (MHC), the initiation of an immune response against that APC is triggered. For full activation to occur, co-receptors, cluster of differentiation 4 (CD4) on T-helper lymphocytes and CD8 on cytotoxic T-lymphocytes, must bind to invariant chains of the MHC. Additionally, co-stimulation from stimulatory ligands on the APCs, such as CD80/86, which bind to CD28 on the T-lymphocyte are needed for full activation (Acuto and Michel, 2003, Cantrell, 1996). Only when these three conditions have been met does a full adaptive immune response against the presented antigen occur. Whilst beneficial to the host immune response, this complex defence mechanism relies on a tight regulation in order to maintain immune tolerance. which is the ability of an individual to ignore "self", while reacting to "non-self". Without such regulation, unrestrained T-lymphocyte activation would contribute to a breakdown in self-tolerance leading to autoimmune damage to the host. Hence, there are inhibitory immune checkpoint pathways, such as the cytotoxic T-cell lymphocyte-associated protein 4 (CTLA-4) or the programmed death receptor 1 (PD-1) and their complementary ligands, CD80 and CD86 (for CTLA-4) as well as programmed death ligand 1 (PD-L1) (for PD-1). The latter of these two pathways exist to control inflammation at sites of antigen presentation to prevent tissue damage. This is identified as people with programme cell death protein 1 (*PDCDI*) polymorphisms have increased predisposition to autoimmune diseases such as systemic lupus erythematosus, atopy, and rheumatoid arthritis (Cheng et al., 2013). In addition, the modulation of the PD-1/PD-L1 signalling axis by some cancers can lead to a loss of immunological control, which has been confirmed as a hallmark of cancer (Mahoney et al., 2015, Hanahan and Weinberg, 2011).

The crystal structure of PD-1 is shown in Figure 1.10. The signalling pathway of PD-1/PD-L1 is shown in Figure 5.1. Briefly, upon PD-1/PD-L1 engagement, two tyrosine residues of the immunoreceptor tyrosine-based inhibition motif (ITIM) and immunoreceptor tyrosine-based switch motif (ITSM) are phosphorylated (Y₂₂₃ and Y₂₄₈ respectively). Y₂₄₈ phosphorylation is conducted by Lck and Fyn. There is thought to be a recruitment of the SH2 (Scr homology 2) domain containing tyrosine phosphatases-1

and 2 (SHP-1 and SHP-2 respectively) to pY₂₄₈ (Figure 5.2). A study by Sheppard et al., 2004 indicate that both SHP-1 and SHP-2 bind to the ITIM of PD-1, whereas SHP-2 binds also to the ITSM (Sheppard et al., 2004). Furthermore, it has been shown by Patsoukis et al., in 2020 that SHP-2 phosphatase activation may be induced by the binding of the C-terminal SH-2 and N-terminal SH-2 domains of SHP-2 to two pY₂₄₈ residues on two optimally-spaced PD-1 receptors (Patsoukis et al., 2020). Upon the binding of SHP-2 to PD-1, a series of dephosphorylation events occur which act to attenuate T-lymphocyte activation, proliferation, and survival. SHP-2 acts to attenuate T-lymphocyte signalling by dephosphorylating the zeta-chain associated protein kinase 70 (ZAP-70)/CD3 ζ signalosome, resulting in reduced protein kinase C- θ (PKC θ) activation and interleukin 2 (IL-2) production (Sheppard et al., 2004, Smith-Garvin et al., 2009). Sheppard et al., 2004 recorded IL-2 production by measuring IL-2 levels using enzyme-linked immunosorbent assay (ELISA) of culture supernatant three days after stimulating T-lymphoblasts with either anti-CD3/IgG (immunoglobulin G) or anti-CD3/PD-L1. Stimulation with anti-CD3/IgG resulted in approximately 2ng of IL-2 per ml of culture medium. This was reduced to approximately 1ng per ml of culture medium when blasts were stimulated with anti-CD3/PD-L1. Western blot analysis confirmed that PKC θ levels remained constant when cells were treated with either anti-CD3/IgG or anti-CD3/PD-L1. However, in the presence of anti-CD3/PD-L1, pT₅₃₈ levels were reduced, indicating a PD-L1 mediated reduction in PKC θ activation state. pT₅₃₈ expression is used as a surrogate of PKC θ activation state. Likewise, T-lymphocyte stimulation using anti-CD3 resulted in ZAP-70 phosphorylation which was subsequently abolished when co-ligated with anti-CD3/PD-1. (Sheppard et al., 2004).

Whilst the mechanisms by which PD-1 and SHP-2 interact are better understood, less is known about the association of SHP-1 and PD-1. Numerous studies have aimed to elucidate a link between this phosphatase and receptor, however, literature to date reports contrasting results. For example, the study in 2004 by Sheppard et al., utilised mass spectrometric identification of phospho-peptide precipitated protein bands to confirm that SHP-1 does bind to the ITSM of PD-1 (Sheppard et al., 2004). However, a study by Yokosuka et al., in 2012 used steady-state Förster resonance energy transfer (FRET) to confirm that whilst SHP-1 was present, it did not directly interact with the ITSM of PD-1 (Yokosuka et al., 2012). These contrasting results highlight the need for the role, and potential interaction of SHP-1 and pY₂₄₈-PD-1 to be confirmed. Critically, a method which can quantify direct protein-protein interactions should be employed. It should be noted that discrepancies between these observed results may arise from two contrasting techniques (FRET, which is *in-situ*, and mass spectroscopy, which is not). In addition to the roles SHP-1 and SHP-2 may play in transducing the inhibitory effects of PD-1, feedback loops have not been studied to search for a role of pY₂₄₈ in regulating the interaction of PD-1 with PD-L1. For example, it remains unknown whether the phosphorylation state of the ITSM of PD-1 bears any impact on the interaction state of the extracellular portion of PD-1 with the ligand PD-L1.

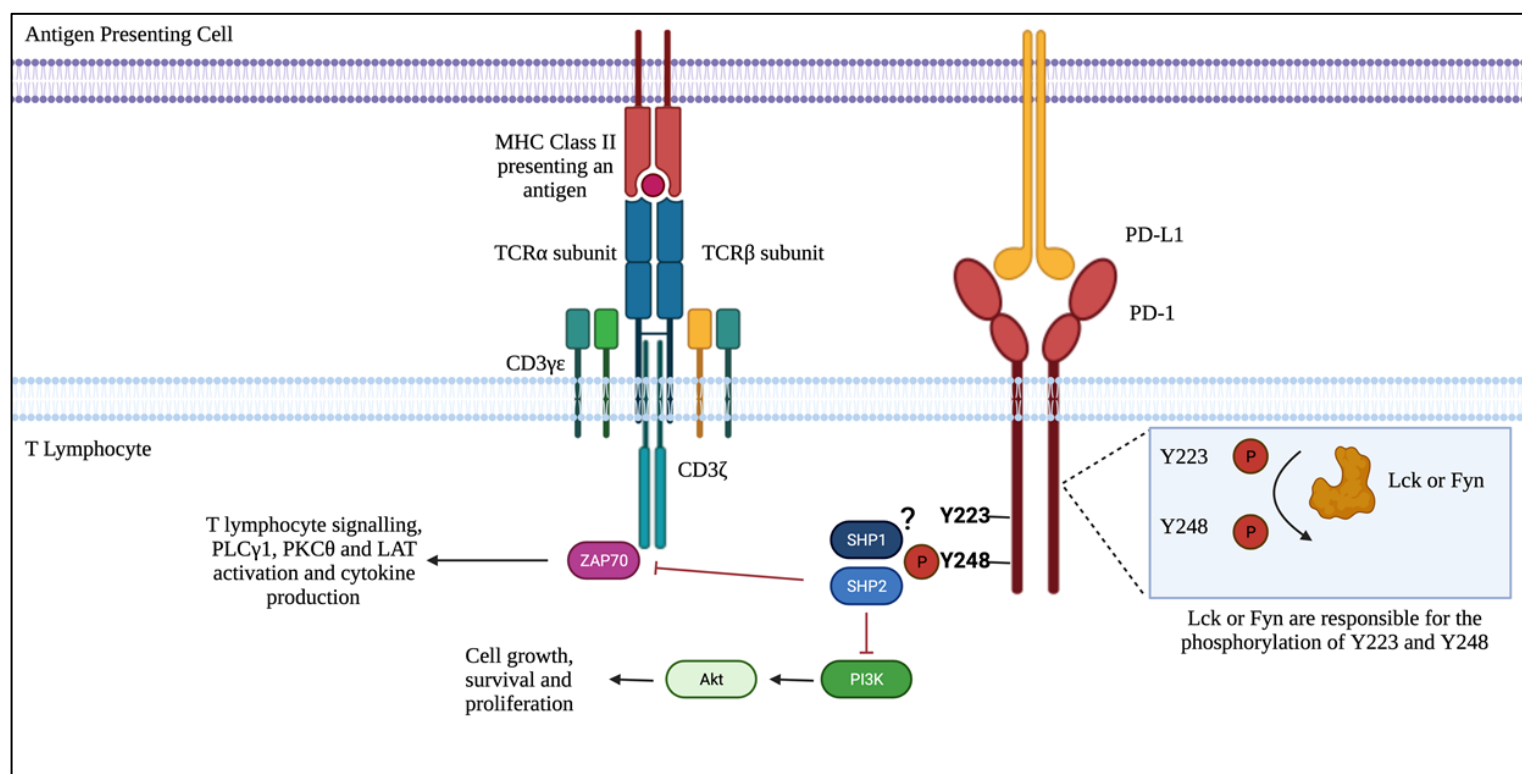


Figure 5.1: PD-1/PD-L1 engagement results in phosphorylation of Y₂₄₈ of the ITSM of PD-1. Upon binding of PD-L1, (presented by a cancer cell or antigen presenting cell (APC)) and PD-1, present on the T-lymphocyte, a series of signalling events occur to attenuate T-lymphocyte signalling (please refer to Figure 1.4). The interaction of receptor and ligand results in the phosphorylation of Y₂₂₃ and Y₂₄₈, located on the ITIM and ITSM of PD-1, respectively. These phosphorylation events are likely to be carried out by Lck or Fyn. Upon phosphorylation of Y₂₄₈, SHP-2 is recruited via its SH-2 domain. This results in the inhibition of the PI3K/Akt signalling pathway, resulting in reduced cell growth, survival, and proliferation. Also attenuated by SHP-2 is T-lymphocyte activation and IL-2 production, this results from a dephosphorylation of ZAP70, located on the CD3ζ chain. What remains poorly understood is to identify whether SHP-1 does bind to the pY₂₄₈ residue. Furthermore, if binding should occur, the activation state, and role of SHP-1 downstream of PD-1 remains unknown.

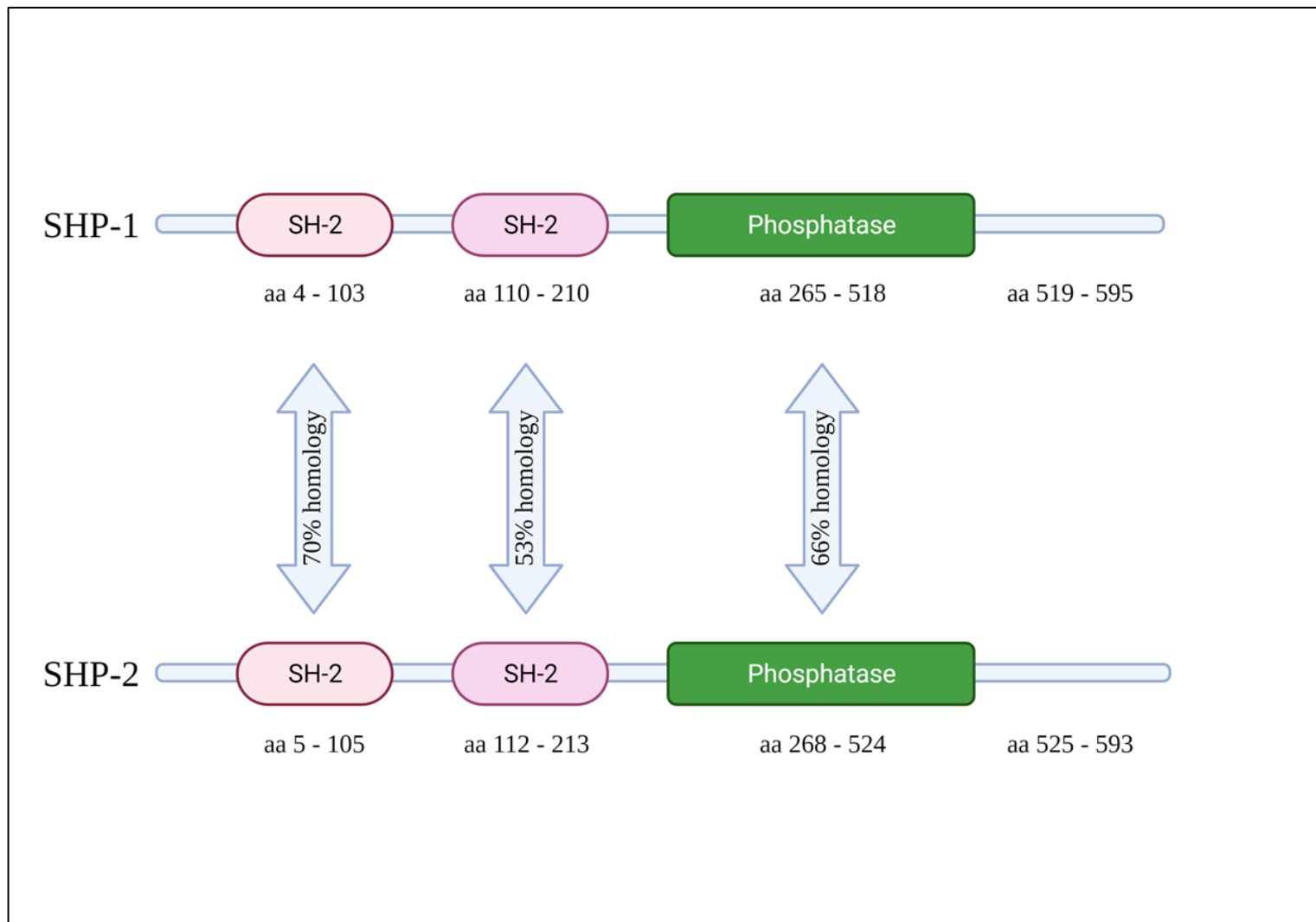


Figure 5.2: Linear structures of SHP-1 and SHP-2. SHP-1 and SHP-2 are protein tyrosine phosphatases that share a high sequence homology. Both phosphatases contain an N-terminus SH-2 domain, followed by a catalytic protein tyrosine phosphatase (PTP) domain and a C-terminal SH2 domain.

In order to elucidate this, time-resolved FRET as opposed to steady-state FRET can be used (immune-FRET (iFRET), detailed in Chapter 2) in conjunction with a precise genetic modification system in order to manipulate the intracellular signalling of PD-1. A genetic modification system which allows for the accurate and specific implementation of point mutations to be introduced into the genome should be used. Clustered Regularly Interspaced Short Palindromic Repeats (CRISPR)-CRISPR associated system (Cas) (CRISPR-Cas) is a novel genome editing tool which allows for the precise targeting of deoxyribonucleic acid (DNA). The advantage of using CRISPR/Cas is its ability to maintain an endogenous protein expression profile.

CRISPR-Cas9 provides a form of acquired immunity in bacteria and archaea (Mojica et al., 2005). In these prokaryotes, CRISPR acts as a genomic memory of previous pathogenic infections. This memory bank is used by Cas proteins which act as guided-endonucleases and introduce double strand breaks (DSBs) if a matching genomic sequence is encountered again (Brouns et al., 2008). CRISPR systems can be classified into six types which are also grouped into two classes. Types 1-3 are the most studied whereas types 4-6 were discovered more recently, in 2015 (Lino et al., 2018). Type 2 CRISPR, which falls into class 2, requires one protein only to scan, bind and cleave target DNA sequences. This system is CRISPR-Cas9 (Makarova et al., 2011). In 2012, Doudna and Charpentier used CRISPR-Cas9 for the first time to introduce DSBs in target DNA (Jinek et al., 2012). The simplicity and specificity of CRISPR-Cas9 systems make it ideal for gene editing, where it holds the ability to introduce site-specific deletions, additions, and point-mutations (Figure 5.3). A second class 2 endonuclease is *Cpf1*, or Cas12. Cas9 recognises an NGG (where N can be A, C, T or G) protospacer adjacent motif (PAM). The PAM site is a short sequence that follows the target-DNA sequence to be cleaved by the Cas protein. This sequence is required for the Cas protein to cleave the DNA strand. Cas12 recognises an optimal PAM sequence of TTTV, however C-containing PAM sites (CTTV, TCTV, TTCV, TYCV etc.) are also recognised (where V can be A, C or G) (Chen et al., 2020). Cas12 has increased sensitivity to guide RNA (ribonucleic acid) mismatches and therefore experiences less off-target recognition and cleavage (Kim et al., 2020).

CRISPR/Cas9 Gene Editing

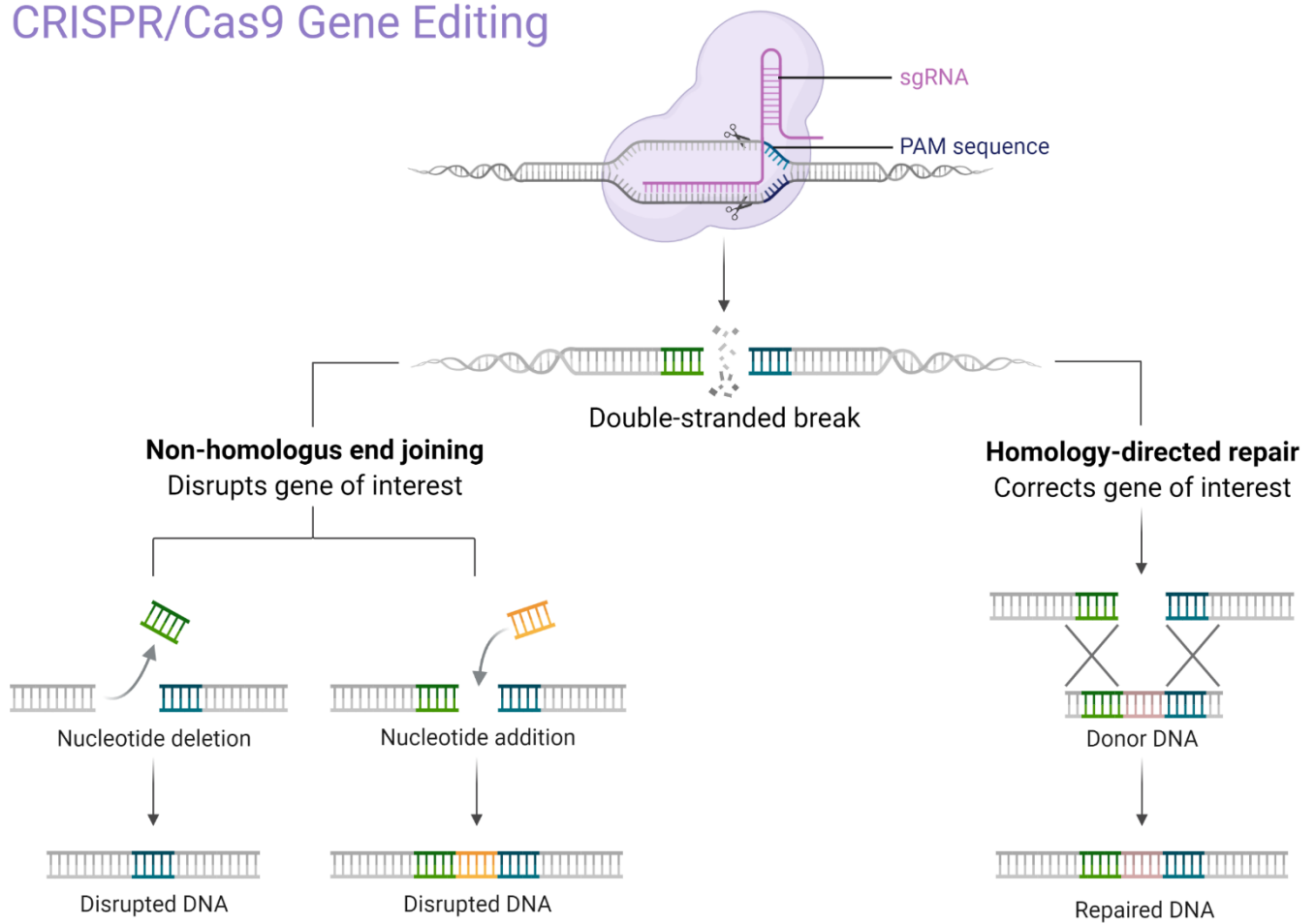


Figure 5.3: An overview of CRISPR/Cas9 for gene editing. The CRISPR/Cas9 system can be used for gene editing in mammalian cells. The Cas9 protein results in the formation of double strand breaks in target DNA. DNA is specifically targeted by designing a guide plasmid which creates Cas9 protein and the guide RNA of choice. Non-homologous end joining results in the disruption of the gene of interest. Homology-directed repair, in the presence of a donor repair template can be used to introduce specific changes to a gene, such as point mutations.

Here, CRISPR-Cas12 has been used with the intention to introduce site-specific point-mutations to the Y₂₄₈ residue of the ITSM of PD-1. Specifically, Y₂₄₈A and Y₂₄₈E point mutations have been created in order to create phospho-inactive and phospho-mimetic 248 residues in PD-1 with the aims to:

- (i) To confirm the interaction of SHP-2 and PD-1, documented in literature, using amplified FRET (aFRET).
- (ii) To elucidate, with a nanoscopic resolution, whether SHP-1 directly interacts with the ITSM of PD-1 using aFRET.
- (iii) To correlate Y₂₄₈ phosphorylation state with PD-1/PD-L1 interaction state using a combination of iFRET and aFRET.

5.2: Results

5.2.1: Creation of CRISPR Guides and Repair Templates

When creating a CRISPR-mediated point mutation, a suitable guide and repair template are required. A suitable guide plasmid must code for the Cas protein which is required to cut the site of interest in the target sequence and also contain a guide sequence. The guide sequence is required for the Cas protein to successfully find the correct site in the target sequence and should contain minimal off-target effects.

When creating a donor-repair template, several methods may be used to create different styles of repair-template, all with varying efficiencies. The use of single stranded inserts with microhomology arms may be employed. These homology arms can be as short as 9bp and are directly incorporated into the primer design. This can reduce the cost of each genetic modification to be made by reducing the amount of cloning steps to be conducted. This also inherently reduces the chance of erroneous mutations and mistakes occurring during the creation of a construct. Critically, the use of microhomology arms has been shown to retain similar CRISPR efficiency as the use of full-length homology arms (Fueller et al., 2020). However, whilst this efficiency is similar, we opted to simultaneously pursue a full-length homology arm route in order to compare the efficiency of both methods and have a multi-tined approach to optimise experiments in the case that one method was unsuccessful.

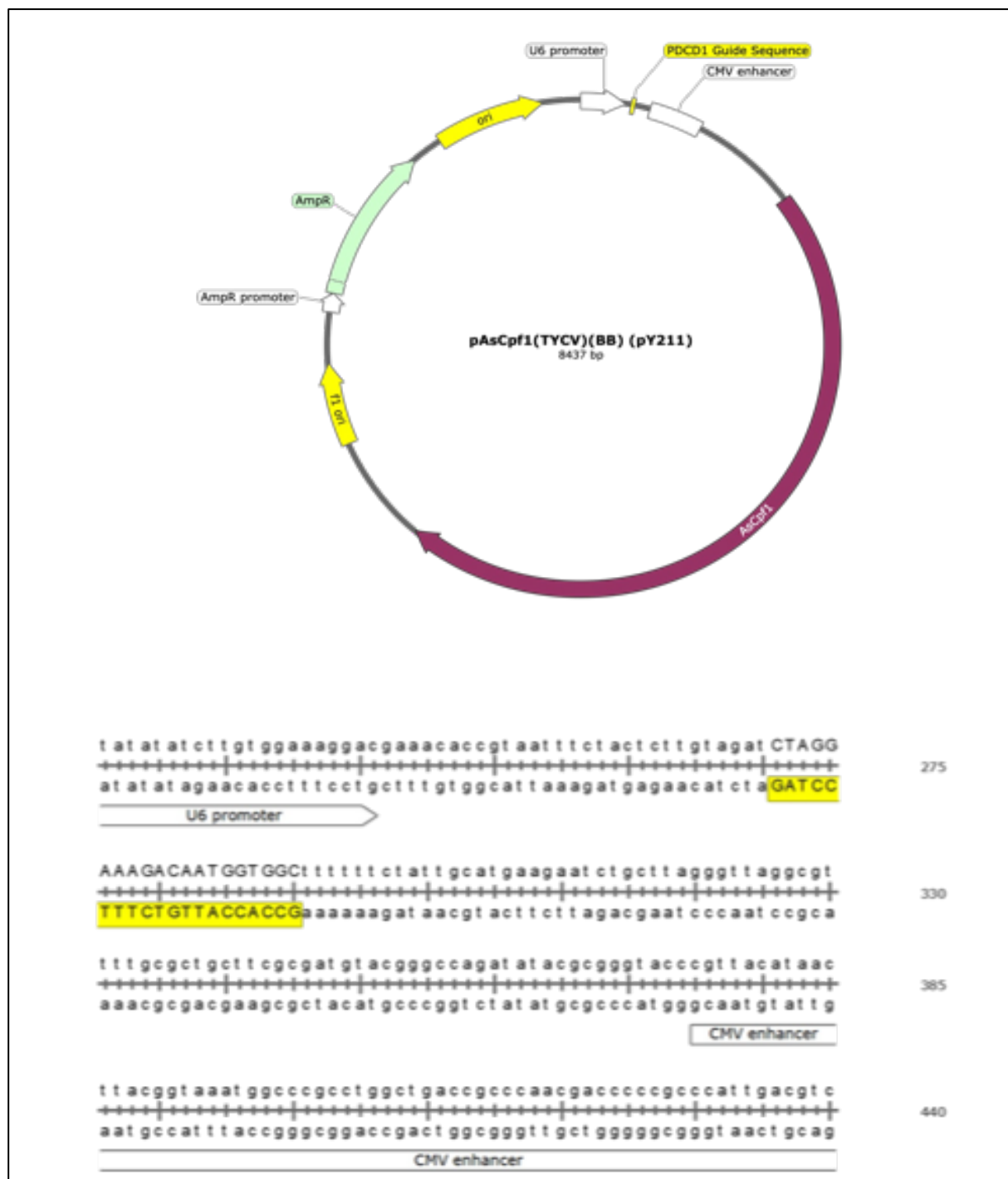


Figure 5.4: A pAsCpf1 (Cas12) guide plasmid was created which contains a guide sequence homologous to the 20 amino acids that follow the Y₂₄₈ locus. Top: An pAsCpf1 plasmid was purchased from Addgene. The plasmid was modified to contain a 20-nucleotide guide sequence homologous to the 20 nucleotides following the Y₂₄₈ residue of *PDCD1*. The plasmid also contains an ampicillin resistance gene for use as a positive selection marker. The PAM site for Cas12 is TCYV. **Bottom:** The sequence highlighted in yellow is a sequence homologous to the 20 nucleotides that follow Y₂₄₈ in the *PDCD1* gene, CTAGGAAAGACAATGGTGGC. This sequence has been introduced by digestion and ligation after the U6 promoter region of the plasmid to allow for successful RNA transcription in targeted cells.

5.2.2: Creation of *PDCDI* Y248-Specific CRISPR Guides

In order to successfully carry out a genetic modification within a cell line using CRISPR, a site-specific guide must be created. The plasmid, pAsCpf1(TYCV)(BB) (pY₂₁₁), was purchased from Addgene and codes for humanised *Cpf1*, or Cas12. As discussed above, Cas12 poses less off target effects than Cas9 whilst maintaining a similar efficiency (Kim et al., 2020). The primers 1 and 2 (see Table 2.3 in Chapter 2) were annealed to create the guide sequence insert. Subsequently plasmid three was opened by restriction digestion with BbsI prior to the insertion of the guide sequence, CTAGGAAAGACAATGGTGGC, which corresponds to amino acids A₂₄₉ to S₂₅₅ of *PDCDI*. This guide sequence is specific for the targeted locus of the *PDCDI* gene with no off-target effects within the exons of the gene. The off-target score for the guide sequence was 48.3, as listed on the webtool Benchling. The guide sequence was inserted after the U6 promoter to allow for the transcription of guide RNA in the target cell. Figure 5.4 outlines the designed CRISPR guide.

5.2.3: Creation of single-stranded Y₂₄₈A and Y₂₄₈E Point Mutation Repair Templates with Microhomology Arms

To facilitate the precise modification of the Y248 residue, either a Y₂₄₈A (a phospho-inactive mutant) or Y₂₄₈E (a phospho-mimetic mutant) donor repair template was created. A first attempt used oligonucleotide pairs which contained 9bp microhomology arms and either the Y₂₄₈A or Y₂₄₈E point mutation. One oligonucleotide per pair (oligonucleotides 5 and 7, See Table 2.3) were phosphorylated on the 5' end using the T4 polynucleotide kinase. The oligonucleotide pairs (5&6 and 7&8) were then annealed and amplified by polymerase chain reaction (PCR) to include the fluorescence protein mNeonGreen (mNG) as a positive selection marker (See Chapter 2). Sanger sequencing confirmed the successful creation of both point mutations and their amplification with mNG (Figure 5.5 and Figure 5.6).

5.2.4: Creation of Donor Repair Templates with Full-Length Homology Arms

In order to carry out the multi-tined approach discussed above, donor repair templates containing full-length homology arms were also created simultaneously to the micro-homology arms approach above. The use of full-length homology arms, 956bp in this instance, requires additional cloning steps compared to micro-homology arms which can be incorporated into the primer design. First, a PCR was conducted with genomic DNA (gDNA) to create the 956bp homology arms. A vector plasmid, pBlueScript, was opened and the homology arms inserted by Gibson assembly. This was verified by Sanger sequencing. The positive selection marker, mNG, was then inserted into the vector. This product was then again opened by PCR and the Y₂₄₈A or Y₂₄₈E repair template were inserted by Gibson assembly. This product was then purified by agarose gel electrophoresis on a 1% agarose gel.

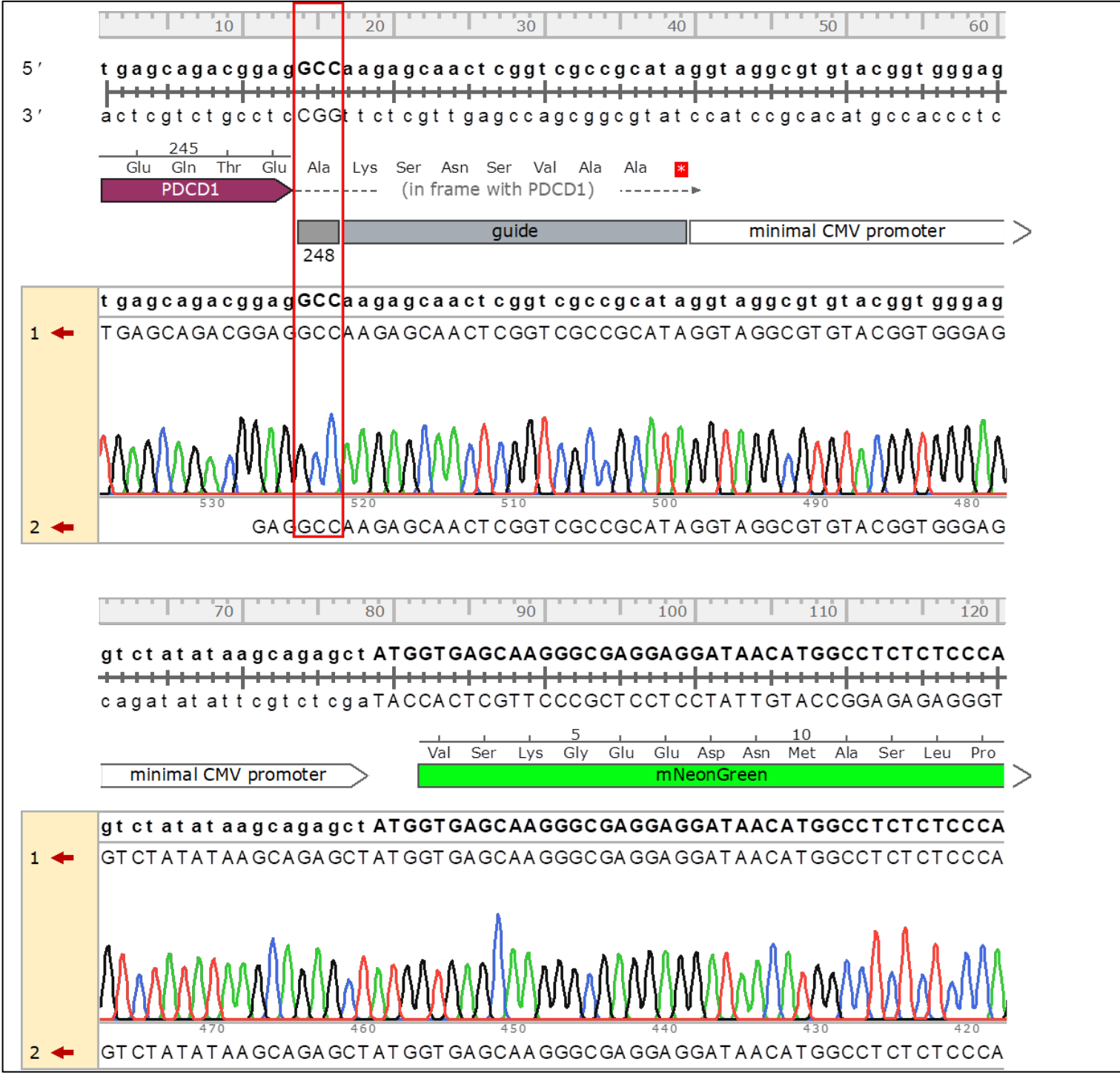


Figure 5.5: Sanger sequencing analysis confirms the creation of the Y₂₄₈A insert. Oligonucleotide 5 was phosphorylated on the 5' end. This was then annealed with oligonucleotide 6 and amplified by PCR to contain the fluorescent protein mNeon Green (mNG). Sanger sequencing identifies the correct insertion of the Y₂₄₈A point mutation and the presence of mNG.



Figure 5.6: Sanger sequencing analysis confirms the creation of the Y₂₄₈E insert. Oligonucleotide 7 was phosphorylated on the 5' end. This was then annealed with oligonucleotide 8 and amplified by PCR to contain the fluorescent protein mNeon Green (mNG). Sanger sequencing identifies the correct insertion of the Y₂₄₈E point mutation and the presence of mNG.

Bands were excised and purified using the Monarch® DNA gel extraction kit following the manufacturer's protocol. The bands were eluted in ultrapure water and quantified using a NanoDrop ND-1000. The product was transformed into competent *E. coli* which were subsequently inoculated into lysogeny broth (LB). Bacteria were miniprep using the Monarch® plasmid mini-prep kit as per the manufacturer's instructions. The purified plasmid was then amplified by PCR to create linear donor templates, quantified, and sent for Sanger sequencing analysis. The correct sequence for each point mutation was confirmed by Sanger sequencing and these are displayed in Figure 5.7 and Figure 5.8, respectively. The created donor repair templates were then ready to be transfected, alongside the CRISPR guide, into the target cells.

5.2.5: Transfection into Leukemic Cell Lines

As with the creation of the donor repair templates, a multi-tined approach was taken to transfect the repair-templates and guides into leukemic T-cell lines, such as Jurkat cells and MOLT-4 cells. These cell lines have long been utilised to study T-lymphocyte biology and signalling (Abraham and Weiss, 2004). However, these cells can prove challenging to transfect (Olden et al., 2018, Ayyadevara and Roh, 2020). Literature has reported some success in transfecting Jurkat cells using cationic lipid-based transfections (Ayyadevara and Roh, 2020, Zheng et al., 2019) as well as electroporation (Curnock and Ward, 2003, Schubert et al., 2021). Therefore, an approach was taken which first evaluated cationic lipid-based transfection and subsequently electroporation-based transfection in order to maximise the chance of successfully transfecting these lymphoblast cell lines.

A literature review performed prior to transfection experiments revealed that Jurkat cells, in a basal state, do not readily express PD-1 at the cell surface. A paper by Sugita et al., 2009 show that basal Jurkat cells have only a 3% expression of PD-1, which is increased to around 20% upon CD3 stimulation (Sugita et al., 2009). The Protein Atlas (www.proteinatlas.org) indicated that of all typical commercial leukemic T cell lines, MOLT-4 cells have the highest basal cell-surface expression of PD-1 (Atlas, 2021). Therefore, MOLT-4 cells were chosen to be transfected.

5.2.5.1: Cationic-Lipid-Based Transfection of MOLT-4 Cells

Following the creation of the donor repair template contained within the pBS vector, experiments were conducted to transfect both the CRISPR guides and repair templates into MOLT-4 cells. We first attempted to transfect the donor repair template with micro-homology arms alongside the CRISPR guides using Lipofectamine 2000. Lipofectamine 2000 transfection was conducted as per the manufacturer's protocol to transfect the CRISPR guide and either Y₂₄₈A donor repair template or Y₂₄₈E donor repair template. Fluorescence activated cell sorting (FACS) analysis 48 hours post-transfection failed to detect a distinct positive population of modified cells.

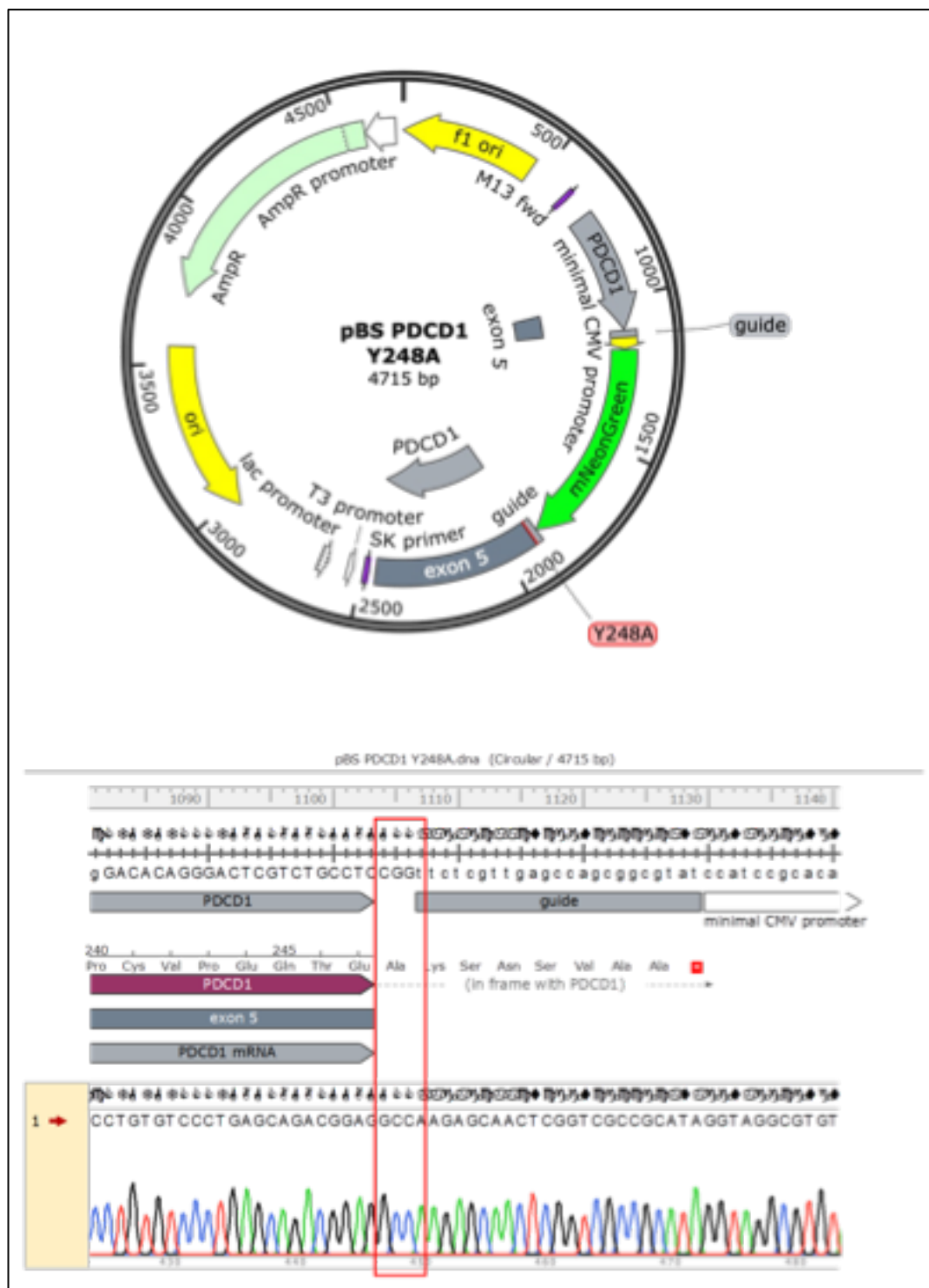


Figure 5.7: The Y₂₄₈A donor repair template with full-length homology arms was successfully cloned: confirmed by Sanger sequencing analysis. **Top Panel:** The pBlueScript (pBS) plasmid was opened by PCR and the Y₂₄₈A-mNeonGreen (mNG) insert was inserted by Gibson Assembly. The plasmid contains a minimal cytomegalovirus (minCMV) promoter, an ampicillin resistance gene, allowing for positive selection pressure, and mNG as a second positive selection pressure. The Y₂₄₈A point mutation is indicated. **Bottom Panel:** The Y₂₄₈A point mutation introduced into the plasmid by Gibson assembly was verified using Sanger sequencing confirmed that at the 248 positions, GCC was present, coding for the desired alanine amino acid (highlighted by the red box).

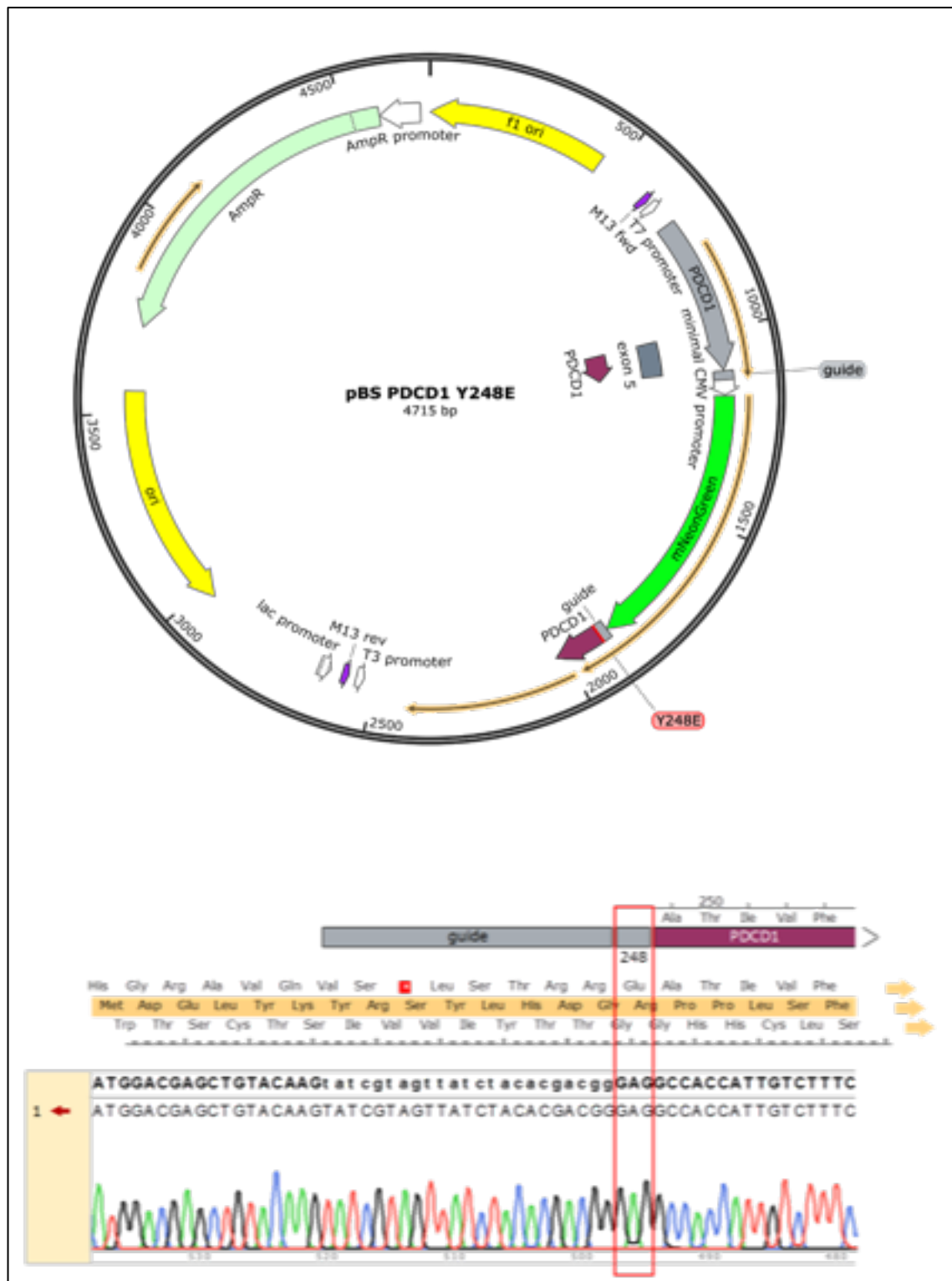


Figure 5.8: The Y₂₄₈E donor repair template with full-length homology arms was successfully cloned: confirmed by Sanger sequencing analysis. **Top Panel:** The pBlueScript (pBS) plasmid was opened by PCR and the Y₂₄₈E-mNeonGreen (mNG) insert was inserted by Gibson Assembly. The plasmid contains a minimal cytomegalovirus (minCMV) promoter, an ampicillin resistance gene, allowing for positive selection pressure, and mNG as a second positive selection pressure. The Y₂₄₈E point mutation is indicated. **Bottom Panel:** The Y₂₄₈E point mutation introduced into the plasmid by Gibson assembly was verified using Sanger sequencing confirmed that at the 248 positions, GCC was present, coding for the desired alanine amino acid (highlighted by the red box).

This was further backed up by gDNA extraction from the transfected cells, amplification, and sequencing. As the results of this transfection may have arisen from a low repair efficiency, the transfection was repeated using the donor repair templates with full-length homology arms. Again, FACS analysis failed to detect positively modified cells. This was confirmed by gDNA extraction and sequencing from the transfected cells. As this lack of transfection efficiency could be attributed to the difficulty transfecting leukemic T-cell lines, two further cationic-lipid-based transfection techniques were conducted using the full-length donor repair template (Figure 5.9A).

The next attempts made at transfecting MOLT-4 cells used Lipofectamine 3000. This was chosen as a recently published manuscript Shi et al., 2018 indicated that Lipofectamine 3000 has increased transfection efficiencies and lower transfection-associated toxicity compared to that of Lipofectamine 2000 (Shi et al., 2018). Lipofectamine 3000 was used as per the manufactures instructions in order to transfect the CRISPR guide plasmid and either Y₂₄₈A or Y₂₄₈E donor repair template plasmids. As was seen with Lipofectamine 2000, a poor transfection efficiency was observed (<1%) as well as high low cell viability (approximately 20%). As the results of this transfection may have arisen from a low transfection efficiency, rather than a problem with the CRISPR-Cas12 system, a transfection using green fluorescent protein (GFP) was carried out. A comparable low level of transfection efficiency was also seen when transfecting GFP into MOLT-4 cells using Lipofectamine 3000, indicating the low positive results arose from a low transfection efficiency (<1%) and low cell viability (approximately 10%) (Figure 5.9B). A simultaneous transfection was carried out to transfect GFP into HeLa cells to assess the ability of the user to transfect correctly. Here, a suitable transfection efficiency was observed (approximately 40%), indicating no operator-related issue was present in previous transfection experiments. The results here are displayed in greyscale (left) and in the GFP channel (right) Figure 5.9C).

The poor transfection results in MOLT-4 cells led to the trial of a different transfection reagent which is proposed to have increased transfection efficiencies in “difficult to transfect” cell lines, FuGENE HD. FuGENE HD has been used to transfect Jurkat E6 cells (Zheng et al., 2019), which was predicted to translate to the ability to also transfect MOLT-4 cells. Transfection was carried out using FuGENE HD as per the manufacturer’s instructions, trialling differing ratios of transfection reagent to DNA (see Chapter 2). Again, a lack of transfection efficiency was observed (<1%). This led us to undertake a different transfection approach, utilising electroporation rather than cationic-lipid reagents (Figure 5.9D).

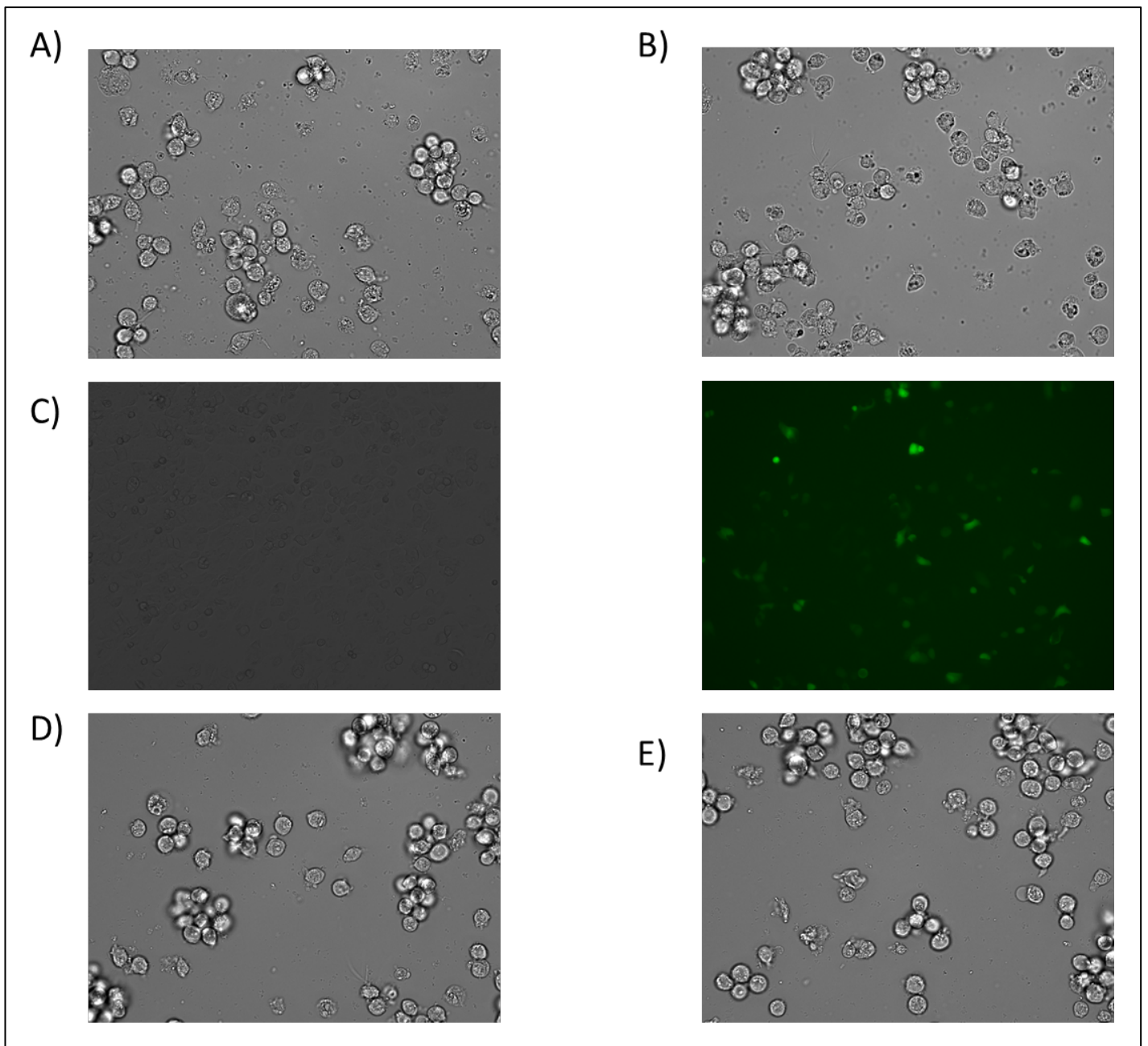


Figure 5.9: Representative images show high transfection cytotoxicity when transfecting MOLT-4 cells with lipid-based or electroporation-based transfection. **A)** A representative image showing transfection cytotoxicity when using Lipofectamine 2000 to transfect the Y₂₄₈A donor-repair template with full-length homology arms, and CRISPR guide, into MOLT-4 cells. The same was observed in multiple wells and observed for the Y₂₄₈E mutation. **B)** A representative image showing transfection cytotoxicity when using Lipofectamine 3000 to transfect GFP into MOLT-4 cells. **C)** A representative imaging showing good transfection efficiency when using Lipofectamine 3000 to transfect GFP into HeLa cells, thus confirming no operator related issues were occurring during previous transfection experiments. **D)** A representative image showing transfection cytotoxicity when using FuGENE HD to transfect the Y₂₄₈A donor-repair template with full-length homology arms, and CRISPR guide, into MOLT-4 cells. The same was observed in multiple wells and observed for the Y₂₄₈E mutation. **E)** A representative image showing transfection cytotoxicity when using an Amax ii nucleofector electroporation device to transfect the Y₂₄₈A donor-repair template with full-length homology arms, and CRISPR guide, into MOLT-4 cells. The same was observed in multiple wells and observed for the Y₂₄₈E mutation.

5.2.5.2: Electroporation-Based Transfection of MOLT-4 Cells

Whilst some literature had reported the ability to transfect leukemic T cell lines using cationic-lipid based transfection, other publications had suggested that MOLT-4 cell are amenable to transfection by electroporation (Agarwal and Tyner, 2016). Therefore, alongside the aforementioned lipid-based transfections, a series of nucleofections were carried out. An Amax Nucleofector II was used to perform electroporation of MOLT-4 cells using the custom-made MOLT-4 electroporation program. As in previous experiments, no transfected cells were observed (<1%) (Figure 5.9E). Future plans to optimise the electroporation approach to transfection would include the use of a nucleofector device with variable settings as opposed to pre-made programs. A paper published by Curnock and Ward., 2003, successfully transfected Jurkat cells using electroporation parameters of 950 μ F, 300V. Other literature has suggested electroporating MOLT-4 cells at 250V for 2ms, resulted in a cell viability of 86% or 79% confirmed via cell counting or MTS assay respectively (Agarwal and Tyner, 2016). The use of an electroporator with increased control over electroporation parameters could therefore yield increased transfection efficiency in MOLT-4 cells, and ultimately successful genetic modifications by CRISPR.

5.3: Discussion

The fundamental scientific aim of this chapter was to provide insight into activation status of PD-1 with regards to its intracellular biochemical signalling. This could elucidate Y₂₄₈ phosphorylation state as an additional biomarker by which to stratify patients for immune checkpoint blockade therapies.

This aim has been reported on by detecting pY₂₄₈ status as well as association of the SHP protein tyrosine phosphatases (PTPs) to this domain. As a variety of literature has uncovered the roles of SHP-2 downstream of PD-1, precise confirmation of whether SHP-1 interacts with the Y₂₄₈ residue of the receptor is lacking. An *in-situ* technique, such as FRET/fluorescence lifetime imaging microscopy (FLIM) would be favoured to probe this signalling event as it naturally occurs whilst reporting on the spatiotemporal dynamics of the proposed event.

Moreover, our ability to precisely measure and quantify cell-cell interactions (Chapters 3 and 4) would allow us to assess whether Y₂₄₈ phosphorylation bears any regulation on the interaction state of PD-1/PD-L1. Had the transfection efficiency have been sufficient to modify the MOLT-4 cells, we would have used our assays to: i) conclusively report with aFRET whether there is an interaction between SHP-1 and Y₂₄₈-PD-1; ii) confirm with aFRET the interaction of SHP-2 and Y₂₄₈-PD-1; iii) correlate the phosphorylation state of Y₂₄₈ with PD-1/PD-L1 interaction state using iFRET and aFRET.

We postulated that an interaction between SHP-1 and E₂₄₈ in the Y₂₄₈E MOLT-4 cell line would occur as the phosphorylated residue acts as a dock for the SH-2 domain of the phosphatase. Moreover, Sheppard et al., 2004 confirmed SHP-1 interactions with PD-1 using mass spectrometric identification

of phospho-peptides precipitated protein bands (Sheppard et al., 2004). Contrastingly, Yokosuka et al., 2012 failed to detect SHP-1/PD-1 interactions when using steady-state FRET. However, steady-state FRET is more sensitive than aFRET to chromophore concentration induced artifacts (Yokosuka et al., 2012). Due to its ability to accurately quantify interactions over a 1-10 nm range, we postulate that aFRET would have been a more suitable tool to assess this direct interaction. This distance constraint would therefore be disrupted for example if an intermediary binding partner were present, thus only yielding positive results if a direct SHP-1/PD-1 interaction was occurring. Conversely, it would be predicted that no SHP-1/PD-1 interaction state would be observed in the Y₂₄₈A cell line due to the lack of a pY docking site for the SH-2 domain of SHP-1. Figure 5.10 outlines the predicted SH-2 interaction between SHP-1 and PD-1 in the Y₂₄₈A and Y₂₄₈E cell lines.

As literature indicated the binding of SHP-2 to Y₂₄₈, it would have been predicted in the confirmatory experiments, that the SH-2 domain of SHP-2 would bind to the E₂₄₈ residue in the Y₂₄₈E cell line but not the A₂₄₈ residue in the Y₂₄₈A line (Smith-Garvin et al., 2009, Sheppard et al., 2004, Patsoukis et al., 2020).

In wild type cells, it could be predicted that some degree of basal interaction of both SHP-1 and SHP-2 may occur to maintain lymphocyte homeostasis, which is subsequently upregulated upon Y₂₄₈ phosphorylation. The predicted result would be that PD-1/PD-L1 interaction increases SHP-1 and SHP-2 interaction with Y₂₄₈, and as a negative control, the use of a PD1/PD-L1 blocking antibody would reduce this level back towards a basal state. As CRISPR/Cas12 has been used to create specific point mutations in the *PDCDI* gene, it could be further used to probe the intracellular signalling events that occur if the above hypotheses were not observed. Should we see no interaction of SHP-1 to pY₂₄₈, we could engineer SHP-2 to contain R₃₂A and R₁₃₈A mutations to inactivate the N and C terminal SH2 domains respectively (Patsoukis et al., 2020). This would abrogate the ability of SHP-2 to bind to pY₂₄₈ via SH-2 domain interaction. If this resulted in a detection of SHP-1/PD-1 interaction, it could then be postulated that SHP-2 outcompetes SHP-1 for pY₂₄₈ binding.

If SHP-1 were still not revealed to interact with pY₂₄₈, it would be pertinent to assess the role of SHP-1 in transducing the signals of alternative immune checkpoints. As there are very few non-invasive methods with sufficient precision to assess PD-1/PD-L1 interaction as iFRET/aFRET, we aimed to also correlate Y₂₄₈ phosphorylation state with PD-1/PD-L1 interaction state. It is known that PD-1/PD-L1 interaction state induces Y₂₄₈ phosphorylation, however whether this acts to provide a negative feedback signal to PD-1/PD-L1 interaction state, remains unknown. To the best of the authors knowledge, this has not been assessed.

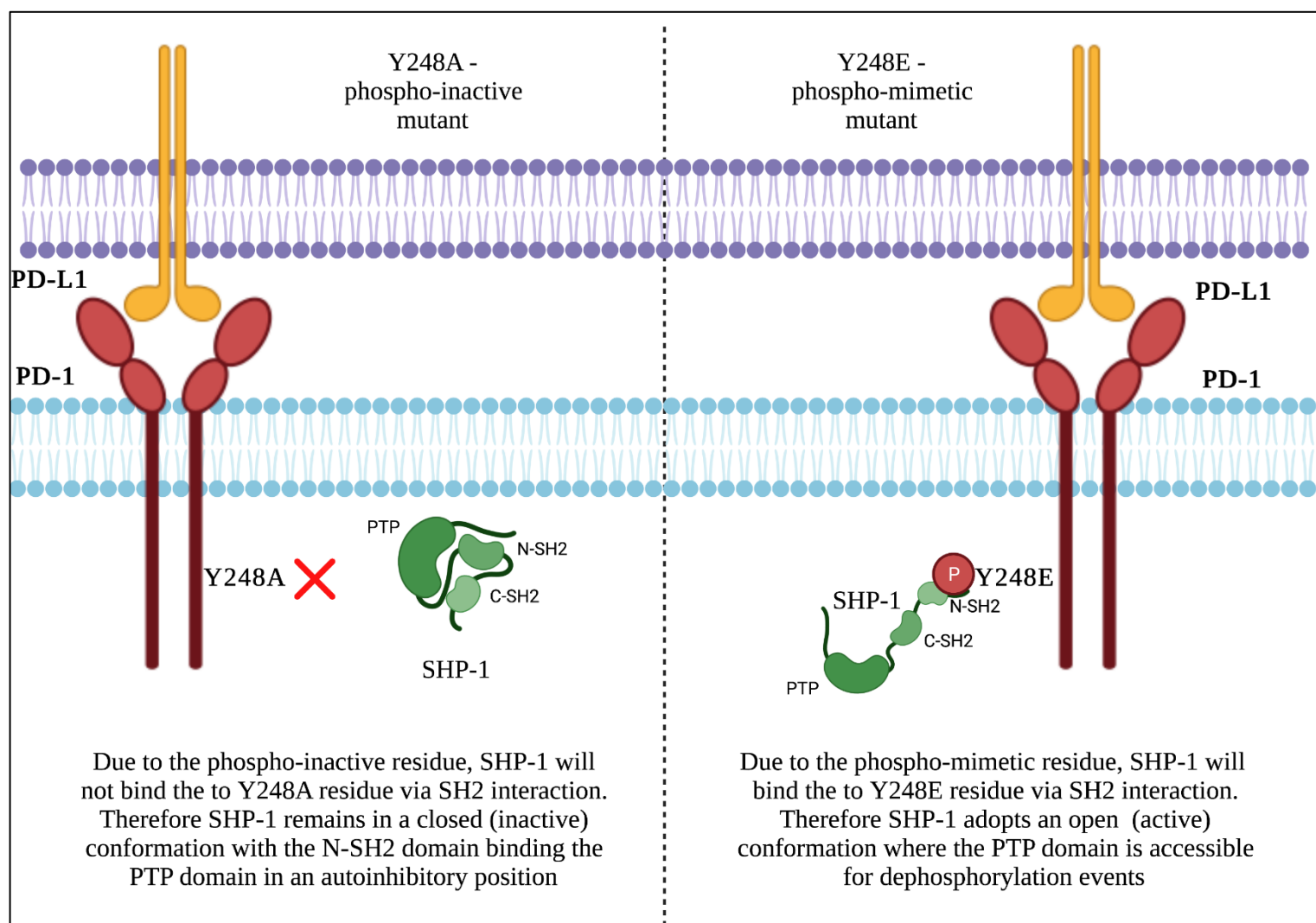


Figure 5.10: Predicted SHP-1/PD-1 interactions. It would be predicted that SHP-1 will bind to the Y₂₄₈E mutant but not the Y₂₄₈A mutant. Binding would occur via the SH-2 domain of SHP-1. Moreover, mutational studies could be carried out to inactivate the SH-2 domains of SHP-2 and determine if SHP-2 outcompetes SHP-1 for pY₂₄₈ PD-1 binding.

As Patsoukis et al., 2020 have shown that a single SHP-2 molecule can bind to two separate pY₂₄₈ residues via its C- and N-terminal SH-2 domains respectively, this gives a rationale that the phosphorylation state of Y₂₄₈ may regulate to some extent the binding of PD-1 and PD-L1. This study gives rise to the concept the PD-1 forms non-covalent dimers by the bridging of PD-1 monomers by SHP-2. Additionally, Patsoukis et al., showed that PD-L1 in its dimeric form, and not its monomeric form, induced a dimerisation of PD-1. This was reduced when in the presence of kinase-inactive Fyn, demonstrating both the role of Fyn in PD-1 signal transduction as well as the requirement for Y₂₄₈ phosphorylation. Excluding iFRET, there are no assays capable of directly measuring PD-1/PD-L1 interaction states *in-situ*. Therefore, implementation of iFRET could uncover a negative-feedback mechanism whereby Y₂₄₈ phosphorylation regulates the binding of PD-1 to PD-L1 by modulation of PD-1 dimerisation status.

To summarise, the cloning required to create a guide plasmid and donor template repair plasmids for both Y₂₄₈A and Y₂₄₈E point mutations were successfully carried out. The sole aim to overcome for this series of experiments will be to optimise transfection for MOLT-4 cells in order to conduct the proposed experiments. The work that would arise from this chapter would be novel, both in terms of contribution and technique, and able to uncover and determine the role of SHP-1 downstream of PD-1, a role that is not yet fully established. Aside from confirming whether SHP-1 plays a crucial role in PD-1 signal transduction, the work that could arise from this chapter would be amenable to studying SHP-1 signalling dynamics in depth. For example, it also remains unknown whether SHP-1 and SHP-2 compete for the pY₂₄₈ domain and whether SHP-2 is able to outcompete SHP-1, which may lead to the results in literature that SHP-2 is the predominant signal transducer. Alternatively, the activation state of SHP-1 could be assessed by aFRET (quantifying the phosphorylation state of the Y₅₃₆ residue) and this could be correlated with both Y₂₄₈ phosphorylation state and PD-1/PD-L1 interaction state. This could answer the more global immune question of exactly how SHP-1 acts in response to immune checkpoint engagement.

Furthermore, this work can lead to the generation of a novel predictive biomarker. Bardhan et al., 2019 indicated that pY₂₄₈ is a marker of PD-1-mediated T-lymphocyte inhibition, as pPD-1⁺ CD8⁺ T-lymphocytes were shown to have impaired function. The clinical implications of this could be that PD-1/PD-L1 interaction state, Y₂₄₈ phosphorylation state, SHP-1 and SHP-2 activation state are used to predict patient response to immune checkpoint blockades. This would vastly improve the immune-oncology field as current immune-oncology therapies are offered to an incorrectly stratified patient subset. This subset of patients is determined for immune-oncology using the expression profile of PD-L1, which does not correspond with PD-1/PD-L1 interaction (Sánchez-Magraner et al., 2020). The result of Y₂₄₈ phosphorylation state as a biomarker could be used in two manners. Firstly, it could be used to assess which patients may benefit from PD-1/PD-L1 therapies, alongside the use of

PD-1/PD-L1 interaction state. Secondly, this phosphorylation state could be used to track patient response to PD-1/PD-L1 therapies. If it is confirmed by aFRET that SHP-1 binds to pY₂₄₈, then SHP-1 activation state and pY₂₄₈-binding state could be used to assess the degree of PD-1/PD-L1 mediated immune evasion a tumour relies on (in comparison to other immune-evasion pathways such as CTLA-4/CD80). This could help in the creation of personalised patient therapies whereby all elucidated biomarkers are quantified and tracked to ensure correct dosing regimens are prescribed.

This could be critical as in a recent NSCLC study, 50% of patients failed to respond to the anti-PD-1 therapy, nivolumab (Theelen and Baas, 2019). Moreover, as one checkpoint is targeted, it may result in the dysregulation of another immune checkpoint (such as CTLA-4/CD80, T-cell immunoreceptor with Ig and ITIM domains (TIGIT), TIM3). Therefore, the work this chapter can generate may elucidate the signal transducers of these other regulatory pathways. This can aid further the search for personalised patient therapies and also the elucidation of resistance-mechanisms to immune checkpoint inhibitors.

Chapter 6: Discussion

6.1: Summary of Results

The scope of this thesis was to apply functional proteomics in the form of time-resolved amplified-Förster resonance energy transfer (FRET) (termed aFRET for intracellular applications and immune-FRET (iFRET) for intracellular immune applications) to quantify immune checkpoint interactions in a range of neoplasia. We set out to implement an assay capable of measuring these intercellular immune interactions at a nanoscopic resolution, reporting on functionality that current quantitative immunohistochemistry (qIHC) fails to detect. Once validated, we sought to identify whether two immune checkpoints, programmed death receptor 1 (PD-1)/ programmed death ligand 1 (PD-L1) and cytotoxic T-cell lymphocyte-associated protein 4 (CTLA-4)/cluster of differentiation (CD) 80 (CD80) could render prognostic value when analysed by iFRET in retrospective and prospective patient samples. iFRET was then used to elucidate a molecular mechanism by which an immune-mediated abscopal effect may be elicited in radiofrequency ablation-treated patients. Lastly, we investigated how PD-1 signalling is transduced within T-lymphocytes by combining novel molecular biology with advanced quantitative functional proteomics.

6.1.1: PD-1/PD-L1 Checkpoint Interaction State is Predictive of Patient Outcome in Malignant Melanoma and Metastatic Non-Small Cell Lung Carcinoma

The use of immune checkpoint ligand expression is widely used to stratify which patients should receive immune checkpoint blockade therapies. The problems with this are two-fold. Firstly, ligand expression is often assessed by classical IHC methods, which lack a high dynamic range and specificity. Should an immunohistochemical assay be used to quantify checkpoint ligand expression, it must be performed in a quantitative and spatially resolved manner. Secondly, ligand expression is not a surrogate for immune checkpoint interactions. The novel findings in Chapter 3 have, for the first time, detected and validated immune-cell tumour-cell interplay in a cell co-culture model prior to demonstrating that, in metastatic melanoma and metastatic non-small cell lung carcinoma (NSCLC), patient outcome is significantly worsened in patients with a lower checkpoint interaction state. The use of ligand expression failed to predict patient outcome. The methodological achievement of this chapter is the application of the coincident time-resolved amplified-FRET (aFRET) to quantitate intercellular receptor-ligand interactions for the first time. To our knowledge, no other technology exists which can resolve, non-invasively, receptor-ligand interactions with a <10 nm resolution and a high dynamic range. The novel biological relevance of these findings is identifying the preferable use of checkpoint ligand functional state, rather than expression levels, as the preferred choice of stratification for patient treatment regimens.

6.1.2: iFRET Can Detect Differential Checkpoint Interactions within RFA-Treated Patients

Once the iFRET assay had been validated in retrospective patient studies for PD-1/PD-L1 and CTLA-4/CD80 in Chapter 3, we sought to apply iFRET to a prospective study. A fraction of colorectal patients with lung metastases acquire resistance to most conventional therapies and are therefore treated with radiofrequency ablation (RFA). In very rare instances, an abscopal effect is observed between the treatments of lungs one and two with RFA. This gave rise to the possibility of iFRET detecting any immune checkpoint mediated mechanisms for the partial abscopal effects observed. Whilst the initial study set up did not allow for the exclusion of intertumoral heterogeneity, iFRET was nevertheless applied to samples from these patients to assess their CTLA-4/CD80 and PD-1/PD-L1 interactions. The first key finding here was that iFRET can detect differences in CTLA-4/CD80 and PD-1/PD-L1 interactions within the same patient. This yields information about how a tumour may be preferentially evading immune detection. Moreover, it was seen that PD-1/PD-L1 interaction states negatively correlated with intratumoral CD3⁺ density in patients. Whilst an interesting finding, the exact role of these CD3⁺ infiltrates remains ill-defined (as they could be responding to infection for example rather than a tumour-specific response). Moreover, other CD marker identification is crucial to isolate precisely which immune-subset of lymphocytes is infiltrating and interacting with the tumour. However, it does identify that immune-cell infiltrates, if spatially quantitated and assessed by iFRET, could help to better identify which immune-cell subsets hold the greatest antitumour potential. Crucially, these findings give rise to the notion that patients should undergo “immune surveyance.” That is, patients should be routinely monitored to assess which pathway(s) and immune-cell subtypes are leading a tumours evasion of the immune system and subsequently what therapies (mono vs dual therapy) should be prescribed to a patient. These combined findings may change the paradigm by which immune checkpoint blockade therapies are prescribed to patients and how their subsequent response is monitored.

6.1.3: CRISPR/Cas12 Coupled to aFRET and iFRET May Elucidate the Intracellular Signalling Dynamics of PD-1 upon PD-L1 Ligation

Upon successfully applying iFRET to cell co-culture models, retrospective, and prospective studies, we planned to couple iFRET with the advance molecular cloning technique CRISPR (Clustered Regularly Interspaced Short Palindromic Repeats)/Cas12 (CRISPR associated system12) to elucidate intracellular PD-1 signalling dynamics. The cytoplasmic tail of PD-1 contains a Y₂₄₈ residue in its immunoreceptor tyrosine-based switch motif (ITSM) which is known to become phosphorylated upon PD-1/PD-L1 engagement. Several studies have identified SH2 domain containing tyrosine phosphatase-2 (SHP-2) as a binding partner to Y₂₄₈, but studies assessing SH2 domain containing tyrosine phosphatase-1 (SHP-1) have given contrasting results, possibly in part due to conflicting techniques used between

studies (Sheppard et al., 2004, Yokosuka et al., 2012). We therefore investigated whether the phosphorylation state of Y₂₄₈ acts as a docking site for SHP-1 using the two-site FRET assay. CRISPR/Cas12 was used to introduce a phospho-inactive (Y₂₄₈A) or phosphomimetic (Y₂₄₈E) mutation to the Y₂₄₈ residue of PD-1. Moreover, we planned to assess whether the phosphorylation state of PD-1 regulated PD-1/PD-L1. Challenges within the molecular cloning were minimal, however challenges arose during the transfection of CRISPR-modified plasmids into MOLT-4 leukemic cells. Despite using a multi-tined approach to transfection, the MOLT-4 cells are yet to be transfected, although all molecular cloning steps were carried out. This chapter brought about the combination of several novel techniques in order to probe the intracellular signalling mechanisms of the PD-1/PD-L1 pathway in tandem with their intercellular modulation.

Whilst these combination of novel techniques and biological findings, which sit at the interface of fundamental research and the clinic, have yielded previously unknown functional proteomics of immune checkpoints, questions surrounding these novel predictive biomarkers remain unanswered.

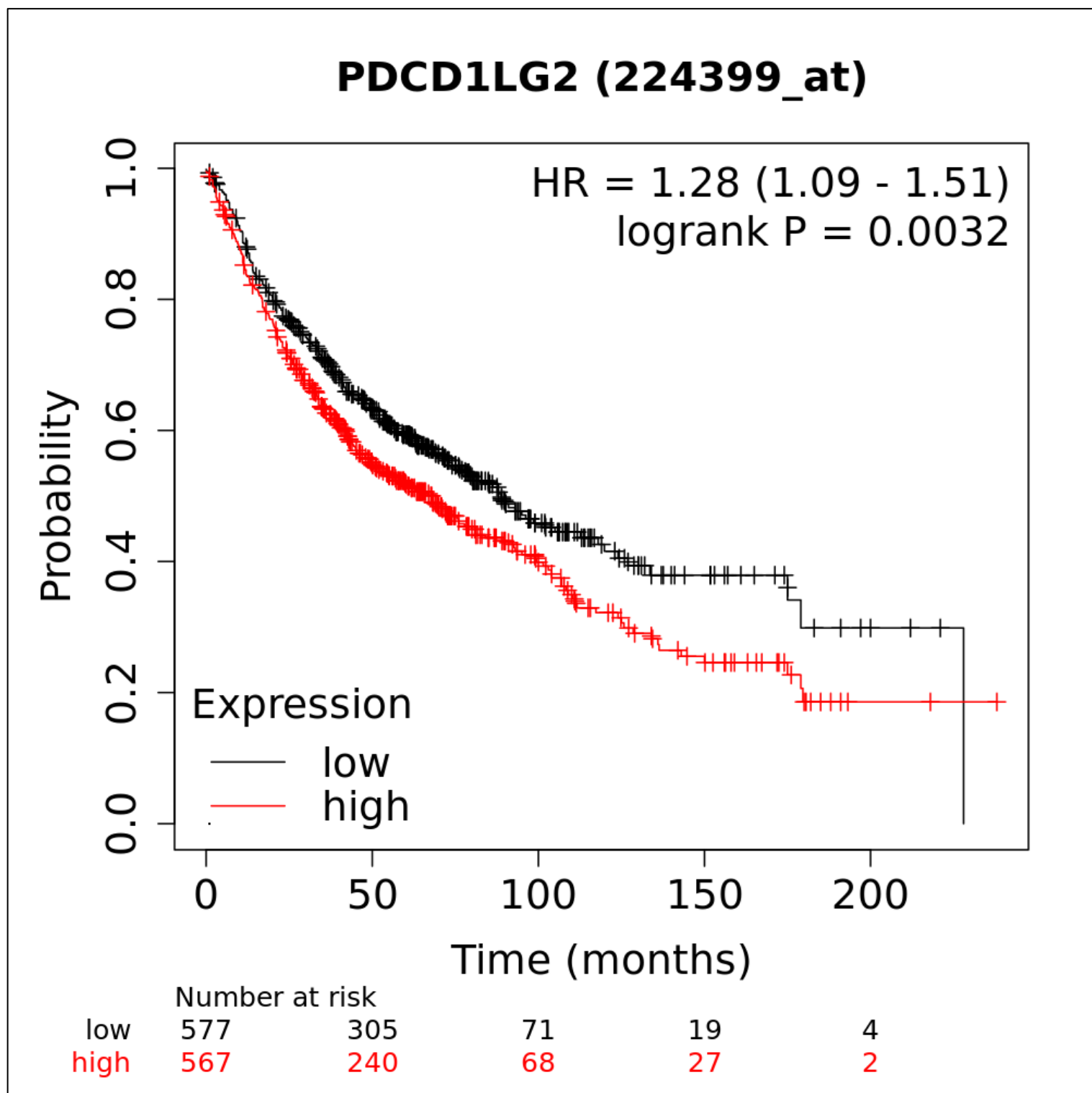


Figure 6.1: Increased PD-L2 mRNA expression significantly correlates with an improved OS in NSCLC. The online tool, KM Plotter, was used to assess whether PD-L2 mRNA expression correlated with clinical outcome in a retrospective NSCLC study. It was observed that a higher median PD-L2 expression correlated with a significantly worsened overall survival ($P=0.032$) in NSCLC. This indicates that PD-L2 mRNA expression may predict patient outcome, although this should be further studied at the quantitative functional proteomic level.

6.2: Future Perspectives

6.2.1: Unravelling the Intracellular Signalling Dynamics of PD-1 and CTLA-4

The first objective that would be set for the continuation of the work carried out in this thesis would be the determination of the intracellular signalling dynamics of both PD-1 and CTLA-4. For PD-1, the CRISPR-modified plasmids and guides would be successfully transfected into MOLT-4 cells or primary human T-lymphocytes. If using primary T-lymphocytes, this would be performed by electroporation after stimulation of the primary T-lymphocytes, which has been shown to significantly improve their transfection efficiency (Zhang et al., 2018). As a previous study has indicated that SHP-1 may bind to Y₂₄₈, (Sheppard et al., 2004), we predict that the nanoscopic resolution of FRET will allow for the confirmation of PD-1/SHP-1 interaction. The effect of the phosphorylation state of Y₂₄₈ on PD-1/PD-L1 interactions, using aFRET and iFRET, with both Y₂₄₈A and Y₂₄₈E modified cells should be investigated. In the same manner aFRET can be exploited to determine which signal transducers associate at the cytoplasmic tail of CTLA-4. Whilst a study has confirmed SHP-2 interacts with the cytoplasmic tail of CTLA-4, aFRET could be used to assess other binding partners, such as SHP-1 (Watson et al., 2016). Moreover, the use of CRISPR/Cas12 could be utilised to assess the regulatory mechanism of cytoplasmic phosphorylation on the CTLA-4/CD80 interaction state.

This could significantly improve cancer prognostics by assessing the functionality of both checkpoint receptors alongside their interaction states. Thus, identifying intracellular phosphorylation events as predictive biomarkers of response to therapy and improving patient stratification.

6.2.2: Assessment of CTLA-4/CD86 and PD-1/PD-L2

Whilst CTLA-4/CD80 and PD-1/PD-L1 interactions have been extensively studied in this thesis and in literature elsewhere, comparatively little is known about the engagement of these receptors with other cognate ligands. The PD-1 receptor has another cognate ligand, PD-L2. Phylogenic studies have shown that PD-L2 evolved from a gene duplication event of primordial PD-L1 (Philips et al., 2020). While PD-L1 is expressed widely on both haemopoietic and non-haemopoietic cells, PD-L2 is restricted to antigen presenting cells (APCs). A study has shown that PD-L2 binding to PD-1 on dendritic cells, results in interleukin (IL)-12 production and T-lymphocyte activation. Moreover, an online tool, KM Plotter, has been used to assess on a retrospective NSCLC study (Györfy et al., 2013) whether PD-L2 mRNA (messenger ribonucleic acid) expression correlated with patient outcome. The tool reported that median PD-L2 expression correlated with a significantly improved outcome (P=0.03, Figure 6.1). This could give rise to the rationale that the functional proteomics of PD-1/PD-L2 could yield prognostic value which is a hypothesis to be tested in the future.

Similar to PD-1, CTLA-4 has two competing ligands, CD80 (B7.1) and CD86 (B7.2). CD86 has been shown to be the preferred co-stimulatory ligand for CD28 on regulatory T-cells (Treg) cells, helping maintain their homeostasis. Comparably to PD-L2, CD86 is constitutively expressed on APCs (Halliday et al., 2020). The same tool was utilised to assess CD86 mRNA expression against patient survival in NSCLC. Here, the lowest quartile of CD86 mRNA expression, rather than the median, indicated that those with a lower CD86 expression experienced a significantly worsened outcome ($P=0.041$, Figure 6.2). This could indicate that, if protein functional states were analysed in a spatiotemporal manner, CD86 could also yield prognostic value. However, whilst mRNA expression may be used to identify potential differentially regulated targets of interest, future studies must ensure that the corresponding protein functional states are analysed to yield the most relevant data.

Furthermore, Zhao et al., 2019 have shown, using steady-state FRET, that PD-L1 and CD80 interact directly in *cis*. The study went on to show that this interaction blocks PD-1 signalling and CTLA-4 signalling whilst preserving CD28 signalling. Thus, an increase in PD-L1/CD80 binding could result in a net increase in immune activation via the stimulation of CD28. However, the ratio of PD-L1 to CD80 may alter the immune phenotype exhibited. If CD80 is in excess of PD-L1, CD80 would act to block PD-1/PD-L1 signalling (by forming PD-L1/CD80 interactions), allowing free CD80 to bind CTLA-4 in *trans*, thus downregulating the immune system (if bound to CTLA-4 on conventional T-lymphocytes). If PD-L1 is in excess of CD80, the CD80/PD-L1 complexes would act to reduce available CD80 to interact with CTLA-4 and free PD-L1 would trigger PD-1/PD-L1 signalling (Zhao et al., 2019). Therefore, as part of the emerging philosophy of quantitative immune surveillance, constant surveillance of CD80-PD-L1 complex dynamics, using a modified iFRET protocol could allow for improved patient stratification and treatment in future work.

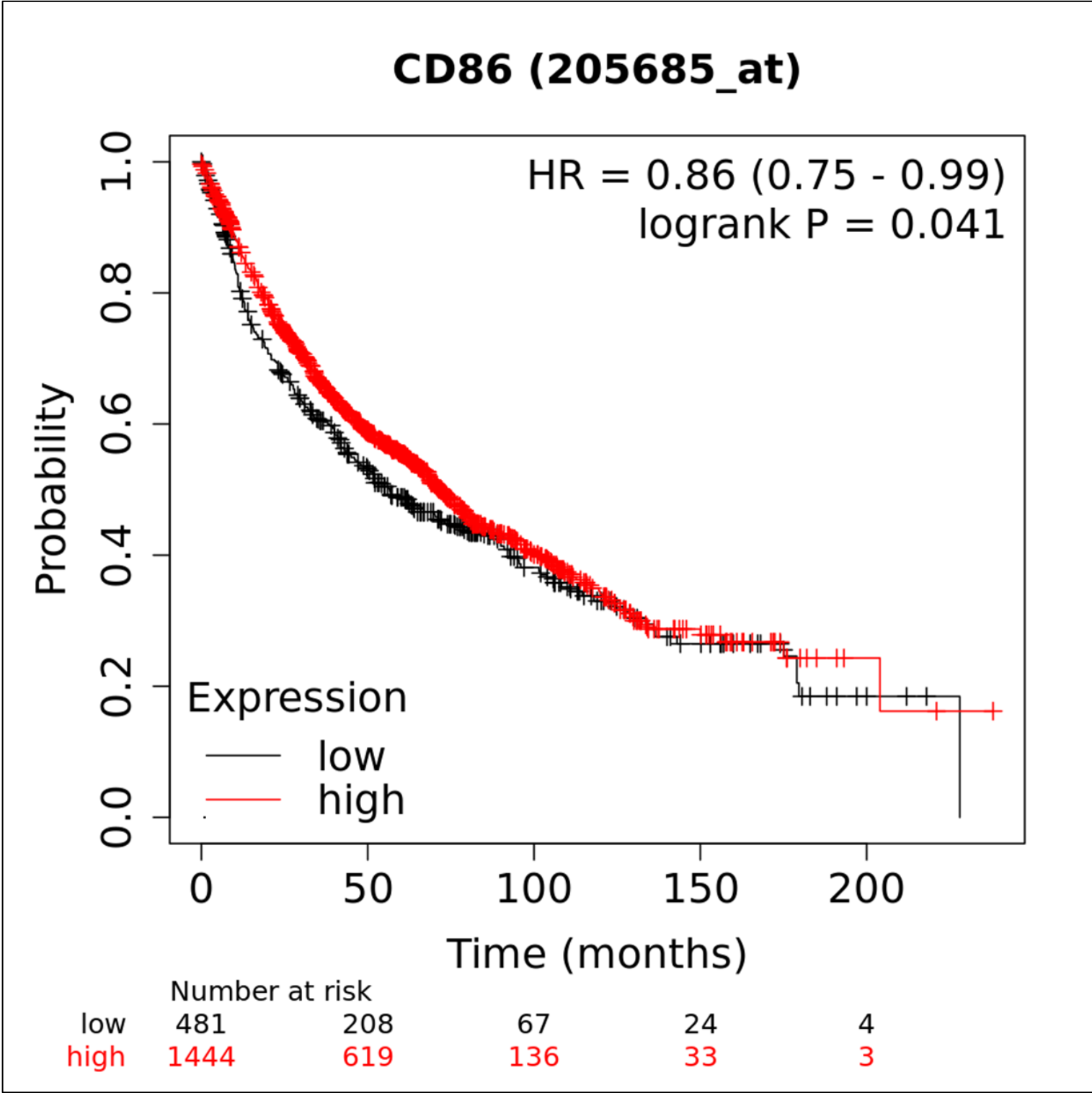


Figure 6.2: Decreased mRNA CD86 expression significantly correlates with a worsened OS in NSCLC. The online tool, KM Plotter, was used to assess whether lower quartile mRNA expression correlated with clinical outcome in a retrospective NSCLC study. It was observed that a lower quartile CD86 expression correlated with a significantly worsened overall survival (P=0.041) in NSCLC. This indicates that CD86 mRNA expression may predict patient outcome, although this should be further studied at the quantitative functional proteomic level. Lower quartile mRNA expression was correlated to overall survival as median mRNA expression failed to correlate with outcome.

6.2.3: Simultaneous Functional Spatial Mapping of Multiple Immune Checkpoints: iFRET and Imaging Mass Spectrometry as Complementary Techniques

The work in this thesis could change the paradigm of immune-oncology through the concept of quantitative immune-surveillance. However, due to the complex nature of the immune system, precise biomarker quantification must be coupled to advanced spatial quantification of the immune-cell subsets that are interacting with a given tumour. Moreover, whilst the work here has, for the first time, quantified checkpoint engagement at a resolution of <10 nm, only two checkpoints have been assessed. A host of known checkpoints are yet to be determined in this manner.

The first point to be addressed would be the spatial quantitation of the immune cells infiltrating the tumour microenvironment. This is likely to consist of a range of immune cells such as macrophages, mast cells, natural killer (NK) cells, dendritic cells and both B- and T-lymphocytes (Giraldo et al., 2019). It will be crucial to create a standardised approach by which these infiltrates are quantified. Of particular importance in the tumour microenvironment are Tregs, tumour-associated macrophages and myeloid-derived suppressor cells (Saleh and Elkord, 2019). Tregs are key mediators of tumorigenesis, constituting 20-50% of circulating CD4⁺ T-lymphocytes in melanoma, NSCLC, gastric and ovarian cancer patients. By contrast, this value is 5-10% in healthy individuals. Tregs promote tumorigenesis by the exerting immunosuppressive functions on effector cells (Saleh and Elkord, 2019). These suppressive functions include production of suppressive cytokines (interleukins(IL)-10, TGF β , IL-35), direct cytotoxicity of effector cells, metabolic arrest and suppression of dendritic cells (Sasidharan Nair and Elkord, 2018). One study has shown that ipilimumab treatment can lead to a depletion of intratumoral Tregs, in the presence of CD68, CD163, Fc γ R expressing macrophages, via antibody-dependant cell-mediated cytotoxicity (Romano et al., 2015). Moreover, it has been seen that anti-PD-1 therapies may lead to an upregulation of other immune checkpoints on Tregs such as TIGIT (T-cell immunoreceptor with Ig and ITIM (immunoreceptor tyrosine-based inhibition motif) domains), TIM-3 (T-cell immunoglobulin mucin-3), LAG-3 (Lymphocyte-activation gene 3) and VISTA (V-domain Ig suppressor of T cell activation). This alludes to the fact that the precise intracellular proteomics of Tregs should be studied in the future, alongside the quantification of Treg interactions with tumour cells. The upregulation of TIGIT, TIM-3, LAG-3 and VISTA present mechanisms whereby secondary resistance to anti-PD-1/PD-L1 and anti-CTLA-4 therapies may arise.

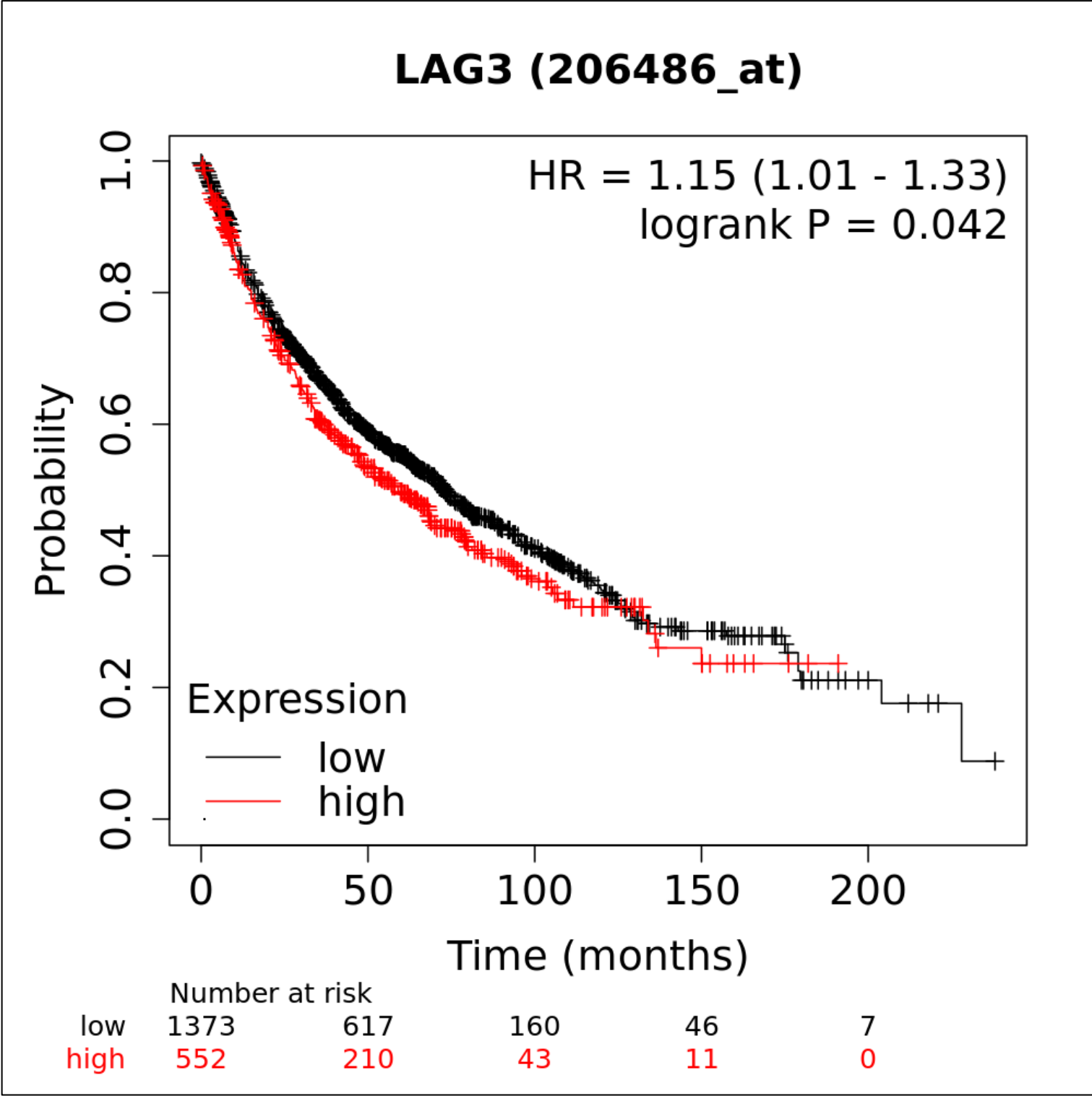


Figure 6.3: Median LAG-3 mRNA expression significantly correlates with a worsened clinical outcome in NSCLC. The online tool, KM Plotter, was used to assess whether median LAG-3 mRNA expression correlated with clinical outcome in a retrospective NSCLC study. It was observed that a higher median LAG-3 expression correlated with a significantly worsened overall survival (P=0.042) in NSCLC. This indicates that LAG-3 mRNA expression may predict patient outcome, although this should be further studied at the quantitative functional proteomic level.

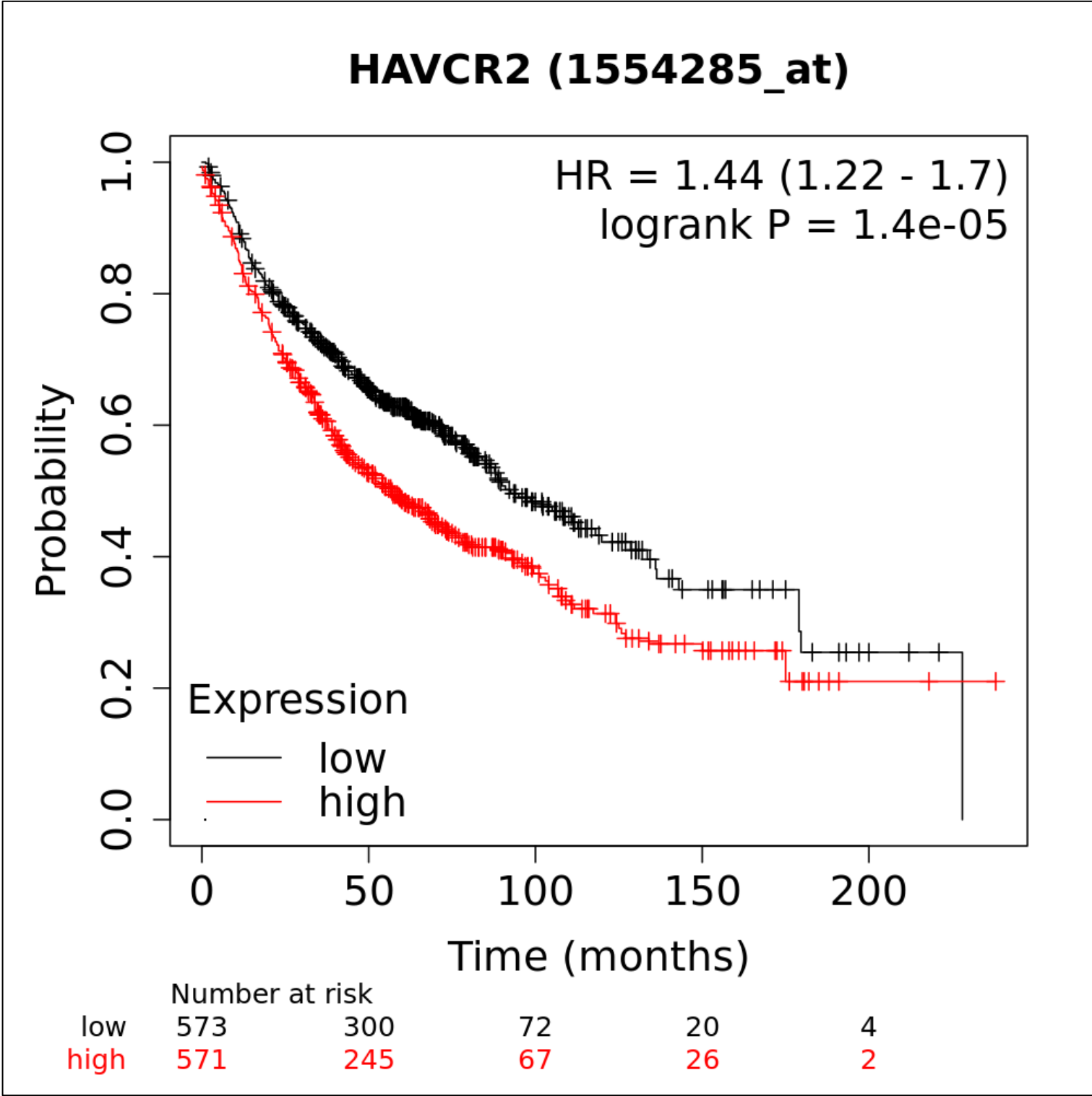


Figure 6.4: Median TIM-3 mRNA expression significantly correlates with a worsened clinical outcome in NSCLC. The online tool, KM Plotter, was used to assess whether median TIM-3 mRNA expression correlated with clinical outcome in a retrospective NSCLC study. It was observed that a higher median TIM-3 expression correlated with a significantly worsened overall survival ($P=1.4 \times 10^{-5}$) in NSCLC. This indicates that TIM-3 mRNA expression may predict patient outcome, although this should be further studied at the quantitative functional proteomic level.

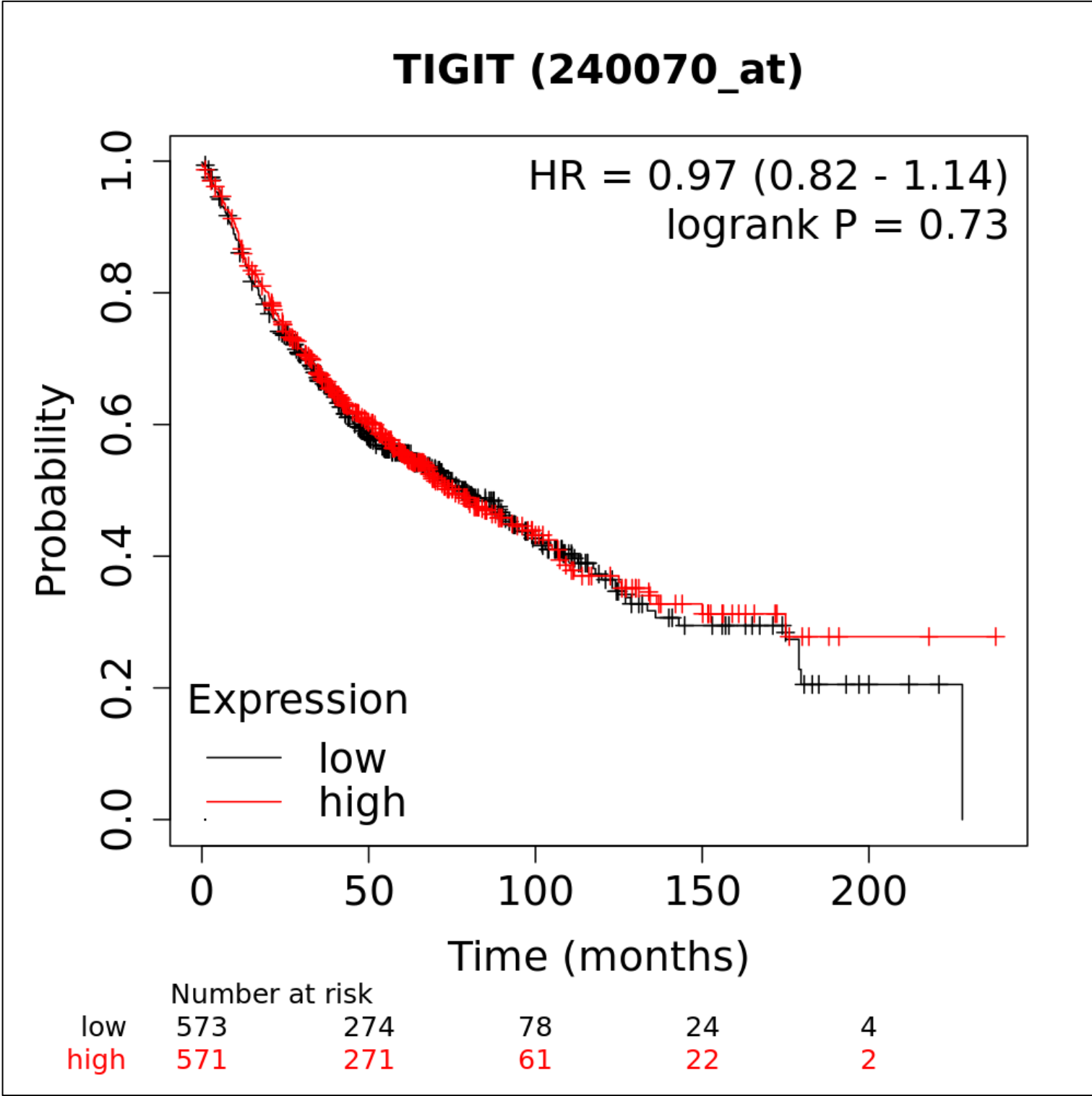


Figure 6.5: Median TIGIT mRNA expression does not correlate with clinical outcome in NSCLC. The online tool, KM Plotter, was used to assess whether median TIGIT mRNA expression correlated with clinical outcome in a retrospective NSCLC study. It was observed that a median TIGIT expression failed to correlate with overall survival (P=0.73) in NSCLC. Whilst this does not identify TIGIT as a potential predictive biomarker at the genomic level, it would be interesting to study the functional proteomics of TIGIT (i.e., receptor-ligand interaction) to determine if TIGIT hold predictive value as a biomarker.

C10orf54 (225372_at)

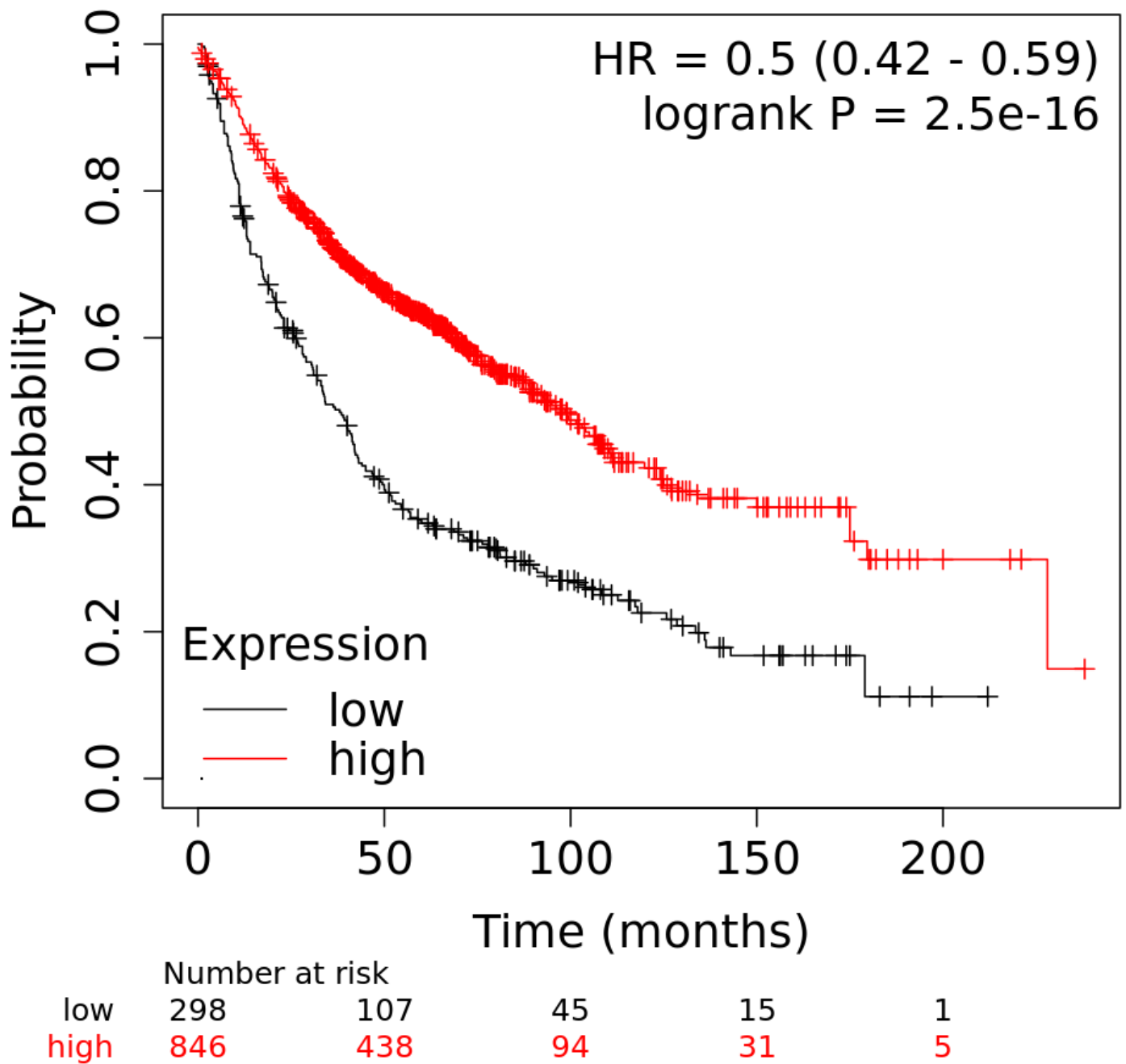


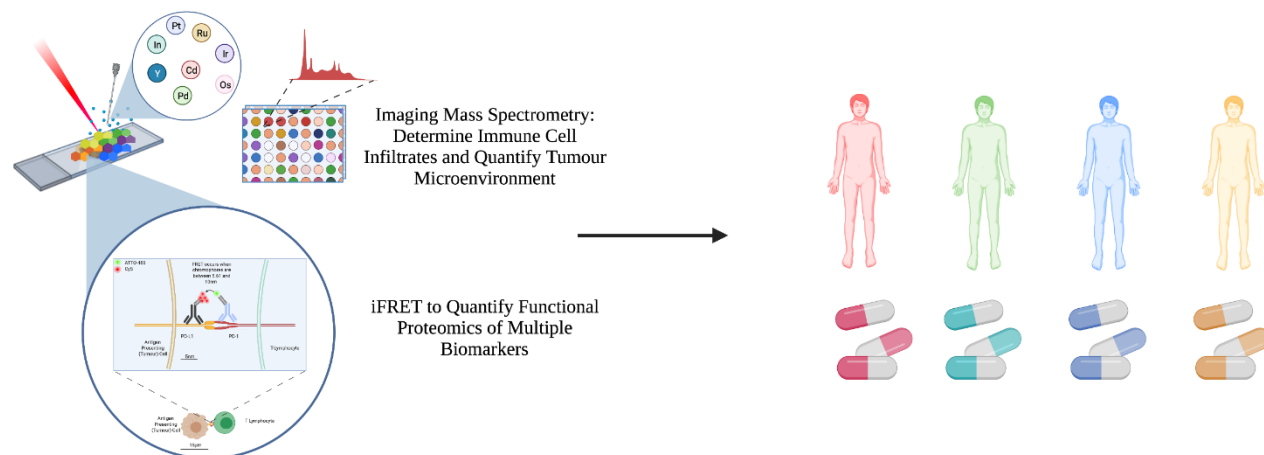
Figure 6.6: Median VISTA mRNA expression correlates with an improved clinical outcome in NSCLC. The online tool, KM Plotter, was used to assess whether median VISTA mRNA expression correlated with clinical outcome in a retrospective NSCLC study. It was observed that a lower median VISTA expression correlated with a significantly worsened overall survival ($P=2.5 \times 10^{-16}$) in NSCLC. This indicates that VISTA mRNA expression may predict patient outcome, although this prediction goes against classical literature, which suggests VISTA expression should correlate with a worsened overall survival by promoting immune evasion and tumorigenesis. Therefore, quantifying the functional proteomics of VISTA will be key in identifying whether it may be a predictive biomarker in cancer.

The targeting of PD-1/PD-L1 and/or CTLA-4/CD80 may apply a selection pressure to intratumoral lymphocytes, resulting in the upregulation of these additional checkpoints. Using the online tool KM Plotter (described above), mRNA expression of TIGIT, TIM-3, LAG-3 and VISTA were used to predict patient outcome in a retrospective NSCLC study. Both increased LAG-3 and TIM-3 mRNA expression correlated with a worsened patient outcome (Figure 6.3 and Figure 6.4, respectively). TIGIT mRNA expression yielded no significant predictive value in the study ($P=0.72$, Figure 6.5) and increased VISTA mRNA expression correlated with an improved patient outcome (Figure 6.6). Whilst genomic analyses can identify differentially regulated genes in disease, this does not necessarily correlate with the functional state of the proteins. Therefore, whilst genomic analysis may elucidate putative immune biomarkers, these analyses should be investigated in parallel to determine whether there are significant correlations with the functional states of the corresponding proteins in immune oncology. These studies should be correlated with the spatial make-up of the immune infiltrates within the tumour microenvironment.

Therefore, a routine spatial mapping of T-lymphocyte subsets, for example, Treg lymphocytes, will be essential in identifying the key checkpoints and mediators that underpin a tumour's evasion from the immune system. This could be achieved, in a sensitive and high-plex manner by imaging mass spectrometry (IMS), paving a way for IMS and iFRET to work in tandem to further immune surveyance, patient stratification and prognoses. In any case, the use of immunohistochemistry in precision medicine and prognostics is warranted, provided it is carried out with suitable sensitivity, precision and spatial resolution. The future direction of quantitative immune surveyance, underpinned by iFRET and IMS is outlined in Figure 6.7.

In this body of work, we have paved a novel path for implementing quantitative immune-surveyance that can complement a range of routine functional proteomics to advance the fields of precision medicine and cancer prognostics.

iFRET in tandem with IMS may aid initial patient stratification and prescription of immunotherapies



iFRET is proposed to routinely assess immune checkpoint interaction evolution within a patient over time, thus allowing for continued precision medicine within a patient

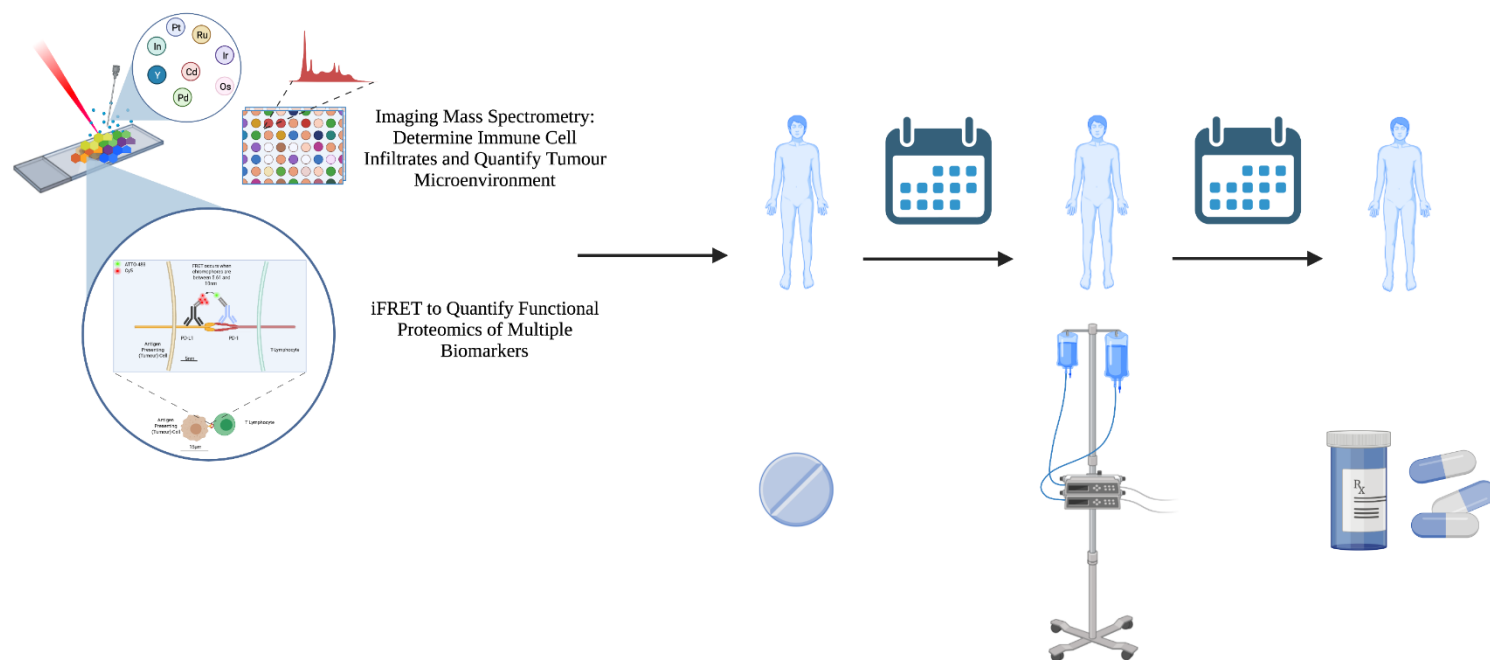


Figure 6.7: Routine patient screening with iFRET and IMS may change the paradigm of current immunotherapy prescriptions. Top panel: We propose that iFRET analysis, combined with quantitative, spatial high-plex proteomics (to map immune cell infiltration, for example) will allow for improved patient stratification, treatment, and prescriptions in cancer. **Bottom panel:** It is further proposed that iFRET may be used as part of a routine quantitative immune surveillance approach which allows for the continued monitoring of patients in a high-plex manner. This would allow for the regular updating of patient prescription and treatment options as well as assessing patient response and predicting acquired resistance to treatment.

Chapter 7: References

- ABRAHAM, R. T. & WEISS, A. 2004. Jurkat T cells and development of the T-cell receptor signalling paradigm. *Nature Reviews Immunology*, 4, 301-308.
- ACUTO, O. & MICHEL, F. 2003. CD28-mediated co-stimulation: a quantitative support for TCR signalling. *Nat Rev Immunol*, 3, 939-51.
- AGARWAL, A. & TYNER, J. W. 2016. RNAi Screening of Leukemia Cells Using Electroporation. *Methods in molecular biology (Clifton, N.J.)*, 1470, 85-94.
- ALSAAB, H. O., SAU, S., ALZHRANI, R., TATIPARTI, K., BHISE, K., KASHAW, S. K. & IYER, A. K. 2017. PD-1 and PD-L1 Checkpoint Signaling Inhibition for Cancer Immunotherapy: Mechanism, Combinations, and Clinical Outcome. *Front Pharmacol*, 8, 561.
- AMARANTE-MENDES, G. P., ADJEMIAN, S., BRANCO, L. M., ZANETTI, L. C., WEINLICH, R. & BORTOLUCI, K. R. 2018. Pattern Recognition Receptors and the Host Cell Death Molecular Machinery. *Frontiers in Immunology*, 9.
- ATKINS, P. & DE PAULA, J. 2009. *Elements of Physical Chemistry*, Great Britain, Oxford University Press.
- ATLAS, T. H. P. 2021. *PDCD1 Cell Atlas* [Online]. The Human Protein Atlas. Available: <https://www.proteinatlas.org/ENSG00000188389-PDCD1/cell> [Accessed 24.08.2021 2021].
- AUTIO, K. A., BONI, V., HUMPHREY, R. W. & NAING, A. 2020. Probody Therapeutics: An Emerging Class of Therapies Designed to Enhance On-Target Effects with Reduced Off-Tumor Toxicity for Use in Immuno-Oncology. *Clin Cancer Res*, 26, 984-989.
- AYYADEVARA, V. & ROH, K. H. 2020. Calcium enhances polyplex-mediated transfection efficiency of plasmid DNA in Jurkat cells. *Drug Deliv*, 27, 805-815.
- BASTIAENS, P. I. & SQUIRE, A. 1999. Fluorescence lifetime imaging microscopy: spatial resolution of biochemical processes in the cell. *Trends Cell Biol*, 9, 48-52.
- BENNETT, C. L., CHRISTIE, J., RAMSDELL, F., BRUNKOW, M. E., FERGUSON, P. J., WHITESELL, L., KELLY, T. E., SAULSBURY, F. T., CHANCE, P. F. & OCHS, H. D. 2001. The immune dysregulation, polyendocrinopathy, enteropathy, X-linked syndrome (IPEX) is caused by mutations of FOXP3. *Nat Genet*, 27, 20-1.
- BEVERLEY, P. 1991. Immunological memory in T cells. *Curr Opin Immunol*, 3, 355-60.
- BISHOP, D. P., COLE, N., ZHANG, T., DOBLE, P. A. & HARE, D. J. 2018. A guide to integrating immunohistochemistry and chemical imaging. *Chemical Society Reviews*, 47, 3770-3787.
- BOIVIN, W. A., COOPER, D. M., HIEBERT, P. R. & GRANVILLE, D. J. 2009. Intracellular versus extracellular granzyme B in immunity and disease: challenging the dogma. *Laboratory Investigation*, 89, 1195-1220.

- BOUSSIOTIS, V. A. 2016. Molecular and Biochemical Aspects of the PD-1 Checkpoint Pathway. *The New England journal of medicine*, 375, 1767-1778.
- BROUNS, S. J., JORE, M. M., LUNDGREN, M., WESTRA, E. R., SLIJKHUIS, R. J., SNIJDERS, A. P., DICKMAN, M. J., MAKAROVA, K. S., KOONIN, E. V. & VAN DER OOST, J. 2008. Small CRISPR RNAs guide antiviral defense in prokaryotes. *Science*, 321, 960-4.
- BRUNKOW, M. E., JEFFERY, E. W., HJERRILD, K. A., PAEPER, B., CLARK, L. B., YASAYKO, S. A., WILKINSON, J. E., GALAS, D., ZIEGLER, S. F. & RAMSDELL, F. 2001. Disruption of a new forkhead/winged-helix protein, scurfy, results in the fatal lymphoproliferative disorder of the scurfy mouse. *Nat Genet*, 27, 68-73.
- BUCHBINDER, E. I. & DESAI, A. 2016. CTLA-4 and PD-1 Pathways: Similarities, Differences, and Implications of Their Inhibition. *American journal of clinical oncology*, 39, 98-106.
- BUMPUS, H. 1928. The apparent disappearance of pulmonary metastases in a case of hypernephroma following nephrectomy. *Journal of Urology*, 20, 185-191.
- CALLAHAN, M. K., POSTOW, M. A. & WOLCHOK, J. D. 2013. Immunomodulatory therapy for melanoma: ipilimumab and beyond. *Clin Dermatol*, 31, 191-9.
- CALLEJA, V., ALCOR, D., LAGUERRE, M., PARK, J., VOJNOVIC, B., HEMMINGS, B. A., DOWNWARD, J., PARKER, P. J. & LARIJANI, B. 2007. Intramolecular and intermolecular interactions of protein kinase B define its activation in vivo. *PLoS Biol*, 5, e95.
- CANTRELL, D. 1996. T CELL ANTIGEN RECEPTOR SIGNAL TRANSDUCTION PATHWAYS. *Annual Review of Immunology*, 14, 259-274.
- CHEN, P., ZHOU, J., WAN, Y., LIU, H., LI, Y., LIU, Z., WANG, H., LEI, J., ZHAO, K., ZHANG, Y., WANG, Y., ZHANG, X. & YIN, L. 2020. A Cas12a ortholog with stringent PAM recognition followed by low off-target editing rates for genome editing. *Genome Biology*, 21, 78.
- CHEN, X., WEI, S., JI, Y., GUO, X. & YANG, F. 2015. Quantitative proteomics using SILAC: Principles, applications, and developments. *Proteomics*, 15, 3175-92.
- CHENG, X., VEVERKA, V., RADHAKRISHNAN, A., WATERS, L. C., MUSKETT, F. W., MORGAN, S. H., HUO, J., YU, C., EVANS, E. J., LESLIE, A. J., GRIFFITHS, M., STUBBERFIELD, C., GRIFFIN, R., HENRY, A. J., JANSSON, A., LADBURY, J. E., IKEMIZU, S., CARR, M. D. & DAVIS, S. J. 2013. Structure and interactions of the human programmed cell death 1 receptor. *J Biol Chem*, 288, 11771-85.
- COONS, A. H., CREECH, H. J. & JONES, R. N. 1941. Immunological Properties of an Antibody Containing a Fluorescent Group. *Proceedings of the Society for Experimental Biology and Medicine*, 47, 200-202.
- CRAGGS, G. & KELLIE, S. 2001. A functional nuclear localization sequence in the C-terminal domain of SHP-1. *J Biol Chem*, 276, 23719-25.

- CURNOCK, A. P. & WARD, S. G. 2003. Development and characterisation of tetracycline-regulated phosphoinositide 3-kinase mutants: assessing the role of multiple phosphoinositide 3-kinases in chemokine signaling. *J Immunol Methods*, 273, 29-41.
- DAVIS, A. A. & PATEL, V. G. 2019. The role of PD-L1 expression as a predictive biomarker: an analysis of all US Food and Drug Administration (FDA) approvals of immune checkpoint inhibitors. *Journal for ImmunoTherapy of Cancer*, 7, 278.
- DE BAÈRE, T., AUPÉRIN, A., DESCHAMPS, F., CHEVALLIER, P., GAUBERT, Y., BOIGE, V., FONCK, M., ESCUDIER, B. & PALUSSIÈRE, J. 2015. Radiofrequency ablation is a valid treatment option for lung metastases: experience in 566 patients with 1037 metastases. *Ann Oncol*, 26, 987-991.
- DE BAERE, T., PALUSSIÈRE, J., AUPERIN, A., HAKIME, A., ABDEL-REHIM, M., KIND, M., DROMAIN, C., RAVAUD, A., TEBBOUNE, N., BOIGE, V., MALKA, D., LAFONT, C. & DUCREUX, M. 2006. Midterm local efficacy and survival after radiofrequency ablation of lung tumors with minimum follow-up of 1 year: prospective evaluation. *Radiology*, 240, 587-96.
- DEBAIZE, L., JAKOBCZYK, H., RIO, A. G., GANDEMÉR, V. & TROADEC, M. B. 2017. Optimization of proximity ligation assay (PLA) for detection of protein interactions and fusion proteins in non-adherent cells: application to pre-B lymphocytes. *Mol Cytogenet*, 10, 27.
- DELAHUNT, B., CHEVILLE, J. C., MARTIGNONI, G., HUMPHREY, P. A., MAGI-GALLUZZI, C., MCKENNEY, J., EGEVAD, L., ALGABA, F., MOCH, H., GRIGNON, D. J., MONTIRONI, R., SRIGLEY, J. R. & MEMBERS OF THE, I. R. T. P. 2013. The International Society of Urological Pathology (ISUP) grading system for renal cell carcinoma and other prognostic parameters. *Am J Surg Pathol*, 37, 1490-504.
- DEN BROK, M. H., SUTMULLER, R. P., NIERKENS, S., BENNINK, E. J., FRIELINK, C., TOONEN, L. W., BOERMAN, O. C., FIGDOR, C. G., RUERS, T. J. & ADEMA, G. J. 2006. Efficient loading of dendritic cells following cryo and radiofrequency ablation in combination with immune modulation induces anti-tumour immunity. *Br J Cancer*, 95, 896-905.
- DUHEN, T., DUHEN, R., MONTLER, R., MOSES, J., MOUDGIL, T., DE MIRANDA, N. F., GOODALL, C. P., BLAIR, T. C., FOX, B. A., MCDERMOTT, J. E., CHANG, S.-C., GRUNKEMEIER, G., LEIDNER, R., BELL, R. B. & WEINBERG, A. D. 2018. Co-expression of CD39 and CD103 identifies tumor-reactive CD8 T cells in human solid tumors. *Nature Communications*, 9, 2724.
- E GRATTON, D M JAMESON, A. & HALL, R. D. 1984. Multifrequency Phase and Modulation Fluorometry. *Annual Review of Biophysics and Bioengineering*, 13, 105-124.

- ENGELHARDT, J. J., SULLIVAN, T. J. & ALLISON, J. P. 2006. CTLA-4 Overexpression Inhibits T Cell Responses through a CD28-B7-Dependent Mechanism. *The Journal of Immunology*, 177, 1052-1061.
- ESENSTEN, J. H., HELOU, Y. A., CHOPRA, G., WEISS, A. & BLUESTONE, J. A. 2016. CD28 Costimulation: From Mechanism to Therapy. *Immunity*, 44, 973-988.
- FARES, J., FARES, M. Y., KHACHFE, H. H., SALHAB, H. A. & FARES, Y. 2020. Molecular principles of metastasis: a hallmark of cancer revisited. *Signal Transduction and Targeted Therapy*, 5, 28.
- FERLAY, J., COLOMBET, M., SOERJOMATARAM, I., PARKIN, D. M., PIÑEROS, M., ZNAOR, A. & BRAY, F. 2021. Cancer statistics for the year 2020: An overview. *Int J Cancer*.
- FÖRSTER, T. 1946. Energy migration and fluorescence. 1946. *J Biomed Opt*, 17, 011002.
- FREEMAN, G. J., BORRIELLO, F., HODES, R. J., REISER, H., GRIBBEN, J. G., NG, J. W., KIM, J., GOLDBERG, J. M., HATHCOCK, K., LASZLO, G. & ET AL. 1993. Murine B7-2, an alternative CTLA4 counter-receptor that costimulates T cell proliferation and interleukin 2 production. *J Exp Med*, 178, 2185-92.
- FUELLER, J., HERBST, K., MEURER, M., GUBICZA, K., KURTULMUS, B., KNOPF, J. D., KIRRMAYER, D., BUCHMULLER, B. C., PEREIRA, G., LEMBERG, M. K. & KNOP, M. 2020. CRISPR-Cas12a-assisted PCR tagging of mammalian genes. *Journal of Cell Biology*, 219.
- GARCÍA-MULERO, S., ALONSO, M. H., PARDO, J., SANTOS, C., SANJUAN, X., SALAZAR, R., MORENO, V., PIULATS, J. M. & SANZ-PAMPLONA, R. 2020. Lung metastases share common immune features regardless of primary tumor origin. *Journal for ImmunoTherapy of Cancer*, 8, e000491.
- GIRALDO, N. A., NGUYEN, P., ENGLE, E. L., KAUNITZ, G. J., COTTRELL, T. R., BERRY, S., GREEN, B., SONI, A., CUDA, J. D., STEIN, J. E., SUNSHINE, J. C., SUCCARIA, F., XU, H., OGURTSOVA, A., DANILOVA, L., CHURCH, C. D., MILLER, N. J., FLING, S., LUNDGREN, L., RAMCHURREN, N., YEARLEY, J. H., LIPSON, E. J., CHEEVER, M., ANDERS, R. A., NGHIEM, P. T., TOPALIAN, S. L. & TAUBE, J. M. 2018. Multidimensional, quantitative assessment of PD-1/PD-L1 expression in patients with Merkel cell carcinoma and association with response to pembrolizumab. *J Immunother Cancer*, 6, 99.
- GIRALDO, N. A., SANCHEZ-SALAS, R., PESKE, J. D., VANO, Y., BECHT, E., PETITPREZ, F., VALIDIRE, P., INGELS, A., CATHELINEAU, X., FRIDMAN, W. H. & SAUTÈS-FRIDMAN, C. 2019. The clinical role of the TME in solid cancer. *British Journal of Cancer*, 120, 45-53.
- GOLUBOVSKAYA, V. & WU, L. 2016. Different Subsets of T Cells, Memory, Effector Functions, and CAR-T Immunotherapy. *Cancers*, 8, 36.

- GROVES, T., SMILEY, P., COOKE, M. P., FORBUSH, K., PERLMUTTER, R. M. & GUIDOS, C. J. 1996. Fyn Can Partially Substitute for Lck in T Lymphocyte Development. *Immunity*, 5, 417-428.
- GUERRERA, I. C. & KLEINER, O. 2005. Application of mass spectrometry in proteomics. *Biosci Rep*, 25, 71-93.
- GYÖRFFY, B., SUROWIAK, P., BUDCZIES, J. & LÁNCZKY, A. 2013. Online survival analysis software to assess the prognostic value of biomarkers using transcriptomic data in non-small-cell lung cancer. *PLoS One*, 8, e82241.
- HALLIDAY, N., WILLIAMS, C., KENNEDY, A., WATERS, E., PESENACKER, A. M., SOSKIC, B., HINZE, C., HOU, T. Z., ROWSHANRAVAN, B., JANMAN, D., WALKER, L. S. K. & SANSOM, D. M. 2020. CD86 Is a Selective CD28 Ligand Supporting FoxP3+ Regulatory T Cell Homeostasis in the Presence of High Levels of CTLA-4. *Frontiers in Immunology*, 11.
- HANAHAN, D. & WEINBERG, R. A. 2000. The hallmarks of cancer. *Cell*, 100, 57-70.
- HANAHAN, D. & WEINBERG, R. A. 2011. Hallmarks of cancer: the next generation. *Cell*, 144, 646-74.
- HANAHAN, D. & WEINBERG, R. A. 2017. Biological Hallmarks of Cancer. In: BAST RC, E. A. (ed.) *Holland-Frei Cancer Medicine*. 9th ed. Hoboken, New Jersey: Wiley-B;ackwell.
- HART, S. P., SMITH, J. R. & DRANSFIELD, I. 2004. Phagocytosis of opsonized apoptotic cells: roles for 'old-fashioned' receptors for antibody and complement. *Clin Exp Immunol*, 135, 181-5.
- HATZIOANNOU, A., BOUMPAS, A., PAPADOPOULOU, M., PAPAFRAGKOS, I., VARVERI, A., ALISSAFI, T. & VERGINIS, P. 2021. Regulatory T Cells in Autoimmunity and Cancer: A Duplicitous Lifestyle. *Frontiers in Immunology*, 12.
- HEIDEGGER, I., PIRCHER, A. & PICHLER, R. 2019. Targeting the Tumor Microenvironment in Renal Cell Cancer Biology and Therapy. *Frontiers in oncology*, 9, 490-490.
- HESS, A., PALUSSIÈRE, J., GOYERS, J. F., GUTH, A., AUPÉRIN, A. & DE BAÈRE, T. 2011. Pulmonary radiofrequency ablation in patients with a single lung: feasibility, efficacy, and tolerance. *Radiology*, 258, 635-42.
- HIAM-GALVEZ, K. J., ALLEN, B. M. & SPITZER, M. H. 2021. Systemic immunity in cancer. *Nature Reviews Cancer*, 21, 345-359.
- HILL, M. M. & HEMMINGS, B. A. 2002. Inhibition of protein kinase B/Akt. implications for cancer therapy. *Pharmacol Ther*, 93, 243-51.
- HOF, P., PLUSKEY, S., DHE-PAGANON, S., ECK, M. J. & SHOELSON, S. E. 1998. Crystal Structure of the Tyrosine Phosphatase SHP-2. *Cell*, 92, 441-450.
- HOFFMANN, R. T., JAKOBS, T. F., REISER, M. F. & HELMBERGER, T. K. 2004. [Radiofrequency ablation of lung tumors and -metastases]. *Radiologe*, 44, 364-9.

- HOTHORN, T. & LAUSEN, B. 2003. On the exact distribution of maximally selected rank statistics. *Computational Statistics & Data Analysis*, 43, 121-137.
- HUGHES, C. E. & NIBBS, R. J. B. 2018. A guide to chemokines and their receptors. *The FEBS journal*, 285, 2944-2971.
- HWANG, J.-R., BYEON, Y., KIM, D. & PARK, S.-G. 2020. Recent insights of T cell receptor-mediated signaling pathways for T cell activation and development. *Experimental & Molecular Medicine*, 52, 750-761.
- INTLEKOFER, A. M. & THOMPSON, C. B. 2013. At the bench: preclinical rationale for CTLA-4 and PD-1 blockade as cancer immunotherapy. *Journal of leukocyte biology*, 94, 25-39.
- JAMES, J. R., OLIVEIRA, M. I., CARMO, A. M., IABONI, A. & DAVIS, S. J. 2006. A rigorous experimental framework for detecting protein oligomerization using bioluminescence resonance energy transfer. *Nature Methods*, 3, 1001-1006.
- JANSSEN, E. M., LEMMENS, E. E., WOLFE, T., CHRISTEN, U., VON HERRATH, M. G. & SCHOENBERGER, S. P. 2003. CD4⁺ T cells are required for secondary expansion and memory in CD8⁺ T lymphocytes. *Nature*, 421, 852-856.
- JENSEN, K., KRUSENSTJERNA-HAFSTRØM, R., LOHSE, J., PETERSEN, K. H. & DERAND, H. 2017. A novel quantitative immunohistochemistry method for precise protein measurements directly in formalin-fixed, paraffin-embedded specimens: analytical performance measuring HER2. *Mod Pathol*, 30, 180-193.
- JINEK, M., CHYLINSKI, K., FONFARA, I., HAUER, M., DOUDNA, J. A. & CHARPENTIER, E. 2012. A programmable dual-RNA-guided DNA endonuclease in adaptive bacterial immunity. *Science*, 337, 816-21.
- JOHNSON, D. B., BORDEAUX, J., KIM, J. Y., VAUPEL, C., RIMM, D. L., HO, T. H., JOSEPH, R. W., DAUD, A. I., CONRY, R. M., GAUGHAN, E. M., HERNANDEZ-AYA, L. F., DIMOU, A., FUNCHAIN, P., SMITHY, J., WITTE, J. S., MCKEE, S. B., KO, J., WRANGLE, J. M., DABBAS, B., TANGRI, S., LAMEH, J., HALL, J., MARKOWITZ, J., BALKO, J. M. & DAKAPPAGARI, N. 2018. Quantitative Spatial Profiling of PD-1/PD-L1 Interaction and HLA-DR/IDO-1 Predicts Improved Outcomes of Anti-PD-1 Therapies in Metastatic Melanoma. *Clin Cancer Res*, 24, 5250-5260.
- KIM, H., LEE, W.-J., OH, Y., KANG, S.-H., HUR, J. K., LEE, H., SONG, W., LIM, K.-S., PARK, Y.-H., SONG, B.-S., JIN, Y. B., JUN, B.-H., JUNG, C., LEE, D.-S., KIM, S.-U. & LEE, S. H. 2020. Enhancement of target specificity of CRISPR–Cas12a by using a chimeric DNA–RNA guide. *Nucleic Acids Research*, 48, 8601-8616.
- KONG, A., LÉBOUCHER, P., LEEK, R., CALLEJA, V., WINTER, S., HARRIS, A., PARKER, P. J. & LARIJANI, B. 2006. Prognostic value of an activation state marker for epidermal growth factor receptor in tissue microarrays of head and neck cancer. *Cancer Res*, 66, 2834-43.

- KRYSTEL-WHITTEMORE, M., DILEEPAN, K. N. & WOOD, J. G. 2016. Mast Cell: A Multi-Functional Master Cell. *Frontiers in Immunology*, 6.
- LAKOWICZ, J. R. 2002. *Topics in Fluorescence Spectroscopy Volume 2: Principles*, Boston, MA, Springer.
- LAM, J. S., LEPPERT, J. T., BELLDEGRUN, A. S. & FIGLIN, R. A. 2005. Novel approaches in the therapy of metastatic renal cell carcinoma. *World J Urol*, 23, 202-12.
- LAUSEN, B. & SCHUMACHER, M. 1992. Maximally Selected Rank Statistics. *Biometrics*, 48, 73-85.
- LÁZÁR-MOLNÁR, E., SCANDIUZZI, L., BASU, I., QUINN, T., SYLVESTRE, E., PALMIERI, E., RAMAGOPAL, U. A., NATHENSON, S. G., GUHA, C. & ALMO, S. C. 2017. Structure-guided development of a high-affinity human Programmed Cell Death-1: Implications for tumor immunotherapy. *EBioMedicine*, 17, 30-44.
- LIN, D. Y.-W., TANAKA, Y., IWASAKI, M., GITTIS, A. G., SU, H.-P., MIKAMI, B., OKAZAKI, T., HONJO, T., MINATO, N. & GARBOCZI, D. N. 2008. The PD-1/PD-L1 complex resembles the antigen-binding Fv domains of antibodies and T cell receptors. *Proceedings of the National Academy of Sciences*, 105, 3011-3016.
- LINO, C. A., HARPER, J. C., CARNEY, J. P. & TIMLIN, J. A. 2018. Delivering CRISPR: a review of the challenges and approaches. *Drug Deliv*, 25, 1234-1257.
- LÖFFLER, M. W., NUSSBAUM, B., JÄGER, G., JURMEISTER, P. S., BUDCZIES, J., PEREIRA, P. L., CLASEN, S., KOWALEWSKI, D. J., MÜHLENBRUCH, L., KÖNIGSRÄINER, I., BECKERT, S., LADURNER, R., WAGNER, S., BULLINGER, F., GROSS, T. H., SCHROEDER, C., SIPOS, B., KÖNIGSRÄINER, A., STEVANOVIĆ, S., DENKERT, C., RAMMENSEE, H.-G., GOUTTEFANGEAS, C. & HAEN, S. P. 2019. A Non-interventional Clinical Trial Assessing Immune Responses After Radiofrequency Ablation of Liver Metastases From Colorectal Cancer. *Frontiers in immunology*, 10, 2526-2526.
- LOHSE, J., PETERSEN, K. H., WOLLER, N. C., PEDERSEN, H. C., SKLADTCHIKOVA, G. & JØRGENSEN, R. M. 2014. Improved Catalyzed Reporter Deposition, iCARD. *Bioconjugate Chemistry*, 25, 1036-1042.
- LOPEZ, J. I. 2016. Intratumor heterogeneity in clear cell renal cell carcinoma: a review for the practicing pathologist. *APMIS*, 124, 153-9.
- LÓPEZ, J. I. & CORTÉS, J. M. 2017. Multisite tumor sampling: a new tumor selection method to enhance intratumor heterogeneity detection. *Hum Pathol*, 64, 1-6.
- MA, X., ZHANG, Y., WANG, S., WEI, H. & YU, J. 2021. Immune checkpoint inhibitor (ICI) combination therapy compared to monotherapy in advanced solid cancer: A systematic review. *Journal of Cancer*, 12, 1318-1333.

- MACKLIN, A., KHAN, S. & KISLINGER, T. 2020. Recent advances in mass spectrometry based clinical proteomics: applications to cancer research. *Clinical Proteomics*, 17, 17.
- MADONNA, G., BALLESTEROS-MERINO, C., FENG, Z., BIFULCO, C., CAPONE, M., GIANNARELLI, D., MALLARDO, D., SIMEONE, E., GRIMALDI, A. M., CARACÒ, C., BOTTI, G., FOX, B. A. & ASCIERTO, P. A. 2018. PD-L1 expression with immune-infiltrate evaluation and outcome prediction in melanoma patients treated with ipilimumab. *Oncoimmunology*, 7, e1405206.
- MAHMOUDI, M. & FAROKHZAD, O. C. 2017. Cancer immunotherapy: Wound-bound checkpoint blockade. *Nature Biomedical Engineering*, 1, 0031.
- MAHONEY, K. M., RENNERT, P. D. & FREEMAN, G. J. 2015. Combination cancer immunotherapy and new immunomodulatory targets. *Nat Rev Drug Discov*, 14, 561-84.
- MAKAROVA, K. S., HAFT, D. H., BARRANGOU, R., BROUNS, S. J., CHARPENTIER, E., HORVATH, P., MOINEAU, S., MOJICA, F. J., WOLF, Y. I., YAKUNIN, A. F., VAN DER OOST, J. & KOONIN, E. V. 2011. Evolution and classification of the CRISPR-Cas systems. *Nat Rev Microbiol*, 9, 467-77.
- MAMESSIER, E., SYLVAIN, A., THIBULT, M. L., HOUVENAEGHEL, G., JACQUEMIER, J., CASTELLANO, R., GONÇALVES, A., ANDRÉ, P., ROMAGNÉ, F., THIBAUT, G., VIENS, P., BIRNBAUM, D., BERTUCCI, F., MORETTA, A. & OLIVE, D. 2011. Human breast cancer cells enhance self tolerance by promoting evasion from NK cell antitumor immunity. *J Clin Invest*, 121, 3609-22.
- MARENGÈRE, L. E. M., WATERHOUSE, P., DUNCAN, G. S., MITTRÜCKER, H.-W., FENG, G.-S. & MAK, T. W. 1996. Regulation of T Cell Receptor Signaling by Tyrosine Phosphatase SHP Association with CTLA-4. *Science*, 272, 1170-1173.
- MARSHALL, J. S., WARRINGTON, R., WATSON, W. & KIM, H. L. 2018. An introduction to immunology and immunopathology. *Allergy, Asthma & Clinical Immunology*, 14, 49.
- MERRITT, C. R., ONG, G. T., CHURCH, S. E., BARKER, K., DANAHER, P., GEISS, G., HOANG, M., JUNG, J., LIANG, Y., MCKAY-FLEISCH, J., NGUYEN, K., NORGAARD, Z., SORG, K., SPRAGUE, I., WARREN, C., WARREN, S., WEBSTER, P. J., ZHOU, Z., ZOLLINGER, D. R., DUNAWAY, D. L., MILLS, G. B. & BEECHEM, J. M. 2020. Multiplex digital spatial profiling of proteins and RNA in fixed tissue. *Nat Biotechnol*, 38, 586-599.
- MILES, J., APPLEBEE, C. J., LÉBOUCHER, P., LOPEZ-FERNANDEZ, S., LEE, D. J., GUARCH, R., WARD, S., PARKER, P. J., LOPEZ, J. I. & LARIJANI, B. 2017. Time resolved amplified FRET identifies protein kinase B activation state as a marker for poor prognosis in clear cell renal cell carcinoma. *BBA Clin*, 8, 97-102.

- MLECNIK, B., VAN DEN EYNDE, M., BINDEA, G., CHURCH, S. E., VASATURO, A., FREDRIKSEN, T., LAFONTAINE, L., HAICHEUR, N., MARLIOT, F., DEBETANCOURT, D., PAIRET, G., JOURET-MOURIN, A., GIGOT, J. F., HUBERT, C., DANSE, E., DRAGEAN, C., CARRASCO, J., HUMBLET, Y., VALGE-ARCHER, V., BERGER, A., PAGÈS, F., MACHIELS, J. P. & GALON, J. 2018. Comprehensive Intrametastatic Immune Quantification and Major Impact of Immunoscore on Survival. *J Natl Cancer Inst*, 110.
- MOJICA, F. J., DÍEZ-VILLASEÑOR, C., GARCÍA-MARTÍNEZ, J. & SORIA, E. 2005. Intervening sequences of regularly spaced prokaryotic repeats derive from foreign genetic elements. *J Mol Evol*, 60, 174-82.
- NGWA, W., IRABOR, O. C., SCHOENFELD, J. D., HESSER, J., DEMARIA, S. & FORMENTI, S. C. 2018. Using immunotherapy to boost the abscopal effect. *Nature Reviews Cancer*, 18, 313-322.
- NORRIS, J. L. & CAPRIOLI, R. M. 2013. Analysis of tissue specimens by matrix-assisted laser desorption/ionization imaging mass spectrometry in biological and clinical research. *Chemical reviews*, 113, 2309-2342.
- NUNES-XAVIER, C. E., ANGULO, J. C., PULIDO, R. & LÓPEZ, J. I. 2019. A Critical Insight into the Clinical Translation of PD-1/PD-L1 Blockade Therapy in Clear Cell Renal Cell Carcinoma. *Curr Urol Rep*, 20, 1.
- OKAZAKI, T. & HONJO, T. 2006. The PD-1-PD-L pathway in immunological tolerance. *Trends Immunol*, 27, 195-201.
- OKEN, M. M., CREECH, R. H., TORMEY, D. C., HORTON, J., DAVIS, T. E., MCFADDEN, E. T. & CARBONE, P. P. 1982. Toxicity and response criteria of the Eastern Cooperative Oncology Group. *Am J Clin Oncol*, 5, 649-55.
- OLDEN, B. R., CHENG, Y., YU, J. L. & PUN, S. H. 2018. Cationic polymers for non-viral gene delivery to human T cells. *J Control Release*, 282, 140-147.
- OSIŃSKA, I., POPKO, K. & DEMKOW, U. 2014. Perforin: an important player in immune response. *Cent Eur J Immunol*, 39, 109-15.
- PALUSSIÈRE, J., MARCET, B., DESCAT, E., DESCHAMPS, F., RAO, P., RAVAUD, A., BROUSTE, V. & DE BAERE, T. 2011. Lung tumors treated with percutaneous radiofrequency ablation: computed tomography imaging follow-up. *Cardiovasc Intervent Radiol*, 34, 989-97.
- PANDA, S. K. & COLONNA, M. 2019. Innate Lymphoid Cells in Mucosal Immunity. *Frontiers in Immunology*, 10.
- PARDOLL, D. M. 2012. The blockade of immune checkpoints in cancer immunotherapy. *Nat Rev Cancer*, 12, 252-64.

- PARRY, R. V., CHEMNITZ, J. M., FRAUWIRTH, K. A., LANFRANCO, A. R., BRAUNSTEIN, I., KOBAYASHI, S. V., LINSLEY, P. S., THOMPSON, C. B. & RILEY, J. L. 2005. CTLA-4 and PD-1 receptors inhibit T-cell activation by distinct mechanisms. *Molecular and cellular biology*, 25, 9543-9553.
- PATSOUKIS, N., DUKE-COHAN, J. S., CHAUDHRI, A., AKSOYLAR, H.-I., WANG, Q., COUNCIL, A., BERG, A., FREEMAN, G. J. & BOUSSIOTIS, V. A. 2020. Interaction of SHP-2 SH2 domains with PD-1 ITSM induces PD-1 dimerization and SHP-2 activation. *Communications Biology*, 3, 128.
- PERRI, F., PISCONTI, S. & DELLA VITTORIA SCARPATI, G. 2016. P53 mutations and cancer: a tight linkage. *Annals of translational medicine*, 4, 522-522.
- PHILIPS, E. A., GARCIA-ESPAÑA, A., TOCHEVA, A. S., AHEARN, I. M., ADAM, K. R., PAN, R., MOR, A. & KONG, X.-P. 2020. The structural features that distinguish PD-L2 from PD-L1 emerged in placental mammals. *Journal of Biological Chemistry*, 295, 4372-4380.
- QIN, S., XU, L., YI, M., YU, S., WU, K. & LUO, S. 2019. Novel immune checkpoint targets: moving beyond PD-1 and CTLA-4. *Molecular Cancer*, 18, 155.
- QURESHI, O. S., KAUR, S., HOU, T. Z., JEFFERY, L. E., POULTER, N. S., BRIGGS, Z., KENEFECK, R., WILLOX, A. K., ROYLE, S. J., RAPPOPORT, J. Z. & SANSOM, D. M. 2012. Constitutive clathrin-mediated endocytosis of CTLA-4 persists during T cell activation. *J Biol Chem*, 287, 9429-40.
- QURESHI, O. S., ZHENG, Y., NAKAMURA, K., ATTRIDGE, K., MANZOTTI, C., SCHMIDT, E. M., BAKER, J., JEFFERY, L. E., KAUR, S., BRIGGS, Z., HOU, T. Z., FUTTER, C. E., ANDERSON, G., WALKER, L. S. & SANSOM, D. M. 2011. Trans-endocytosis of CD80 and CD86: a molecular basis for the cell-extrinsic function of CTLA-4. *Science*, 332, 600-3.
- RAMA, N., MONTEIRO, A., BERNARDO, J. E., EUGÉNIO, L. & ANTUNES, M. J. 2009. Lung metastases from colorectal cancer: surgical resection and prognostic factors☆. *European Journal of Cardio-Thoracic Surgery*, 35, 444-449.
- RAO, P., ESCUDIER, B. & DE BAERE, T. 2011. Spontaneous Regression of Multiple Pulmonary Metastases After Radiofrequency Ablation of a Single Metastasis. *CardioVascular and Interventional Radiology*, 34, 424-430.
- ROACH, C., ZHANG, N., CORIGLIANO, E., JANSSON, M., TOLAND, G., PONTO, G., DOLLED-FILHART, M., EMANCIPATOR, K., STANFORTH, D. & KULANGARA, K. 2016. Development of a Companion Diagnostic PD-L1 Immunohistochemistry Assay for Pembrolizumab Therapy in Non-Small-cell Lung Cancer. *Appl Immunohistochem Mol Morphol*, 24, 392-7.
- ROMANO, E., KUSIO-KOBIALKA, M., FOUKAS, P. G., BAUMGAERTNER, P., MEYER, C., BALLABENI, P., MICHIELIN, O., WEIDE, B., ROMERO, P. & SPEISER, D. E. 2015.

- Ipilimumab-dependent cell-mediated cytotoxicity of regulatory T cells ex vivo by nonclassical monocytes in melanoma patients. *Proc Natl Acad Sci U S A*, 112, 6140-5.
- ROSS, K. & JONES, R. J. 2017. Immune checkpoint inhibitors in renal cell carcinoma. *Clin Sci (Lond)*, 131, 2627-2642.
- ROWSHANRAVAN, B., HALLIDAY, N. & SANSOM, D. M. 2018. CTLA-4: a moving target in immunotherapy. *Blood*, 131, 58-67.
- SALEH, R. & ELKORD, E. 2019. Treg-mediated acquired resistance to immune checkpoint inhibitors. *Cancer Lett*, 457, 168-179.
- SÁNCHEZ-MAGRANER, L., MILES, J., BAKER, C. L., APPLEBEE, C. J., LEE, D. J., ELSHEIKH, S., LASHIN, S., WITHERS, K., WATTS, A. G., PARRY, R., EDMEAD, C., LOPEZ, J. I., MEHTA, R., ITALIANO, A., WARD, S. G., PARKER, P. J. & LARIJANI, B. 2020. High PD-1/PD-L1 Checkpoint Interaction Infers Tumor Selection and Therapeutic Sensitivity to Anti-PD-1/PD-L1 Treatment. *Cancer Res*, 80, 4244-4257.
- SANSOM, D. M. & WALKER, L. S. K. 2019. Dimers Aren't Forever: CD80 Breaks up with PD-L1. *Immunity*, 51, 972-974.
- SASIDHARAN NAIR, V. & ELKORD, E. 2018. Immune checkpoint inhibitors in cancer therapy: a focus on T-regulatory cells. *Immunol Cell Biol*, 96, 21-33.
- SCHMIDT, A., OBERLE, N. & KRAMMER, P. 2012. Molecular Mechanisms of Treg-Mediated T Cell Suppression. *Frontiers in Immunology*, 3.
- SCHUBERT, M. S., THOMMANDRU, B., WOODLEY, J., TURK, R., YAN, S., KURGAN, G., MCNEILL, M. S. & RETTIG, G. R. 2021. Optimized design parameters for CRISPR Cas9 and Cas12a homology-directed repair. *Scientific Reports*, 11, 19482.
- SCHUELLER, G., KETTENBACH, J., SEDIVY, R., STIFT, A., FRIEDL, J., GNANT, M. & LAMMER, J. 2004. Heat shock protein expression induced by percutaneous radiofrequency ablation of hepatocellular carcinoma in vivo. *Int J Oncol*, 24, 609-13.
- SCHWAMBORN, K., KRIEGSMANN, M. & WEICHERT, W. 2017. MALDI imaging mass spectrometry - From bench to bedside. *Biochim Biophys Acta Proteins Proteom*, 1865, 776-783.
- SHARMA, A. & RUDRA, D. 2019. Regulatory T cells as therapeutic targets and mediators. *International Reviews of Immunology*, 38, 183-203.
- SHEPPARD, K. A., FITZ, L. J., LEE, J. M., BENANDER, C., GEORGE, J. A., WOOTERS, J., QIU, Y., JUSSIF, J. M., CARTER, L. L., WOOD, C. R. & CHAUDHARY, D. 2004. PD-1 inhibits T-cell receptor induced phosphorylation of the ZAP70/CD3zeta signalosome and downstream signaling to PKCtheta. *FEBS Lett*, 574, 37-41.

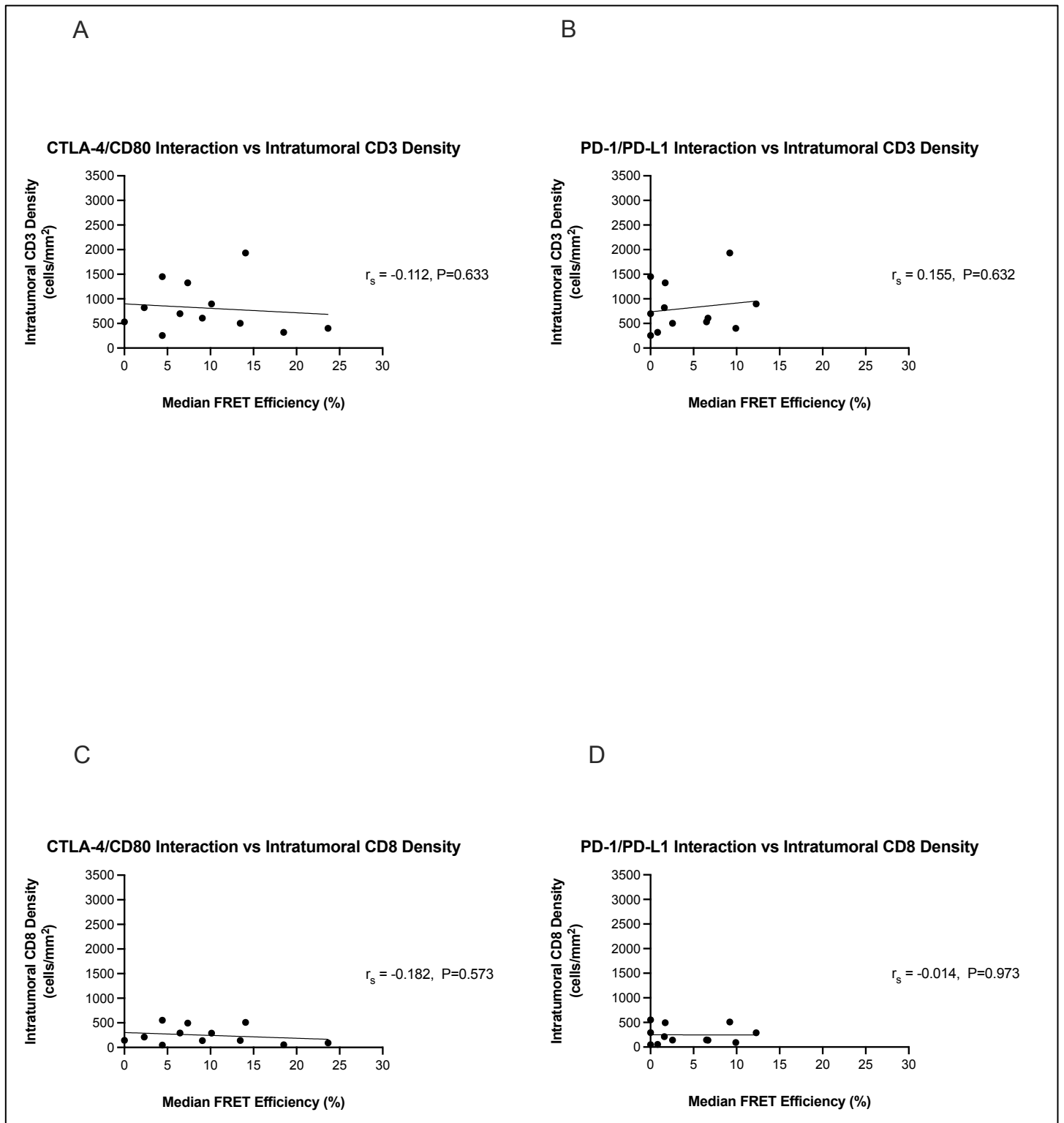
- SHI, B., XUE, M., WANG, Y., WANG, Y., LI, D., ZHAO, X. & LI, X. 2018. An improved method for increasing the efficiency of gene transfection and transduction. *International journal of physiology, pathophysiology and pharmacology*, 10, 95-104.
- SINHA, A. & MANN, M. 2020. A beginner's guide to mass spectrometry-based proteomics. *The Biochemist*, 42, 64-69.
- SMITH-GARVIN, J. E., KORETZKY, G. A. & JORDAN, M. S. 2009. T cell activation. *Annu Rev Immunol*, 27, 591-619.
- SÖDERBERG, O., LEUCHOWIUS, K. J., GULLBERG, M., JARVIUS, M., WEIBRECHT, I., LARSSON, L. G. & LANDEGREN, U. 2008. Characterizing proteins and their interactions in cells and tissues using the in situ proximity ligation assay. *Methods*, 45, 227-32.
- SOMMER, U., ECKSTEIN, M., AMMANN, J., BRAUNSCHWEIG, T., MACHER-GÖPPINGER, S., SCHWAMBORN, K., HIEKE-SCHULZ, S., HARLOW, G., FLORES, M., WULLICH, B., WIRTH, M., ROTH, W., KNÜCHEL, R., WEICHERT, W., BARETTON, G. & HARTMANN, A. 2020. Multicentric Analytical and Inter-observer Comparability of Four Clinically Developed Programmed Death-ligand 1 Immunohistochemistry Assays in Advanced Clear-cell Renal Cell Carcinoma. *Clin Genitourin Cancer*, 18, e629-e642.
- SONG, G., OUYANG, G. & BAO, S. 2005. The activation of Akt/PKB signaling pathway and cell survival. *J Cell Mol Med*, 9, 59-71.
- STAMPER, C. C., ZHANG, Y., TOBIN, J. F., ERBE, D. V., IKEMIZU, S., DAVIS, S. J., STAHL, M. L., SEEHRA, J., SOMERS, W. S. & MOSYAK, L. 2001. Crystal structure of the B7-1/CTLA-4 complex that inhibits human immune responses. *Nature*, 410, 608-611.
- STUMPF, M., ZHOU, X., CHIKUMA, S. & BLUESTONE, J. A. 2014. Tyrosine 201 of the cytoplasmic tail of CTLA-4 critically affects T regulatory cell suppressive function. *European journal of immunology*, 44, 1737-1746.
- SUGITA, S., USUI, Y., HORIE, S., FUTAGAMI, Y., YAMADA, Y., MA, J., KEZUKA, T., HAMADA, H., USUI, T., MOCHIZUKI, M. & YAMAGAMI, S. 2009. Human Corneal Endothelial Cells Expressing Programmed Death-Ligand 1 (PD-L1) Suppress PD-1+ T Helper 1 Cells by a Contact-Dependent Mechanism. *Investigative Ophthalmology & Visual Science*, 50, 263-272.
- SUN, Z., FOURCADE, J., PAGLIANO, O., CHAUVIN, J. M., SANDER, C., KIRKWOOD, J. M. & ZAROOR, H. M. 2015. IL10 and PD-1 Cooperate to Limit the Activity of Tumor-Specific CD8+ T Cells. *Cancer Res*, 75, 1635-44.
- TEMPLETON, A. J., MCNAMARA, M. G., ŠERUGA, B., VERA-BADILLO, F. E., ANEJA, P., OCAÑA, A., LEIBOWITZ-AMIT, R., SONPAVDE, G., KNOX, J. J., TRAN, B., TANNOCK, I. F. & AMIR, E. 2014. Prognostic role of neutrophil-to-lymphocyte ratio in solid tumors: a systematic review and meta-analysis. *J Natl Cancer Inst*, 106, dju124.

- THEELEN, W. S. M. E. & BAAS, P. 2019. Pembrolizumab monotherapy for PD-L1 $\geq 50\%$ non-small cell lung cancer, undisputed first choice? *Annals of translational medicine*, 7, S140-S140.
- TUMEH, P. C., HARVIEW, C. L., YEARLEY, J. H., SHINTAKU, I. P., TAYLOR, E. J., ROBERT, L., CHMIELOWSKI, B., SPASIC, M., HENRY, G., CIOBANU, V., WEST, A. N., CARMONA, M., KIVORK, C., SEJA, E., CHERRY, G., GUTIERREZ, A. J., GROGAN, T. R., MATEUS, C., TOMASIC, G., GLASPY, J. A., EMERSON, R. O., ROBINS, H., PIERCE, R. H., ELASHOFF, D. A., ROBERT, C. & RIBAS, A. 2014. PD-1 blockade induces responses by inhibiting adaptive immune resistance. *Nature*, 515, 568-71.
- VALEUR, B. & BERBERAN-SANTOS, M. N. 2013. *Molecular fluorescence : principles and applications*, Weinheim, Germany, Wiley-VCH Verlag GmbH & Co. KGaA.
- VEERIAH, S., LEBOUCHER, P., DE NAUROIS, J., JETHWA, N., NYE, E., BUNTING, T., STONE, R., STAMP, G., CALLEJA, V., JEFFREY, S. S., PARKER, P. J. & LARIJANI, B. 2014. High-throughput time-resolved FRET reveals Akt/PKB activation as a poor prognostic marker in breast cancer. *Cancer Res*, 74, 4983-95.
- VERMA, N., BURNS, S. O., WALKER, L. S. K. & SANSOM, D. M. 2017. Immune deficiency and autoimmunity in patients with CTLA-4 (CD152) mutations. *Clinical & Experimental Immunology*, 190, 1-7.
- WANG, C. & FAKIH, M. 2021. Targeting MSS colorectal cancer with immunotherapy: are we turning the corner? *Expert Opin Biol Ther*, 21, 1347-1357.
- WANG, K.-Y., WU, C., SHIMAJIRI, S., ENOMOTO, T., KUBOTA, H., AKIYAMA, H. & OHMIYA, Y. 2020. Quantitative immunohistochemistry using an antibody-fused bioluminescent protein. *BioTechniques*, 69, 302-306.
- WANG, W., LIU, L., SONG, X., MO, Y., KOMMA, C., BELLAMY, H. D., ZHAO, Z. J. & ZHOU, G. W. 2011. Crystal structure of human protein tyrosine phosphatase SHP-1 in the open conformation. *Journal of cellular biochemistry*, 112, 2062-2071.
- WATSON, H. A., WEHENKEL, S., MATTHEWS, J. & AGER, A. 2016. SHP-1: the next checkpoint target for cancer immunotherapy? *Biochem Soc Trans*, 44, 356-62.
- WIDENMEYER, M., SHEBZUKHOV, Y., HAEN, S. P., SCHMIDT, D., CLASEN, S., BOSS, A., KUPRASH, D. V., NEDOSPASOV, S. A., STENZL, A., AEBERT, H., WERNET, D., STEVANOVIĆ, S., PEREIRA, P. L., RAMMENSEE, H. G. & GOUTTEFANGEAS, C. 2011. Analysis of tumor antigen-specific T cells and antibodies in cancer patients treated with radiofrequency ablation. *Int J Cancer*, 128, 2653-62.
- WIECZOREK, M., ABUALROUS, E. T., STICHT, J., ÁLVARO-BENITO, M., STOLZENBERG, S., NOÉ, F. & FREUND, C. 2017. Major Histocompatibility Complex (MHC) Class I and MHC Class II Proteins: Conformational Plasticity in Antigen Presentation. *Frontiers in Immunology*, 8.

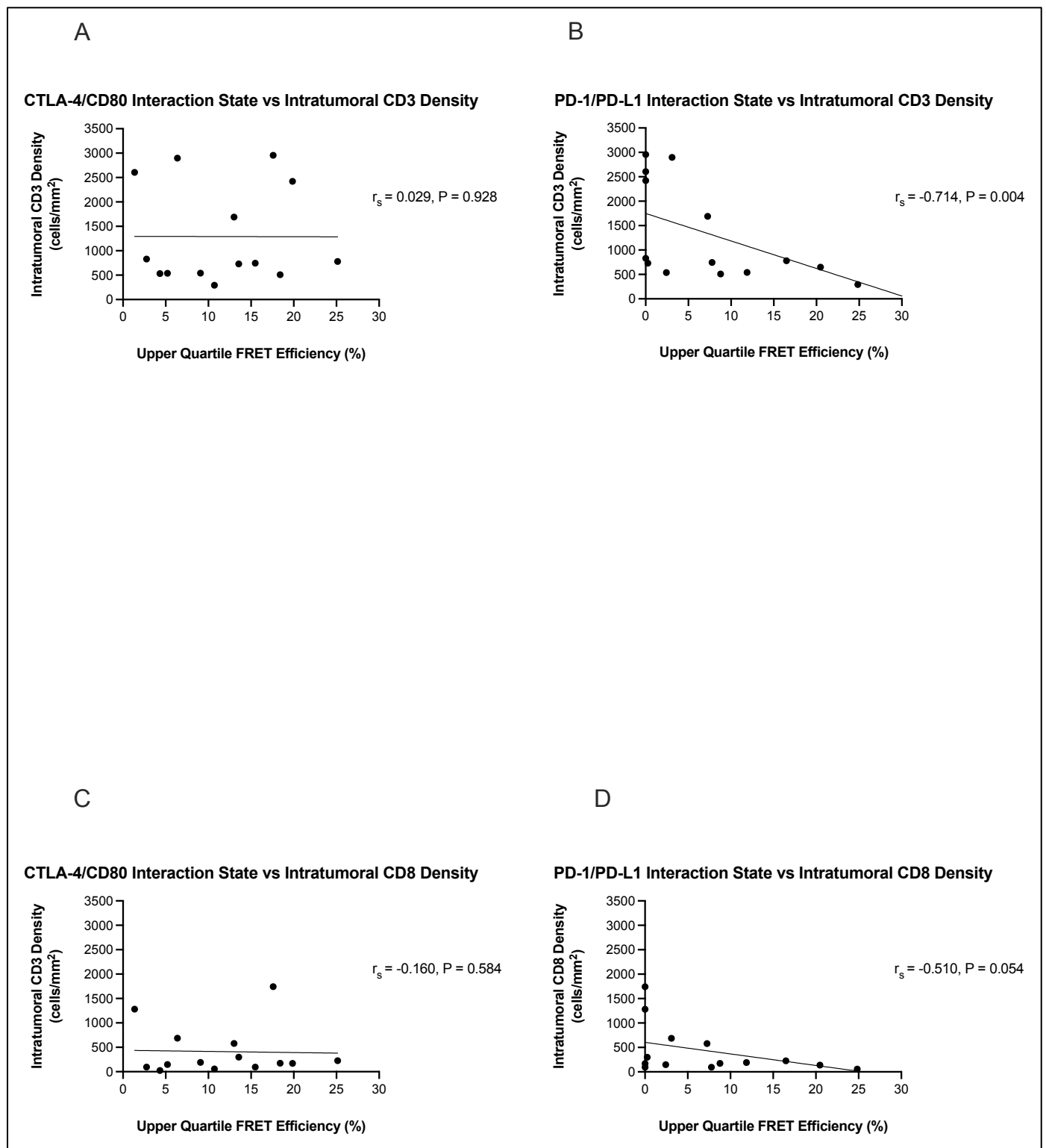
- WOUTERS, F. S. & BASTIAENS, P. I. H. 2000. Imaging Protein-Protein Interactions by Fluorescence Resonance Energy Transfer (FRET) Microscopy. *Current Protocols in Cell Biology*, 7, 17.1.1-17.1.15.
- WU, W. C., SUN, H. W., CHEN, H. T., LIANG, J., YU, X. J., WU, C., WANG, Z. & ZHENG, L. 2014. Circulating hematopoietic stem and progenitor cells are myeloid-biased in cancer patients. *Proc Natl Acad Sci U S A*, 111, 4221-6.
- YANG, J., LIU, L., HE, D., SONG, X., LIANG, X., ZHAO, Z. J. & ZHOU, G. W. 2003. Crystal Structure of Human Protein-tyrosine Phosphatase SHP-1. *Journal of Biological Chemistry*, 278, 6516-6520.
- YOKOSUKA, T., TAKAMATSU, M., KOBAYASHI-IMANISHI, W., HASHIMOTO-TANE, A., AZUMA, M. & SAITO, T. 2012. Programmed cell death 1 forms negative costimulatory microclusters that directly inhibit T cell receptor signaling by recruiting phosphatase SHP2. *J Exp Med*, 209, 1201-17.
- ZAK, K. M., GRUDNIK, P., MAGIERA, K., DÖMLING, A., DUBIN, G. & HOLAK, T. A. 2017. Structural Biology of the Immune Checkpoint Receptor PD-1 and Its Ligands PD-L1/PD-L2. *Structure*, 25, 1163-1174.
- ZHANG, J.-M. & AN, J. 2007. Cytokines, inflammation, and pain. *International anesthesiology clinics*, 45, 27-37.
- ZHANG, W., SLOAN-LANCASTER, J., KITCHEN, J., TRIBLE, R. P. & SAMELSON, L. E. 1998. LAT: The ZAP-70 Tyrosine Kinase Substrate that Links T Cell Receptor to Cellular Activation. *Cell*, 92, 83-92.
- ZHANG, X., SCHWARTZ, J. C., GUO, X., BHATIA, S., CAO, E., LORENZ, M., CAMMER, M., CHEN, L., ZHANG, Z. Y., EDIDIN, M. A., NATHENSON, S. G. & ALMO, S. C. 2004. Structural and functional analysis of the costimulatory receptor programmed death-1. *Immunity*, 20, 337-47.
- ZHANG, Z., QIU, S., ZHANG, X. & CHEN, W. 2018. Optimized DNA electroporation for primary human T cell engineering. *BMC Biotechnol*, 18, 4.
- ZHAO, Y., LEE, C. K., LIN, C. H., GASSEN, R. B., XU, X., HUANG, Z., XIAO, C., BONORINO, C., LU, L. F., BUI, J. D. & HUI, E. 2019. PD-L1:CD80 Cis-Heterodimer Triggers the Co-stimulatory Receptor CD28 While Repressing the Inhibitory PD-1 and CTLA-4 Pathways. *Immunity*, 51, 1059-1073.e9.
- ZHENG, Y., FANG, Y. C. & LI, J. 2019. PD-L1 expression levels on tumor cells affect their immunosuppressive activity. *Oncol Lett*, 18, 5399-5407.
- ZHU, J., YAMANE, H. & PAUL, W. E. 2010. Differentiation of effector CD4 T cell populations. *Annual review of immunology*, 28, 445-489.

ZHU, J. C., YAN, T. D. & MORRIS, D. L. 2008. A systematic review of radiofrequency ablation for lung tumors. *Ann Surg Oncol*, 15, 1765-74.

Appendix



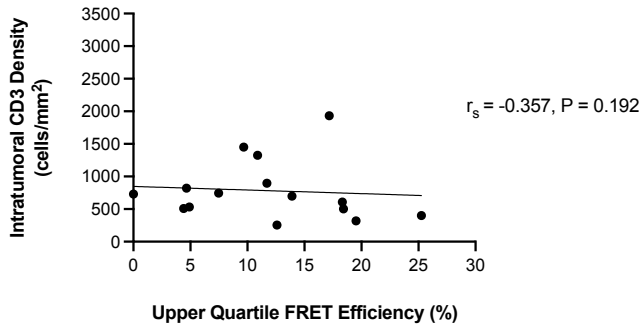
Appendix 1.1: Median CTLA-4/CD80 and PD-1/PD-L1 interaction states fail to correlate with intratumoral lymphocyte infiltration in lung two (post-RFA) **A)** Median CTLA-4/CD80 interaction states failed to correlate with intratumoral CD3⁺ infiltration in samples taken from lung two, $r_s = -0.112, P=0.633$. **B)** Intratumoral CD3⁺ infiltration did not correlate with median PD-1/PD-L1 interaction in samples from lung two, $r_s = 0.155, P=0.632$. **C)** CD8⁺ infiltration failed to correlate with median CTLA-4/CD80 interaction state, $r_s = -0.182, P=0.573$. **D)** Median PD-1/PD-L1 interaction state did not correlate with intratumoral CD8⁺ infiltration in biopsies from lung two, $r_s = -0.014, P=0.973$.



Appendix 2.2: Upper Quartile PD-1/PD-L1 interaction states correlate with intratumoral CD3⁺ infiltration in lung one (pre-RFA). **A)** Upper quartile CTLA-4/CD80 interaction states failed to correlate with intratumoral CD3⁺ infiltration in samples taken from lung one, $r_s = -0.029, P = 0.928$. **B)** Intratumoral CD3⁺ infiltration significantly and negatively correlated with upper quartile PD-1/PD-L1 interaction in samples from lung one, $r_s = -0.714, P = 0.004$. **C)** CD8⁺ infiltration failed to correlate with upper quartile CTLA-4/CD80 interaction state, $r_s = -0.160, P = 0.584$. **D)** Upper quartile PD-1/PD-L1 interaction state negatively correlated with intratumoral CD8⁺ infiltration in biopsies from lung one, $r_s = -0.510, P = 0.054$, albeit with no significant difference. However, the result presented here is approaching statistical significance.

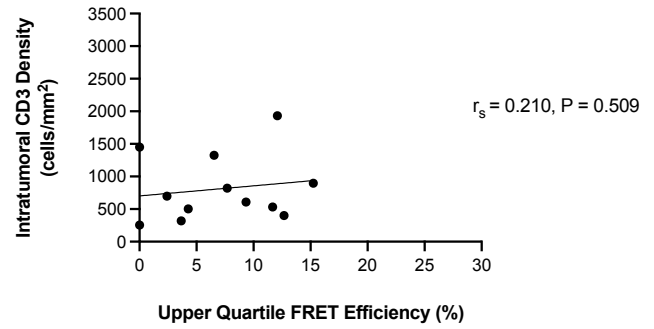
A

CTLA-4/CD80 Interaction State vs Intratumoral CD3 Density



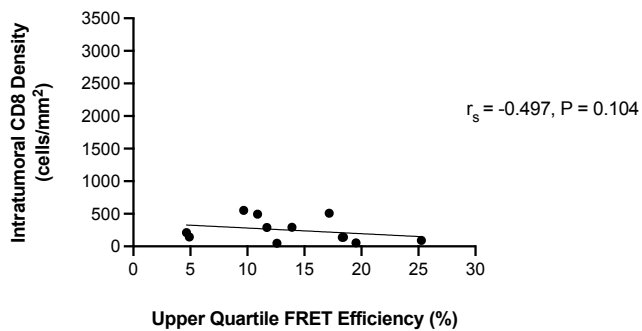
B

PD-1/PD-L1 Interaction State vs Intratumoral CD3 Density



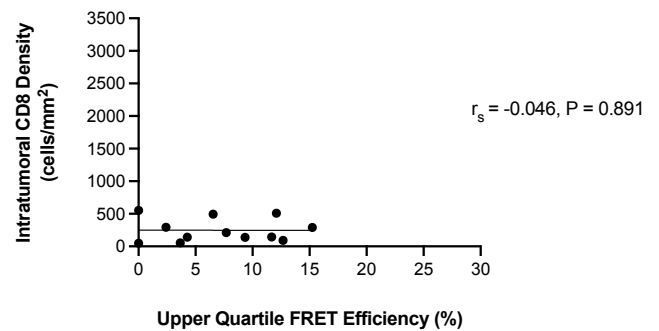
C

CTLA-4/CD80 Interaction State vs Intratumoral CD8 Density



D

PD-1/PD-L1 Interaction State vs Intratumoral CD8 Density



Appendix 3.3: Upper quartile CTLA-4/CD80 and PD-1/PD-L1 interaction states fail to correlate with intratumoral lymphocyte infiltration in lung two (post-RFA) **A)** Upper quartile CTLA-4/CD80 interaction states failed to correlate with intratumoral CD3⁺ infiltration in samples taken from lung two, $r_s = -0.357$, $P = 0.192$. **B)** Intratumoral CD3⁺ infiltration did not correlate with upper quartile PD-1/PD-L1 interaction in samples from lung two, $r_s = 0.210$, $P = 0.509$. **C)** CD8⁺ infiltration failed to correlate with upper quartile CTLA-4/CD80 interaction state, $r_s = -0.497$, $P = 0.104$. **D)** Upper quartile PD-1/PD-L1 interaction state did not correlate with intratumoral CD8⁺ infiltration in biopsies from lung two, $r_s = -0.046$, $P = 0.891$.